Summer 8-15-2019

Correlated SEM, FIB, and TEM Studies of Material Collected by the NASA Stardust Spacecraft

Brendan Albert Haas
Washington University in St. Louis

WASHINGTON UNIVERSITY IN ST. LOUIS

Department of Physics

Dissertation Examination Committee:
Ryan Ogliore, Chair
Martin H. Israel, Co-Chair
Bradley L. Jolliff
Brian Rauch
Kun Wang

Correlated SEM, FIB, and TEM Studies of Material Collected by the NASA Stardust Spacecraft

by
Brendan Albert Haas

A dissertation presented to
The Graduate School
of Washington University in
partial fulfillment of the
requirements for the degree
of Doctor of Philosophy

August 2019
St. Louis, Missouri

Table of Contents

List of Figures

List of Tables

Acknowledgments

This thesis is the result of years of work that could not have been accomplished without the support of family, friends, and colleagues. My advisors, first Christine Floss and then Ryan Ogliore, have been fantastic sources of knowledge whose doors were always open. I've always been thankful that Christine was willing to take a chance on me as an untested graduate student and allow me to study some of the rarest materials in the Solar System. She was always kind and attentive and I miss her deeply. I'm grateful that Ryan was willing to step in and take me under his wing so shortly after arriving at Washington University. He has done a wonderful job of joining my project and guiding me towards the end of my dissertation. The time and effort that both Christine and Ryan dedicated towards my personal growth as a scientist and a researcher is something that I will always appreciate.

The other members of the Laboratory for Space Sciences at Washington University, known to most as the '4th floor', have also been extremely supportive of my work. Tim Smolar has spent countless hours helping me repair faulty equipment and has always been emotionally supportive during stressful times. Kevin Croat dedicated many days to teaching me how to use the lab's complex equipment, and he dedicated even more days to answering my unrelenting follow-up questions. Evan Groopman, Joben Lewis, and Pierre Haenecour were all like mini-advisors to me and they helped me grow from the lab's rookie into the lab's hardened veteran. The lab's new graduate students, Kainen Utt, Nate Conway, and Andrew Diaz, have been a welcoming group who are always happy to commiserate with me.

Outside of the 4th floor, Rhonda Stroud from the Naval Research Laboratory was extremely helpful through her collaborations with our group in studying the Stardust foils. She taught me many useful experimental techniques and helped introduce me to the field of microanalysis.

Andrew Westphal from the University of California at Berkeley was also a fantastic collaborator who patiently performed exceedingly difficult sample extractions for us while also being an excellent source of information regarding the Stardust mission. Our collaborators Anton Kearsley and Mark Burchell, who helped us with the creation of our analog foils, were also much appreciated. I'd also like to acknowledge NASA's support in this project through their funding of the NASA Earth and Space Science Fellowship (NESSF) which provided the funds for much of the work described in this thesis. NASA's support of Christine's research prior to the NESSF was also instrumental in allowing us to perform the initial studies that demonstrated that this research was feasible and worthwhile.

Finally, I'd like to thank the family and friends whose love and kindness have allowed me to survive my journey through graduate school. Matt Reisman and Nara Higano were great friends who were also smart enough to assist me on the toughest homework problems, just to name a few of the dozens of friends who have supported me during my studies. My parents, Bert and Sally, were always fully supportive of my studies even when they didn't understand what exactly I was doing, showing that their love knows no boundaries. And I'm so glad that I was able to share the doctoral journey with Kim, my fiancée. I love you and I look forward to our lives together.

Brendan Albert Haas

Washington University in St. Louis

August 2019

In memory of Christine Floss.

Abstract of the Dissertation

Correlated SEM, FIB, and TEM Studies of Material Collected by the NASA Stardust Spacecraft

by

Brendan Albert Haas

Candidate for Doctor of Philosophy in Physics

Washington University in St. Louis, 2019

Professor Ryan Ogliore, Chair

Professor Martin H. Israel, Co-Chair

The objective of this thesis is to describe the study of cometary materials returned by NASA's Stardust mission. The majority of the research presented in this thesis focuses on improving our characterization and understanding of the fine (< 1 μm) component of comet Wild 2. Investigations of the Stardust foils are conducted with correlated Scanning Electron Microscopy (SEM), Focused Ion Beam (FIB) sample preparation, and Transmission Electron Microscopy (TEM). Investigations of the Stardust aerogels are conducted with plasma ashing sample preparation followed by detailed characterization of the material with TEM. Additional studies of the Stardust interstellar foils, as well as the use of a Convolutional Neural Network (CNN) to search images of the Stardust foils for impact features, are also presented.

As a part of this thesis I have developed a new technique for analyzing the Stardust aerogels through the use of plasma ashing sample preparation. This technique is an improvement upon previous attempts to separate cometary materials from the aerogel through the use of HF vapor etching. Plasma ashing allows for cometary materials trapped within the Stardust aerogels to be deposited directly onto TEM grids allowing for detailed characterization of the cometary material with minimal interference from the aerogel itself.

The correlated SEM/FIB/TEM studies of the Stardust foils demonstrated here nearly double the number of Stardust craters that have been elementally and structurally characterized in scientific literature. The crater impactor residues were largely composed of combinations of silicates and iron-nickel sulfides that, following impact, rapidly quenched into amorphous melt layers. Two craters were found to contain signatures of the refractory minerals spinel and taenite, indicating a component of the Wild 2 fines originated in the inner Solar System. However, the lack of crystalline material throughout the crater residues suggests that the fine component may largely be composed of amorphous silicates that likely formed in the outer Solar System. Additionally, the submicron Stardust craters appeared enriched in volatile elements relative to CI chondrites, further suggesting that the fine component of Wild 2 originated from a reservoir that was separate from the more refractory coarse (> 1 μm) component.

The Stardust aerogel samples returned carbon-rich and potential oldhamite grains. Carbon-rich materials have not been previously observed in the Stardust foils, likely due to the violent collection methods, and the result suggests the ashing technique may be used to better characterize components of the Wild 2 fines that have been difficult to investigate. The presence of oldhamite in the Stardust aerogels would be scientifically significant as it is formed in highly reducing conditions and has only been identified in enstatite chondrites and enstatite achondrites. As a result, our results may call into question the Warren gap hypothesis, which would prohibit the presence of such highly reduced materials in the outer Solar System at the time that comet Wild 2 accreted.

Chapter 1: Introduction

1.1 Chapter 1: Introduction

The objective of this thesis is to describe the characterization of cometary and interstellar material collected by NASA's Stardust spacecraft through the use of Scanning Electron Microscopy (SEM), Energy-Dispersive X-ray Spectroscopy (EDXS), Focused Ion Beam (FIB) sample preparation, Transmission Electron Microscopy (TEM), and Selected Area Electron Diffraction (SAD), with a focus on correlating these laboratory studies with early Solar System evolution and processes. This chapter provides a brief introduction to the following chapters in this thesis.

1.2 Chapter 2: Background

Chapter 2 focuses on the history of cometary and Stardust mission studies. This chapter discusses the motivations for NASA's Stardust mission, the nature of the Stardust sample collector, and the results of studies of the cometary material thus far. Chapter 2 further discusses our motivation for continuing the study of the materials returned by Stardust, particularly the fine (submicron) component of Wild 2. The chapter concludes by discussing the goals of the research presented in the following chapters of this thesis.

1.3 Chapter 3: Methods

Chapter 3 discusses the sample preparation and analysis techniques that I applied during the study of analog, cometary, and interstellar materials. Sample preparation techniques include FIB extractions and plasma ashing. Characterization and analysis of the studied material was largely conducted with SEM, TEM, EDXS, and SAD techniques. This chapter also details the plasma asher sample preparation techniques that were developed as a part of this thesis.

1.4 Chapter 4: Analog Foils

Chapter 4 is an adaptation of a peer-reviewed journal article and three conference abstracts regarding the behavior of analog materials fired through a light gas gun at flight-spare Stardust foils in order to replicate the impact processing experienced on the foils present on the Stardust sample collector: "Survival of Refractory Presolar Grain Analogs During Stardust-like Impact into Al Foils: Implications for Wild 2 Presolar Grain Abundances and Study of the Cometary Fine-Fraction" by Croat T. K., Floss C., Haas B. A., Burchell M. J., and Kearsley A. T. (**2015**) Meteoritics and Planetary Science, 50:1378-1391; "Characterizing Comet 81P/Wild 2 with Acfer 094 Analog Foils" by Haas B. A., Croat T. K., Floss C., Kearsley A. T., and Burchell M. J. (**2015**) in the 78th Annual Meeting of the Meteoritical Society, Abstract #5141; "Characterizing Comet 81P/Wild 2 with Acfer 094 Analog Foils" by Haas B. A., Croat T. K., Floss C., Kearsley A. T., and Burchell M. J. (**2016**) in the 47th Lunar and Planetary Science Conference, Abstract #1597; and "Characterizing Comet 81P/Wild 2 with Tagish Lake Analog Foils" by Haas B. A., Floss C., Kearsley A. T., and Burchell M. J. (2017) in the 80th Annual Meeting of the Meteoritical Society, Abstract #6246. This chapter studies the effect of foil impact processing on analog samples composed of TiC, TiN, SiC, SiN, and material from the Acfer 094 and Tagish Lake meteorites through the use of SEM and FIB-TEM techniques. These results provide insight into the low survival rate of presolar grains in the Stardust foils, the effect of impactor size on impactor survival rates, the lack of carbonates observed in Stardust samples, and the difficulty of replicating Stardust impact processing in a laboratory setting. The analog samples investigated in this chapter were created by our collaborators Anton Kearsley and Mark Burchell at the University of Kent.

1.5 Chapter 5: Stardust Cometary Foils

Chapter 5 is an adaptation of a journal article submitted for publication and three conference abstracts regarding the composition of Stardust foil impact craters investigated with correlated SEM and FIB/TEM analysis techniques: "FIB-TEM analysis of cometary material in 6 sub-micron craters on Stardust foil C2113N-A" has been accepted for publication in the Christine Floss memorial issue of Meteoritics and Planetary Science; "Characterization of the Fine Component of Comet Wild 2: Analysis of 11 Stardust Craters from Foil C2010W" by Haas B. A., Croat T. K., and Floss C. (**2016**) in the 79th Annual Meeting of the Meteoritical Society, Abstract #6386; "The Composition of Surviving Fine-Grained Cometary Material in Stardust Al Foil Craters" by Croat T. K., Haas B. A., and Floss C (**2016**) in the 47th Lunar and Planetary Science Conference, Abstract #2204; and "FIB/STEM Investigation of Four Impact Craters from the Stardust Comet Sample Return Mission Foils" by Haas B. A., Stroud R. M., and Floss C. (**2017**) in the 2017 Microscopy & Microanalysis Meeting. This chapter details FIB-TEM analysis done on 21 Stardust craters extracted from foils C2010W, C2113N-A, C2113N-B, and C2118N-B. We characterize the cometary material present in these foils in order to better constrain the composition, particularly of the fine (submicron) component of comet 81P/Wild 2. Work done on the C2113N-B and C2118N-B foils was done in collaboration with Rhonda Stroud at the Naval Research Laboratory.

1.6 Chapter 6: Stardust Interstellar Foils

Chapter 6 is an adaptation of the conference abstract "FIB/STEM Study of 2 Stardust ISPE Craters from Foil 1031N1,1" by Haas B. A., Stroud R. M., and Floss C. (**2017**) in the 80th Annual Meeting of the Meteoritical Society, Abstract #6316. This chapter details the FIB-TEM analysis done on two craters identified in foil present on the interstellar portion of the Stardust sample

collector. This work was done in collaboration with Rhonda Stroud at the Naval Research Laboratory.

1.7 Chapter 7: Analog and Stardust Aerogels

Chapter 7 is largely an adaptation of two conference abstracts regarding the sample preparation and following TEM analysis of analog and Stardust sample collector aerogel samples: "Application of Plasma Ashing to the Study of Stardust Mission Aerogel Samples" by Haas B. A., Ogliore R. C., and Floss C. (**2017**) in 48th Lunar and Planetary Science Conference, Abstract #2058; and "Study of Fine-Grained Material Recovered from a Stardust Aerogel Track Using Plasma Asher Preparation" by Haas B. A., Ogliore R. C., Westphal A. J., Croat T. K., and Floss C. (**2018**) in 49th Lunar and Planetary Science Conference, Abstract #2245. Aerogel sample collectors on the Stardust spacecraft were effective at decelerating and capturing incoming material, but the insulating nature of the aerogels complicates in situ analysis of this material with traditional electron microscopy techniques. This project aims to free and study cometary materials by destroying the surrounding aerogel with plasma ashing techniques. This work was done in collaboration with Andrew Westphal of the University of California, Berkeley.

1.8 Chapter 8: Convolutional Neural Networks for Finding Foil Features

Chapter 8 describes the use of machine learning in the form of a convolutional neural network (CNN) as a means of identifying features present on the Stardust foils. This chapter details the use of Python packages Tensorflow and Keras to design and use a simple CNN that is capable of identifying features on pre-acquired high-resolution SEM scans of Stardust foils. This project aims to minimize the need for human searches of images of these features, potentially saving dozens of man-hours of labor needed to adequately search thousands of foil images.

1.9 Chapter 9: Conclusions

Chapter 9 provides concluding remarks regarding the results and scope of the work presented in this thesis.

Chapter 2: Background

2.1 Preface

The study of astrophysical objects, outside of cosmic ray studies, typically relies upon the collection and analysis of electromagnetic radiation. Meteoritic material can be studied in greater detail due to its abundance on Earth and the higher precision of laboratory techniques compared to remote-sensing techniques. As of January 2019, over 60,000 unique meteorites have been named and cataloged (www.lpi.usra.edu/meteor/). Meteorites can be difficult to link to parent bodies, but thus far all established parent body sources originated from the inner Solar System. Despite the abundance of meteorites available for study, no unambiguously cometary samples have been recovered on Earth.

The lack of proven cometary material available for study leaves a gap in our understanding of the Solar System's evolution. Knowledge regarding the solid components that accreted to form planetesimals in the Kuiper Belt (beyond the orbit of Neptune) is extremely limited. Recent observations and models indicate that Kuiper Belt objects, though a small fraction of the total Solar System mass, compose >99% of the small bodies in the Solar System (Farinella & Davis 1996; Bottke *et al*., 2005; Schlichting *et al*., 2012). Some material believed to constitute the outer Solar System has been collected in the form of interplanetary dust particles (IDPs), but the histories of the bodies that they originated from are unknown. Collection of material from a known outer Solar System body would allow for the comparison of inner and outer solar nebula materials on a submicron level. By observing the differences between these two types of materials, we could constrain existing models or forge new ideas regarding the origin and mixing of materials in the early Solar System.

2.2 NASA's Stardust Mission

Given the lack of cometary material available for study on Earth, obtaining proven cometary material tied to a specific Solar System body required a sample return mission. NASA's Stardust mission launched on 7 February 1999 with the primary goal of encountering comet 81P/Wild 2, collecting particulate material from its coma, and returning to Earth with these samples (Brownlee *et al.*, 2003). The spacecraft also had a secondary goal of collecting interstellar dust (ISD) while traveling to the comet.

2.2.1 Stardust's Encounter with Comet 81P/Wild 2

Comet 81P/Wild 2 is a Jupiter family comet that, prior to 1974, orbited between a perihelion at 4.9 AU and an aphelion at 25 AU (Sekanina & Yeomans, 1985). Jupiter family comets are believed to have formed and resided within the Kuiper belt, and thus Wild 2 is likely a sample of outer solar nebula materials as well as presolar materials (Sekanina 2003). In 1974 the comet's proximity to Jupiter altered its orbit to having a perihelion at 1.58 AU and an aphelion at 5.2 AU (Tsou *et al.*, 2004). As a result, at the time of the Stardust mission Wild 2 had completed only five perihelion passages (Tsou *et al.*, 2004), minimizing solar damage to the comet while also positioning the comet within reach of a sample return mission.

During Wild 2's passages through the inner Solar System the comet experiences heating and ice sublimation. As a result, the comet produces dozens of jets of gas and dust that originate from subsurface regions (Brownlee *et al*., 2004). These jets contribute to forming the comet's coma, providing the source of the particulate matter that the Stardust spacecraft collected.

The Stardust spacecraft's encounter with Wild 2 occurred on 2 January 2004 at a distance of 1.86 AU from the Sun. Stardust's closest approach was 236.4 ± 1 km from Wild 2's nucleus (Tsou *et al*., 2004). Wild 2 was orbiting at a heliocentric speed of 26.4 km/s as it overtook the

Stardust spacecraft, resulting in a relative speed of 6.12 km/s compared to the spacecraft (Tsou *et al*., 2004).

2.2.2 Stardust's Collection of Interstellar Particles (ISPs)

The secondary objective of the Stardust spacecraft was to collect and return ~100 interstellar particles >0.1 μm in size. Contemporary interstellar dust originates from the local interstellar diffuse cloud that crosses paths with the Solar System's orbit through the Milky Way (Frisch 1994). While travelling to Wild 2 the opportunity was seized to collect interstellar particles. The backside of the Wild 2 sample collector served as the Stardust interstellar dust collector and was exposed to the interstellar dust stream for 195 days in 2000 and 2002 (Westphal *et al.*, 2014a). While the interstellar dust collector had a much longer exposure time than the cometary collector, the fluence of ISPs throughout the mission was far lower than the fluence of cometary particles during the spacecraft's encounter with Wild 2. ISP fluence calculations based upon data from the Ulysses and Galileo spacecrafts suggested that the interstellar dust collector would only contain 120 interstellar particles, with only a third of them measuring larger than two microns in diameter (Landgraf *et al*., 1999). The result was that the cometary collectors were much more heavily impacted than their interstellar counterparts (Stroud *et al*., 2014).

Current understanding of ISPs is limited. Interstellar dust is massively influential on many interstellar processes such as the formation of stars, but much of our knowledge of interstellar dust is based on astronomical observations that lack the ability to analyze this material on the submicron scale. Presolar grains, isotopically anomalous particles that survived the formation of the Solar System, have been identified in primitive meteorites, but studies of presolar grains have often focused on exotic minerals such as silicon carbide, graphite, and nanodiamonds due to their refractory nature (Zinner 2014). Additionally, much of the interstellar dust is unlikely to contain

the extreme isotopic anomalies that define presolar grains (Zhukovska *et al*., 2008). Presolar grains also represent primordial interstellar dust (ISD) and may not be representative of the ISD currently present in our Solar System. Stardust's capture of ISPs allows for in situ chemical analysis of the interstellar medium, making the few observed impacts in the Stardust interstellar dust collector critical to improving our knowledge of the interstellar medium.

2.2.3 The Stardust Sample Collector

An image of the Stardust sample collector is shown in Figure 2.1 (Tsou *et al*., 2003). The exposed area of each side of the sample collector consists of 1039 cm^2 of ultra low-density silica aerogel and 153 cm^2 of 101.6 μm thick 1100 aluminum foil (Tsou *et al*., 2003). The aerogel is composed of 132 capture cells for each side that are 3 cm thick on the cometary side and 1 cm thick on the interstellar side. The foils on each side are divided into 150 short foils measuring 1.3 cm by 0.23 cm and 146 long foils measuring 3.3 cm by 0.23 cm (Tsou *et al*., 2003). The aerogel was selected as a capture material because of its extremely low density, which was expected to decelerate the hypervelocity impactors while minimizing the damage inherent to the collection process. Impacts on aerogel more closely resemble penetration events than cratering ones because the impacting material loses speed as a continual process due to the aerogel's low density (Burchell *et al*., 2008a). Additionally, experiments on analog aerogel impactors found an aerogel coating built around the impacting particles as they decelerated, potentially protecting the particle (Tsou 1995). The aluminum foils were added to the collector to aid in the extraction of the aerogel tiles but were also found to contain numerous impacts.

The two collection media have each proven to have distinct advantages in capturing impacting material. The low-density aerogel tiles successfully decelerated and captured many coarse (>1 μm) impactors (Zolensky *et al*., 2008b). These particles formed bulbous impact

features in the aerogel with the terminal particles lying at the end of the impactor track (Figure 2.2). These terminal particles can be extracted using an automated keystone system that carefully cuts around and extracts entire impactor tracks from the aerogel tiles (Westphal *et al*., 2004). The terminal particles have been studied to better characterize the coarse component of comet Wild 2. The fine (<1 μm) component of the comet proved more difficult to study in the aerogel tracks. Fine grains largely did not survive as terminal particles and were instead spread across the aerogel's large (mm scale) bulbous impact features (Trigo-Rodrígues *et al*., 2008). As a result, the fine component of Wild 2 has been studied far less than the coarse component (Westphal *et al*., 2017).

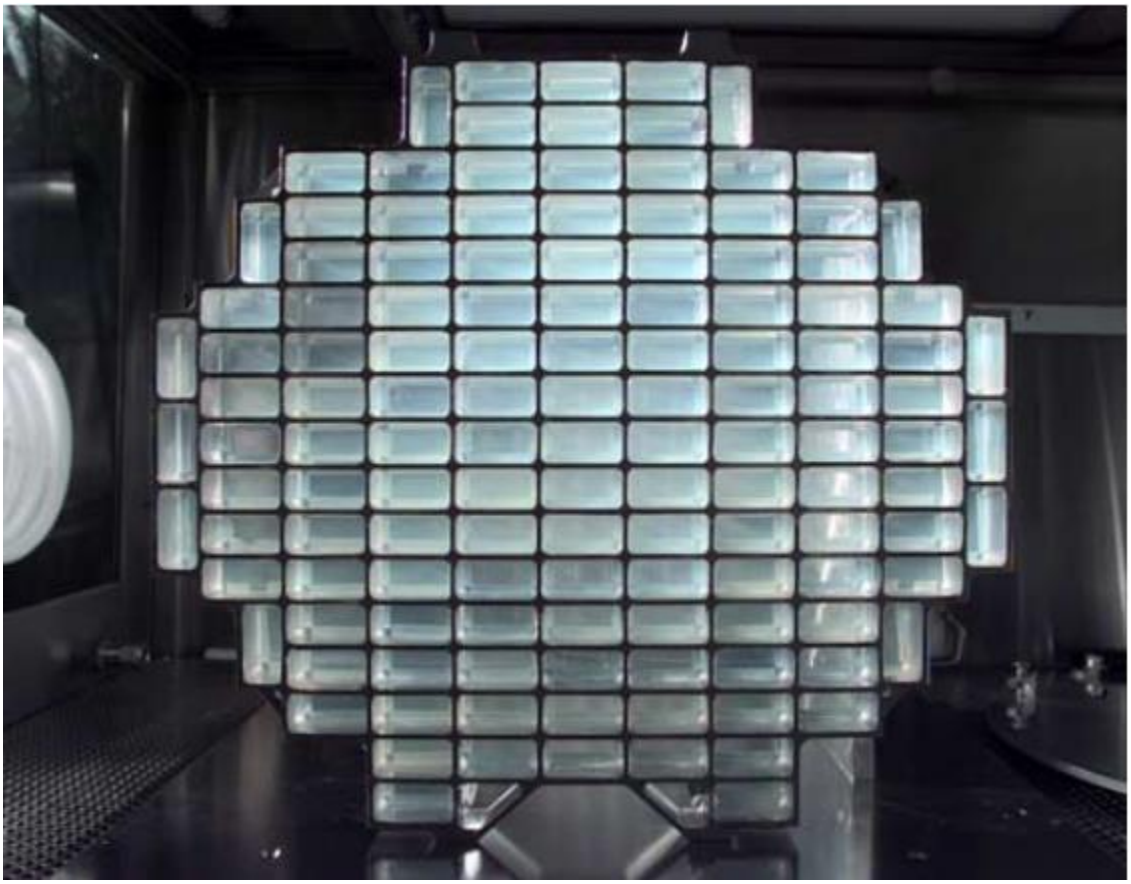

FIGURE 2.1: Figure 18 from Tsou *et al*., (2003). Image of the Stardust cometary and interstellar sample collector. The light blue aerogel tiles are surrounded and secured by the aluminum foils which are wrapped around the tray wall frames.

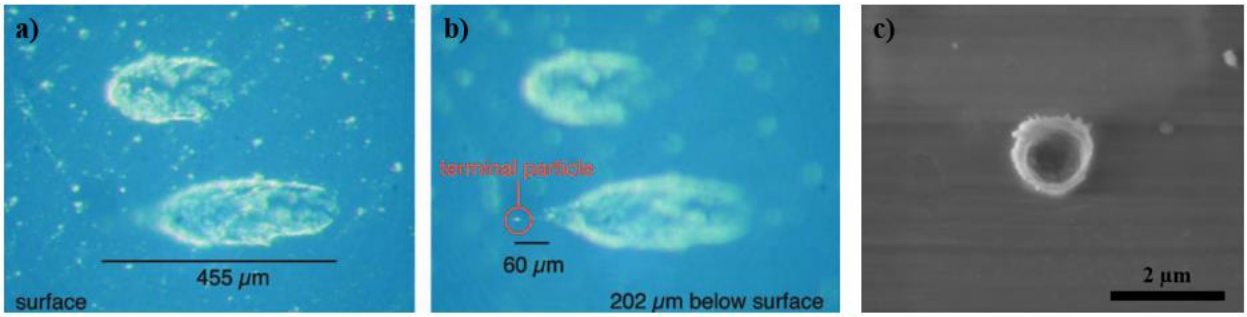

FIGURE 2.2: Images of the Stardust collection media after hypervelocity impacts by cometary material. a) and b) are from Figure 1 in Westphal *et al.* (2004a). A bulbous impact feature has formed in the aerogel tile as a result of decelerating the material, at least some of which is now present as a terminal particle at the end of the track. c) An impact crater present on Stardust foil C2010W.

Despite not being designed for sample collection, the Stardust foils have several advantages allowing them to complement the studies of the aerogels. Impactors in the foils were fully contained in micron-scale impact craters (Figure 2.2). As a result, fine grained impactors were more densely concentrated in the foil craters than in the bulbous impact features in the aerogel. The Stardust foils trade the Si contamination of the aerogel for the Al contamination of the foil, and the foils are also conductive and can easily be studied with electron microscopy techniques. Hypervelocity collection with the foils is noticeably more destructive than with the lower density aerogels. During impacts with higher density materials the front of the projectile slows but is crushed by the rear of the projectile as the impacted material cannot move away quickly enough, resulting in a shock wave (Burchell *et al.*, 2008). Despite the more destructive deceleration effects of the foils relative to the aerogels, studies of micron-scale and submicron impactors have frequently reported finding surviving crystalline impactor material in the crater residues (Leroux *et al.*, 2008; Leroux *et al.*, 2010; Stroud *et al.*, 2010). The foils are thus a promising avenue of study for analyzing the fine component of comet Wild 2. Intact crystalline material in submicron craters allows for study of the mineralogy of individual fine impactors, and the concentration of

fine grains into small impact craters allows for an easier analysis of the fine component's bulk composition.

2.3 Previous Investigations of the Stardust Aerogels

The Stardust aerogels successfully decelerated and captured many coarse impactors as terminal particles at the end of tracks within the aerogel tiles (Zolensky *et al*., 2008b). Solid, non-fragmenting grains produced long, thin tracks with coarse cometary particles surrounded by a protective cap of compressed aerogel (Westphal *et al*., 2017). While all aerogel tracks contained components that were modified to various degrees by the molten silica that lined the track walls (Ishii *et al*., 2008), some of the coarse solid grains contained well-preserved interiors. Thermal capture effects appeared to only influence the outer micrometer of larger grains while thermal inertia protected the interiors, resulting in coarse grains being better preserved than fine ones (Brownlee *et al*., 2012).

Several properties of the comet's coarse material were immediately surprising to researchers. The cometary material appeared more 'meteoritic' than many had anticipated. Microchondrules and micro-CAIs (calcium-aluminum-rich inclusions), which most likely formed in the hot inner Solar System, were identified within the cometary material, defying the common belief that comets formed in isolation in the outer Solar System (Simon *et al*., 2008; Chi *et al*., 2009). The coarse component showed depletions in volatile elements (Brownlee *et al.*, 2012). Additionally, though the cometary material was isotopically heterogeneous, almost no presolar material was present (McKeegan *et al*., 2006). Presolar grains are a minor component of meteorites, but many expected to observe a far higher presolar grain abundance than has been reported in studies of the collected Wild 2 material. The coarse Wild 2 material collected by the aerogels was largely produced in high-temperature environments and later transported past the

orbit of Neptune, where these components accreted ice and organic components to form the comet (Brownlee *et al*., 2012).

The studied coarse components, which composed the majority of the collected mass, suggested a complex history for Wild 2's formation. Wild 2's coarse material was mostly composed of materials formed at high temperatures, but the comet had preserved its originally accreted solids (Brownlee *et al*., 2012). Many of the Wild 2 particles were found to be chondrule or chondrule-like fragments (Nakamura *et al*., 2008; Joswiak *et al*., 2012; Ogliore *et al*., 2012a). The meteoritic materials present within the coarse particles were extremely diverse, and could not be matched to any existing chondrite classes (Brownlee *et al*., 2012). Wild 2 thus appeared to differ from asteroids when comparing its location to the source of its accreted materials. While asteroids are dominated by locally produced materials, Wild 2 appears to be dominated by materials that formed far from where the comet accreted.

The early solar nebula contained multiple rock forming regions that created coarse materials seen in chondrites such as chondrules and CAIs. The majority of the studied coarse materials in the Stardust aerogels appear to be products of these regions that also contributed to the materials observed in chondrites. The coarse cometary material suggests that the materials that made comets derived from all dust-bearing regions of the Solar System, and that the coarse Wild 2 material is characterized by the diversity of its materials (Brownlee *et al*., 2012). However, the lack of mm-scale components collected during the Stardust mission makes it difficult to draw a direct comparison to many meteoritic components (e.g., chondrules and CAIs), which are frequently larger in size than the collected Wild 2 particles.

The fine (submicron) component of Wild 2 has proven more difficult to study in the aerogels. Many of the fine grains collected in the aerogel tiles were components of larger

aggregate impactors that were disaggregated and spread across millimeter-scale bulbous impact features (Burchell *et al*., 2008). The difficulty in studying the fine grains captured by the aerogel has resulted in less overall study of this component of Wild 2. However, characterizing the fine component of comet Wild 2 is critical to fully understanding the processes that contributed to its formation. Coarse particles typically form in fundamentally different ways than fine particles, with processing such as heating, aqueous alteration, and increased formation times necessary to form larger particles. Fine grains often form from processes such as direct condensation from a gaseous mixture, and thus sample different regions and processes than coarse grains. Current studies aiming to characterize comet Wild 2 are heavily biased towards the study of coarse materials, resulting in an incomplete picture of the processes and regions that contributed to the comet's formation.

Investigations of the fine grains have returned a variety of results on a particle-by-particle basis. Sub-micron particles from aerogel track 80 had solar abundances of Fe, Mg, and S when averaged together, but individually had a wide range of compositions, suggesting that the fine grains are consistent with thermally unprocessed primordial dust close to solar composition (Stodolna *et al*., 2012). Grains smaller than 2 microns in size have a wide range of O isotopic compositions, indicating that Wild 2 fine grains are either a diverse sampling of inner Solar System reservoirs or ancient outer-nebula dust (Ogliore *et al*., 2015). These results have differentiated the fine component from the coarse component's high-temperature origins.

The source of the Wild 2 fines could be determined through comparison of the Wild 2 fine volatile components with solar compositions. Materials formed in the inner Solar System would be depleted in volatiles relative to CI chondrites whereas materials inherited from the Solar System's parent molecular cloud would not (Ogliore *et al*., 2015). However, the dispersion of the

fine grains across bulbous impact features in the aerogel tiles, as well as the intermixing with the aerogel, makes bulk elemental analysis of the fines difficult in that medium.

2.4 Previous Investigations of the Stardust Foils

The difficulties in analyzing the impact craters on the Stardust foils has resulted in fewer studies of the foil impactors than the aerogel impactors. The relatively recent application of focused ion beam (FIB) sample preparation to the field of microanalysis has allowed researchers to extract and thin cross sections of these craters and thus probe the impactor residues present in the foils.

Craters studied on the cometary foils have largely been a micron in scale and were composed primarily of combinations of iron sulfides and silicates (Leroux *et al*., 2008; Leroux *et al*., 2010; Stroud *et al*., 2010). Despite the violent impact conditions, crystalline material has been relatively common within crater residues. Poorly crystalline graphite and a chromite grain have been observed in submicron craters (Stroud *et al*., 2010). Olivine, forsterite, enstatite, and pyroxene grains have also been observed in micron-scale impact craters (Leroux *et al*., 2008; Leroux *et al.*, 2010). Overall 10 out of 22 studied Stardust craters (Leroux *et al*., 2008; Leroux *et al*., 2010; Stroud *et al*., 2010) have contained surviving crystalline impactors, suggesting that the Stardust foils are a good source of information regarding the mineralogy of the Wild 2 fine component. Sulfur loss also appeared minimal within the studied craters, further indicating that the impact processing may have been less severe than initially predicted (Leroux *et al*., 2008; Stroud *et al*., 2010). The impactors' concentration into crater residues (rather than diffuse, bulbous impact tracks) allows for bulk elemental analyses of the comet's fine component that are more difficult to perform on the aerogel samples. For these reasons, continued study of the Stardust foils appears to be a promising means of improving characterization of the cometary fines on a

particle-by-particle basis as well as in terms of describing the bulk elemental composition of the fines.

2.5 Goals of the Presented Studies

Though the Stardust spacecraft returned with samples in 2006, many questions remain about the material collected by the spacecraft and how this material can help in characterizing Wild 2, and by extension, provide insight into the formation and composition of outer Solar System bodies. The fine component of the comet has proven particularly difficult to characterize given the collection media and collection velocities required for the Stardust mission. This thesis primarily aims to perform these tasks:

• Improve our understanding of the impact processing in the Stardust foils

-How are aggregate impactors processed compared to single-grain impactors?

-Are organic materials capable of surviving the impact processing?

• Improve our understanding of the fine component of Wild 2

-How is the fine component of Wild 2 fundamentally different from the coarse component?

-What is the source of the Wild 2 fines?

While the majority of the work presented in this thesis focuses on the study of cometary samples returned by the Stardust spacecraft, or the study of analogs to better understand the foils' impact processing, I also worked on several projects that are indirectly related to these tasks during my doctoral studies. Chapter 7 and Chapter 8 of this thesis thus present separate, secondary goals for this thesis:

• Extract and characterize two craters from the Stardust interstellar foils

• Create an automated image searching algorithm to improve crater detection on the Stardust foils

Chapter 3: Methods

3.1 Preface

Many of the materials collected with the Stardust mission sample collector were extremely small, with individual impactors ranging in size from microns (μm) to a few hundred nanometers (nm). Additionally, these materials were collected at a relative speed of 6.1 km/s, resulting in interaction and mixing with the collector materials. As a result, electron microscopy techniques are useful for characterizing this material, and a variety of techniques are necessary to prepare the samples for these types of analysis. This chapter discusses sample preparation techniques and data analysis methods for Scanning Electron Microscopy (SEM) and Transmission Electron Microscopy (TEM).

3.2 Scanning Electron Microscopy (SEM)

Initial imaging and elemental characterization of analog, cometary, and interstellar foil samples were performed with Washington University's JEOL JSM-840A scanning electron microscope (SEM) and Tescan Mira3 field emission scanning electron microscope (FE-SEM). SEM instruments take advantage of the small interaction volume of electrons in order to obtain high-resolution images and elemental characterizations of samples. Conductive materials are particularly well-suited to SEM analysis as they can be examined with a wide range of electron beam voltages and currents.

The incident electron beam interacts with a sample in a variety of ways (Figure 3.1). The incoming electrons ionize atoms present in the sample. Secondary electrons can be produced when an incident electron interacts inelastically with an electron in the sample. The incident electron imparts some of its energy to ionize an atom in the sample. The freed electron likely experiences numerous elastic and inelastic collisions within the sample, but can escape the sample's surface if

it still has sufficient energy. For most metallic samples secondary electrons only escape the sample when generated within the top 5 nm of the sample's surface, depending on the sample's composition (Seiler 1983). As a result, secondary electrons can be collected and measured to generate an image of the sample's surface at the high magnifications necessary to observe features only tens of nanometers in size. Secondary electrons are particularly well suited for imaging the Stardust foil impact craters as their small interaction volumes allow for detailed imaging of the crater topography.

Backscatter electrons and Auger electrons can also be used to obtain surface images. Backscatter electrons originate from the electron beam and are reflected out of the sample by elastic scattering interactions with atoms in the sample. Backscatter electrons have the advantage of being sensitive to the atomic number of the sample's nuclei. Higher-Z elements have higher electron densities that result in higher backscatter electron counts, and thus can provide contrast between different atomic compositions present in the sample. However, backscatter electrons can originate from deeper in the sample owing to their higher energies and have their effective resolution limited by their increased interaction volume relative to secondary electrons. As a result, the majority of the imaging performed during the work presented in this thesis was done using secondary electrons. Auger electrons form when the electron beam creates an inner-shell vacancy in an atom in the sample and an outer-shell electron fills this vacancy, emitting a characteristic photon. If the photon has sufficient energy it can free another electron from the same atom if the photon interacts with it. This freed electron is an Auger electron. Auger electrons typically have lower energies than secondary and backscatter electrons and are only capable of escaping from the top several angstroms of the sample, making them extremely surface sensitive. However, the Stardust foils examined in this thesis typically build up a thin (several angstrom)

layer of organic contamination upon exposure to the atmosphere that must be removed prior to elemental characterization of the sample with Auger techniques (Stroud *et al*., 2014). Additionally, the topography of the craters make sputtering techniques used to remove this contamination difficult to apply. As a result, the work presented in this thesis does not utilize Auger spectroscopy.

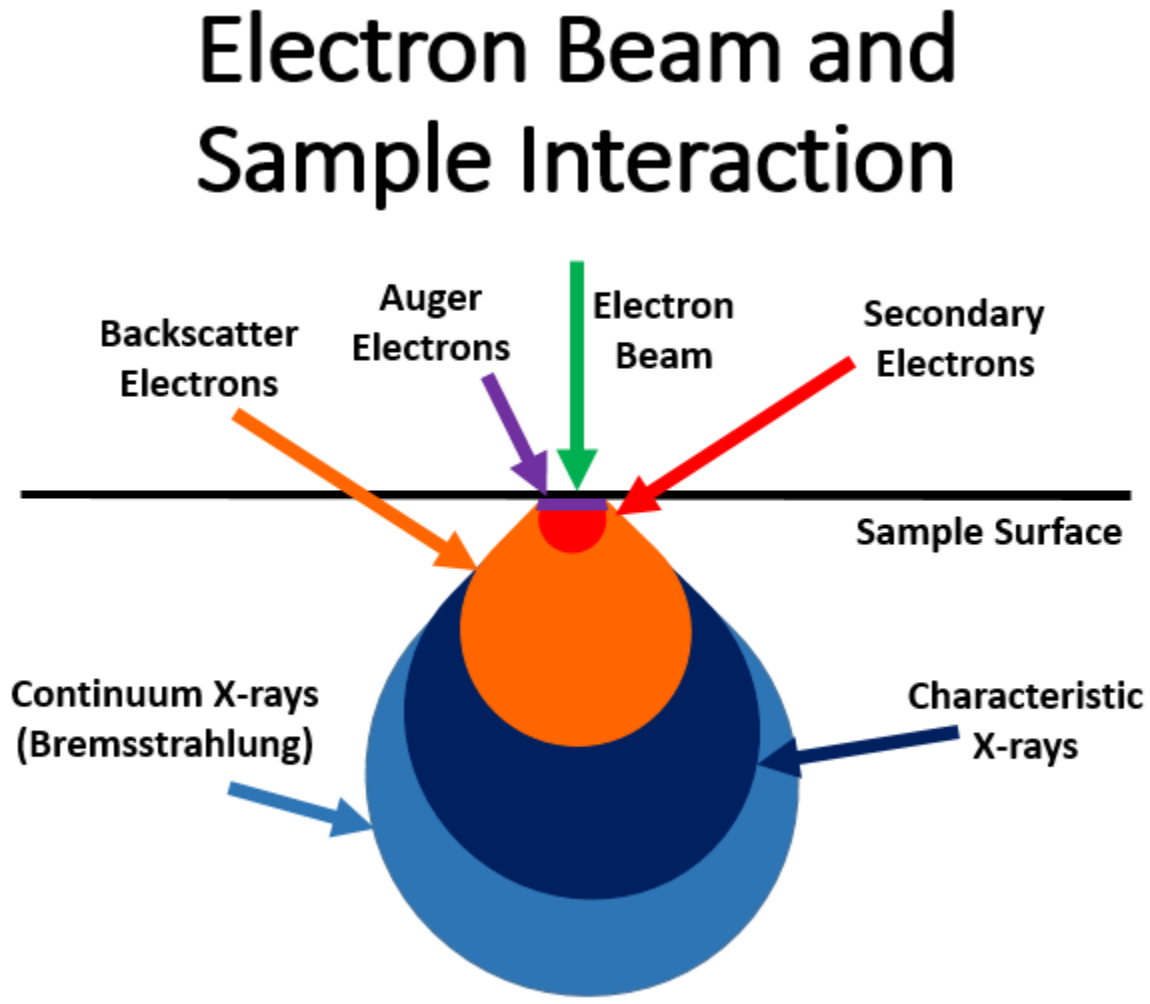

FIGURE 3.1: Electron beam interaction with a sample. The colored regions represent the relative volumes from which each listed interaction output can escape. Exact volume interactions vary heavily by sample material and primary beam energy.

3.3 Focused Ion Beam (FIB) Sample Preparation

The FIB-SEM, though initially utilized in the semiconductor industry, has become an increasingly popular instrument for preparing samples for further TEM analysis. The FIB-SEM

is primarily used to extract and thin samples with a focused ion beam that is capable of performing fine cuts with an accuracy of several nanometers. FIB-SEM sample preparation is necessary for the study of analog and Stardust foils with the TEM.

FIB-SEM instruments operate by combining the imaging capabilities of a traditional SEM instrument with the imaging and milling capabilities of a focused ion beam. The orientations of the FIB-SEM components in the sample chamber are shown in Figure 3.2. A central electron column focuses an electron beam onto the sample, producing backscatter and secondary electrons than can be collected to produce an image of the sample. A focused ion beam, angled 52° relative to the electron column, is produced when a gallium reservoir is placed in contact with a tungsten needle in a strong electric field. Heated gallium flows to the tip of the tungsten needle and forms a Taylor cone as a result of the gallium's surface tension resisting the force of the electric field. The tip's small size (on the scale of several nanometers) results in a large electric field forming at the tip, resulting in ionization and field emission of the gallium present at the tip. These gallium ions are typically accelerated to energies between 1 and 25 KeV and then focused onto the sample with electrostatic lenses, resulting in a spot size on the order of several nanometers.

The gallium ion beam hits the surface and mills a small amount of the material it interacts with, resulting in the creation of secondary ions, free neutral atoms, and secondary electrons. These secondary ions and secondary electrons can be collected to produce an image that is used in conjunction with the images produced by the collection of backscatter or secondary electrons created by the electron column. The gallium ion beam's small spot size, coupled with the ability to reposition the sample and change the beam's rastering pattern, allows for the beam to selectively mill away unwanted parts of the sample. This allows isolation of cross sections of the impact craters present in analog and Stardust foil samples (Figure 3.3).

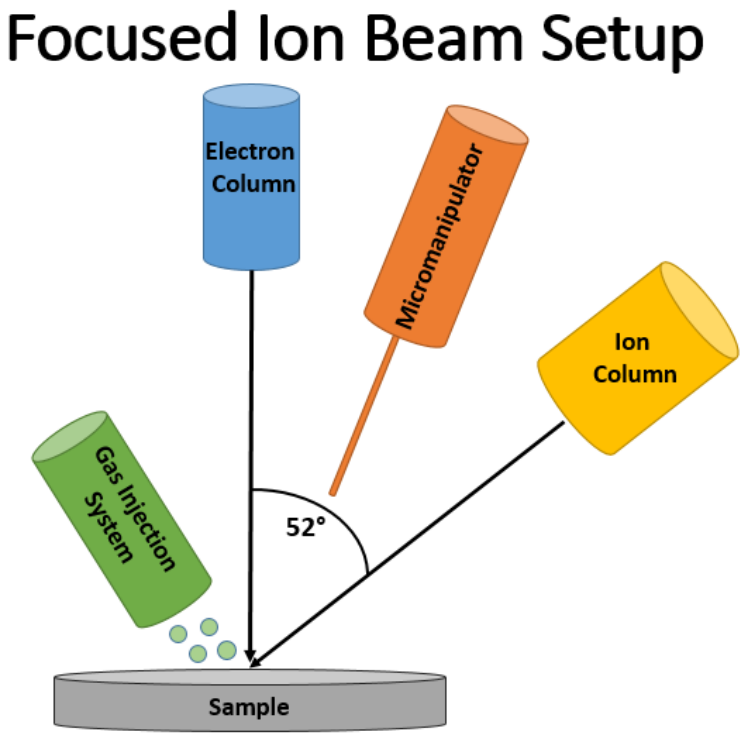

FIGURE 3.2: The structure of the FIB's electron column, ion column, gas injection system (GIS), and micromanipulator relative to the sample.

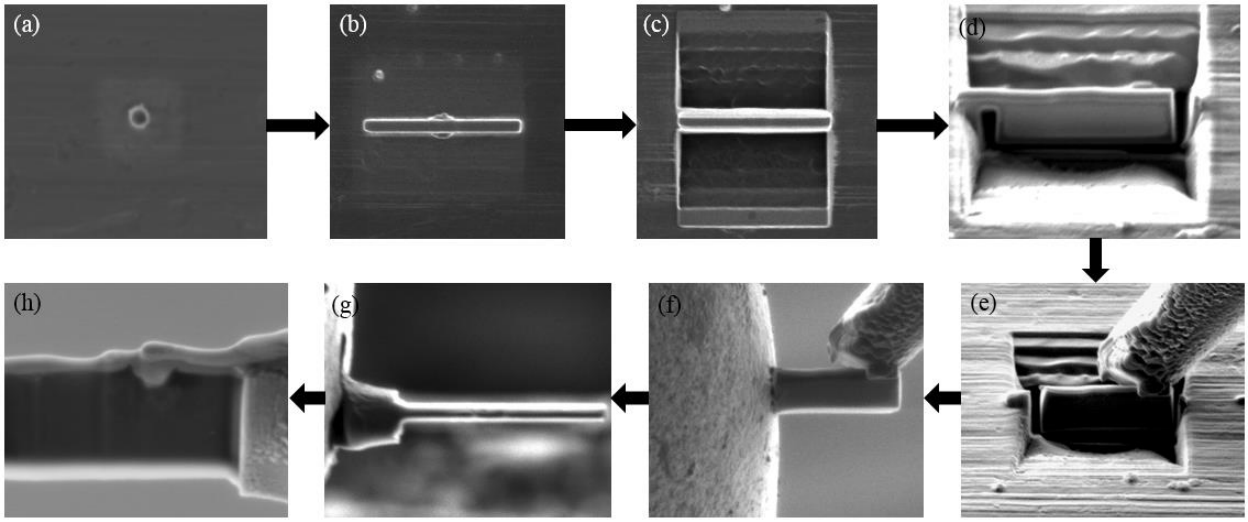

FIGURE 3.3: The FIB sample preparation and extraction process. a) The crater (~650 nm in diameter) is identified and b) covered in a protective Pt coat. c) Stairstep milling is performed on either side of the crater so that d) further milling underneath and to the side of the crater can be performed. e) While the crater is still attached on one side, the omniprobe needle is attached with Pt deposition to the sample before the final cut is performed, freeing the cross section from the aluminum substrate. f) The sample is extracted, repositioned, and attached to a TEM grid using Pt deposition. g) The sample is thinned to electron transparency (< 250 nm), h) resulting in a cross section of the original crater.

In addition to milling, the ion beam, and to a lesser extent the electron beam, can deposit material via ion beam induced deposition. A gas injection system (GIS) introduces a gas to the sample chamber close to the sample surface. The gas adsorbs to the surface of the sample. Scanning the surface with the electron or ion beam then decomposes the gas into volatile and non-volatile components, with the volatile component leaving the chamber through the vacuum pump. The non-volatile component remains as a deposition on the sample. This deposition can be used to protect the sample surface from further damage from the ion beam or to bond two surfaces together. Both of these applications are utilized to extract Stardust foil thin sections (Figure 3.3). While a variety of gases can be utilized to deposit different elements onto the sample, my work largely utilized trimethyl(methylcyclopentadienyl) platinum ($C_5H_4CH_3Pt(CH_3)_3$) in order to use Pt as a deposition material. Work conducted in collaboration with Rhonda Stroud at the Naval Research Laboratory on the interstellar Stardust foils also utilized naphthalene ($C_{10}H_6$) in order to use C as a deposition material.

In addition to the GIS, a piezoelectric tungsten Omniprobe micromanipulator can be inserted into the sample chamber to assist with sample extraction. The micromanipulator's needle-like shape and small tip radius of 500 nm allows for small sample cross sections to be attached to it and manipulated within the sample chamber (Figure 3.2; Figure 3.3).

3.4 Plasma Ashing

Stardust aerogels are extremely insulating and their collected cometary materials cannot be studied in situ with traditional electron microscopy techniques. Plasma ashing is a technique for destroying the Stardust aerogel in order to free the collected cometary material so that it can be studied with SEM or TEM instruments.

Our plasma ashing was performed using an SPI Plasma Prep II Etcher/Asher. The instrument contains a cylindrical quartz chamber sealable to 133.3 Pa. The asher draws a carrier gas (e.g., CF_4 or O_2) over the sample and RF power, provided by a crystal-controlled oscillator at 13.56 MHz, ionizes the gas under vacuum. When using CF_4 as a carrier gas the asher creates a plasma of CF_3^+ and F^- ions, while using O_2 gas creates a plasma of O^+ and O^- ions. F^- ions combine with Si present in the aerogel, forming the gas SiF_4, which is then removed from the chamber by the vacuum pump. O ions interact with organic material, potentially removing terrestrial contamination from the sample. However, all of our studies of Stardust aerogels involved the use of TEM grids covered by a carbon mesh, so only CF_4 was used as a carrier gas in our study of Stardust materials. After destroying the aerogel surrounding the captured cometary materials, the materials are deposited onto an SEM stub or TEM grid for further analysis.

F^- ions interact with a variety of elements, as well as with Si present in cometary materials. F plasma exposure time needs to be sufficiently long to result in the majority of the aerogel being destroyed, but also needs to be minimized to prevent excessive damage to the collected cometary materials. Stardust aerogels are extremely porous, with over 98% of the aerogel volume composed of ambient gases (Burchell *et al.*, 2006). As a result, the aerogel's effective surface area is significantly larger than any collected cometary material, allowing for it to be destroyed before excessive damage is caused to collected cometary material. Copper, aluminum, quartz, and some carbon compounds have shown resistance to F plasma ashing and are effective materials for housing the aerogel samples during the ashing process.

3.5 Sample Preparation for Plasma Ashing

The Stardust aerogel's extremely low density, coupled with the small impact track sizes, make preparing the samples for ashing challenging. The aerogels need to be fully surrounded by

their container in order to prevent them from escaping, but must simultaneously be accessible by the plasma created in the plasma asher.

The setup for the aerogel prior to ashing is shown in Figure 3.4. The aerogel sample is placed directly on top of a TEM grid so that collected material is deposited directly onto the TEM grid as ashing occurs. A Si base with a thin (100 nm) Si_3N_4 window is placed on top of the TEM grid and the aerogel, trapping the aerogel between the TEM grid and the Si_3N_4 window. The setup is sandwiched between a Cu cap and base due to copper's resistance to F plasma. A hole in the Cu cap allows for F plasma to reach the Si_3N_4 window and the aerogel sample.

Typical Si_3N_4 ashing rates by F plasma at the standard operating pressure of 34.4 kPa are ~34 nm/min (Williams *et al.*, 2003), allowing the F plasma to penetrate the 100 nm Si_3N_4 window after roughly 3 minutes of exposure to the F plasma. The Si_3N_4 window thus prevents the loss of the aerogel during transportation and pressure changes in the chamber while still allowing for the F plasma to eventually reach and ash the aerogel sample. Ashing rates for SiO_2, the composition of the Stardust aerogel, are similar to those for Si_3N_4 (Williams *et al.*, 2003). However, the aerogel's extreme porosity greatly increases its effective surface area (Burchell *et al.*, 2006) allowing for it to be destroyed on a timescale of minutes despite typical aerogel keystone dimensions on the scale of hundreds of microns.

Stardust aerogel tracks are extracted from the aerogel tiles using an automated keystone system (Westphal *et al*., 2004a). Further manipulation of the aerogels is difficult due to their low density and small sizes. The placement of the Stardust aerogels onto the TEM grids was performed by Andrew Westphal at the Berkeley Space Sciences Laboratory. Aerogel manipulation and positioning onto the TEM grid after extraction was performed using an eyelash tool coupled with an alpha ionizer to neutralize static charge and prevent unpredictable movements in the aerogels.

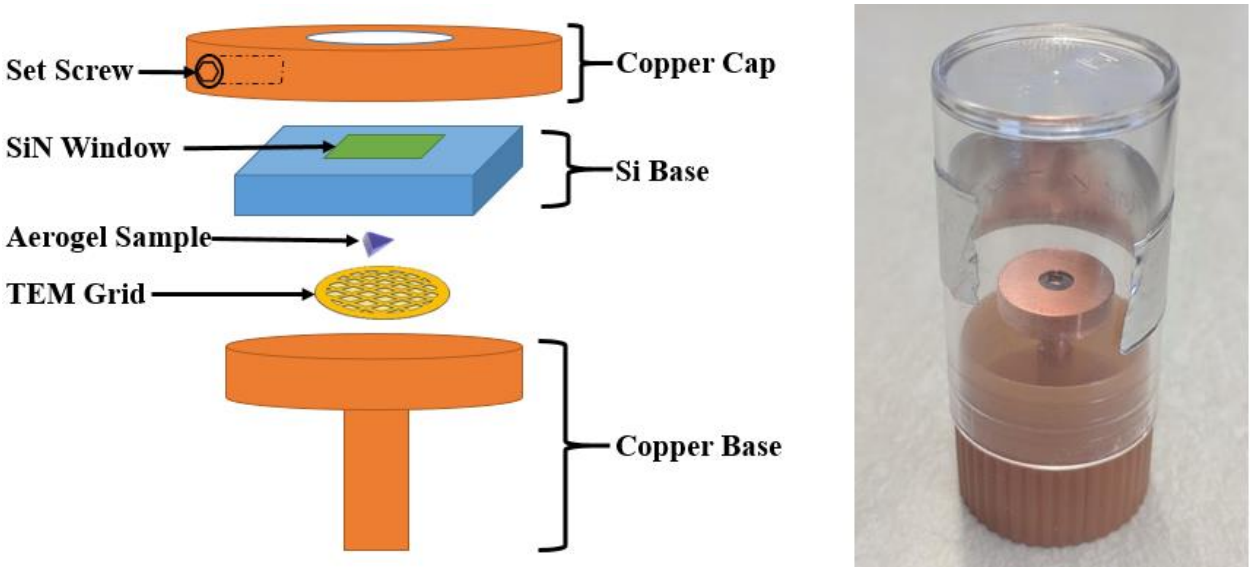

FIGURE 3.4: Aerogel sample preparation prior to the application of plasma ashing. A TEM grid rests on top of a Cu base. The aerogel sample is placed on top of the TEM grid and then trapped in place above the TEM grid by a Si base (5 mm x 5 mm x 200 μm) with a thin (1.5 mm x 1.5 mm x 100 nm) Si_3N_4 window. The structure is held together with a Cu cap that is secured to the Cu base with a set screw. The full structure is shown on the right with the structure secured within a protective plastic canister.

3.6 Transmission Electron Microscopy (TEM)

The TEM is used for microstructural and elemental analyses of materials following sample preparation with the FIB or the plasma asher. The TEM generates a beam of high energy electrons (typically 160 to 200 KeV) and aims this beam at a thin (typically < 250 nm) sample. The relativistic electrons pass through the sample and impinge upon a scintillating screen. Image contrast results from electrons scattering or being absorbed as they pass through the sample. Elements with larger atomic numbers typically have a higher electron density and scatter more incoming electrons resulting in these regions appearing darker in traditional bright-field imaging. Modern TEM instruments can image at high enough magnifications to identify individual atoms, though most TEMs have resolutions on the scale of nanometers.

In addition to bright-field and dark-field imaging, the TEM can be used to record a specimen's diffraction pattern by projecting the back focal plane of the objective lens onto the scintillating screen. The image at the back focal plane is the Fourier transform of the electron wave scattered by the specimen. The result is a bright central spot of unscattered electrons (the central DC spot of the 2-D Fourier transform that represents the overall brightness of the image) is visible in addition to spots from scattered electrons. Crystalline materials result in preferential scattering of the electron beam along angles that satisfy the Bragg reflection conditions, which depend upon the crystal's orientation relative to the incident electron beam. The preferential scattering creates a pattern of bright spots with the bright central spot that is known as a selected area diffraction (SAD) pattern. Comparing the SAD pattern to known crystal orientations and scattering patterns allows for the determination of the sample's crystal structure and the crystal structure's orientation. Amorphous samples have no preferred scattering direction and instead show diffusely illuminated SAD patterns. In this way SAD can be used to structurally characterize a sample.

Some TEM instruments can be operated in, or only operate as, scanning transmission electron microscopes (STEM). STEM instruments differ from traditional TEM by scanning a focused beam of electrons across the sample in a raster pattern rather than providing a constant electron illumination across the sample. STEM allows for spatially coordinating signals in the TEM such as characteristic X-rays and thus can be useful for elementally characterizing a sample as a whole rather than through the combination of many individual spot analyses. Elemental mapping as well as some of the sample imaging presented in this thesis was performed on STEM instruments.

TEM investigations performed at Washington University were performed using two instruments, a JEOL 2000FX TEM equipped with a NORAN ultra-thin window energy dispersive X-ray spectrometer (EDXS) and a JEOL high-resolution JEM-2100F TEM equipped with a Bruker QUANTAX EDXS. TEM investigations performed in collaboration with Rhonda Stroud at NRL utilized two instruments, a JEOL 2200 FS STEM equipped with an Oxford Aztec SDD-EDXS and a Nion UltraSTEM 200 aberration-corrected STEM.

3.7 Energy Dispersive X-Ray Spectroscopy (EDXS)

An incident electron beam creates orbital vacancies in lower level electron shells that are then filled by upper-shell electrons, emitting characteristic X-rays in the process (Figure 3.1). Measurement of the energies and counts of these X-rays allows for elemental characterization of the sample, a process called energy dispersive X-ray spectroscopy (EDS or EDXS). EDXS can be performed on both SEM and TEM instruments with an X-ray collector. However, the interaction volume from which X-rays can escape a thick sample in the SEM is typically on the scale of microns. Thus, for the foil craters studied in this thesis, which range between ~200 nm and 10 μm in diameter, SEM-EDXS results in a measurement of the bulk composition of the crater residues. Additionally, when the sample is much smaller than the interaction volume, SEM-EDXS has a large background resulting from a measurement of the substrate beneath the sample, such as the Al foil surrounding the crater residues in the Stardust foil samples. TEM-EDXS, due to the thinner samples and fine electron beam spot size, can elementally characterize samples on a finer scale than SEM-EDXS and typically has smaller background effects. Quantification of SEM-EDXS spectra need to correct for the atomic number effects, absorption, and fluorescence (ZAF) of the sample, whereas sufficiently thin samples in the TEM can be approximated with simpler Cliff-Lorimer techniques. Since TEM-EDXS requires a thin sample, much of the impacting material is

not present for measurement in the TEM as it is lost during the FIB preparation process. SEM-EDXS and TEM-EDXS are presented as complementary techniques for the elemental characterization of samples studied in this thesis.

3.8 EDXS Quantification

Cliff-Lorimer analysis is a technique for simplifying the quantification of elements present in samples measured with TEM-EDXS (Cliff & Lorimer, 1975). Cliff-Lorimer analysis assumes that the sample is infinitely thin, removing the need to account for X-ray absorption (A) and fluorescence (F) when quantifying samples with X-ray spectra. For samples that are too thick for this approximation to return accurate results, corrections for these factors (ZAF corrections) need to be made.

3.8.1 Cliff-Lorimer Analysis

Cliff-Lorimer analysis assumes that the sample is sufficiently thin to ignore absorption or fluorescence of X-rays within the sample. As a result, it is widely used for quantifying thin samples studied in the TEM. The weight concentrations of two elements, denoted as C_A and C_B, are related to the measured intensities of the elements, I_A and I_B, with a Cliff-Lorimer factor k_{AB}:

$$\frac{C_A}{C_B} = k_{AB}\frac{I_A}{I_B} \tag{3.1}$$

Equation 3.1 is the Cliff-Lorimer equation. k_{AB} in equation 3.1 is a sensitivity factor. The value of k_{AB} varies based upon the elements being measured as well as the TEM-EDXS system used and the TEM operation factors such as the TEM voltage.

In order to solve for C_A and C_B in equation 3.1 we use k_{AB} values previously obtained through the analysis of standards with known weight concentrations. We can acquire values for I_A and I_B through measurements of the sample and add another equation to the system (assuming

the sample is only composed of elements A and B) in order to have a solvable system of two equations with two unknowns:

$$C_A + C_B = 100\% \tag{3.2}$$

Expanding the Cliff-Lorimer technique to samples containing more than two elements can be done by including additional equations. Moving to a sample composed of three elements (A, B, and C), we can add the following equations to Equation 3.1 in order to obtain three equations to solve for three unknowns:

$$\frac{C_C}{C_B} = k_{CB}\frac{I_C}{I_B} \tag{3.3}$$

$$C_A + C_B + C_C = 100\% \tag{3.4}$$

Thus, by establishing k factors through the analysis of standards, one can then calculate the atomic composition of samples, assuming the standards and samples were measured in the same instrument under similar conditions.

Cliff-Lorimer analysis works so long as the sample is sufficiently thin. The point at which a sample becomes too thick for reliable Cliff-Lorimer results is when absorption and fluorescence effects become significant compared to the desired accuracy. Typically Cliff-Lorimer analysis is considered unreliable once the bremsstrahlung absorption effects in the sample become noticeable (Williams & Carter, 1996). This effect is noted by measuring the background of a spectrum in windows above and below the elements of interest. Bremsstrahlung spectra typically peak around 1.5 KeV in TEM-EDXS spectra, and thus windows taken above this point (for example, from 2.4-2.5 KeV or 2.6-2.7 KeV) that do not overlap peaks from measured elements can serve as good comparisons to determine the extent of the bremsstrahlung in a spectrum's background (Williams

& Carter, 1996). If the effect of Bremsstrahlung on the spectrum's background becomes too strong or apparent the use of software accounting for ZAF corrections is recommended.

3.8.2 ZAF Corrections

Samples too thick for Cliff-Lorimer analysis can be quantified with ZAF-corrected k-factor techniques or with standards-based ZAF corrections.

ZAF-corrected k-factor techniques utilize equations similar to equations 3.1-3.4 but assume that the k-factors in these equations account for absorption (A) and fluorescence (F) effects. Quantification on thick samples can be performed with ZAF-corrected k-factor techniques if the k-factors can be approximated with previous standard measurements (Newbury & Ritchie, 2015). We use ZAF-corrected k-factor techniques for quantifying SEM-EDXS spectra through comparison to more accurate TEM-EDXS spectra on the same samples, where TEM-EDXS spectra are assumed to be more accurate as they are thin enough for Cliff-Lorimer approximations. However, ZAF-corrected k-factor techniques are less accurate than quantification performed with standards-based ZAF corrections.

Standards-based ZAF corrections use measurements of standards to accurately account for a sample's atomic number (Z), the absorption of X-rays within a sample (A), and the fluorescence of X-rays within a sample (F). Absorption occurs when less energetic X-rays (generally from lower-Z elements) are absorbed after emission but before exiting the sample (generally by higher-Z elements). Fluorescence occurs when a more energetic X-ray fluoresces a lower energy X-ray from a lower-Z element within the sample. Correcting for these factors (ZAF corrections) is possible, but is exceedingly complex and iterative. As a result, nearly all ZAF corrections are performed with sophisticated software, which in this thesis takes the form of NIST DTSA-II software (Ritchie 2011; Ritchie 2012).

Chapter 4: Analog Foils

4.1 Preface

Adapted from the following papers and conference abstracts:

Croat T. K., Floss C., Haas B. A., Burchell M. J., & Kearsley A. T. (**2015**), "Survival of Refractory Presolar Grain Analogs During Stardust-like Impact into Al Foils: Implications for Wild 2 Presolar Grain Analogs During Stardust-like Impact into Al Foils", *Meteoritics & Planetary Science*, **50**, 1378-1391, URL https://doi.org/10.1111/maps.12474.

Haas B. A., Croat T. K., Floss C., Kearsley A. T., & Burchell M. J. (**2015**), "Characterizing Comet 81P/Wild 2 with Acfer 094 Analog Foils", in "78th Annual Meeting of the Meteoritical Society", Abstract #5141, URL https://www.hou.usra.edu/meetings/metsoc2015/pdf/5141.pdf.

Haas B. A., Croat T. K., Floss C., Kearsley A. T., & Burchell M. J. (**2016**), "Characterizing Comet 81P/Wild 2 with Acfer 094 Analog Foils", in "47th Lunar and Planetary Science Conference", Abstract #1597, Lunar and Planetary Institute, Houston, URL https://www.hou.usra.edu/meetings/lpsc2016/pdf/1597.pdf.

Haas B. A., Floss C., Kearsley A. T., & Burchell M. J. (**2017**), "Characterizing Comet 81P/Wild 2 with Tagish Lake Analog Foils", in "80th Annual Meeting of the Meteoritical Society", Abstract #6246, URL https://www.hou.usra.edu/meetings/metsoc2017/pdf/6246.pdf.

4.2 Introduction

While not initially designed as sample collection media, the cometary side of the Stardust foils were found to contain hundreds of cometary impact craters while the interstellar side contained a handful of interstellar impact craters. However, high speed (6.1 km/s for cometary impactors and up to 20 km/s for interstellar impactors) impact processing in the foils was not well understood. Prior to the return of the Stardust sample collector it was unclear which impacting materials would survive the sudden deceleration and relatively high shock pressures that were

inherent to the foil collection process. Additionally, initial analyses of the impactor material contained in these craters indicated that the collected material was biased against the survival of certain materials. Presolar grain abundances, which are generally a good indicator of the degree to which a given sample has preserved the original starting material from the solar nebula, were much lower than expected in the cometary foils (McKeegan *et al*., 2006; Stadermann *et al*., 2008). Given the high collection speed, it is possible that the presolar grains, as well as other impactor components such as volatiles, organic materials, and crystalline materials were preferentially destroyed, altered, or diluted during the capture process.

The Stardust spacecraft's cometary collection speed of 6.1 km/s falls within the range of speeds attainable by material fired in modern light-gas gun (LGG) experiments. LGGs can fire well-characterized grains into flight-spare Stardust foils at speeds similar to those experienced by the Stardust spacecraft, thus simulating the Stardust encounter (Burchell *et al*., 1999). A diagram of the LGG is shown in Figure 4.1. Operation of the University of Kent's LGG, which was used to create all analog foils studied in this thesis, is described in Burchell *et al*., (1999). A pendulum is released and strikes the firing pin. The firing pin is pushed into the base of a cartridge with enough force to ignite the primer and set off the cartridge. This action accelerates a piston towards a sabot located in the launch tube. Hydrogen gas present in the pump tube is compressed. An aluminum bursting disc in the breech connects the pump and launch tubes. A nylon sabot is located at the breech end of the launch tube and aids in the acceleration and positioning of the material that is being fired towards the flight-spare Stardust foils. The sabot is intercepted by a stop plate at the end of the blast tank while the fired material continues through two laser-light curtains that are used to confirm the speed of the fired material. The fired material continues onward through the target chamber and impacts the flight-spare Stardust foils at its end. Using the LGG the

cometary impact processing can be replicated in the laboratory with a variety of materials. Studying the resulting foil craters allows for researchers to better understand the foil impact processing.

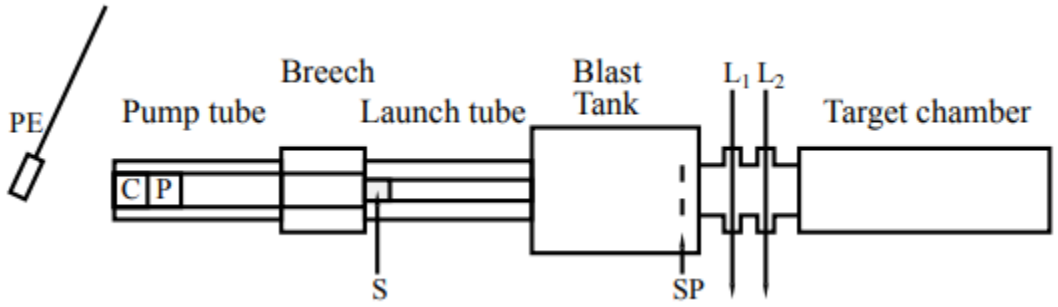

FIGURE 4.1: Figure 8 from Burchell *et al*. (1999) showing the schematic diagram of the LGG used to produce the analog foils studied in this thesis. The pendulum (PE), cartridge (C), piston (P), sabot (S), stop plate (SP), and lasers (L_1 and L_2) are labeled.

A number of analog foil experiments were conducted following the return of the Stardust sample collector. Silica and soda-lime glass projectiles were utilized to describe the relationship between impactor diameter and the resulting crater diameter (Kearsley *et al*., 2006; Price *et al*., 2010). Crystalline impactors were examined to determine that crystalline materials observed in the crater residues were likely components of Wild 2 rather than post-impact recrystallizations (Wozniakiewicz *et al*., 2012a). Further studies investigated the behavior of specific minerals (e.g. olivine, diopside, pyrrhotite) during impact processing, observing phenomena such as volatile loss and amorphization of crystalline impactors (Kearsley *et al*., 2008; Wozniakiewicz *et al*., 2009; Wozniakiewicz *et al*., 2012b). However, most of the craters investigated in these studies were far larger (> 5 μm in diameter) than any craters that would have been created by impactors representing the fine component of Wild 2. Additionally, these studies did not investigate aggregate impactors composed of a variety of materials. Nearly all Stardust cometary foil craters, even those created by submicron impactors, are the result of aggregate impactors, and thus these studies were not fully representative of the impact conditions experienced by Wild 2 material

(Croat *et al*., 2016). As a result, we worked with Anton Kearsley and Mark Burchell at the University of Kent in order to create three new analog foils with their LGG in order to investigate how smaller impactors and aggregate impactors may be altered during the sample collection process: Refractory (TiC/TiN/SiC/SiN) grain analog foils, Acfer 094 analog foils, and Tagish Lake meteorite analog foils. In studying these foils we hoped to learn more about how smaller and aggregate impactors behave during the collection process and thus help to explain some of the biases seen in the studies of the Stardust foils (e.g., the lack of presolar grains and organic materials).

The refractory grain analog foils served to investigate the effect of impact processing on individual, highly refractory grains. SiC is a common, highly refractory mineral observed in presolar grain studies. Presolar grain abundances in the Stardust foils were far lower than expected (McKeegan *et al*., 2006; Stadermann *et al*., 2008). The study of these analog foils served to demonstrate how refractory grains are affected by the spacecraft's collection conditions. These analog foils thus helped us to determine whether refractory presolar grains could survive the collection conditions.

4.3 Refractory (SiC/SiN/TiC/TiN) Analog Foils

The study of the refractory analog foils was largely motivated by the lack of presolar grains observed in studies of the Stardust foils. The study of these foils allowed us to investigate the condition and survival of small (mostly submicron) refractory mineral grains within Al foil craters. Work on these foils encompassed craters created by SiC, SiN, TiC, and TiN impactors. However, I only conducted work on some TiC and TiN impactors. Work on SiC and SiN impactors, as well as some Ti-containing impactors, was performed by my colleague Kevin Croat. As a result, this

portion of the thesis will focus on the results of the Ti-containing impactors that I studied. SiC's are a better presolar grain analog, as SiC's are a common form for presolar grains. However, for the purpose of investigating refractory impactors, the TiC and TiN impactors are effective analogs, given that each of these materials are similarly refractory (SiC melts at 2730 °C while TiN and TiC melt at 3160 °C and 2930 °C, respectively). The full results of this study can be found in the Croat *et al*. (2015) paper referenced in Chapter 4.1 of this thesis.

4.3.1 Refractory Analog Samples and Experimental Methods

The grains utilized for this analog foil experiment were crystalline refractory phases mostly submicron in size, including natural diamond, synthetic TiN, synthetic TiC, synthetic SiC, synthetic alumina (Al_2O_3), synthetic Si_3N_4, and natural olivine (Fo_{90}). I focused my study on TiN and TiC impacting grains, with melting temperatures of 3160 °C and 2930 °C, respectively. TEM images of the grains collected prior to creation of the analog foils showed the median grain sizes were 500-700 nm, though individual grain diameters could range from 100 nm to several µm. Kevin Croat performed TEM investigations of unfired grains and observed that the crystal structures matched expected phases (TiN: a = 4.35Å [FCC]; TiC: a = 4.25Å [FCC]).

The mixture of refractory materials was cemented together with polyvinyl acetate in order to create sufficiently large (~100 µm) aggregate projectiles for firing with a LGG. These projectiles were then shot at normal incidence into flight spare Stardust mission Al 1100 foil using the two stage LGG at the University of Kent (Burchell *et al*., 1999). The impact speed of the shot was measured at 6.05 km/s, which is comparable to the capture speed (6.12 km/s) of Wild 2 cometary particles (Tsou *et al*., 2004). Previous analog experiments have demonstrated that weaker aggregate particles may fragment in the LGG during the firing process, resulting in impacts

by a wide range of particle sizes, including many of the separated subgrain components (Kearsley *et al*., 2009).

Kevin Croat performed SEM-EDXS analyses on 1350 craters from two randomly selected 1.8 by 1.3 mm areas of the cratered Al foil. 758 of the craters were dominated by Ti or Si signals, allowing for further FIB-TEM study to focus on craters created by SiC, SiN, TiC, and TiN impactors. The median diameter of the Si- and Ti-containing craters were 1.5 μm and 2.0 μm, respectively, which indicates many of the craters were created by single-grain impactors that were roughly the size of our measured grain diameters (Price *et al*., 2010). Additionally, ~85% of the Si- and Ti- containing craters showed only Ti or Si signals in the SEM-EDXS spectra, but not both, further indicating that the fired material fragmented into single-grain impactors during the LGG's firing process.

Eight Ti-rich craters were extracted and thinned to electron transparency with Washington University's FEI Quanta 3-D FIB instrument. Each FIB cross section was extracted from the crater's center for consistency. Extracted Ti-containing craters sampled the overall crater size population, with crater diameters ranging from 1.0 μm to 7.1 μm. Larger craters were extracted to observe changes in properties as a function of crater-projectile size. Measured grain diameters may not be truly representative of the impactors as the two-dimensional nature of FIB sections means the full length of the grains may not have been sampled during the study. Nonetheless, grain aspect ratios were measured as a means of demonstrating grain deformation. Grain aspect ratios were calculated by using the grain dimension perpendicular to the foil surface as the numerator and the grain dimension parallel to the surface as the denominator. As a result, aspect ratios less than 1.0 indicate flattening (Table 4.1). TEM investigations of the Ti-containing grains were performed with Washington University's JEOL 2000FX. Lattice parameter determinations

for the impacting phases were calibrated by assuming a 4.05Å spacing for diffraction spots from the Al lattice in the foil substrate. Distinguishing between TiC and TiN was difficult due to the weakness of C and N signals in SEM and TEM-EDXS spectra. When differentiating between the TiC and TiN lattice spacings (4.35Å and 4.25Å, respectively) was not possible the crater phases are listed as TiC/TiN (see Table 4.1). Crater names, diameters, surviving grains, surviving grain sizes, surviving grain aspect ratios, and phases are listed in Table 4.1.

TABLE 4.1: Crater names, diameters, surviving grain numbers and sizes, grain aspect ratios and phases. Crater diameter is measured from the centers of raised crater rims. Crater Ti6's surviving grain count and size were made uncertain by damage during the FIB process and is thus labeled with an asterisk. Grain aspect ratios were calculated by dividing the grain dimension perpendicular to the foil surface by the grain dimension parallel to the foil surface (values less than 1.0 indicate flattening). When EDXS and SAD analysis could not differentiate between TiC and TiN the phase is labeled as TiC/TiN.

Crater Name	Crater diameter (μm)	No. of surviving grains	Surviving grain size range (nm)	Avg. Grain Aspect Ratio	Phase
Ti4	1.0	1	325	1.8	TiN
Ti3	1.6	2	270-330	0.7	TiN
Ti5	2.5	3	80-400	0.8	TiC/TiN
Ti6	5.2	2*	330-450*	0.6	TiC
Ti9	5.4	3	580-720	0.5	TiC/TiN
Ti7	5.6	6	240-580	0.7	TiN
Ti1	5.7	5	115-425	0.8	TiC/TiN
Ti8	7.1	2	520-880	0.5	TiC

4.3.2 Refractory Analog Foil Results

Significant amounts of surviving crystalline material were located in the crater bottoms (Table 4.1). The refractory crystals generally appeared well-preserved despite the high-speed impact conditions. Though the true grain dimensions cannot be obtained because of the two-dimensional nature of FIB sections, aspect ratios less than 1.0 indicate that grain flattening and/or fragmenting likely occurred. Larger impactors (corresponding to larger craters) tended to be broken into smaller fragments and be more flattened. Individual grain aspect ratios in craters less

than 5 microns in size averaged 0.93 while for craters greater than 5 microns in size they averaged 0.66.

The majority of surviving crystalline material was located in the crater bottoms, with minimal material located in the crater walls. No surviving material was observed in the rims of the craters despite the fact that most presolar grains detected in the Stardust foils were located in the raised rims of large craters (Floss *et al*., 2013). Smaller craters had smaller raised rims, with the smallest crater (Ti4) completely lacking a raised rim (Figure 4.2).

Smaller craters (<5 μm) typically showed less alteration than larger craters. Craters Ti4 and Ti5 (diameters 1.0 μm and 2.5 μm, respectively), extracted as a single FIB section, are shown in Figure 4.2. Both craters were formed by submicron TiN impactors. Crater Ti4 had a single 450 nm by 230 nm crystalline grain with a diffraction pattern matching that of TiN (a = 4.28Å [FCC]). No Ti was detected in the crater outside of the grain. The Ti4 grain has an ellipticity of ~1.8 and retained this shape even after an impact with its long axis perpendicular to the foil. The Ti4 projectile impacted with its major axis perpendicular to the Al foil, resulting in a carrot-like crater shape and a depth/diameter ratio of 1.0. The grain did not partially melt and recrystallize on the crater floor nor did it undergo plastic deformation, indicating that it was not significantly modified by the impact. This is consistent with previous reports of recovery of unmelted wollastonite in similar analog experiments (Wozniakiewicz *et al*., 2012a). The slightly larger Ti5 crater also contained surviving TiN crystallites (Figure 4.2). Three separate crystalline fragments were found (two ~400 nm diameter grains at the bottom and a ~80 nm grain along the side wall). Diffraction patterns (a = 4.16Å [FCC]) and EDXS spectra were consistent with TiN. The crater depth/diameter ratio was 0.9, though the crater was wider than the Ti4 impact; the crater cross section diameter of Ti4 was reduced to 42% of the full diameter at half height while the crater

cross section diameter of Ti5 was reduced to 85% of the full diameter at half height. No impurities or anomalies were visible in the Al substrate beneath either crater. As a result, a crater's depth appears to depend on the impact angle of elliptical projectiles, which is consistent with earlier investigations of wollastonite impactors (Wozniakiewicz *et al*., 2012a).

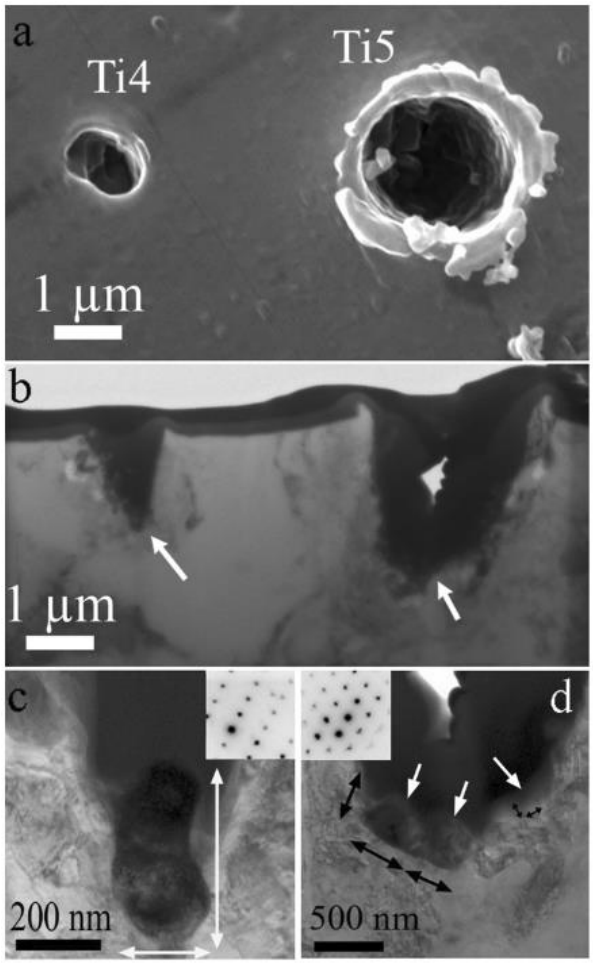

FIGURE 4.2: a) FIB-SEM image of the adjacent Ti4 and Ti5 craters. b) TEM image of the FIB section containing both craters. The deposited protective Pt layer appears dark above the lighter Al substrate. Surviving grain locations are indicated by white arrows. c) Surviving TiN projectile in crater Ti4 with dimensions indicated by white arrows. d) Surviving elliptical TiN projectile with two larger fragments on the crater floor and a small fragment in the crater wall of crater Ti5. Grain positions are indicated by white arrows while grain dimensions are indicated by black arrows.

Larger (>5 µm) craters all contained multiple surviving crystal fragments. Crater Ti1 (5.7 µm in diameter) is shown in Figure 4.3. The original projectile is broken into five crystalline fragments which appear partially flattened on impact with average aspect ratios of 0.8. EDXS and

SAD results (a = 4.17Å [FCC]) were consistent with TiN. Crater Ti7 (5.6 µm in diameter) contained six surviving crystalline fragments on the crater floor with EDXS and SAD results (a = 4.35Å) consistent with TiC (Figure 4.4). Crater Ti9 (5.4 µm in diameter) had two larger surviving crystalline clumps, both of which were chemically and structurally consistent with TiN (Figure 4.4). In all the Ti-rich large craters with surviving crystalline grains the surviving crystalline grain fragments are flattened in the direction of impact, with these craters having an average aspect ratio of 0.66 (Table 4.1).

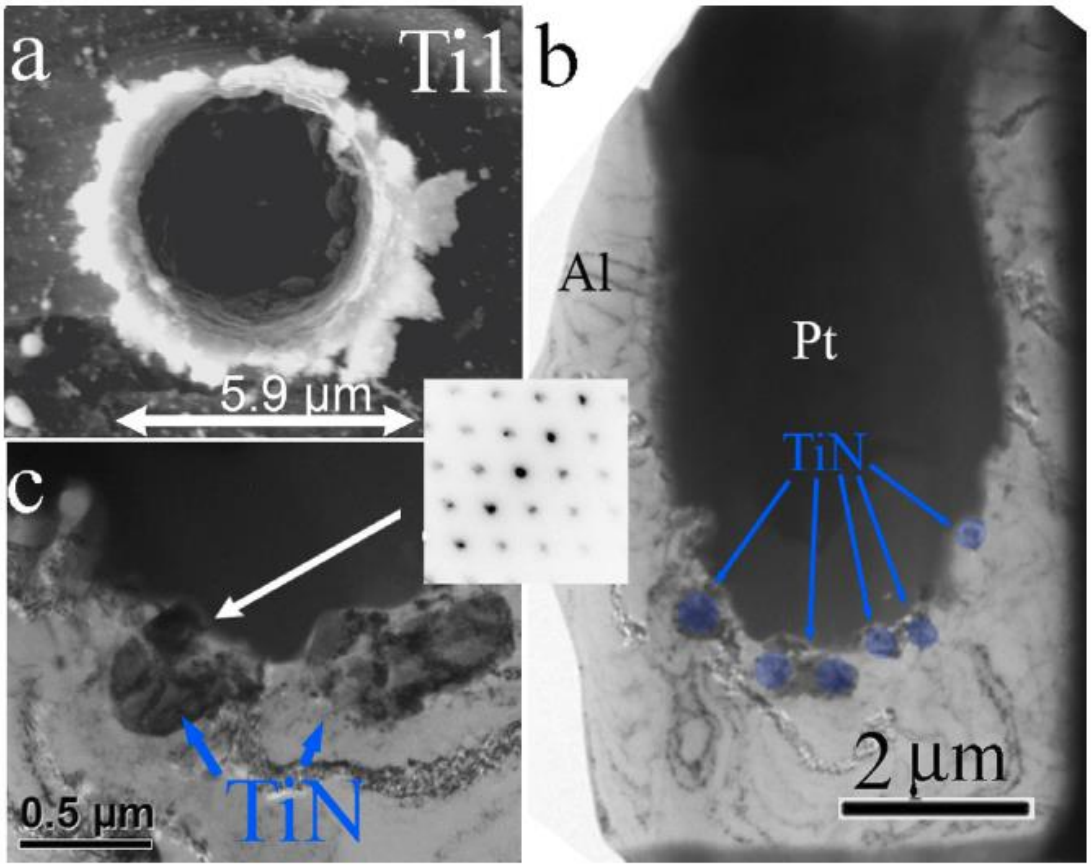

FIGURE 4.3: a) FIB-SEM image of crater Ti1 with the measured lip-to-lip diameter. b) TEM image of crater Ti1 FIB cross section showing a dark Pt-filled crater with multiple TiN crystalline fragments (highlighted and indicated by arrows) at the crater's bottom. c) Close-up TEM image of the two largest crystalline fragments with inset FCC diffraction pattern from the left fragment (consistent with TiN).

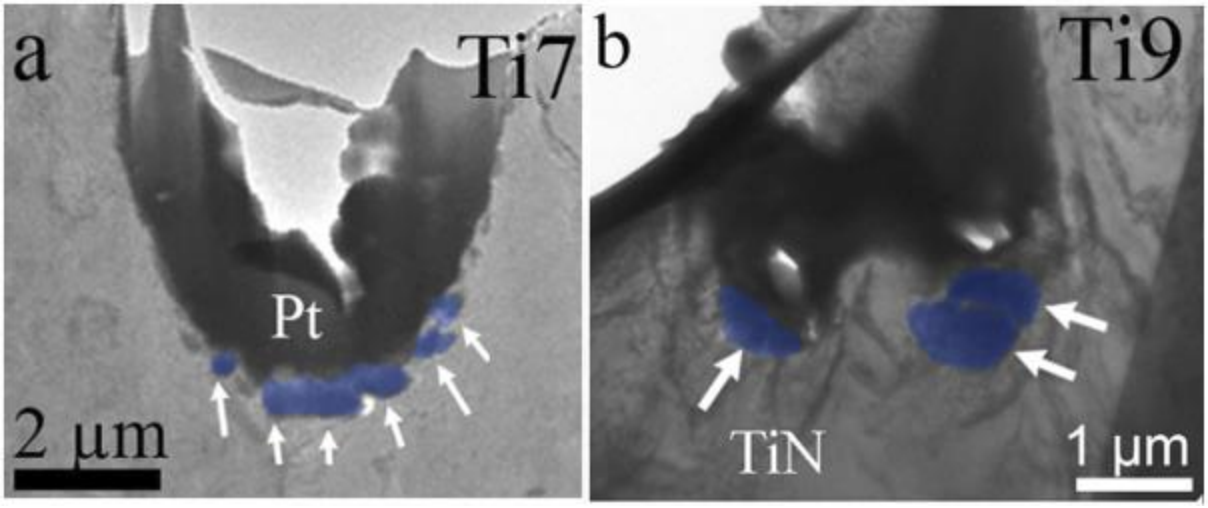

FIGURE 4.4: a) TEM image of crater Ti7 with the TiC grains highlighted in blue. b) TEM image of crater Ti9 with surviving grains highlighted in blue.

4.3.3 Refractory Analog Foil Discussion

Our analog test shot results show that submicron refractory grains can survive Stardust-like impacts into Al foil. Many of the grains are preserved well enough to allow chemical and structural investigations that adequately reflect their properties prior to impact. Combining the results presented with Kevin Croat's investigations of craters created by Si-containing impactors, we conclude that SiCs that are comparable in size to presolar SiCs should survive intact in small craters. This is most evident in the preservation of the elliptical TiN grain after an impact with its long axis perpendicular to the foil surface (Figure 4.2). These results are consistent with previous reports of surviving crystalline fragments of larger (>20 µm) mineral projectiles in impacts on aluminum at similar (6 km/s) speed (Burchell *et al*., 2008b; Wozniakiewicz *et al*., 2012a). Study of residues created by 10-12 µm olivine grains after similar high-velocity impacts also reported the presence of surviving crystalline material through the use of Raman spectroscopy (Foster *et al*., 2013). However, this study did note that the olivine Raman peaks were shifted due to significant strain in the samples post-impact (Foster *et al*., 2013). All of our refractory TiN and

TiC impactors remained crystalline. Our larger (>5 μm) impactors showed fragmentation and flattening and thus can help explain the Raman shifts seen in this previous study.

Almost all of the surviving crystalline material in our craters was found on the crater bottom, with no surviving material observed on the crater rims. These results differ from the presolar grain abundances from the Stardust Wild 2 craters which showed very low abundances of presolar grains, and in the four cases where such grains were found, all were in the raised crater rims (Stadermann *et al*., 2008; Floss *et al*., 2013). However, these studies were predominantly made on extremely large craters (30-300 μm in diameter) and thus our observations of submicron craters may not be directly comparable. Additionally, the materials we investigated are significantly more refractory than many presolar silicates, further complicating comparisons with previous studies.

The changes in the condition of our surviving crystallites as a function of impactor-crater size may help to explain the inconsistencies between our small crater results and the SIMS studies of mostly larger (30-300 μm) Stardust craters (e.g., Stadermann *et al*., 2008). Crystalline grains in craters >5 μm in size were considerably lower than those of smaller craters. Many of the impactors were identical phases, suggesting that larger projectiles experience more partial melting and/or plastic deformation. The peak temperatures and pressures to which larger projectiles are subjected thus appear to be larger as well. This transition in the observed behavior of projectiles as a function of size coincides with a transition in the projectile size to crater size relationship near this crater diameter (Price *et al*., 2010) wherein craters less than 2 μm in diameter often lack a raised rim. We similarly observed the lack of a raised rim in crater Ti4 (1.0 μm diameter).

Roughly 95% of the measurement areas for the Wild 2 presolar grain abundance determinations were from craters >30 μm in size (Floss *et al*., 2013) and any surviving material

was likely subjected to higher peak temperatures, leading to more intense modification. The isotopic anomalies associated with any presolar grains in these craters would likely become diluted during the collision through isotopic exchange with any surrounding partially molten material (Floss *et al*., 2013). This presolar grain destruction via diffusion of anomalies would be further magnified for presolar silicates, which are considerably less refractory than SiC. The presence of some surviving presolar grains in raised crater rims, none of which were likely as refractory as SiC, suggests that these regions experienced less extreme temperatures and pressures or more rapid cooling, allowing for the retention of their isotopic anomalies.

Our Ti-containing refractory analogs suggest that the survival of a typical ~500 nm presolar SiC grain (Amari *et al*., 1994) may depend on whether it impacts alone as a single grain in a submicron Al foil crater, or whether it impacts as part of a larger aggregate of material in a large crater. Presolar grains that impact as larger aggregates can experience multiple phases of compressive shock that lead to higher peak temperatures relative to single-grain impactors (Wozniakiewicz *et al*., 2012b). Presolar grain abundance estimates based on large craters may therefore be inaccurate (Floss *et al*., 2013) due to isotopic dilution on impact. However, the intact condition of TiC and TiN in our small craters suggests that more accurate presolar grain determinations may come from NanoSIMS measurements of small craters, which is the approach taken by Leitner *et al*. (2010, 2012). They estimate the abundance of O-rich presolar grains in small Stardust craters as ~1100 ppm, although with high uncertainties due to finding only one O-rich presolar grain among ~1000 crater measurements. This estimate, when accounting for the large confidence interval as a result of finding only a single presolar grain, overlaps with the corrected estimate of 600-800 ppm from the large crater SIMS measurements (Floss *et al*., 2013).

However, the precision of the small crater approach is limited by the laborious nature of locating and measuring thousands of small craters using the NanoSIMS.

In addition to providing insights into presolar grain abundances, the intact survival of grains in our small craters suggests that FIB-TEM investigations of such grains can provide a complementary means to study the Stardust fine fraction. FIB-TEM studies of 22 Al foil craters in the 1-3 μm size range have been reported (Leroux *et al*., 2008; Leroux *et al*., 2010; Stroud *et al*., 2010), and these are predominantly consistent with impacts of submicron olivine, pyroxene, and Fe-rich sulfides or aggregates of these. 10 of the 22 studied craters contained surviving crystalline material, further indicating that small Stardust foil craters are likely to contain surviving grains representative of the fine component of comet Wild 2. Many of the less-refractory grains in these studies were rendered amorphous by the impact or suffer from shock metamorphism. However, relatively large intact crystals like those seen in our refractory analogs are seen in some cases (e.g., enstatite in crater 2 of Leroux *et al*., [2008] and chromite in crater b4 of Stroud *et al*., [2010]), and these reinforce the fact that surviving crystalline grains are also present in the Stardust cometary foils. The thin layers of amorphous melt in some layers of these studies make it clear that less-refractory phases will undergo major modification on capture and that intact, crystalline grains are not the typical result of capture in Al foils. Further analysis of analog foils, particularly those composed of fine-grained aggregate impactors, are required to fully investigate the extent of such modifications.

4.3.4 Refractory Analog Foil Summary and Conclusions

My FIB-TEM study of the Ti-containing refractory Stardust analog craters demonstrated that TiC, TiN, and other comparably refractory phases (e.g., SiC) can survive high-speed impact into Al foils. The refractory grains often survived as intact crystals, though flattening in the grains

indicated that minor melting and plastic deformation still occurred. Moreover, an elliptical TiN grain (crater Ti4) was able to survive an impact with its long axis perpendicular to the foil with no evidence of flattening. Taken together, these FIB-TEM results suggest that grains found at the bottom of small Al foil craters present opportunities to make chemical, structural, and potentially isotopic measurements on material that is representative of the original Wild 2 samples.

While TiN and TiC survive in crystalline form in somewhat larger craters (5-10 μm diameter), these surviving projectiles are more commonly found in multiple fragments strewn across the crater floor and sometimes in the crater walls. Furthermore, the grain fragments are normally flattened in the direction of impact, indicating greater modification on impact via partial melting or plastic deformation. We confirm the transition seen in the crater-to-projectile diameter relationship as the impactor size decreases below ~3 μm (Price *et al*., 2010). The smallest (<2 μm) craters formed by impact of single refractory grains and lack the prominent raised rims seen around the larger ones, which may bias the detection of craters in this size range using visual or automated crater searches (e.g., Ogliore *et al*., 2012).

The evidence for greater modification on impact as projectile size increases may explain the low presolar grain abundances for Wild 2 that were derived primarily from SIMS measurements of 30-300 μm diameter craters (Floss *et al*., 2013). The higher peak temperatures reached in larger impacts result in melting and subsequent isotopic dilution of smaller presolar grains (Floss *et al*., 2013). The only surviving presolar grains found in >50 μm craters were in the grain rims, despite the fact that most material is in the crater bottom, suggesting that only at the crater's perimeter are grains insufficiently heated or are quenched rapidly enough to preserve their isotopic anomalies. The survival of grains in the smaller craters (<2 μm) suggests that more

accurate presolar grain estimates could come from SIMS measurements of such craters (a method pursued by Leitner *et al*. [2010, 2012]).

The relatively pristine condition of the fine grains in small, single-grain impact craters shows that Al foil Stardust samples are a complementary way to study the Wild 2 fine fraction without mixing and melting with surrounding aerogel. Rapid nondestructive surveys of small craters with SEM-EDXS can in most cases determine the dominant elements present in the surviving material at the crater bottom. Thus, one can target FIB-TEM studies on subsets of craters that contain grains of the desired composition and size (utilizing impactor diameter to crater diameter relationships such as those in Price *et al*. [2010]).

4.4 Acfer 094 Analog Foils

Our study of refractory analog foils demonstrated that crystalline impactors, particularly those belonging to single, submicron grains, are capable of surviving hypervelocity impacts into the Stardust foil collectors. The refractory analog results indicated that FIB-TEM analyses of craters ~1 micron in size could yield a better characterization of the Wild 2 fine component. However, while the refractory grains showed signs of minor melting and deformation, the results did not fully align with previous studies of Stardust craters. Surviving crystalline material has been observed in 1-3 μm Stardust cometary craters, but the vast majority of these craters contained thin, amorphous layers indicative of rapid melting and quenching following the material's impact (Leroux *et al*., 2008; Leroux *et al*., 2010; Stroud *et al*., 2010). One major difference between the Stardust craters and previous analog foil studies was the structure of the impactors. While many analog studies had focused on the survival of individual mineral grains such as wollastonite or olivine (e.g., Wozniakiewicz *et al*., 2012b and Foster *et al*., 2013), the behavior of aggregate impactors composed of a variety of grains was still poorly understood. Studies of over 500 small

craters with EDXS techniques revealed that ~40% of the studied craters were mixtures of silicate and sulfide components, indicating that a large portion of the foil craters were created by aggregate impactors (Price *et al*., 2010; Stroud *et al*., 2010). Investigating aggregate impactors in analog foil experiments allows us to better replicate the impact processing that Wild 2 material experienced. As a result, we can better understand the biases that may exist in the captured Wild 2 material (e.g., the lack of presolar grains) and better characterize comet Wild 2, particularly its fine component, with the materials returned by the Stardust spacecraft.

4.4.1 Acfer 094 Analog Samples and Experimental Methods

The material that we used for this study came from meteorite Acfer 094. Acfer 094 is an ungrouped primitive carbonaceous chondrite that is among the least altered meteorites ever recovered (Newton *et al*., 1995). Acfer 094's fine-grained matrix is largely composed of anhydrous and amorphous material and appears to have experienced minimal aqueous and thermal alteration (Greshake 1997). The lack of alteration suggests that material from Acfer 094 would be one of the best meteoritic analogs for comet Wild 2, which spent the majority of its life beyond the orbit of Neptune. Preparation of the material was similar to the preparation used for the creation of the refractory analog foils. Matrix material from Acfer 094 was ground into a fine powder with a mortar and pestle and was cemented together with a polyvinyl acetate in order to create sufficiently large (~100 μm) aggregate projectiles for firing with a LGG. These projectiles were then shot at normal incidence into flight spare Stardust mission Al 1100 foil using the two stage LGG at the University of Kent (Burchell *et al*., 1999). The impact speed of the shot was measured at 6.05 km/s, which is comparable to the capture speed (6.12 km/s) of Wild 2 cometary particles (Tsou *et al*., 2004). Previous analog experiments have demonstrated that weaker aggregate particles may fragment in the LGG during the firing process, resulting in impacts by a

wide range of particle sizes, including many of the separated subgrain components (Kearsley *et al*., 2009). The composition of Acfer 094's matrix material, as reported in Wasson & Rubin (2010), is shown in Table 4.2. The matrix is dominated by Si-, Mg-, and Fe-bearing phases but also has significant S, Ca, and Al.

TABLE 4.2: Mean matrix composition in Acfer 094 as reported in Table 3 of Wasson & Rubin (2010). The matrix is dominated by Si-, Mg-, and Fe-bearing phases. The low totals are primarily due to the presence of cracks and surface roughness in the analyzed Acfer 094 thin section, though the presence of carbonates is also a contributing factor.

Element	**Mean Wt. %**	**Std. Dev. Wt. %**
SiO_2	31.30	0.51
Al_2O_3	1.81	0.12
Cr_2O_3	0.409	0.026
MnO	0.214	0.019
CaO	2.526	0.093
MgO	16.23	0.67
FeO	29.62	0.54
Na_2O	0.270	0.013
K_2O	0.222	0.02
S	2.96	0.22
Total	84.12	0.64

Researcher Kevin Croat and I performed SEM-EDXS analyses on 201 craters on the cratered Al foil. Crater diameters ranged from ~500 nm to ~15 µm. SEM-EDXS spectra were collected with a 10 kV primary beam with 200 seconds of livetime on Washington University's JEOL JSM-840A SEM. The beam voltage was chosen to minimize the beam interaction volume while also giving sufficient overvoltage for Fe-K peak quantification. Initial SEM-EDXS results were qualitative in nature and were used for the selection of craters for further analysis with FIB-TEM analysis. Mg, Si, Fe, Ca, and S were all clearly visible in the collected spectra. Quantification of the SEM-EDXS results was performed following FIB-TEM analysis. Sensitivity factors using ZAF-corrected k-factor techniques were determined through comparison with TEM-EDXS results acquired on the same craters. Quantification was only performed on the

most abundant elements (Si, Fe, Mg, S, and Ca). Al, though composing a significant fraction of the Acfer 094 matrix, was excluded due to interference from the Al present in the foil. Uncertainties in the measurements, estimated through differences in TEM-EDXS and SEM-EDXS spectra, were roughly ± 5%.

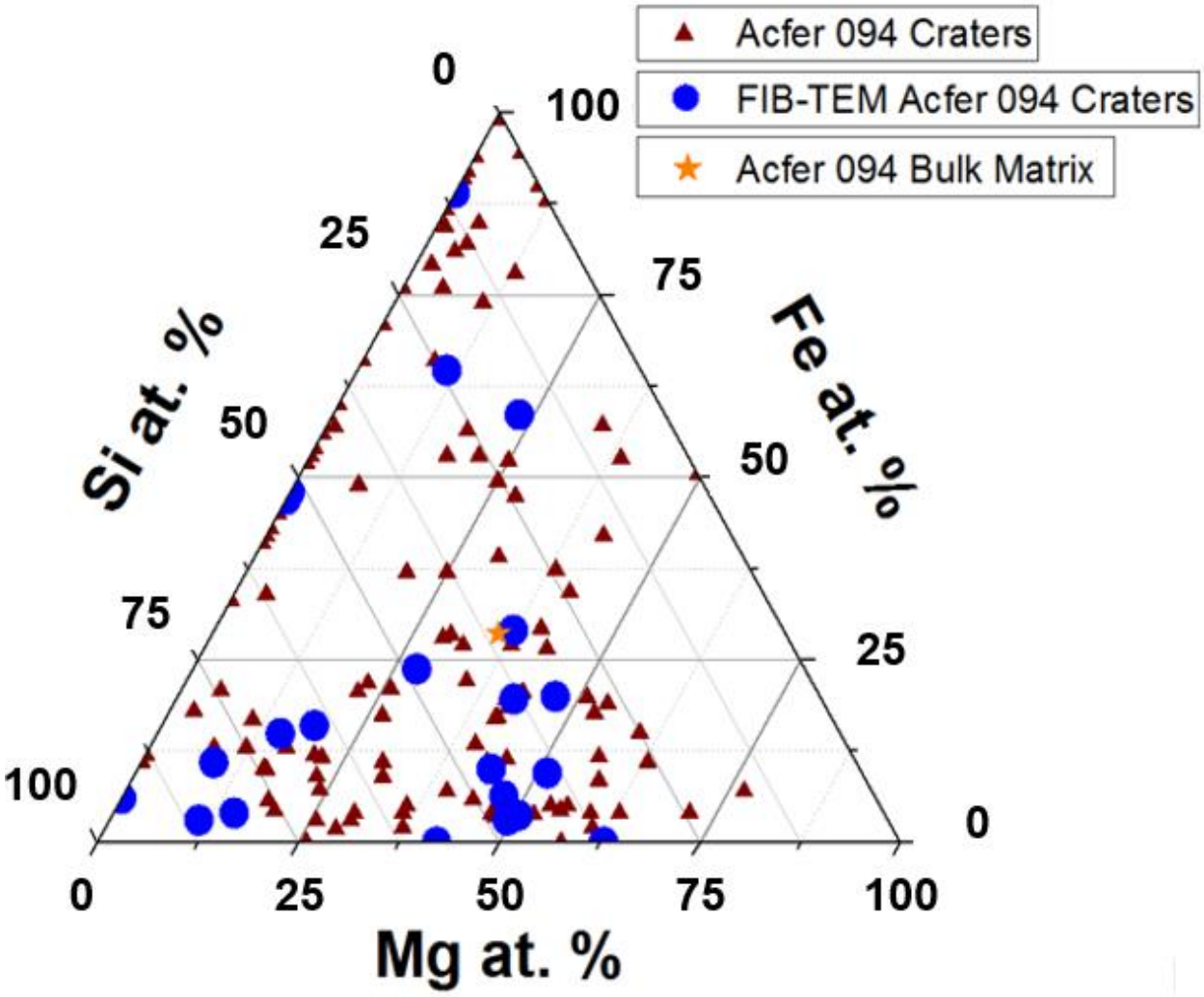

FIGURE 4.5: Ternary plot of SEM-EDXS results of 201 Acfer 094 analog foil craters, with the total Mg, Si, and Fe at. % normalized to 100%. Mg, Si, and Fe are shown as they were the three most abundant elements in nearly all craters and S abundances were typically correlated with Fe abundances. Ca abundances were typically only a few at. % in craters in which it was present. 22 craters, indicated by larger blue circles, were selected for further investigation with FIB-TEM techniques. The Acfer 094 bulk matrix composition (taken from Wasson & Rubin [2010]) is shown as an orange star. Uncertainties on the measurements are within ± 5%.

SEM-EDXS results are summarized in a ternary plot shown in Figure 4.5. The examined craters showed a wide range of Fe, Si, and Mg elemental abundances. Al contents of the craters could not be determined due to the Al foil background. Craters were selected for further FIB-TEM analysis so as to contain a range of these abundances to ensure a variety of impacting materials were sampled.

22 craters were selected for further analysis with FIB-TEM techniques. Craters of varying size were extracted to allow for comparison between different size impactors. Four extracted craters had diameters ranging from ~500 nm to ~900 nm, twelve had diameters ranging from ~1.0 µm to ~2.3 µm, and six had diameters ranging from ~5.0 µm to 10.0 µm (Figure 4.6). The SEM-EDXS results for these craters are summarized in Figure 4.5. FIB extraction and thinning was performed on Washington University's FEI Quanta 3D FIB. Craters were thinned to 100-150 nm. TEM analysis was performed on Washington University's JEOL 2000 TEM.

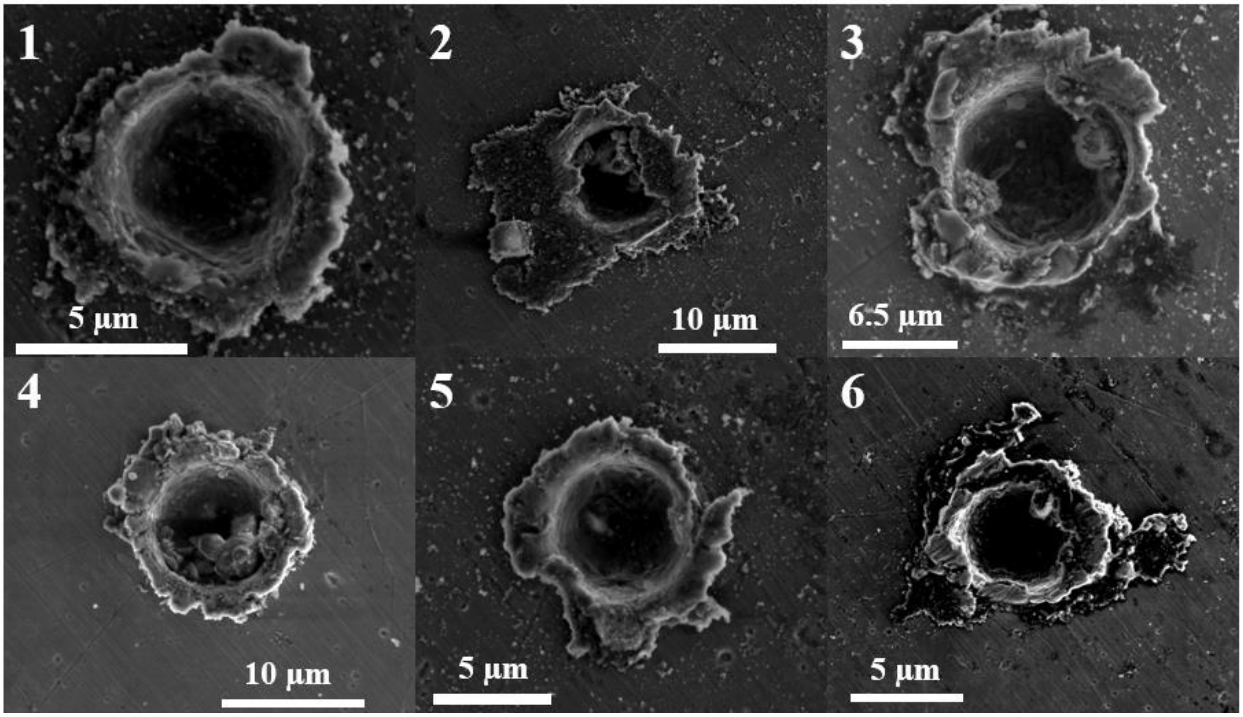

FIGURE 4.6: FIB-SEM images of the six large Acfer 094 analog craters with diameters between 5 µm and 10 µm taken immediately prior to FIB extraction.

4.4.2 Acfer 094 Analog Foil Results

No surviving crystalline material was observed in the 22 Acfer 094 craters examined with FIB-TEM techniques despite the abundance of crystalline material observed in our previous study of refractory TiC and TiN impactors. All craters had amorphous melt layers that were typically thickest along the crater bottoms but spread upwards along the crater walls. Impactor material was not detected in the crater lips. The craters typically contained rounded, bowl-shaped crater bottoms consistent with a single, compact impactor. The impact residues were dominated by compositionally homogeneous melt layers that were largely composed of either Si/Mg/Fe, Fe/S/Ni, or combinations of the two (Figure 4.7). Al was also present in the majority of the examined melt layers, demonstrating that the impactors mixed with the foil substrate prior to quenching. Heavy Al incorporation into the residue melts has been reported in previous analog studies (e.g., Wozniakiewicz *et al*., 2012b), though these studies have typically focused on craters larger than our small- (450-900 nm) and medium- (1-3 µm) sized craters.

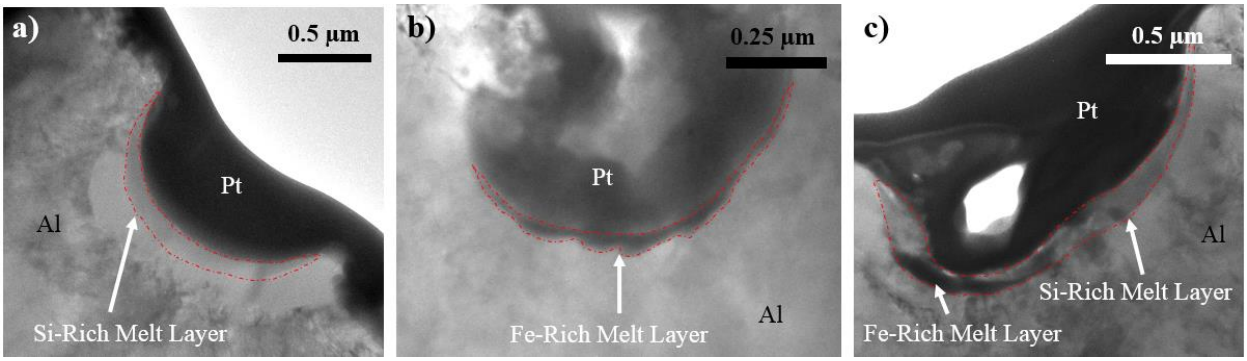

FIGURE 4.7: Bright-field TEM images of three of the medium- (1-3 µm) sized Acfer 094 analog craters. The melt layers composed of impactor material are highlighted. a) Shows a crater containing a brighter Si-rich melt layer, b) shows a crater containing a darker Fe-rich melt layer, and c) shows a crater containing both types of melt layers.

Signs of excessive alteration were present throughout the crater residues. The homogeneity of the crater residues indicated that the impactor residue had been thoroughly melted and mixed together prior to quenching. Two of the medium-sized analog craters and four of the large-sized

analog craters had melt layers containing Fe-vesicles (Figure 4.8) within Si-rich melt layers. The observed Fe-vesicles are similar in size, shape, and composition to those observed in studies of space weathering in lunar regolith (Keller & McKay 1997). Studies of iron vesicles in lunar olivine suggest that material involved in high velocity impacts does not need to reach the vapor phase for Fe-metal to segregate out and become insoluble in surrounding silicate material (Noble *et al*., 2015). Fe present in our Si- and Mg-rich melt layers likely separated itself out from the surrounding melt following similar processes, indicating the impactor material was either vaporized or fully liquefied allowing for Fe-transport before recrystallization of the surrounding Si- and Mg-rich material. The complete lack of sulfur within these vesicles indicates that the vesicles were likely not remnants of iron-sulfide impactors that had intermixed with more Si-rich residues. The presence of Fe-vesicles in our craters were consistent with previous studies of Si- and Fe-containing analog foil impactors, where Fe-vesicles were commonly seen (Wozniakiewicz *et al*., 2012b). However, the craters containing Fe-vesicles in Wozniakiewicz *et al*., (2012b) were far larger (≥50 μm) than the craters we investigated in our own study.

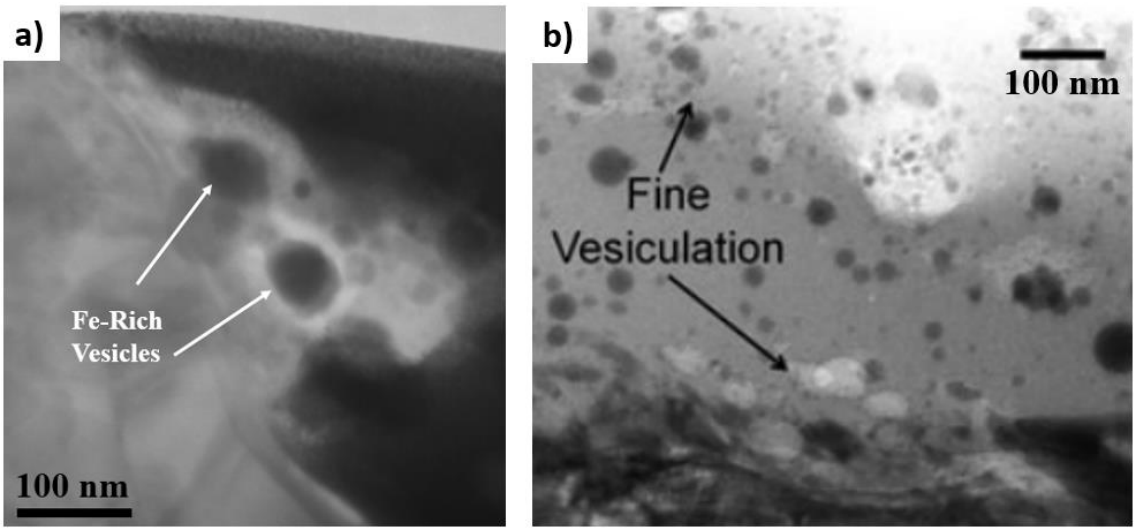

FIGURE 4.8: a) Bright-field TEM images of Fe-rich vesiculation occurring in one of the medium-sized (1-3 μm) Acfer 094 analog foil craters. b) Bright-field TEM image of vesiculation occurring in a large (≥50 μm) analog foil crater taken from Figure 15 of Wozniakiewicz *et al*., (2012b).

Volatile loss was also noted within the Fe-rich melt layers. 8 of the 22 craters contained melt layers or portions of melt layers that were composed entirely of iron sulfide impactors. Fe/S ratios within these melt layers were compared to Fe/S ratios in samples of extra, unfired Acfer 094 material that was not used during the creation of the Acfer 094 analog foils (Figure 4.9). Fe/S ratios in the unfired Acfer 094 material were calculated with SEM-EDXS spectra using similar techniques for the quantification of the crater residues described in Chapter 4.4.1. The average Fe/S ratio of iron sulfides identified in the Acfer 094 analog craters was nearly 4 times as large as the average Fe/S ratio in unfired Acfer 094 matrix material (12.1 and 3.1, respectively). Additionally, the Fe/S ratios in our unfired Acfer 094 material included Fe contributions from non-sulfide components (e.g., silicates), indicating that S-loss within the sulfides was likely greater than a factor of 4. The extreme S loss seen in our analog craters differed from previous studies of Stardust foils, where Fe/S ratios were more closely aligned with the unfired Acfer 094 material (Figure 4.9) (Leroux *et al*., 2008).

4.4.3 Acfer 094 Analog Foil Discussion

The ubiquitous melt layers observed in all of the Acfer 094 analog craters attest to the high temperatures and pressures experienced by the impactor materials. The homogeneity of the melt layers, coupled with the Al incorporation into these melt layers, indicates that the impacting material was thoroughly melted alongside the impacted Al and these materials fully intermixed prior to the resolidification of the material.

The extent of the alteration in the Acfer 094 analog craters is demonstrated through the formation of Fe-vesicles and the loss of S from the iron sulfide impactors. Fe-vesicles require the impactor melt to remain liquid sufficiently long for the Fe to dissociate and migrate from the more Si- and Mg-rich surrounding melt, indicating that the initial temperatures reached were either large

or quenching was sufficiently slow. Volatile loss, in this case S present in iron sulfides, also indicates that temperatures and pressures reached during the impact must have been large.

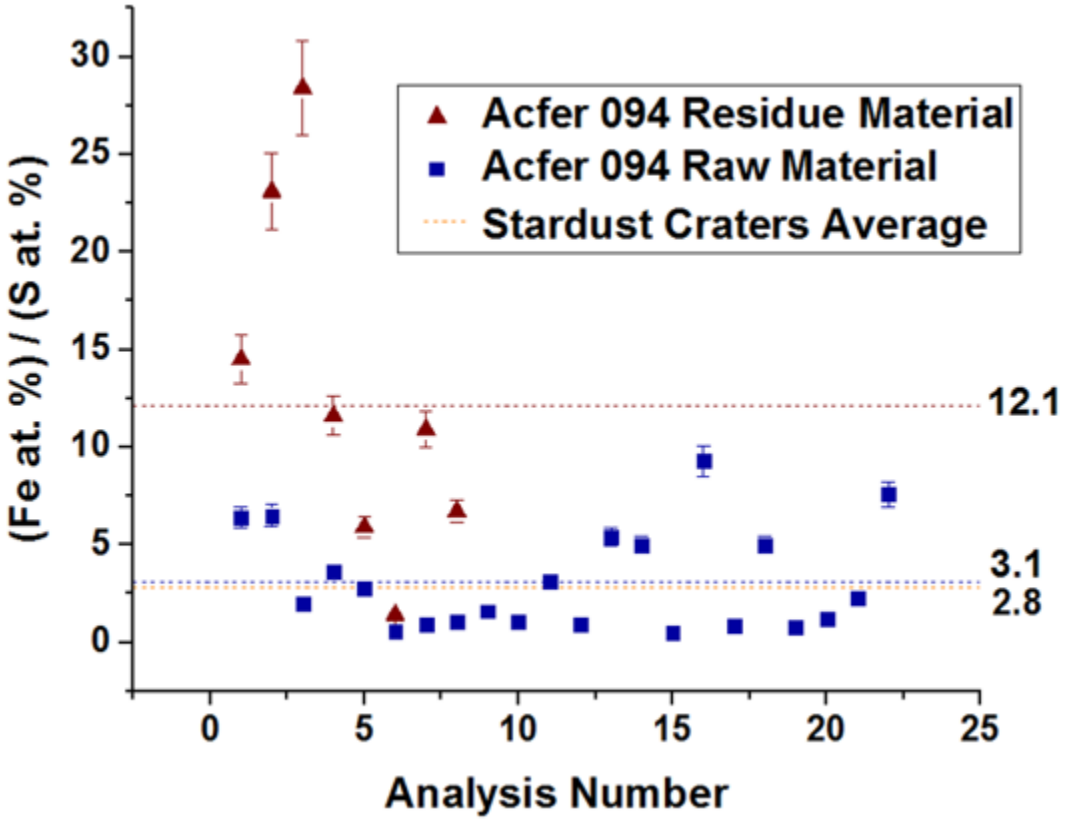

FIGURE 4.9: Comparison of Fe/S ratios in iron sulfides seen in our Acfer 094 analog craters and Fe/S ratios seen in unfired Acfer 094 material. The average Fe/S ratio of our fired iron sulfides (12.1) was nearly 4 times as large as the average Fe/S ratio of unfired Acfer 094 matrix material. Also listed is the Stardust craters average for iron sulfide impactors taken from prior FIB-TEM analyses of Stardust craters in Leroux *et al*., (2008).

The alteration seen in these analog foils is difficult to compare with previous analog experiments. Our previous investigations of refractory impactors found surviving crystalline material in nearly all craters, but the impactors in the Acfer 094 analog material had much lower melting points. Olivines and pyroxenes are the most abundant crystalline phases in the Acfer 094 matrix (Greshake 1996), but these materials have melting points below 2000 °C, whereas our Ti-rich impactors had melting points closer to 3000 °C. Furthermore, the impactors in the refractory

analogs were frequently single-grain impactors, whereas the Acfer 094 impactors were aggregate grains. Large portions of the Acfer 094 matrix (20-80 % by vol.) are amorphous (Greshake 1996) and would not have returned crystalline material regardless of the impacting conditions. Investigations of Fe- and Si- containing impactors have returned Fe-vesicles similar to our own studies, but these investigations focused on craters orders of magnitude larger than our own (Wozniakiewicz *et al*., 2012b). As a result, they likely had much higher peak temperatures and pressures and such signs of excessive alteration were expected. The importance of impactor scale is emphasized by the sizes of the craters containing Fe-vesicles. No vesicles were observed in the small (500-900 nm) craters, 2 were observed in the medium (1-3 μm) craters, and 4 were observed in the large (5-10 μm) craters, indicating that larger impactors experience prolonged liquification. Larger craters may also have shown additional S loss, but the presence of only 8 iron sulfide melt layers in the craters was insufficient to reach that conclusion. Larger craters were expected to show more signs of alteration given the refractory analogs showed additional flattening in larger craters, but even the largest refractory impactors contained surviving crystalline material. Our Acfer 094 analog foil results do not appear inconsistent with previous analog studies, though the impactors' differing compositions and sizes make direct comparisons with previous investigations difficult.

The excessive alteration present in the Acfer 094 analogs differed from the results seen in previous investigations of authentic Stardust foils. While no surviving crystalline material was present in our 22 Acfer 094 analog foil craters, previous investigations of Stardust foils returned crystalline material in 10 out of 22 investigated craters (Leroux *et al*., 2008; Leroux *et al*., 2010; Stroud *et al*., 2010). While the matrix materials are dominated by amorphous phases (ranging between 20-80% by volume) and some of the impactors may have been fully amorphous prior to

impact, it remains unlikely that none of the impactor material was crystalline (Greshake 1996). Additionally, prior Stardust investigations did not report that iron vesicles were observed. The S-loss in our analog craters also separates our results from the authentic Stardust studies. Stardust craters containing iron sulfides have returned Fe/S ratios similar to those observed in the unfired Acfer 094 material, as shown in Figure 4.9. However, iron sulfides in our Acfer 094 analog craters had Fe/S ratios inflated by nearly a factor of 4 relative to these previous Stardust results due to the loss of S during the impact processing. The lack of crystalline material, the presence of Fe-vesicles, and the large S-loss from iron sulfides all indicate that our analog craters were experiencing more alteration than the Stardust foils.

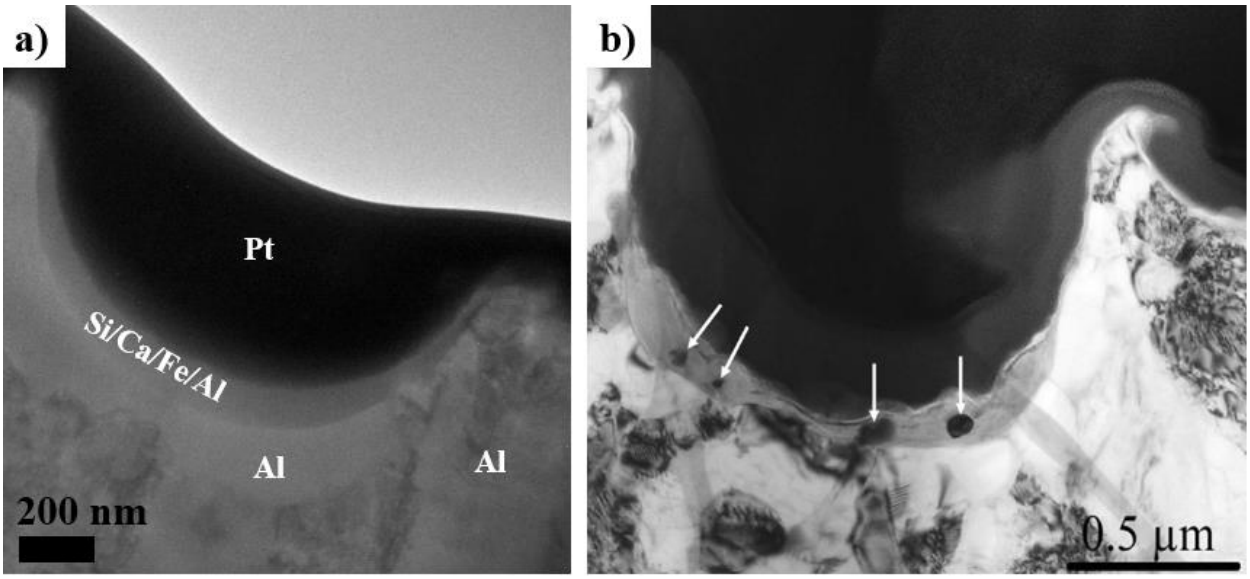

FIGURE 4.10: Comparison of impactor melt layers seen in our Acfer 094 analog studies and the impactor melt layers seen in studies of authentic Stardust foils. a) TEM bright-field image showing our amorphous melt layer of Si/Ca/Fe/Al sandwiched between the Al substrate and the protective Pt cap. b) TEM bright-field image taken from Figure 6 of Leroux *et al*., (2008) that highlights surviving crystallites. Whereas our melt layers were thoroughly amorphous and homogenized, previous Stardust foils have returned surviving crystalline material within surrounding melt layers.

The cause for the differences between our Acfer 094 foils and the Stardust foils is still unresolved. The analog experiments attempted to reproduce the Stardust conditions as accurately as possible using flight-spare Stardust foils and velocities within 2% of those reported by the

Stardust spacecraft. One difference between the Stardust mission foils and our own is the temperature of the material and the foil. While the analog experiments were conducted in a laboratory at room temperature, the material from comet Wild 2 and the Stardust foils were considerably colder. We do not know the temperature of the cometary material prior to impact, and no temperature measurements were made on the Stardust collector itself during the mission. However, a temperature sensor was present on a hinge attached to the Stardust return capsule. Temperature readings from this hinge (available at https://pds-smallbodies.astro.umd.edu /holdings/sdu-c-src-2-temps-v1.0/DOWNLOAD/) indicate that it was approximately -9 °C during the spacecraft's encounter with Wild 2. The impact of this temperature difference can be estimated through a naïve calculation of an impactor's kinetic energy and the additional energy needed to raise the colder aluminum to room temperature. Estimating the laboratory's temperature as 23 °C at the time of the firing, we find the Stardust foils were 32 °C colder than those in the laboratory. The kinetic energy (mass times velocity squared) of a pure silicon sphere with a diameter of 0.5 µm and a density of 2.65 g/cm^3 moving at 6.1 km/s is 2.8 * 10^{-9} Joules. The energy required to raise a 2 µm by 2 µm by 2 µm cube of aluminum by the 32 °C difference in temperature is thus the specific heat of Al times the mass of the Al cube times the change in temperature. Using an Al density of 2.7 g/cm^3 and a specific heat of Al of .9 J/(g*K), the energy needed to change the block of Al is 6.22 * 10^{-10} Joules. However, given the order of magnitude difference between this result and the particle's kinetic energy, it appears unlikely that the difference in foil temperature is the source of the large differences in alteration seen in the Acfer 094 analogs and the authentic Stardust foils.

Another potential cause of the excessive alteration in our analog foils is the difference in compressive strengths between our analog materials and Wild 2 materials. Comet surfaces have

low compressive strengths. Studies of comet comet 67P/Churyumov-Gerasimenko estimated its surface compressive strength at 100 Pa (roughly 5 orders of magnitude lower than concrete), with an upper limit of 800 Pa (Heinisch *et al*., 2018). However, our analog materials were cemented together with a polyvinyl acetate in order to prepare the sample for firing with the LGG. The low compressive strength of the Wild 2 material may have resulted in a different partitioning of the impactors' energy, resulting in less alteration to the Wild 2 materials.

The most likely explanation for the difference between the Acfer 094 analogs and the Stardust foils is the additional acceleration event needed to conduct the analog experiment. From the center of mass frame of the Stardust spacecraft, the collector was stationary before it was impacted by (and thus decelerated) the cometary material at 6.1 km/s. However, during the LGG experiments, the analog material must first be accelerated from an unmoving state to 6.1 km/s before it is decelerated less than a millisecond later through impact with the flight spare Stardust foils. It appears likely that the firing of the material imparts energy into the particles other than through the particles' gain in kinetic energy, and thus the material is heated prior to impact with the foil. As a result, the analog foils do not seem to perfectly replicate the Stardust collection conditions and show additional levels of alteration that are unexpected despite the violent collection conditions.

4.4.4 Acfer 094 Analog Foil Summary and Conclusions

The alteration seen in the Acfer 094 analog foils attests to the high temperatures and pressures experienced by the impactor materials. The lack of crystalline material, the incorporation of Al from the foil substrate into the impactor melt layers, the presence of Fe-vesicles in larger craters, and the loss of sulfur all indicate that the impactor material is heavily altered during the deceleration process in the foils.

The presence of Fe-vesicles in the medium and large craters confirms the earlier results of the refractory analogs that indicated that larger impactors were more heavily altered by the collection process. None of the 4 small craters, 2 of the 12 medium craters, and 4 of the 6 large craters contained Fe-vesicles, indicating that larger craters experienced prolonged liquification allowing for Fe-migration within the melt layers. Similarly, the larger refractory craters were flattened further than the small refractory craters, indicating that higher peak temperatures and pressures are reached during larger impacts.

The extreme alteration observed in our craters helps to explain the lack of presolar grains seen in previous studies of the Stardust foils. Our results showed aggregate impactors melting together to form homogenous melt layers, which would dilute any isotopic anomalies present in the impacting material. Additionally, no impactor material was seen in the crater rims, indicating that it is rare for impactor material to avoid the crater floors and walls where heavy alteration occurs.

The alteration seen in our Acfer 094 analog craters is far more extreme than the alteration seen in previously investigated Stardust craters. Though the lack of crystalline material may be the result of amorphous impactors, our observed S-loss and Fe-vesicles have not been reported in previous investigations of Stardust impactors. The analog foils appear to have experienced more alteration than the Stardust foils and may not perfectly replicate the spacecraft's collection conditions. As a result, drawing conclusions about which specific materials may or may not be capable of surviving the Stardust foil impact conditions is difficult, particularly when no surviving crystalline material is observed in our Acfer 094 analog residues.

4.5 Tagish Lake Meteorite Analog Foils

The second aggregate impactor selected for analog foil studies was matrix material from the Tagish Lake meteorite. Following the refractory analog studies we selected aggregate impactors to better replicate the Wild 2 impactors. Material from the Tagish Lake meteorite was chosen to complement the analog Acfer 094 experiments that aimed to investigate potential biases in the cometary material returned by the Stardust foils. Tagish Lake is an ungrouped type 2 carbonaceous chondrite known for containing an abundance of organic materials (Brown *et al*., 2000). Organic materials were expected to be a sizable component of comet Wild 2, and a N isotopic anomaly has been observed in a crater from the Stardust foils, indicating that some organic material may survive impact processing (Stadermann *et al*., 2008). However, no organic carbon has been observed in FIB-TEM studies of the Stardust foils (Leroux *et al*., 2008; Leroux *et al*., 2010; Stroud *et al*., 2010). Through study of analog craters created with the relatively organic-rich Tagish Lake meteorite material we aimed to investigate the potential bias against these carbonaceous materials in the Stardust foils.

4.5.1 Tagish Lake Analog Samples and Experimental Methods

The material used for this study came from the matrix of the Tagish Lake meteorite. Tagish Lake is a carbonaceous chondrite containing ~2.6 wt. % organic carbon (Grady *et al*., 2002). Approximately 3.7 wt. % carbon in Tagish Lake derives from Fe- and Mg-rich carbonates, and minor amounts of nanodiamonds and silicon carbides have been identified during isotope analyses (Brown *et al*., 2000). The majority of Tagish Lake's matrix material consists of phyllosilicates, most likely intergrown serpentine and saponite, but olivine, magnetite, and iron-nickel sulfides are also abundant (Brow *et al*., 2000). The Tagish Lake meteorite shows significantly more aqueous

alteration than Acfer 094, but the meteorite's high organic carbon and carbonate abundances make it a good analog for investigating the survival of these carbonaceous materials in the Stardust foils.

Preparation of the material was similar to the preparation used for the creation of the refractory and Acfer 094 analog foils. Matrix material from the Tagish Lake meteorite was ground into a fine powder with a mortar and pestle and was cemented together with a polyvinyl acetate in order to create sufficiently large (~100 μm) aggregate projectiles for firing with a LGG. These projectiles were then shot at normal incidence into flight spare Stardust mission Al 1100 foil using the two stage LGG at the University of Kent (Burchell *et al*., 1999). The impact speed of the shot was comparable to the capture speed (6.12 km/s) of Wild 2 cometary particles (Tsou *et al*., 2004). Previous analog experiments have demonstrated that weaker aggregate particles may fragment in the LGG during the firing process, resulting in impacts by a wide range of particle sizes, including many of the separated subgrain components (Kearsley *et al*., 2009).

I performed SEM-EDXS analyses on 52 craters on the cratered Al foil. Crater diameters ranged from 0.8-4.0 μm. I focused exclusively on smaller and medium-sized craters in order to minimize potential impact alterations given the excessive alteration seen in the larger analog craters in our previous experiments. SEM-EDXS spectra were collected with a 10 kV primary beam with 300 seconds of livetime on Washington University's JEOL JSM-840A SEM. The beam voltage was chosen to minimize the beam interaction volume while also giving sufficient overvoltage for Fe-K peak quantification. Initial SEM-EDXS results were considered qualitative in nature given the difficulty in obtaining measurable signals from the studied craters and the assumption that later TEM-EDXS analyses would return far more accurate results. Of the 52 examined craters, only 17 craters returned observable Si or Mg signals. The remaining craters only returned C or Al signals. All craters contained weak C signals in their EDXS-spectra, but

these signals were possibly the result of a thin organic contamination layer known to form on the foils, particularly after the foils are exposed to an electron beam (Kearsley *et al*., 2010).

Eight craters with observable Si or Mg signals were selected for further study with FIB-TEM analysis. Crater diameters ranged from 1.1 µm to 4.0 µm. FIB extraction and thinning was performed on Washington University's FEI Quanta 3D FIB. Craters were thinned to 100-150 nm. TEM analysis was performed on Washington University's JEOL 2000 TEM.

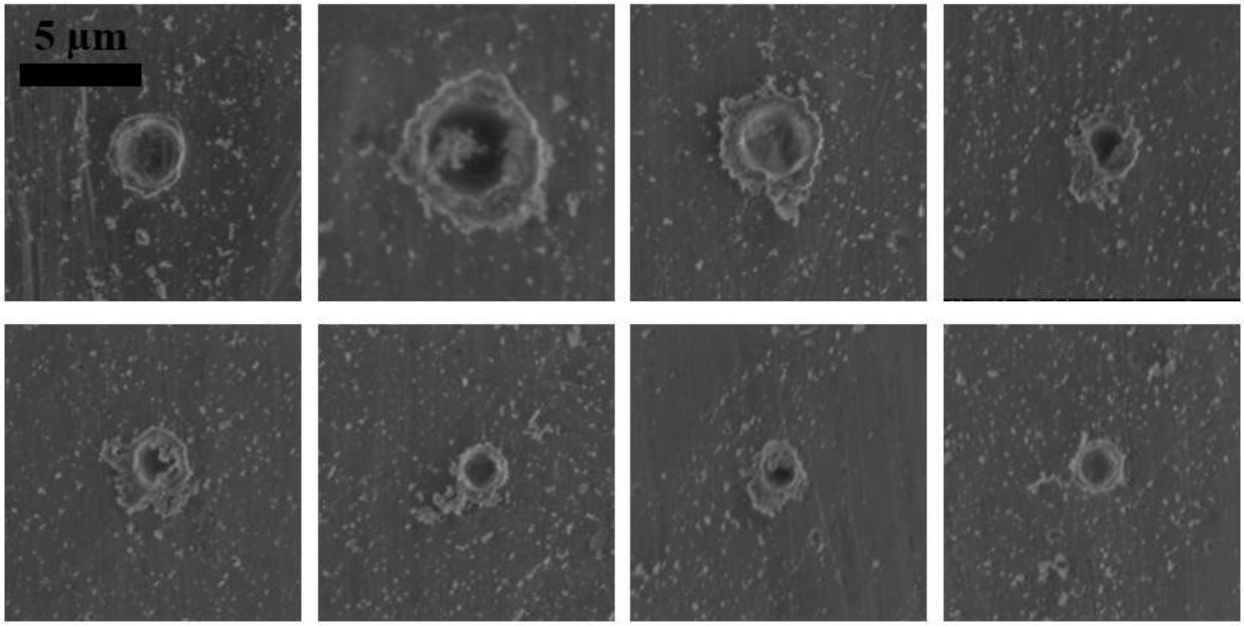

FIGURE 4.11: Secondary electron images of eight Tagish Lake analog craters selected for further study with FIB-TEM techniques.

4.5.2 Tagish Lake Analog Foil Results

TEM investigation of the craters revealed deep, bowl-shaped craters, indicative of impacts by a single, dense body. All eight craters contained thin (10-50 nm) melt layers that coated the crater floors and walls. Melt material was not observed in the crater rims.

Two craters contained large gaps in their melt layers that have not been previously seen in our analog impactors nor in previous investigations of Stardust materials (Figure 4.12). Tagish Lake analog crater #1 had two bulbous melt layers on the left side separated by an empty gap. The discontinuity in the melt layers, coupled with the melt layers becoming thicker just prior to the

discontinuity, were both unusual features of the melt layer. Tagish Lake analog crater #3 had a melt layer that bends up and over a void separating it from the Al substrate. Following the impact, volatile material must have become gaseous and formed a pocket of air that survived sufficiently long for the foil to quench the rest of the molten impactor materials. The gaps in the melt layers appear to indicate the loss of impacting volatile material during impact processing.

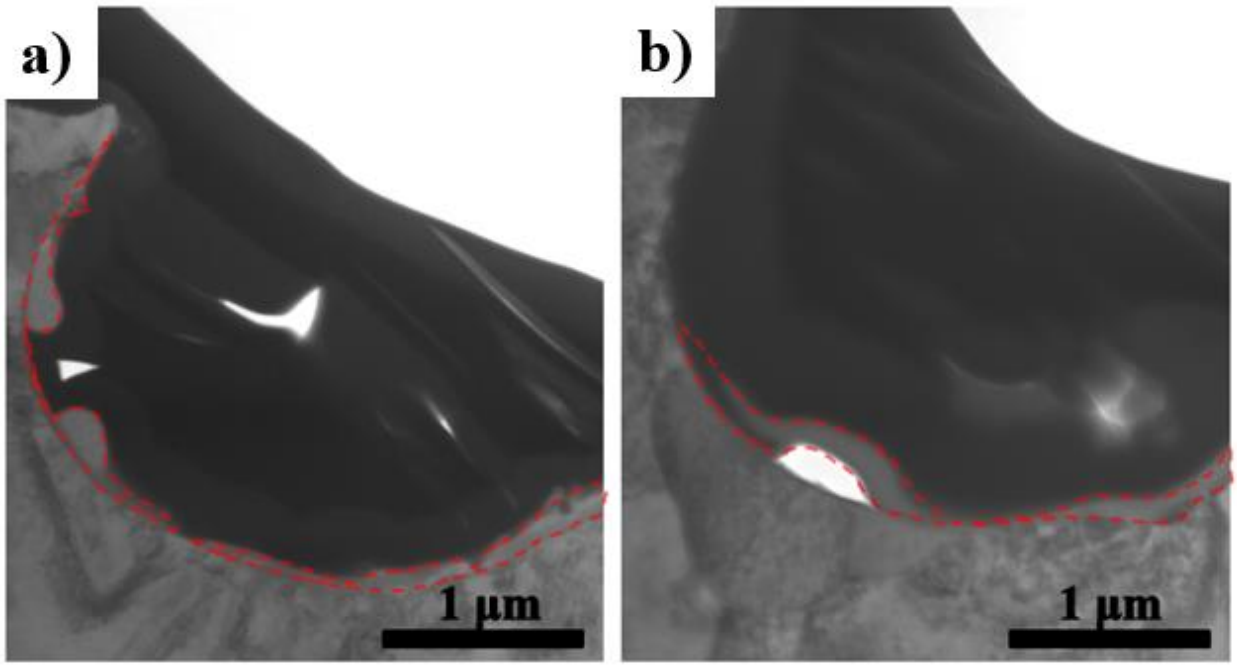

FIGURE 4.12: TEM bright-field images of the crater melt layers (outlined in red) with unusual morphologies in the Tagish Lake analog foils. a) Tagish Lake crater #1 has two bulbous melt layers on the left side separated by an empty gap. b) Tagish Lake crater #3 has a melt layer that bends up and over a void separating it from the Al substrate. The gaps in the melt layers potentially indicate the loss of impacting volatile material during impact processing.

The residue layers in the craters did not contain any surviving crystalline material. The impactor melt had formed a thoroughly amorphous layer that was later quenched by the surrounding Al foil. TEM-EDXS analysis revealed that the melt layers were largely composed of O/Si/Mg/Fe, with S and Ni present within Fe-rich residues. Crater melt layers were fairly homogeneous, with Si/Mg ratios within any individual melt layer varying by no more than ± 5 at. % across different TEM-EDXS spot analyses performed on the residues aside from crater #1

(Figure 4.12). Crater #1 was unusual in that the Si/Mg ratios of the bulbous, separated portion of the melt layer were distinct from the Si/Mg ratios in the rest of the residue layer. Al was also present throughout the melt layers, suggesting melting and mixing with the Al substrate was widespread. Fe was present in the melt layers, but not as differentiated vesicles, unlike our previous Acfer 094 analog foil experiments. The homogenization of the melt layers, coupled with the Al incorporation indicates that they likely experienced full melting, but quenched sufficiently quickly to prevent vesiculation from occurring.

The crater residues showed a wide range of Mg/Si/Fe ratios (Figure 4.13). The variety of compositions suggests that I sampled a variety of aggregate impactors. O, Mg, Fe, Si, and Al were the most abundant elements in the melt layers. S and Ni were both trace (< 1 at. %) in the residues, suggesting most of the Fe is not the result of iron-nickel sulfides. Si/(Mg + Fe) ratios were .15 or less for 5 of the crater residues. These values are far too low for olivine or phyllosilicates, suggesting that these residues may have resulted from other Mg and Fe carriers (e.g., carbonates) that are present in the Tagish Lake meteorite. Two particularly Fe-rich residues may have contained magnetite, which is abundant in Tagish Lake (Brown *et al*., 2000). Trace (< 1 at. %) Ca was observed in all of the crater residues, with two craters containing significant (> 5 at. %) Ca that could be the result of a calcite grain. One crater contained ~2 at. % Mn. Mn is known to be present in carbonates within the Tagish Lake meteorite at abundances up to 1 wt. %, potentially explaining its presence in this crater, though it also could have been a component of the serpentine matrix (Brown *et al*., 2000). Trace Cr was also present in three of the crater residues, suggesting that small chromite grains may have been present in the impacting aggregate grains.

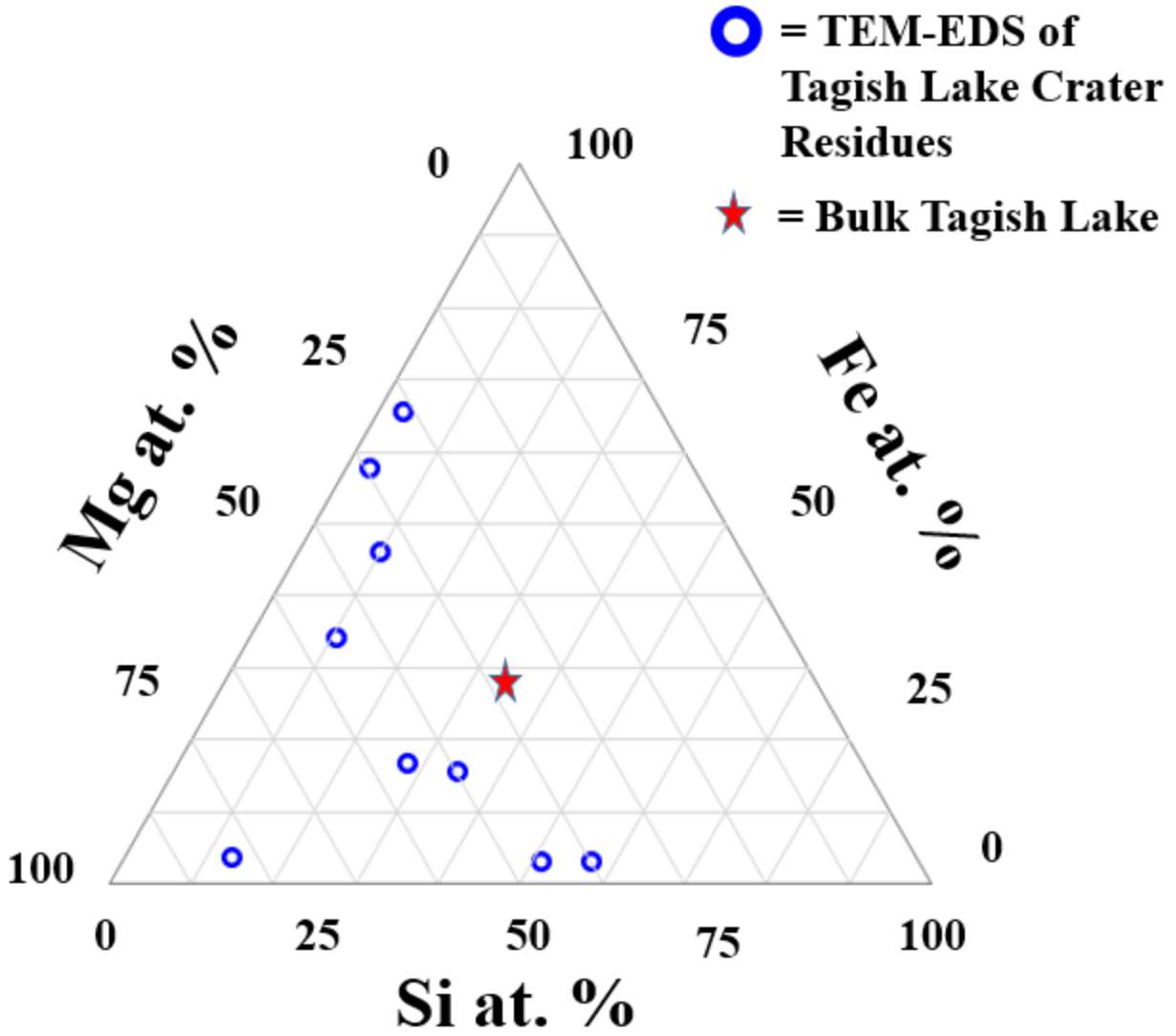

FIGURE 4.13: Ternary plot summarizing the TEM-EDXS results of the 8 Tagish Lake analog crater residues with the total Mg, Si, and Fe at. % normalized to 100%. 9 points are present on the plot due to crater #1 having two regions with distinct compositions. The other 7 craters were compositionally homogenous throughout, with Si and Mg atomic abundances varying by no more than ± 5% throughout the residues. The bulk Tagish Lake composition comes from Brown *et al.* (2000).

The unusual crater morphologies, the Si/(Fe+Mg) ratios, and the presence of Mn suggested that carbonates were components of the aggregate impactor. However, despite these factors and the abundance of organic carbon and carbonates in the Tagish Lake meteorite, C was only present within crater #1 (Figure 4.14). The C abundance was not reflected in the crater's SEM-EDXS spectrum, which was dominated by the Al peak from the foil substrate. Crater #1 also had unusual

melt layer morphology, but the lack of C in crater #3, which also showed signs of volatile loss in its morphology, prevents us from establishing a clear connection between C abundance and crater morphology.

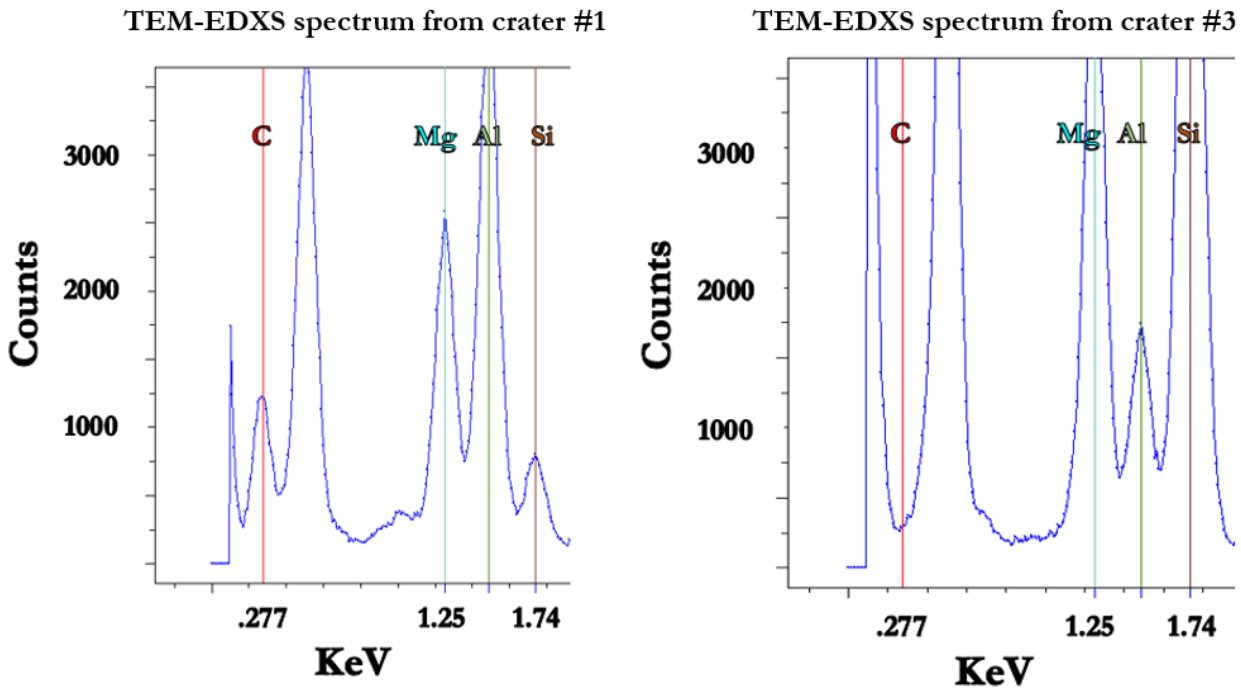

FIGURE 4.14: TEM-EDXS spectra from spot analyses performed on Tagish Lake analog craters #1 and #3. Crater #1 was the only one to show a C signature, though both crater #1 and #3 had unusual melt layer morphologies.

4.5.3 Tagish Lake Analog Foil Discussion

A large component of the Tagish Lake matrix is composed of phyllosilicates such as serpentine and saponite (Brown *et al*., 2000), suggesting that Si or Mg should have been present in a majority of the craters. However, roughly two-thirds of the craters studied with SEM-EDXS had no Si or Mg signals, compared to less than half of the Acfer 094 analog craters containing no Si, Mg, or Fe signals. The lack of significant Si or Mg within two-thirds of the craters studied with SEM-EDXS may be a result of the small craters containing too little Si or Mg-rich residue to be seen over the signal from the adjacent Al peak. Additionally, phyllosilicates are likely to be more easily destroyed than other silicates such as olivine and may have been lost on impact. The

volatility of C-rich impactors may also have resulted in craters that do not contain observable residue when examined by SEM-EDXS. Minor C peaks were observable in the SEM-EDXS spectra of all craters. However, crater #1, which did contain observable C in TEM-EDXS analyses, did not have a noticeably larger C peak in its SEM-EDXS spectra than the other craters that did not contain C within their melt layers. As a result the C peak seen in all SEM-EDXS spectra is predominantly from the C contamination present on top of the foils rather than any residue within the craters. Some of the empty craters may have contained C residues, but identifying them would not have been possible, potentially resulting in additional craters without strong SEM-EDXS signals.

Si/(Fe+Mg) ratios in the craters were typically lower than expected given the abundance of phyllosilicates within Tagish Lake's matrix. Previous evaporation experiments (Hashimoto 1983) have demonstrated that SiO_2 is more volatile than MgO. Additionally, laser heating experiments (Gerasimov *et al*., 2000) have shown preferential loss of Si over Mg from glasses. However, previous investigations of analog craters formed by phyllosilicate impactors have shown that, while volatile loss does occur, cation to Si ratios are largely unaffected (Wozniakiewicz *et al*., 2015). As a result, the low Si/(Fe+Mg) ratios are unlikely to be the result of preferential Si loss from less refractory phyllosilicate impactors. The low Si/(Fe+Mg) ratios are more likely to be the result of the aggregate impactors containing less Si than expected. Magnetite is common in Tagish Lake and could have contributed Fe without additional Si (Brown *et al*., 2000). Mg-, Fe-, and Ca-rich carbonates are abundant in the Tagish Lake meteorite and also could have contributed Fe and Mg without Si, further suggesting that carbonates were a possible component of the impacting material.

Previous investigations of phyllosilicate impactors (Wozniakiewicz *et al*., 2015) found extensive vesiculation and volatile loss within their residue layers. My results showed far less alteration, with no vesicle formation occurring in the craters. Though this may indicate that our impactors contained a variety of materials that are more refractory than phyllosilicates, the difference in results is most likely due to crater sizes. While my study focused on craters roughly 1-4 µm in diameter, Wozniakiewicz *et al*., (2015) focused on craters over 30 µm in diameter. As a result, the differences between their results and my own is likely due to small craters generally showing less signs of alteration, as is evident in the previous investigations of refractory and Acfer 094 analog materials.

Despite the abundance of C within the Tagish Lake meteorite, C was only observed in part of the residue of a single crater in this study. The lack of C in our residues may have been the result of a small sample size (8) or our inability to screen for C-rich craters with SEM-EDXS spectra. However, the unusual crater morphologies present in two of our craters point to large proportions of our impactors being composed of volatiles. Additionally, the Si/(Fe+Mg) ratios throughout and the small presence of Mn in one crater suggest that carbonates were a component of the impacting material. Definitively proving that these results are due to carbonate impactors being destroyed during impact processing is challenging. Previous investigations of calcite impactors, while showing widespread melting, volatile loss, and vesiculation, showed that original calcite mineralogy could survive the impact process, suggesting that similar impactors in our own experiments should have been identified with TEM-EDXS studies (Wozniakiewicz *et al*., 2015). However, the study investigated pure calcite impactors rather than aggregates, and thus their craters were far more likely to contain remaining C-rich residues (Wozniakiewicz *et al*., 2015).

The investigated Tagish Lake analog craters appear to have suffered from volatile and C loss, but definitively proving so requires further study.

4.5.4 Tagish Lake Analog Foil Summary and Conclusions

The alteration seen in the Tagish Lake analog foils was similar to that seen in our previous investigation of Acfer 094 analog foils. Crater residues were dominated by amorphous, glassy melt layers largely composed of Si-, Mg-, and Fe-rich materials. The Tagish Lake craters showed less extensive alteration due to their lack of vesiculation, but these results are likely due to our exclusion of large (> 5 μm) impact craters in this study.

The Tagish Lake meteorite analog foils showed many signs indicating the potential loss of carbonaceous or volatile impactors during impact processing. The increase in craters lacking SEM-EDXS signals, the unusual crater morphologies present in two craters, the overall low Si/(Fe+Mg) ratios, and the Mn present in one crater could all be indicative of carbonaceous impactors that lost their carbon due to the high temperatures and pressures involved with capturing these materials on aluminum foils. Only a single crater contained any surviving carbon in its residue layer. These results indicate that the lack of carbonaceous material in the Stardust foils is likely due to its destruction as a result of the violent collection process. However, definitively proving that our analog craters were the result of carbonaceous impactors is difficult, particularly when the Acfer 094 analog craters have indicated that our analog craters are likely to have been altered even more heavily than the authentic Stardust craters. A larger analog crater sample size, coupled with a thorough analysis of the materials prior to firing, would greatly improve our understanding of carbonaceous material loss in the foils.

Carbonates have been identified in previous investigations of the Stardust aerogels (Wirick *et al*., 2007; Flynn *et al*., 2008). However, concerns over the aerogel's purity prior to Stardust's

launch, as well as possible postmission contamination of the aerogel, have made it difficult to definitively identify these materials as cometary. Confirmation of surviving carbonates on the Stardust foils would greatly strengthen our evidence for carbonates in the Wild 2 fine material. However, our analog studies suggest that surviving carbonate material on the Stardust foils is likely rare as a result of the collection conditions.

4.6 Conclusions of the Stardust Foil Analog Studies

Our study of analog foil impactors focused on three types of impactors: Refractory grains, aggregate grains composed of material from the Acfer 094 meteorite matrix, and aggregate grains composed of material from the Tagish Lake Meteorite matrix.

The refractory analog foils demonstrated that refractory materials are capable of surviving intact in the craters, particularly when created by smaller, single-grain impactors. The smallest craters created by these impactors showed the least alteration, suggesting that future investigations of Stardust foils should focus on smaller (micron-scale) impact craters in order to maximize the chances of finding crystalline material as well as obtain less biased samples of comet Wild 2.

The Acfer 094 analog foils showed excessive alteration in their residue layers. No crystalline material was observed, Al was incorporated throughout the amorphous melt layers, Fe-vesiculation occurred in six craters, and S-loss was seen throughout iron sulfide impactors. Larger craters (>5 μm) appeared to show additional alteration, in the form of Fe-vesicles, confirming the findings of the refractory analogs that larger craters will be more heavily altered than smaller ones. The excessive alteration also suggests that aggregate impactors are more likely to be altered than single-grain, crystalline impactors. The excessive alteration seen in these aggregate impactors provides insight into why presolar grains are rare in studies of the Stardust foils. Impactors experience widespread melting, indicating that dilution of the presolar grains' isotopic anomalies

likely occurs. Our results also suggested that the analogs are imperfect replicas of the Stardust craters. The excessive S-loss and formation of Fe-vesicles present in our analogs have not been observed in previous investigations of the Stardust foils, suggesting that our method of creating analog foils results in more damage to the impactors than the Stardust mission's sample collection methods. As a result, drawing conclusions about which specific materials may or may not be capable of surviving the Stardust foil impact conditions is difficult, particularly when no surviving crystalline material is observed in our Acfer 094 analog residues.

The Tagish Lake foils returned results similar in many ways to the Acfer 094 foils. Impactors were reduced to thoroughly amorphous melt layers with many signs of potential volatile loss. The increase in craters lacking SEM-EDXS signals, the unusual crater morphologies present in two craters, the overall low Si/(Fe+Mg) ratios, and the Mn present in one crater could all be indicative of carbonaceous impactors that were largely destroyed during impact processing. One crater did contain carbon, indicating that carbonaceous materials can survive the Stardust impact conditions to some degree. Carbonaceous material is most likely to be observed in small (≤1 μm) craters, but our results indicate that carbon is likely to be extremely rare in the Stardust impact residues.

Given the excessive alteration in the analog craters relative to authentic Stardust studies, it is difficult to draw direct conclusions about the Stardust foils with our analog impactors. However, our studies of the analog foils did suggest that smaller Stardust craters are generally less altered. Smaller (<5 μm) Stardust craters are more time consuming to study owing to the need to locate them and the relatively small amount of material in them compared to large craters or terminal particles in the Stardust aerogel. However, our analog studies suggest that micron-scale craters

are the most promising way to study the fine component of comet Wild 2, and further foil studies are necessary to complement the relatively few craters that have been studied thus far.

Chapter 5: Stardust Cometary Foils

5.1 Preface

This chapter is adapted from three conference abstracts and a journal article accepted for publication:

Haas B. A., Croat T. K., & Floss C. (**2016**), "Characterization of the Fine Component of Comet Wild 2: Analysis of 11 Stardust Craters from Foil C2010W", in "79th Annual Meeting of the Meteoritical Society", Abstract #6386, URL https://www.hou.usra.edu/meetings/metsoc2016/pdf/6386.pdf.

Croat T. K., Haas B., & Floss C. (**2016**), "The Composition of Surviving Fine-Grained Cometary Material in Stardust Al Foil Craters", in "47th Lunar and Planetary Science Conference", Abstract #2204, Lunar and Planetary Institute, Houston, URL https://www.hou.usra.edu/meetings/lpsc2016/pdf/2204.pdf.

Haas B. A., Stroud R. M., & Floss C. (**2017**), "FIB/STEM Investigation of Four Impact Craters from the Stardust Comet Sample Return Mission Foils", *Proceedings of Microscopy & Microanalysis* **23**, 2190-2191, URL https://doi.org/10.1017/S1431927617011618.

Haas B. A., Floss C., & Ogliore R. C. "FIB-TEM analysis of cometary material in 6 sub-micron craters on Stardust foil C2113N-A", accepted for publication in the Christine Floss memorial issue of *Meteoritics & Planetary Science*.

5.2 Introduction

NASA's Stardust spacecraft encountered comet 81P/Wild 2 on 2 January 2004, successfully capturing rocky particulate coma samples at 6.12 km/s and returning them to Earth on 15 January 2006 (Brownlee *et al*., 2006). The collected material constitutes our only unambiguously cometary material available for study and thus continues to be critical to our characterization of outer solar system material (Zolensky *et al*., 2008b).

The Stardust sample collector utilized two separate media to capture impacting cometary material: 1) ultra-low density silica aerogel tiles and 2) aluminum foils covering the scaffolding surrounding the aerogel tiles. The aerogel tiles successfully decelerated and captured many coarse

(> 1 μm) impactors, allowing for detailed characterization of the comet's coarse component (Zolensky *et al*., 2008b). Many of the fine (< 1 μm) grains collected in the aerogel tiles were components of larger aggregate impactors that were disaggregated and spread across millimeter-scale bulbous impact features (Burchell *et al*., 2008a). Investigations of these fine grains have returned a variety of results on a particle-by-particle basis. Sub-micron particles from aerogel track 80 had solar abundances of Fe, Mg, and S when averaged together, but individually had a wide range of compositions, suggesting that the fine grains are consistent with thermally unprocessed primordial dust close to solar composition (Stodolna *et al*., 2012). Grains smaller than 2 microns in size have a wide range of O isotopic compositions, indicating that Wild 2 fine grains are either a diverse sampling of inner Solar System reservoirs or ancient outer-nebula dust (Ogliore *et al*, 2015). These results have differed from studies of coarse Wild 2 materials that frequently have high-temperature origins and volatile element depletions, and appear to have formed far from where comet Wild 2 accreted (Brownlee *et al*., 2012). Further investigations of the Stardust fine materials are needed to clarify the source of these materials.

The aluminum foils on the sample collector allow us to directly study the fine impactors. The foils were heavily cratered by sub-micron impactors (Kearsley *et al*., 2008; Price *et al*., 2010) and are conductive, allowing for the identification and study of these impact craters with electron microscopy. Cometary material in the foils is concentrated in residues located in the crater bottoms, lacking the dispersion issues present in the aerogel tracks. Surviving crystalline material has been found in a number of Stardust foil craters (Leroux *et al*., 2008) that analog studies indicate are surviving cometary grains rather than recrystallizations (Wozniakiewicz *et al*., 2012a). Our analog foil studies of refractory and Acfer 094 material have also shown that smaller impactors typically experience less alteration during the capture process and as a result are less likely to

experienced conditions that could result in the loss of volatiles present in the impactors. The micron-scale craters on the Stardust aluminum foils are thus a promising source of information regarding comet Wild 2's fine grain component and can help constrain the volatile component and the source of the Wild 2 fines.

The source of the Wild 2 fines could be determined through comparison of the Wild 2 fine volatile components with solar compositions. Materials formed in the inner Solar System would be depleted in volatiles relative to CI chondrites whereas materials inherited from the Solar system's parent molecular cloud would not (Ogliore *et al*., 2015).

Studying micron-scale impactors in the Stardust foils provides the unique ability to directly analyze Wild 2's fine component. However, few attempts have been made to characterize craters of this size on the Stardust cometary foils. Preliminary SEM-EDXS studies of craters ranging from 200 nm to 5 μm in diameter were qualitative, identifying that 56% of these craters were combinations of silicates and sulfides with another 36% of these craters containing only one of these phases (Hörz *et al*., 2006). Three studies have analyzed 22 micron-scale Stardust impact craters (Leroux *et al*., 2008; Leroux *et al*., 2010; Stroud *et al*., 2010), but these craters are only a small sample of the craters present on the foils. Through the study of additional micron-scale impact craters on the Stardust foils we aim to better characterize the fine component of comet Wild 2 and better understand the origins of this complex outer Solar System body.

5.3 Stardust Foil C2010W

Stardust foil C2010W was located on the left side of the Stardust sample collector (Figure 5.1). The foil was heavily cratered. Whereas many of the Stardust foils had only a few craters larger in size than 1 micron, Stardust foil C2010W had over 300 identified micron-scale craters

after it was initially mapped with SEM imaging. As a result, it appeared to be an ideal foil for further characterization of comet Wild 2's fine component.

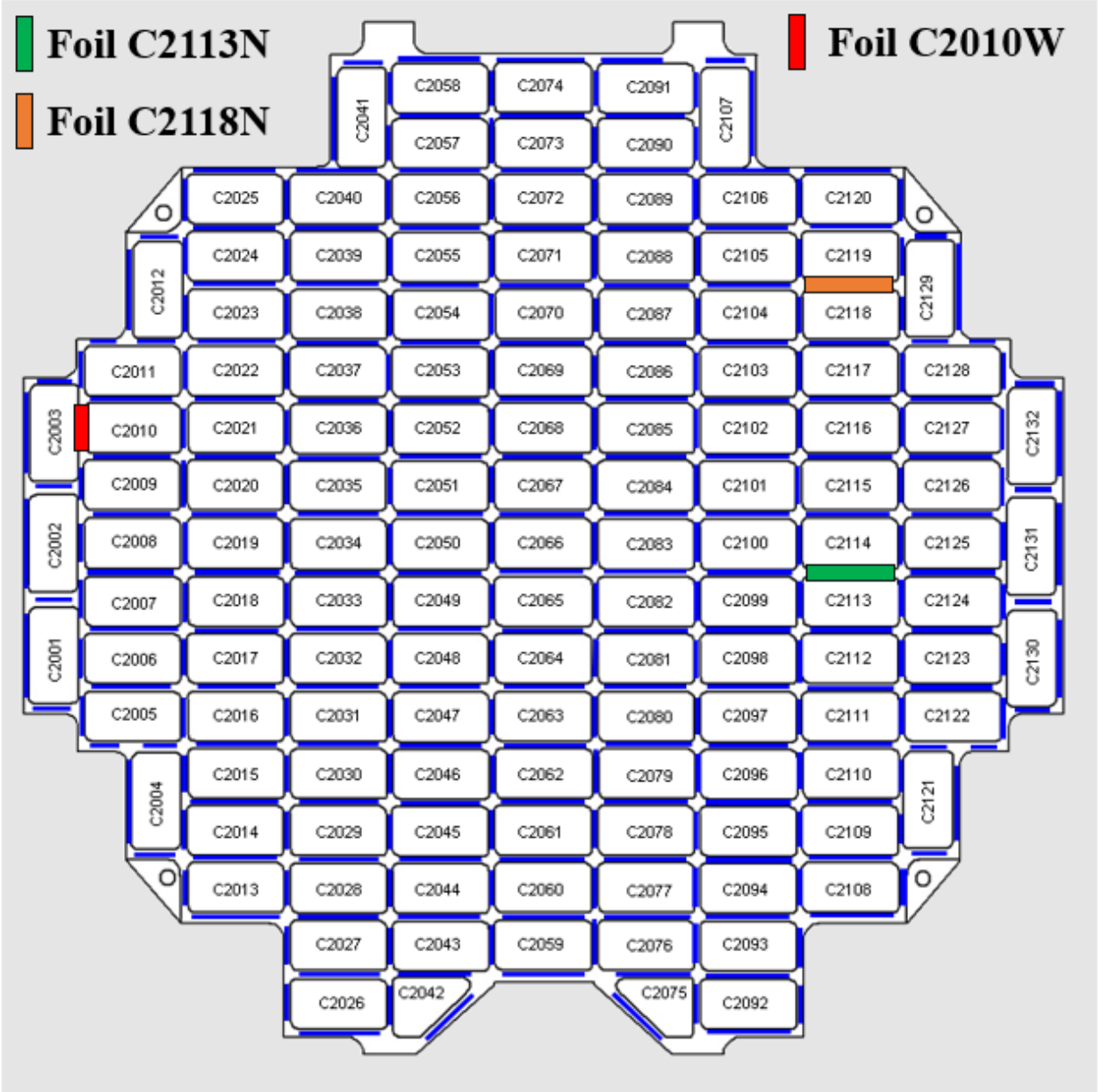

FIGURE 5.1: Stardust cometary tray diagram (with labeled aerogel tiles) indicating the position of the cometary foils studied during this thesis. The diagram is available at https://curator.jsc.nasa.gov/stardust/sample_catalog/cometary/level2foils.cfm. Aluminum foils are labeled 'W' or 'N' for their positioning 'West' and 'North' of the correspondingly labeled aerogel tiles. Hence, foil C2010W, whose study is detailed in this subchapter of the thesis, is located to the left of aerogel tile C2010. Study of the foils C2113N and C2118N are detailed in later subchapters of this thesis.

5.3.1 Stardust Foil C2010W Experimental Methods

Initial SEM scanning identified 346 craters with diameters larger than 0.5 μm on the 1.7 by 10.6 mm scanned area of the foil. SEM-EDXS spectra were collected from 150 of these craters with diameters between 0.5 μm and 7.2 μm with a 10 kV primary beam and 200s livetime on Washington University's JEOL JSM-840A SEM. The beam voltage was chosen to minimize the beam interaction volume while also giving sufficient overvoltage for Fe-K peak quantification. Mg, Fe, Si, S, and Ca were all clearly detectable among the crater spectra. SEM-EDXS quantification was performed through the use of ZAF-corrected k-factors, with the k-factors determined through comparison with TEM-EDXS results from craters after they were extracted via the FIB, as well as by setting the bulk average C2010W composition from 150 craters to match the CI values (as suggested by Flynn *et al*., [2006]).

11 craters with diameters between 0.71 and 3.28 μm were selected for further analysis based upon the initial qualitative SEM-EDXS results. The selected craters contained a wide range of elemental abundances in order to allow for the detailed study of a range of impacting cometary material, with focus placed on craters displaying silicate or silicate-sulfide compositions. Additionally, we focused on craters with relatively high Fe/S ratios, as the S loss in our analog craters indicated that craters lacking S alongside strong Fe signals were more likely to contain heavily altered, and thus amorphous, materials. Cross sections of these craters were extracted and thinned to 100-150 nm, preserving material for potential isotope analyses, with Washington University's FEI Quanta 3D FIB-SEM. TEM analysis was conducted on Washington University's JEOL 2000 TEM. TEM-EDXS spectra were quantified using Cliff-Lorimer techniques with pre-acquired k values derived from standards.

5.3.2 Stardust Foil C2010W Results

The SEM-EDXS results were largely consistent with previous investigations of Stardust craters (Hörz *et al*., 2006; Leroux *et al*., 2008) in which craters were characterized as containing residues from silicates, sulfides, or mixtures of the two. The fractions of craters with detectable Mg, Si, Fe, S, and Ca from the surviving cometary material were 77%, 82%, 85%, 83%, and 38%, respectively. The average compositions of the surviving material in 130 craters (20 were excluded due to low counts in the spectra) are shown in Figure 5.2, compared to the composition of CI chondrites (Lodders 2003). Mg and Ca are grouped in the ternary plots of Figure 5.2 due to the frequency with which Ca takes the place of Mg in common minerals (e.g., olivine). The craters are labeled as either containing silicate, sulfide, silicate plus sulfide, or Ca-rich (> 10 at. % Ca) impactors. The S abundances in the craters, relative to the Fe abundances, were roughly consistent with CI chondrite values (Lodders 2003) and did not demonstrate excessive S loss as was seen in our previous investigation of the Acfer 094 analog craters. The Fe-S-Mg grain compositional distribution was largely consistent with values obtained during the study of aerogel-captured fine grains (Stodolna *et al*., 2012). Comparisons to the Si contents in the aerogel fine grains are difficult to make due to the large Si background from the aerogel. However, the combination of silicates, sulfides, and aggregates containing both silicates and sulfides were largely consistent with previous investigations of micron-scale Stardust foil impact craters (Hörz *et al*., 2006).

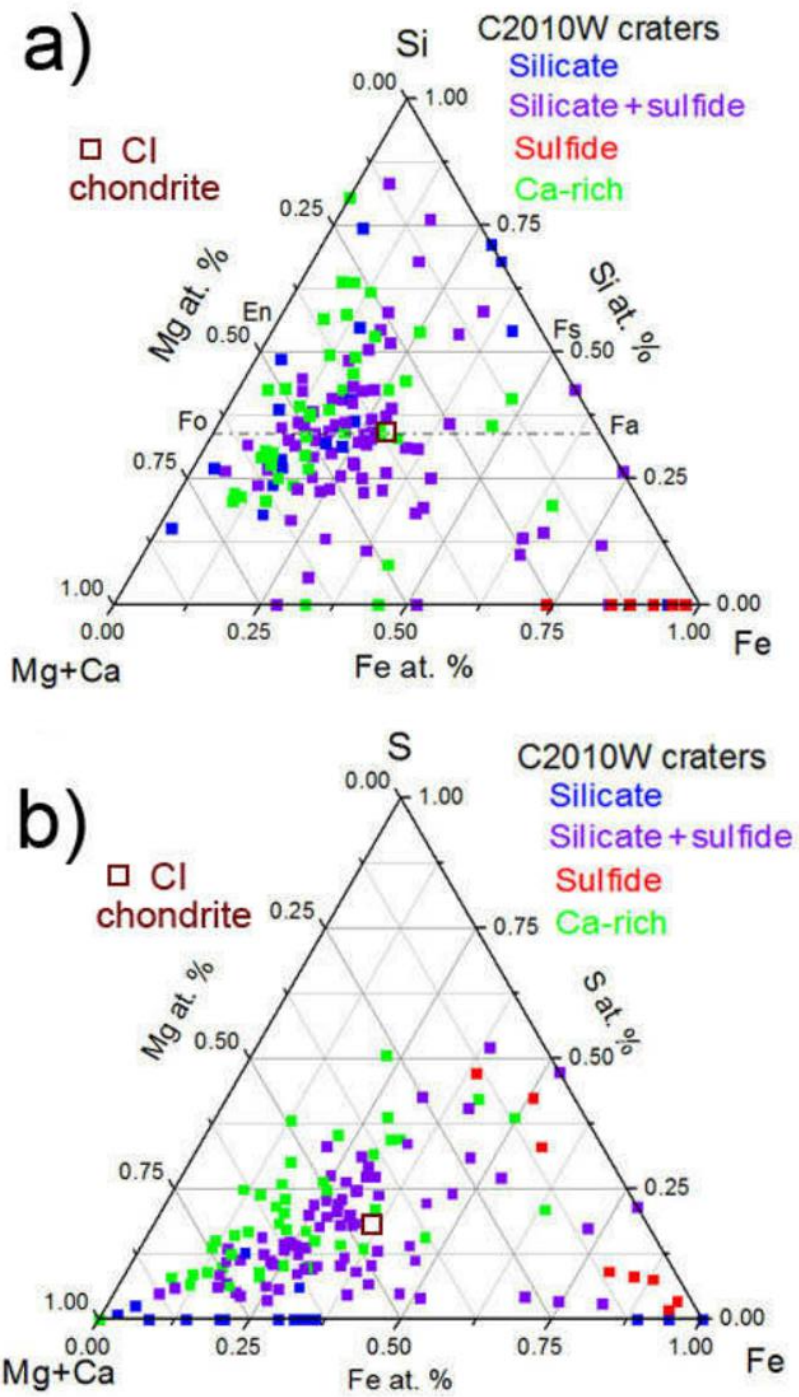

FIGURE 5.2: Ternary composition diagrams of a) Fe-Si-(Mg+Ca) and b) Fe-S-(Mg+Ca) showing the average composition of the surviving material in 130 C2010W Stardust craters along with the average composition of CI chondrites (taken from Lodders *et al*., [2003]). Crater compositions are normalized to be composed entirely of the elements indicated in the ternary plot. The type of impactor (silicate, sulfide, silicate and sulfide aggregate, or Ca-rich [> 10 at. % Ca]) are shown for each crater.

11 craters were extracted and studied with FIB-TEM techniques. One impactor melt layer was dominated by an Fe-melt that was largely the result of an Fe-contaminant native to the foil (Figure 5.3). Fe-rich contaminants roughly a micron in size are known to be present in the Al foils (Stroud *et al*., 2014). The location of the large Fe-rich grain below the Al-substrate to the side of the crater, coupled with the complete lack of other elements (e.g., sulfur) in the TEM-EDXS spectrum of the grain, indicated that it was a native Fe-rich contaminant. The melt layer at the bottom of this crater was dominated by Fe-rich residues, indicating that the majority of the melt was likely the result of the contaminant melting during the impact processing. As a result, this crater was excluded from further analyses.

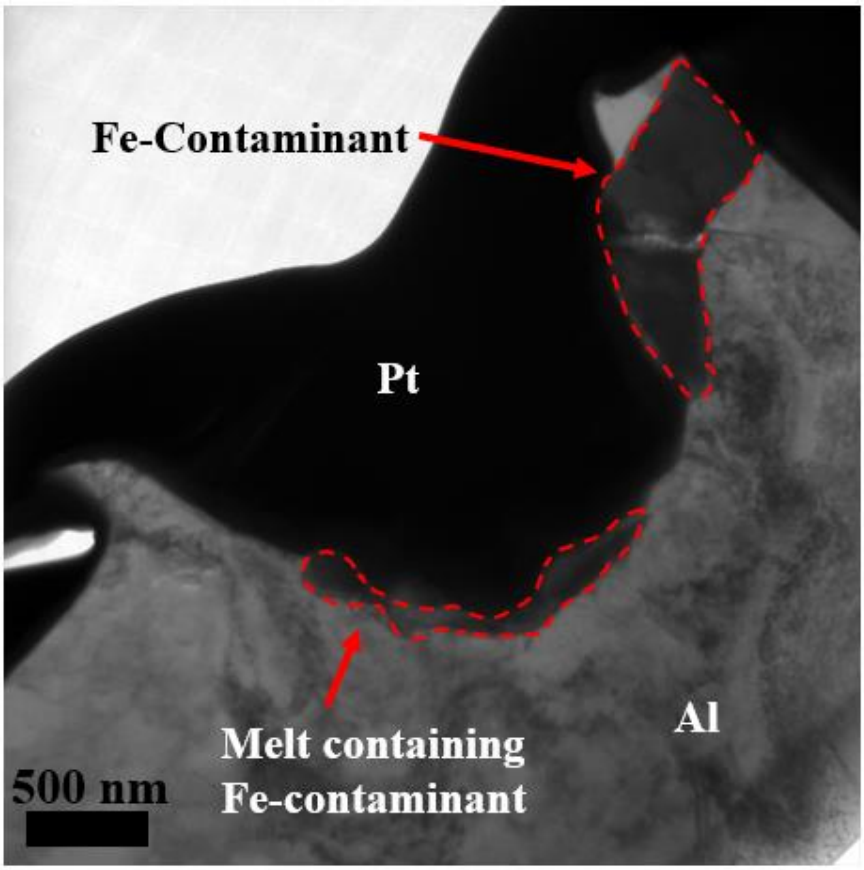

FIGURE 5.3: TEM bright-field image showing the presence of an Fe-contaminant native to the Stardust foil. The presumed cometary material impacted the foil directly on top of the Fe-contaminant, making analysis of any cometary material difficult.

The other 10 extracted craters (Figure 5.4) showed no obvious signs of terrestrial contamination. Eight of the craters contained rounded, bowl-shaped craters, indicative of an impact by a dense, compact object. Two of the craters had far wider melt layers, demonstrative of impacts by more dispersed aggregate grains (Figure 5.5). None of the examined craters contained any surviving crystalline material. The crater residues were dominated by amorphous melt layers coating the bottom and sides of the craters.

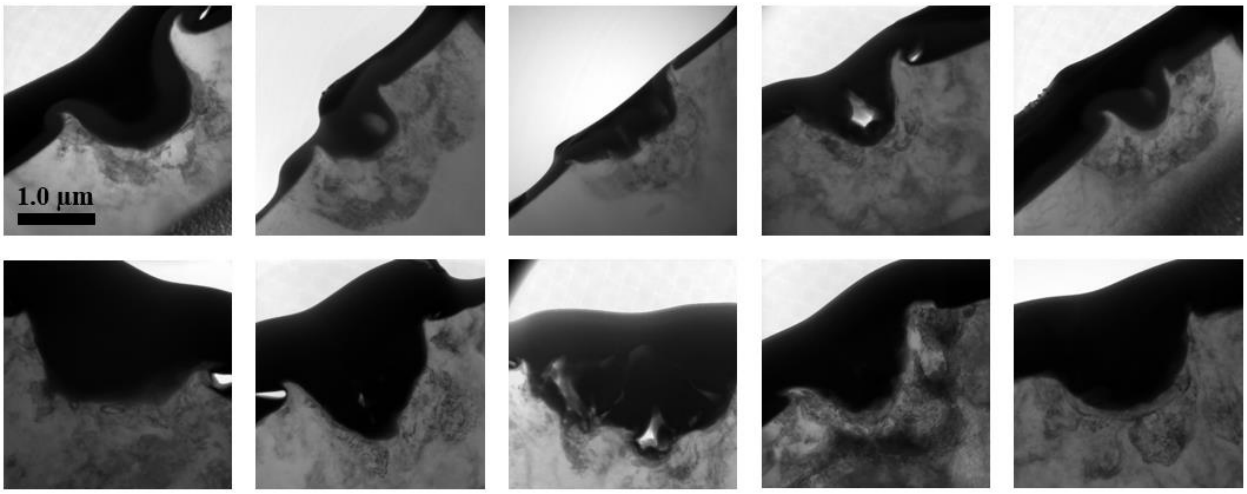

FIGURE 5.4: TEM bright-field images of the other 10 examined Stardust craters from foil C2010W. The scale bar for all 10 images is the same.

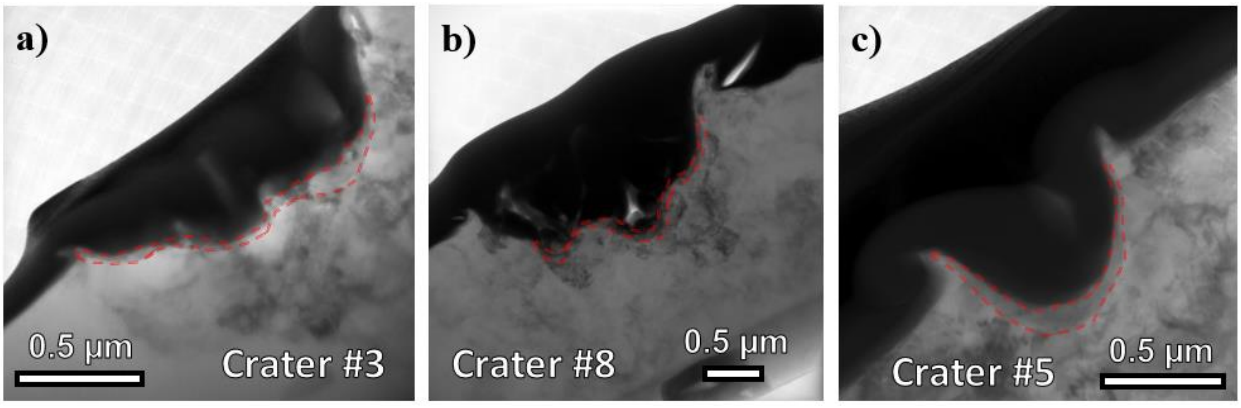

FIGURE 5.5: TEM bright-field images of the two craters from Stardust foil C2010W with wider, shallower melt layers are shown in a) and b). A deeper, bowl-shaped melt layer is shown for comparison in c).

Five of the crater melt layers were homogeneous in composition, with melt layer compositions varying by no more than ± 5 at. % for any element present in the melt layers. The other five craters had heterogeneous melt layers with compositions varying wildly depending upon the location in the melt where TEM-EDXS analyses were conducted (Figure 5.6). The TEM-EDXS results largely agreed with the initial SEM-EDXS results indicating that the craters were largely composed of Si- and Mg-rich impactors and iron sulfides, as well as aggregates of these two types of impactors, with aggregate impactors comprising the majority of the investigated craters.

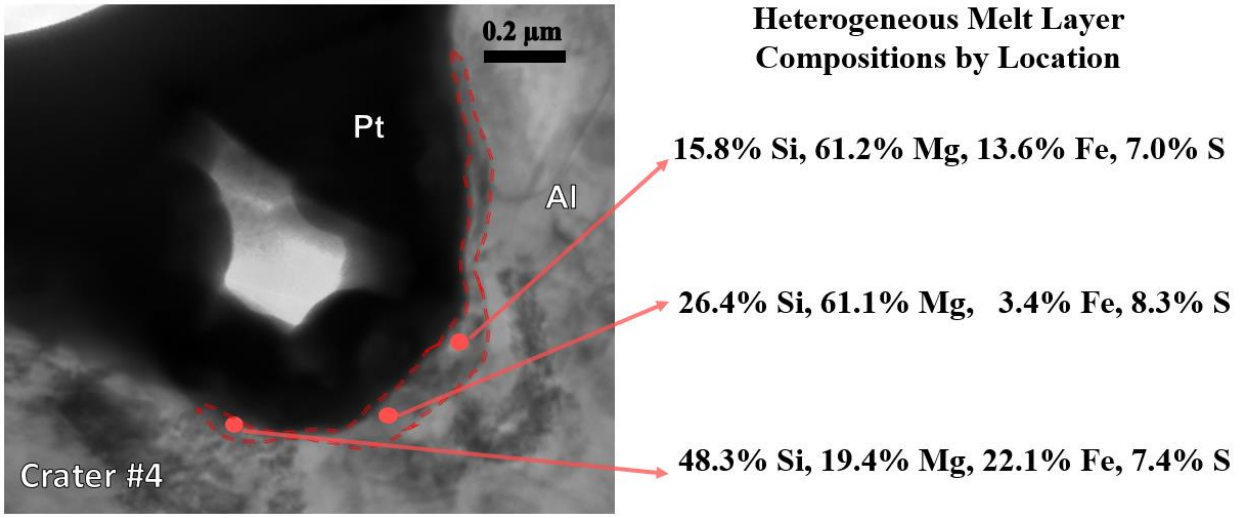

FIGURE 5.6: Elemental abundances varying by region in heterogeneous crater #4 from Stardust foil C2010W.

The homogeneous crater compositions are shown in Figure 5.7. Overall crater compositions were calculated by averaging TEM-EDXS spot analyses performed throughout the crater residues. The bulk Si/Mg ratios in the homogeneous craters were close to 1, resulting in the crater compositions approaching enstatite ($MgSiO_3$) in the low-Fe limit. The Stardust craters contained slightly less Mg relative to Si than is present in CI chondrites (Lodders 2003).

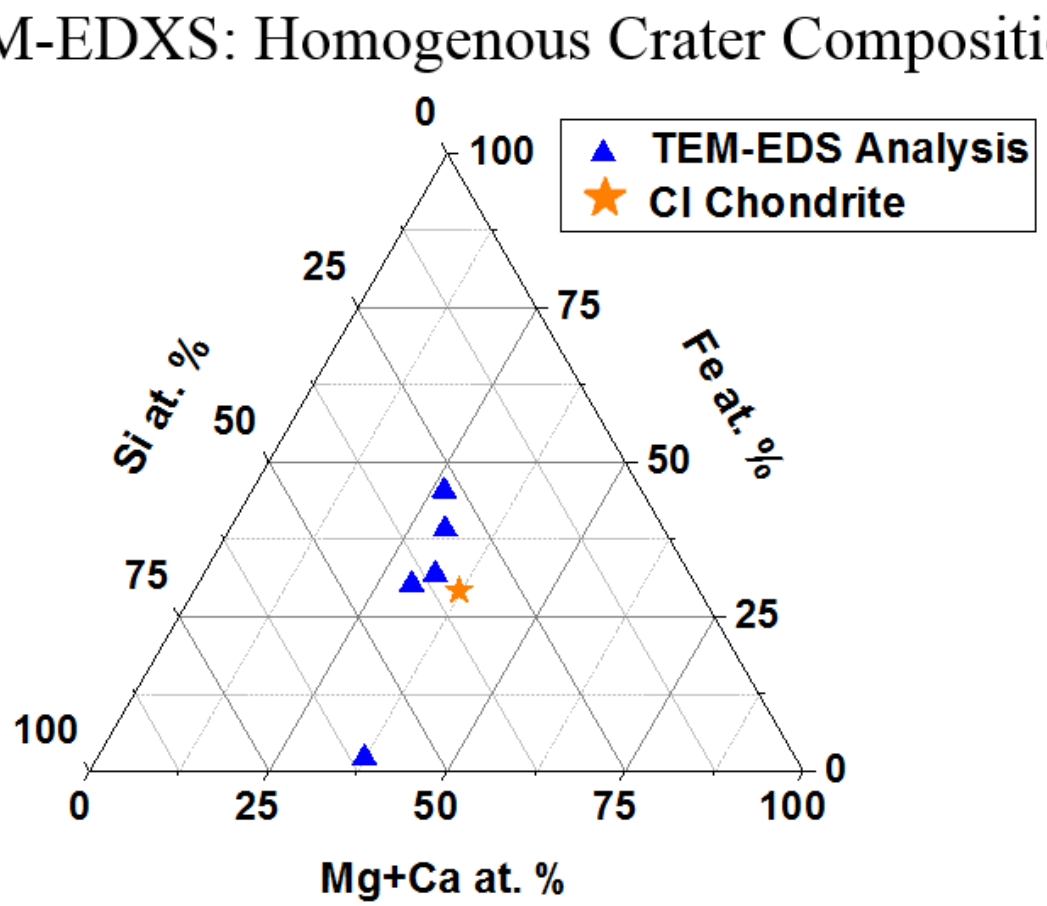

FIGURE 5.7: Si-Fe-(Mg+Ca) ternary plot of the homogeneous crater compositions from Stardust foil C2010W. The total Si, Fe, Mg, and Ca at. % is normalized to 100% for each crater residue. Crater compositions were calculated through averaging TEM-EDXS values acquired from multiple spot analyses in the craters. Elemental abundances did not vary by more than ± 5 at. % within any one crater's residue layer. CI chondrite composition is shown for comparison (Lodders 2003).

The residues of the heterogeneous craters greatly varied in composition throughout their melt layers (Figure 5.8). The heterogeneous craters were dominated by Si- and Mg-rich materials coupled with iron sulfides like the homogeneous craters. The compositional variance throughout their melt layers indicates that the impactors were aggregates of many different impacting subgrains that experienced incomplete melting and rapid solidification.

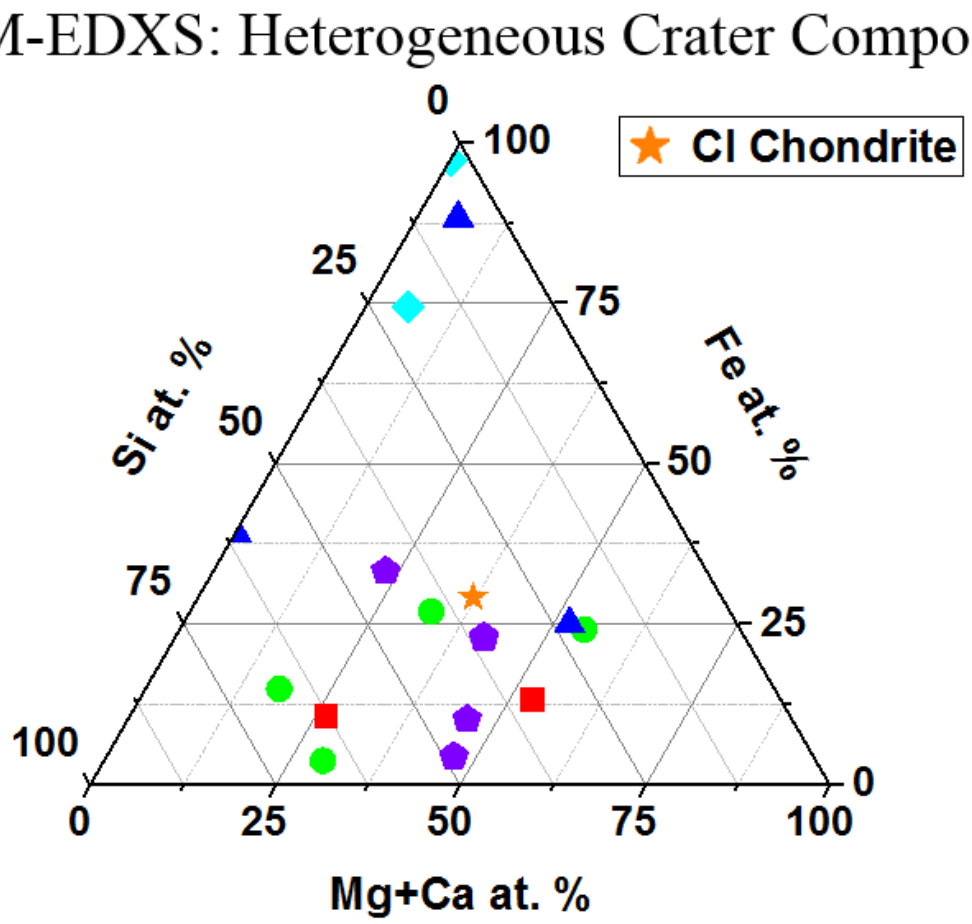

FIGURE 5.8: Si-Fe-(Mg+Ca) ternary plot of different crater compositions (from individual TEM-EDXS spot analyses) from the five heterogeneous crater residues from Stardust foil C2010W. Different spectra from the same crater share the same color and shape. The total Si, Fe, Mg, and Ca at. % is normalized to 100% for each crater residue. CI chondrite composition is shown for comparison (Lodders 2003).

Regions composed entirely of iron sulfides did not exist in our crater residues due to the widespread melting in the crater residues. However, there were many subregions dominated (> 50 at. %) by iron sulfide components. Iron sulfide-rich areas in the crater residues generally showed relatively low Fe/S ratios, with an average Fe/S ratio in the craters of 2.0 (Figure 5.9). This was expected given that we partially selected craters for further FIB-TEM analysis based upon the presence of low Fe/S ratios in our initial SEM-EDXS analyses. Definitively identifying the Fe and S contributions from iron sulfides is difficult. Most of the Si- and Mg-rich regions of

the melt also contained Fe, indicating that Fe was likely contributed from materials besides iron sulfides. Given the widespread melting and mixing within the crater residues, Fe/S ratios are likely inflated by this Fe that was contributed by non-sulfide phases. Additionally, S loss, though minimal in previous Stardust investigations (Leroux *et al*., 2008) cannot be ruled out due to the violent collection conditions. Regardless, some of the craters with low Fe/S ratios were consistent with potential pyrrhotite or troilite impactors. Iron sulfides with similar Fe/S ratios are relatively common in Wild 2 aerogel tracks (Zolensky *et al*., 2008b).

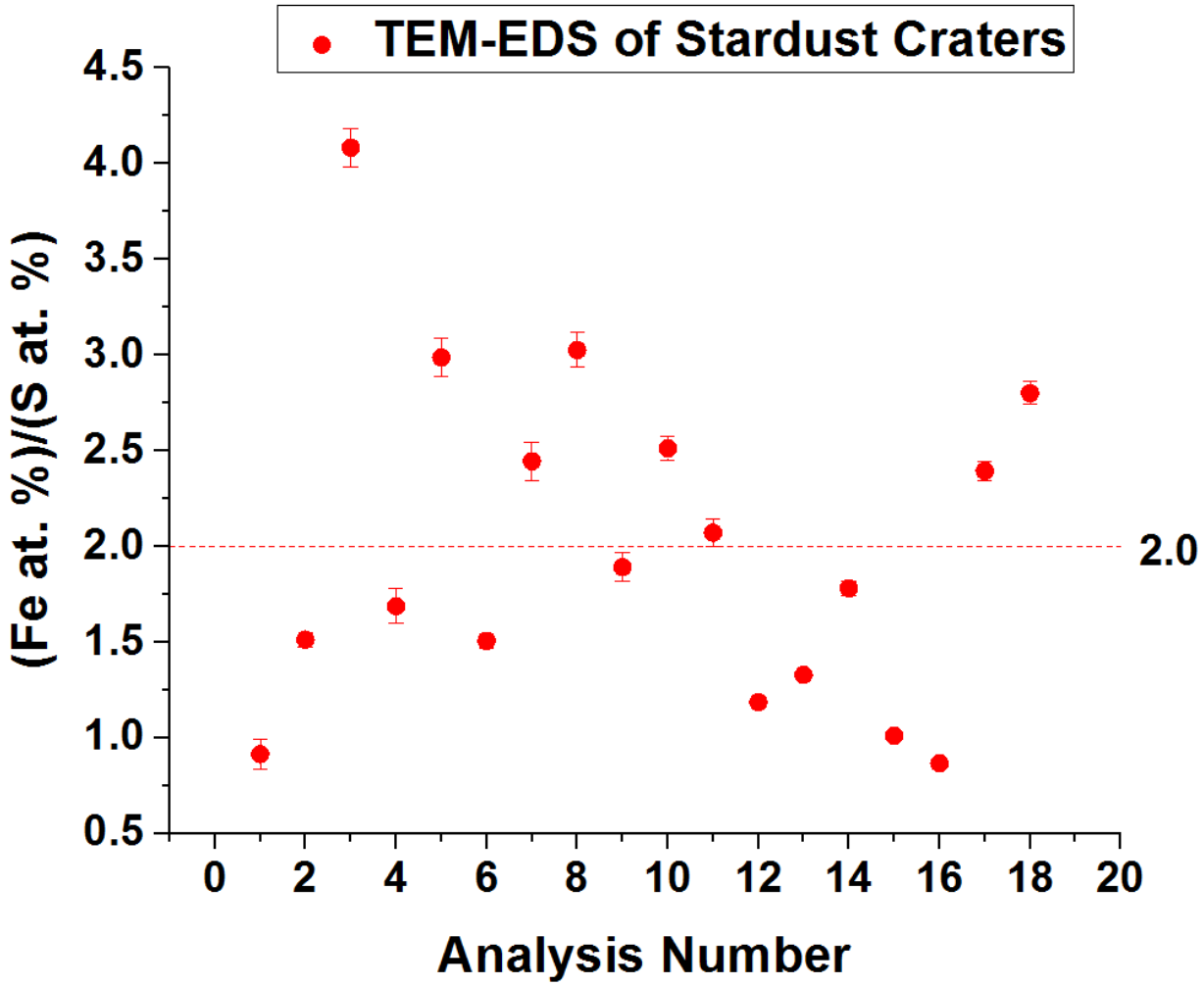

FIGURE 5.9: Fe/S ratios from TEM-EDXS spot analyses conducted on crater residues in foil C2010W. The average Fe/S ratio across the crater residues was 2.0.

A more detailed view of the sulfide-rich compositions is shown in Figure 5.10. The regions containing abundant S frequently contained Ni, with Ni values in the sulfides ranging up to 4.6 at. % in the 8 craters containing iron sulfide residues. Pentlandite, if present, is rare, with an upper limit of 8.3% of the iron sulfides in our craters resulting from pentlandite impactors.

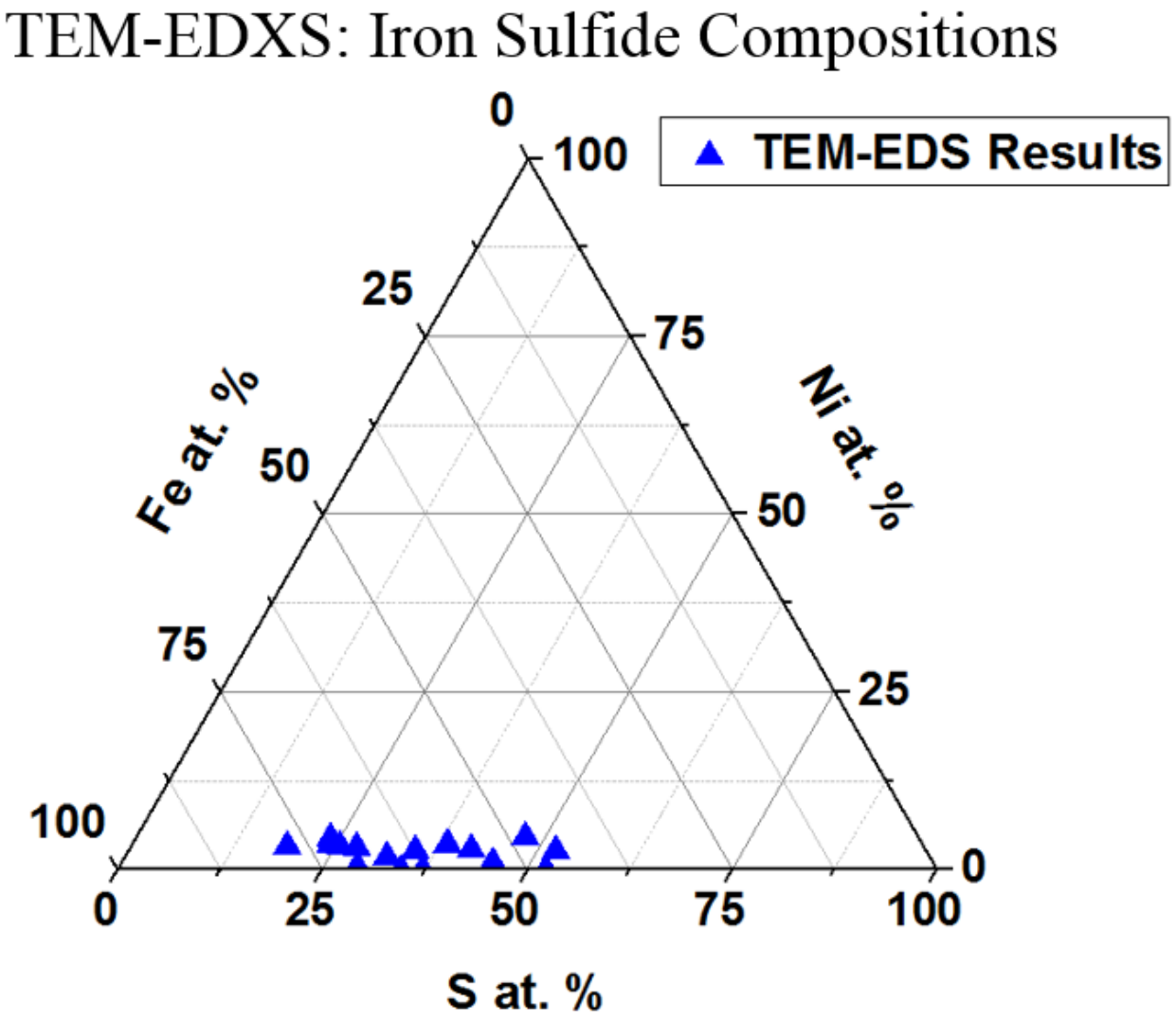

FIGURE 5.10: S-Fe-Ni ternary plot of iron sulfides present in the C2010W craters. The total S, Fe, and Ni at. % is normalized to 100% for each crater residue.

Besides Si, Mg, Fe, S, and Ni, several elements were present throughout the crater residues. Ca was present in 7 out of 10 craters, though only in small amounts (up to 4.2 at. %). 2 craters contained small amounts of Cr (~1 at. %), and 1 crater contained trace (< 0.5 at. %) Mn.

5.3.3 Stardust Foil C2010W Discussion

The examined craters were largely combinations of Si- and Mg-rich material and iron nickel sulfides, despite focusing on micron-scale craters. The prevalence of aggregate impactors demonstrates that the majority of the individual grains composing the Stardust fine component are much smaller than 0.5 μm. Most crystalline grains observed in prior studies (Leroux *et al*., 2008) are closer to ~50 nm in diameter. As a result, though our refractory analog foils suggested single-grain impactors were the most likely to survive the impact processing, it appears that finding craters composed of single-grain impactors on the Stardust foils is unlikely when probing craters created by fine (<1 μm) impactors.

Our crater morphologies and elemental compositions were largely consistent with previous studies of the Stardust foils. Previous SEM-EDXS analyses of the foils noted that the majority of micron-scale craters were aggregates of Mg- and Si-rich materials and iron sulfides (Hörz *et al*., 2006), similar to our SEM-EDXS and TEM-EDXS results.

Definitively identifying the Mg- and Si-rich component of our impactors is difficult. Our cross section thicknesses (100-150 nm) are larger than many of the crystalline subgrains seen in previous Stardust investigations (Leroux *et al*., 2008; Stroud *et al*., 2010), preventing us from isolating an individual impactor. Additionally, the amorphous melt layers indicate that impacting material mixed with other subgrains composing the aggregate. Si, Mg, and Fe abundances were consistent with a combination of olivine and pyroxene impactors combined with iron nickel sulfides. Glasses with embedded metal and sulfides (GEMS) are a potential Wild 2 component that are consistent with our observations. GEMS are combinations of amorphous silicates and iron sulfides with a wide range of potential compositions. GEMS constitute a large percentage of IDPs, which are widely believed to be cometary in origin (Keller & Messenger, 2011). Fe/Si ratios in GEMS have been observed to range from 0.09 to 1.63, and Mg/Si ratios in GEMS have been

observed to range from 0.05 to 1.44 (Keller & Messenger, 2011). All of our homogeneous craters fall within these ranges, and the majority of the spot analyses conducted on our heterogeneous craters have also fallen within these ranges. Previous investigations have indicated that GEMS are a likely component of comets. Astronomical observations have shown comets contain abundant amorphous silicates (Hanner 2003). Studies of fine grained Wild 2 components in the Stardust aerogels have found amorphous silicates and iron sulfide vesicles constituting GEMS-like material to be abundant (Stodolna *et al*., 2012). As a result, GEMS remain a likely source for the materials present in our crater residues.

Fe/S ratios in our craters were relatively low when compared to previous Stardust and analog crater investigations (Figure 5.11). Previous analyses of iron sulfides in Stardust craters were also low, with average Fe/S ratios of 3.4 (Leroux *et al*., 2008). Given that our Fe/S ratios were even lower, our craters appear to have undergone less volatile loss than the previously investigated craters, and thus likely experienced lower peak temperatures and pressures than previous investigations.

Trace elements in the residues provide insight into minor phases within the Wild 2 material. The presence of Cr in two craters suggests that small chromite particles are part of the Wild 2 component. Earlier investigations by Stroud *et al*. (2010) observed a surviving crystalline chromite grain in a submicron Stardust crater, strengthening this claim. Mn was observed in crater residues by Leroux *et al*. (2008) as a trace (< 0.5 at. %) inclusion in olivine and pyroxene residues, suggesting that the silicate impactors in our crater that contained Mn may also have been the result of olivine or pyroxene impactors. Ca, present in seven of our craters, is frequently associated with refractory materials such as calcium-aluminum-rich inclusions (CAIs). However, the lack of Ti in the craters suggests that CAIs are not the source of the observed Ca. Pyroxene grains are a more

probable source for the observed Ca. Pyroxene grains have been observed and lined with Ca abundance in Stardust foil residues (Leroux *et al*., 2008), and low Ca-pyroxenes are common in Stardust aerogel tracks (Jacob *et al*., 2009). Ca/Si ratios were low enough throughout our residues for Ca to have been fully contributed by low-Ca pyroxenes. However, given the thorough melting of the crater residues it is possible that a number of phases contributed the observed Ca.

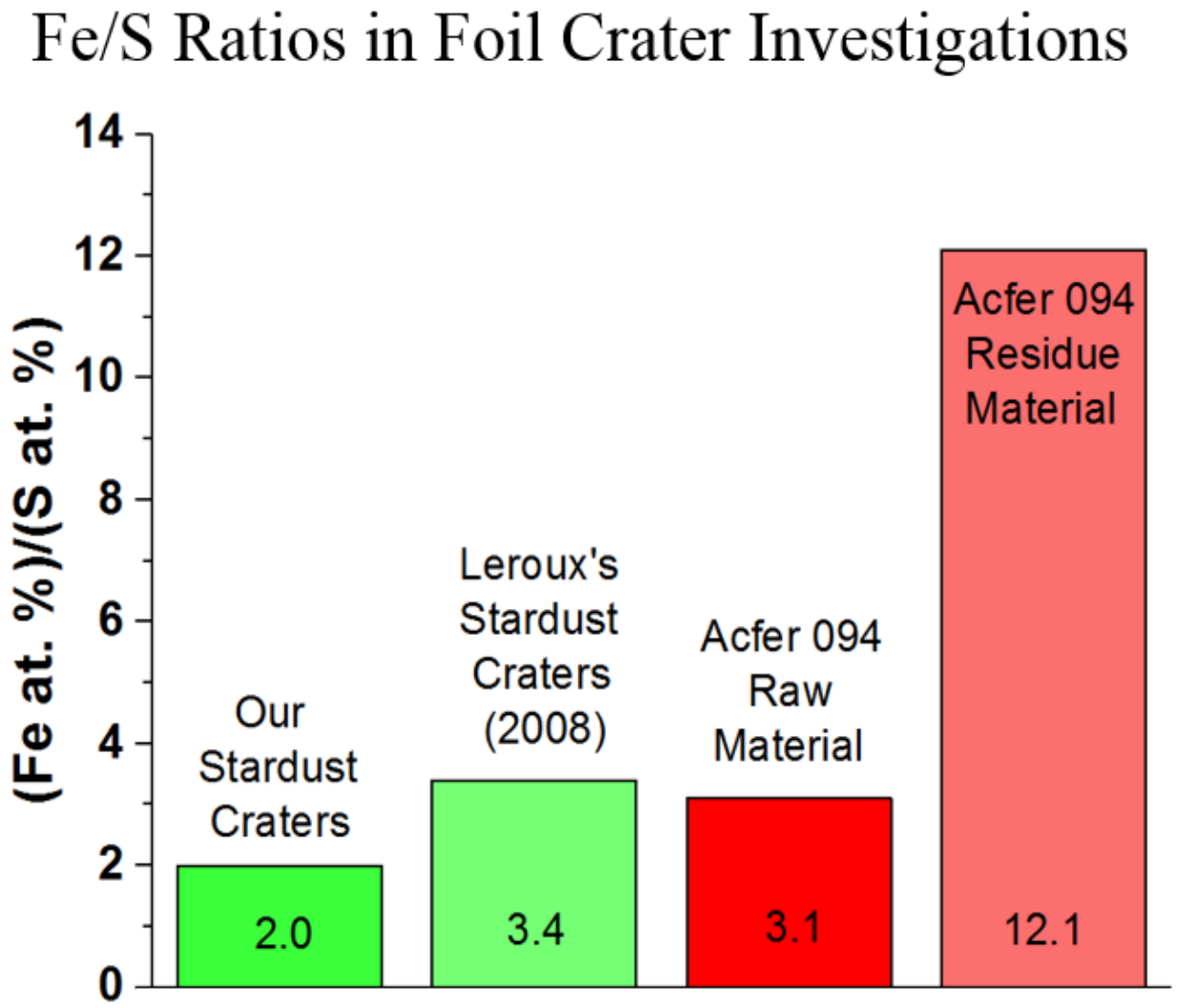

FIGURE 5.11: Fe/S ratios in our Stardust craters versus Fe/S ratios in Leroux *et al*. (2008), our Acfer 094 unfired material, and our post-impact Acfer 094 material. The low Fe/S values in our Stardust craters suggest that volatile loss was low and alteration as a result of impact processing should be minimal in comparison to these previous studies.

The lack of crystalline material in the crater residues was unexpected. Previous investigations of similarly-sized Stardust craters identified crystalline material in 10 out of 22 studied Stardust craters (Leroux *et al*., 2008; Leroux *et al*., 2010; Stroud *et al*., 2010). However, we observed no crystalline material in our 10 uncontaminated craters. Our craters did not show any signs of excess alteration. No vesiculation occurred, and our Fe/S ratios were lower than previously investigated Stardust craters that contained crystalline material (Leroux *et al*., 2008). Given the violent impact conditions, the amorphization of crystalline impactors cannot be ruled out. However, as the craters show no signs of excess alteration, it appears more probable that the craters were amorphous (e.g., GEMS) prior to impact.

Clustering has been observed in the Stardust foils and aerogels, though explanations for this phenomenon that satisfy all the conditions of the Stardust mission have yet to be reached (Westphal *et al*., 2008). Foil C2010W was heavily cratered, with hundreds of craters larger than a micron in size whereas most foils only have a few such features. As a result, the impactors present on the foil may be the result of a cluster of material that shared a common origin and thus had similar properties such as a lack of crystalline material. This cluster of material would have only started slowly separating shortly before impact with the Stardust spacecraft, allowing the full cluster to impact Stardust foil C2010W. In this scenario it becomes far more likely to observe a large number of Stardust craters that do not contain surviving crystalline material. The wide range of elemental compositions seen in our heterogeneous craters indicate that the impacting cluster would need to be an aggregate of silicates and iron-nickel sulfides with a similarly large range of compositions. Our results are generally consistent with GEMS impactors, suggesting that GEMS or GEMS-like materials composed the impacting cluster that resulted in our amorphous crater

residues. However, a better understanding of Stardust impact processing is required to prove that any impactor material was amorphous prior to collection given the high collection speeds.

5.3.4 Stardust Foil C2010W Conclusions

I examined 11 micron-scale craters from Stardust Foil C2010W with SEM and FIB-TEM techniques. One crater was contaminated by a Fe-rich grain native to the Stardust foils. The crater compositions were largely consistent with previous SEM-EDXS (Hörz *et al*., 2006) and TEM-EDXS studies (Leroux *et al*., 2008) that have observed the craters contain a combination of Si- and Mg-rich materials and iron-nickel sulfides. 5 of our craters contained extremely heterogeneous melt layers, indicating that individual subgrains of the impacting aggregate grains have a wide range of compositions. Our studies also observed crater morphologies and impactor melt layer distributions that were similar to previous FIB-TEM studies of Stardust craters (Leroux *et al*., 2008; Leroux *et al*., 2010; Stroud *et al*., 2010).

The Si- and Mg-rich components of our residues are consistent with combinations of crystalline materials such as olivine and pyroxene subgrains, amorphous silicates such as in GEMS, or combinations of the two. However, the lack of surviving crystalline material in our craters made it difficult to distinguish between these possibilities. Our Fe/S ratios were relatively low (~2.0 on average), and our craters also showed a lack of vesiculation, indicating that our craters show a similar level of alteration to previous Stardust studies (Leroux *et al*., 2008) and less alteration than our previous analog studies. The Cr we observed in two craters also suggest that chromite grains constitute a component of the Wild 2 fines given that chromite has been observed in a previously investigated submicron Stardust crater (Stroud *et al*., 2010).

The lack of crystalline material in our studied Stardust craters differed from the abundance of crystalline material observed in previous investigations of Stardust craters; 10 of 22 previously

investigated craters contained surviving crystallites whereas none of our 10 uncontaminated craters contained any crystalline material (Leroux *et al*., 2008; Leroux *et al*., 2010; Stroud *et al*., 2010). Our craters lacked signs of significant alteration such as S loss or vesiculation. The lack of significant alteration within the crater residues, coupled with the high crater density on foil C2010W, suggests that the foil was impacted by a dense cluster of compositionally heterogeneous amorphous silicates and sulfides such as GEMS. Thus, these results imply that a larger portion of the Wild 2 fine component is amorphous than was suggested by previous FIB-TEM analyses of the Stardust foils (Leroux *et al*., 2008; Leroux *et al*., 2010; Stroud *et al*., 2010). However, despite previous observations of clustering on the Stardust sample collector (Westphal *et al*., 2008), it is difficult to prove that amorphous material in our crater residues was amorphous prior to impact given the high temperatures and pressures reached during the collection process.

5.4 Stardust Foils C2113N-B and C2118N-B

Our study of Stardust foil C2010W did not identify any surviving crystalline material, despite focusing on craters roughly a micron in size. We theorized that, due to the unusually large number of craters present on the foil, as well as our focus on examining craters from a relatively small region of a single foil, that the foil may have been impacted by a large cluster of particles that were amorphous prior to impact. Impact clustering has been observed on the Stardust sample collector, but no explanation for this phenomenon has yet been reached that agrees with our understanding of the Stardust mission conditions (Westphal *et al*., 2008). In order to avoid potentially analyzing craters formed from similar clusters of impacting material, I decided to focus on two new Stardust foils, C2113N-B and C2118N-B. The "-B" notation for these foils indicates that they are only one subsection (in this case, the second subsection, with the first subsection labeled "-A") of the full foils C2113N and C2118N.

5.4.1 Stardust Foils C2113N-B and C2118N-B Experimental Methods

Foils C2113N-B and C2118N-B were both fully imaged with secondary electrons by Washington University's Tescan Mira3 FE-SEM. Only two craters with diameters larger than one micron were identified on each foil, for a total of four identified craters across the foils (C2113N-B #1, C2113N-B #2, C2118N-B #1, and C2118N-B #2). The crater diameters ranged from 1.5 µm to 4.8 µm (Figure 5.12). SEM-EDXS spectra were collected from each crater using a 10 kV primary beam and 300s livetime. The beam voltage was chosen to minimize the beam interaction volume while also giving sufficient overvoltage for Fe-K peak quantification. Mg, Fe, Si, and S were all clearly detectable among the crater spectra. Weak Ni signals were also observed in three craters, and one crater (C2118N-B #2) also contained weak Ca signals.

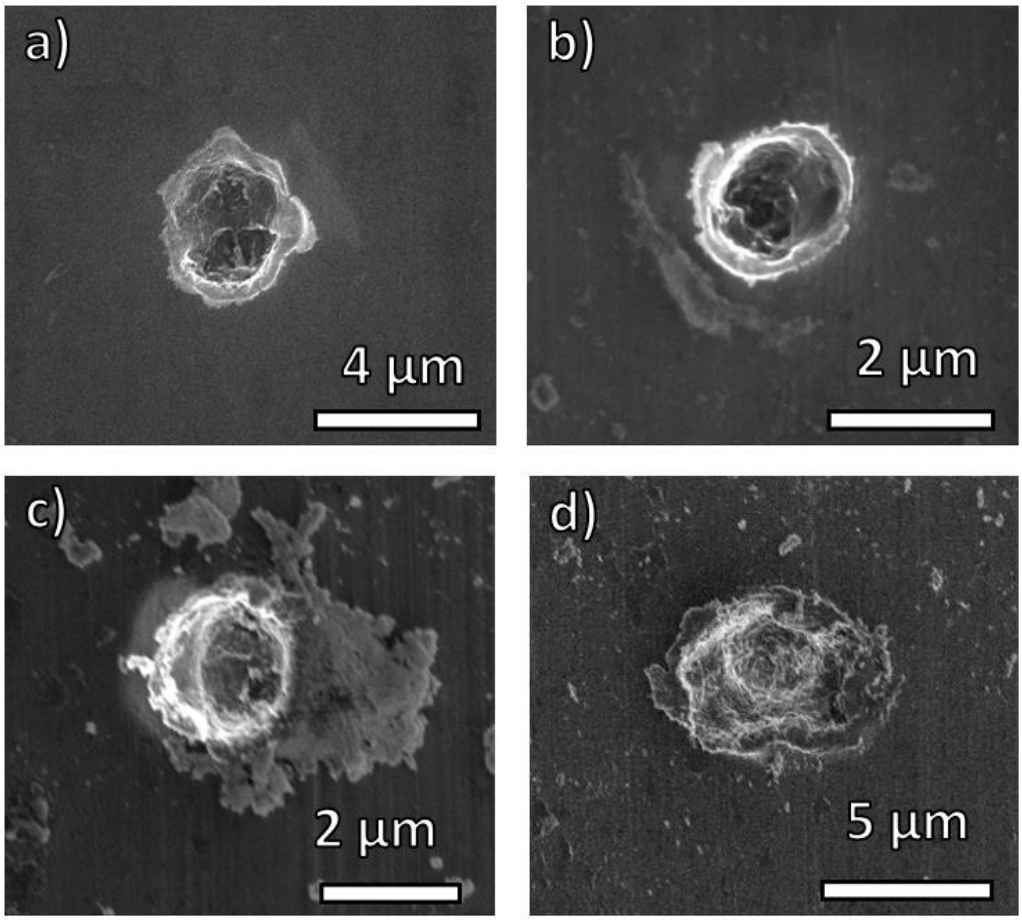

FIGURE 5.12: Secondary electron images of Stardust craters a) C2113N-B #1 b) C2113N-B #2 c) C2118N-B #1 and d) C2118N-B #2.

The craters all appeared to contain cometary residue, based upon initial qualitative SEM-EDXS results, and were selected for further analysis with FIB-TEM techniques. Cross sections of these craters were extracted and thinned to 100-150 nm, preserving material for potential isotope analyses, with Washington University's FEI Quanta 3D FIB-SEM. Further thinning and analysis was performed in collaboration with Rhonda Stroud at NRL. Final FIB cross section polishing was performed with NRL's FEI Helios FIB operated at 8 kV in order to minimize damage to the preserved cometary material. High-resolution imaging and EDXS mapping were performed with NRL's Nion UltraSTEM 200 aberration-corrected STEM operated at 200 kV. Bright-field (BF), high angle annular dark-field (HAADF) images, medium angle annular dark-field (MAADF) images, and STEM-EDXS maps of the craters were collected. STEM-EDXS quantification was performed using Bruker Espirit 2.0 software with precalculated K-factors for Cliff-Lorimer analysis.

5.4.2 Stardust Foils C2113N-B and C2118N-B Results

The studied craters had varying morphologies (Figure 5.13). One of the extracted craters (C2113N-B #1) had a double indentation indicative of a complex aggregate impactor of varying density. However, only one of the indentations contained significant impactor residue. The other three craters had rounded crater bottoms suggestive of a compact impactor. Depth/diameter ratios in the craters ranged from 0.50 to 0.68. Residue thicknesses were variable across the crater bottoms, ranging from 10 nm to 250 nm.

The crater melt layers were dominated by homogeneous mixtures of Mg- and Si-rich materials coupled with iron nickel sulfides. Crystallinity of the material was not determined due to the use of a STEM instrument rather than a traditional TEM instrument. STEM instruments

raster across the image, allowing for the creation of detailed elemental maps of the crater residues. However, the lack of a stationary beam prevents the application of SAD analyses.

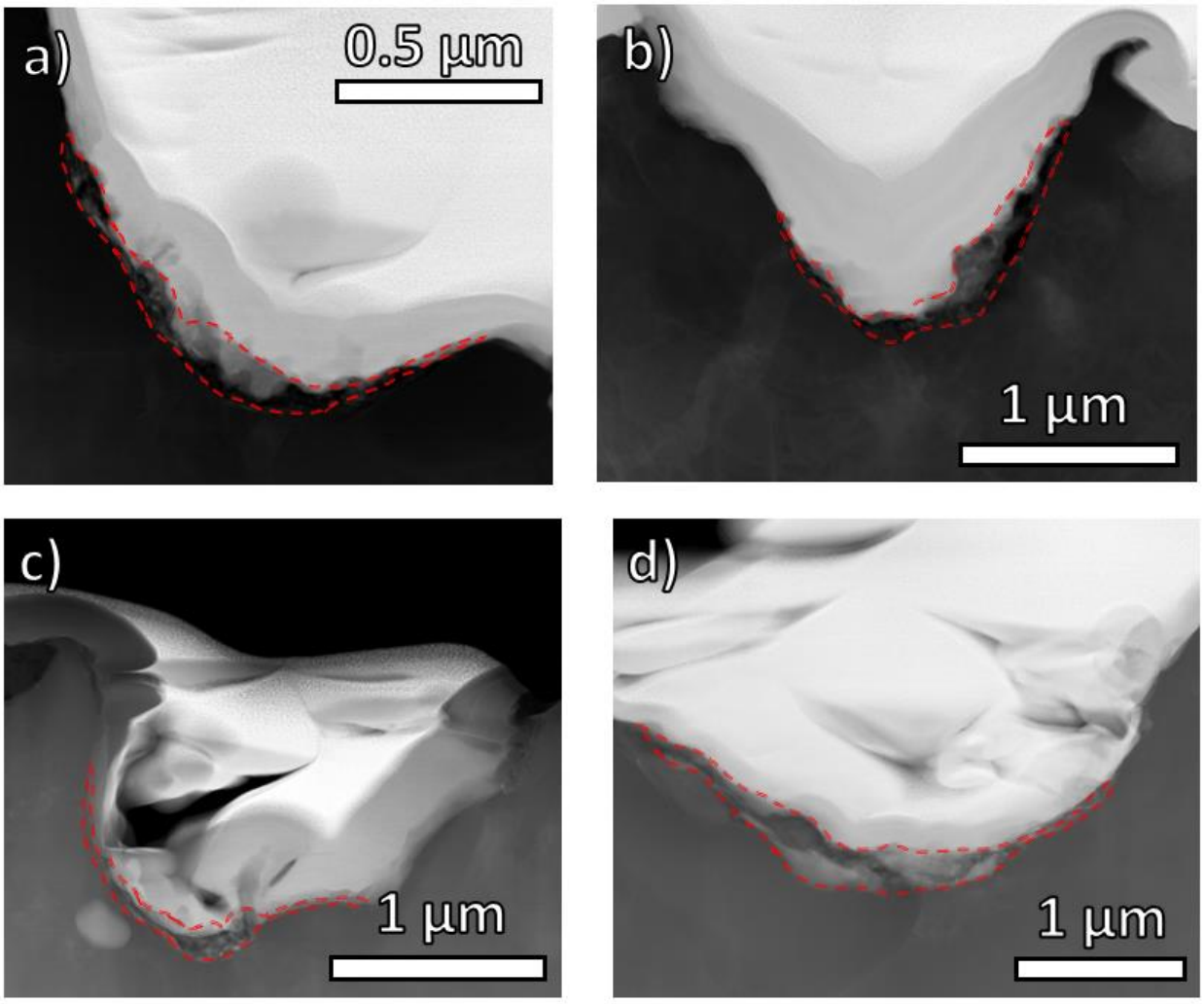

FIGURE 5.13: STEM high angle annular dark-field (HAADF) images of cometary residue in Stardust craters a) C2113N-B #1 b) C2113N-B #2 c) C2113N-B #1 and d) C2118N-B #2, with residue layers highlighted in red. The Pt cap applied during FIB preparation appears lighter than the Al substrate below.

Crater C2113N-B #1's residue and elemental maps of this residue are shown in Figure 5.14. The crater was dominated by Mg- and Si-rich material. The crater residues were heterogeneous, with more iron-nickel sulfides present further up along the crater's walls. O, Si, and Mg abundances were generally consistent with impactors of olivinic compositions. Ni-rich regions were present in the Mg- and Si-rich material closer to the crater bottoms (Figure 5.15 and

Table 5.1). Ni/Fe ratios were large for the Ni hotspots, reaching values as high as 0.5, suggesting that taenite was present in the impactor residue.

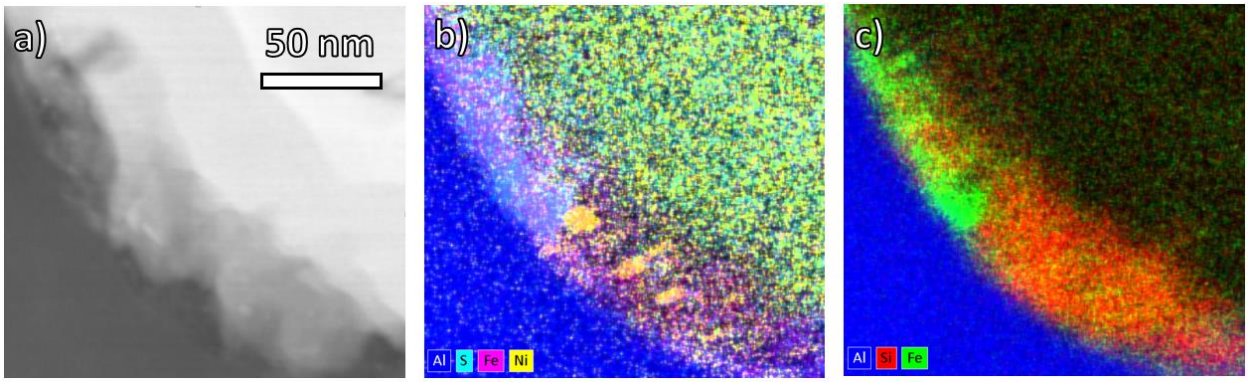

FIGURE 5.14: a) STEM HAADF image of residue in crater C2113N-B #1 and the corresponding b) Al/S/Fe/Ni STEM-EDXS and c) Al/Si/Fe STEM-EDXS maps of the residue. Distinct Ni-rich regions are seen in b), and heterogeneity in crater residues are seen in the separation of Fe- and Si-rich melts in c). The STEM-EDXS maps are created by additively combining pixel color values for each element. Pixel locations are determined through peak heights at each location rather than background-normalized counts.

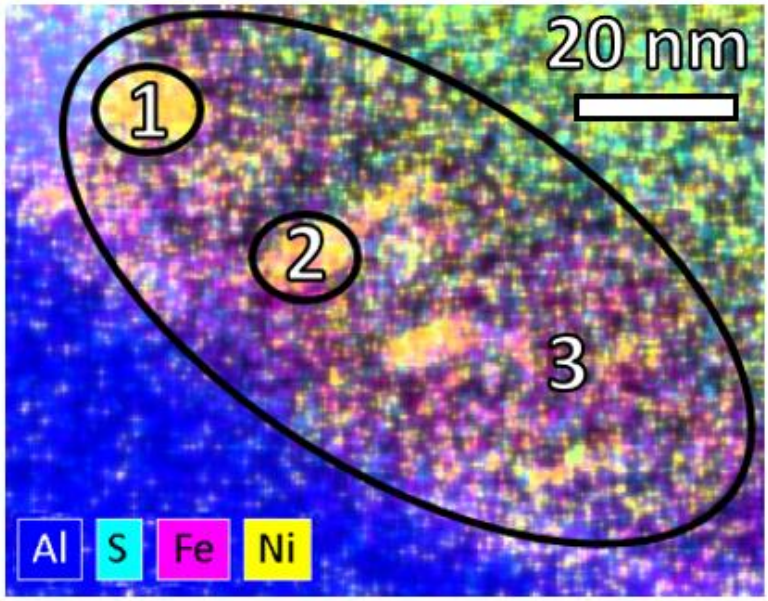

FIGURE 5.15: Al/S/Fe/Ni STEM-EDXS map of residue in crater C2113N-B #1 with quantified regions labeled. Quantification results are shown for these three regions in Table 5.1.

TABLE 5.1: STEM-EDXS Quantification of the regions shown in Figure 5.15.

Region	O at. %	Mg at. %	Si at. %	S at. %	Fe at. %	Ni at. %
1	63.5 ± 12.6	21.0 ± 2.0	11.5 ± 0.9	0.77 ± 0.09	0.36 ± 0.02	0.18 ± 0.02
2	61.7 ± 13.6	17.4 ± 1.9	15.4 ± 1.2	0.49 ± 0.09	0.33 ± 0.02	0.09 ± 0.01
3	55.4 ± 7.6	21.3 ± 1.7	12.3 ± 0.7	3.6 ± 0.2	2.10 ± 0.07	0.14 ± 0.01

Crater C113N-B #2, similar to the previous crater, was dominated by Mg- and Si-rich material with minor Fe and S abundances. Ni was not detected as a component of these iron sulfides. The Si, Fe, and S-rich regions composing the majority of the crater were largely consistent with residue from a Mg-rich olivine and S-rich iron sulfides. One region of the crater was unusually Mg-rich, with low Si and Fe abundances and a Mg/O ratio of 4 (Figure 5.16 and Table 5.2). Though the Mg/O ratio is inconsistent with most mineralogies, this ratio is consistent with spinel ($MgAl_2O_4$). Given our inability to accurately measure Al due to contamination from the foil substrate we excluded Al from STEM-EDXS quantification analyses. As a result, this region is likely the result of a spinel impactor, though this cannot be confirmed definitively due to our inability to accurately probe Al abundances in the crater residues.

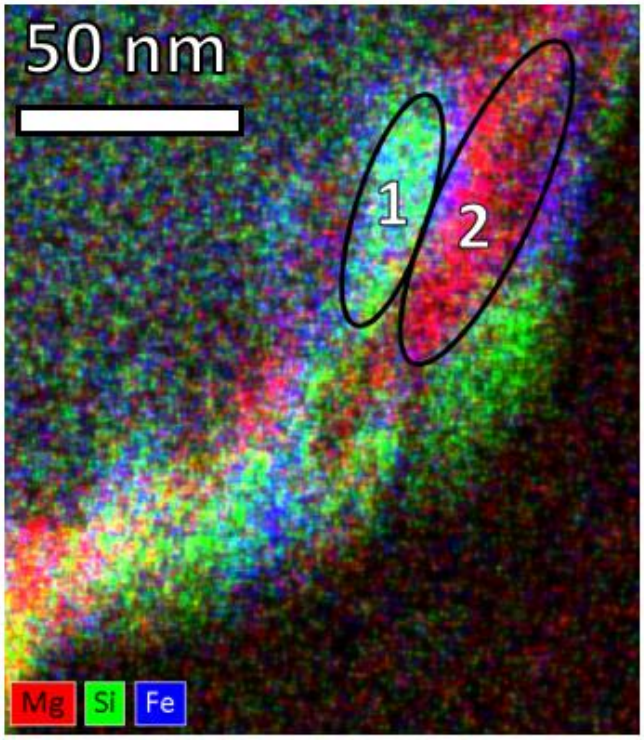

FIGURE 5.16: Mg/Si/Fe STEM-EDXS map of residue in crater C2113N-B #2 with quantified regions labeled. Region 1 was more representative of the crater as a whole, containing abundant Mg and Si with traces of iron sulfides. Region 2 highlights the Mg-rich region we suggest originated from a spinel impactor. Quantification results are shown for these two regions in Table 5.1.

TABLE 5.2: STEM-EDXS quantification of the regions shown in Figure 5.16.

Region	O at. %	Mg at. %	Si at. %	S at. %	Fe at. %
1	67.8 ± 10.6	13.6 ± 1.3	12.7 ± 0.8	3.6 ± 0.2	2.2 ± 0.1
2	77.7 ± 11.6	19.0 ± 1.6	2.1 ± 0.2	0.85 ± 0.06	0.13 ± 0.01

Crater C2118N-B #1, similar to the previous craters, contained a heterogeneous residue layer largely composed of Mg, Si, Fe, and S with minor Ni present (Figure 5.17). Close correlation between Fe and S abundances, coupled with close correlation between Mg and Si abundances, suggest that the crater impactors were a combination of pyroxene and olivine impactors along with S-rich iron sulfides. Mg, Si, and O abundances were consistent with a combination of olivine and pyroxene subgrains. Fe and S abundances were generally consistent with pyrrhotite and troilite.

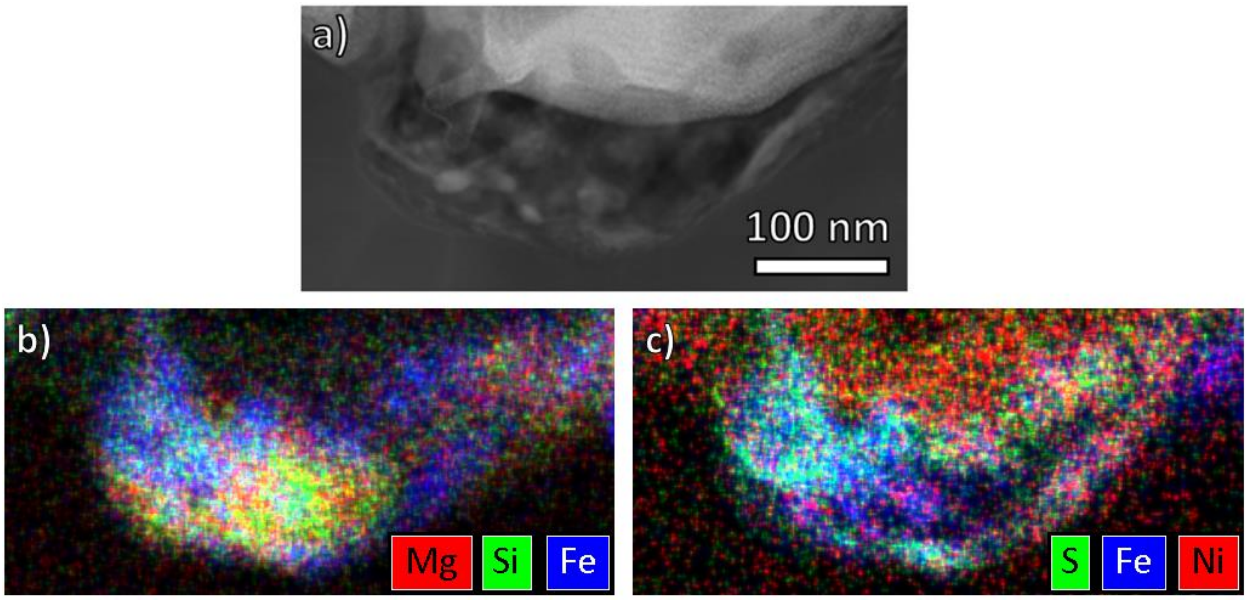

FIGURE 5.17: a) STEM HAADF image of residue in crater C2118N-B #1 and the corresponding b) Mg/Si/Fe STEM-EDXS and c) S/Fe/Ni STEM-EDXS maps of the residue. Si and Mg were closely correlated with one another, and S, Fe, and Ni were closely correlated with one another.

Crater C2118N-B #2, similar to the previous craters, contained a combination of Mg- and Si-rich materials alongside iron-nickel sulfides (Figure 5.18). Crater residues were heterogeneous, with variations in relative O, Si, and Mg abundances that were consistent with combinations of

olivine and pyroxene subgrains. Iron sulfides in the craters were consistent with pyrrhotite and troilite. Ca was also present throughout the crater in small amounts (< 1 at. %).

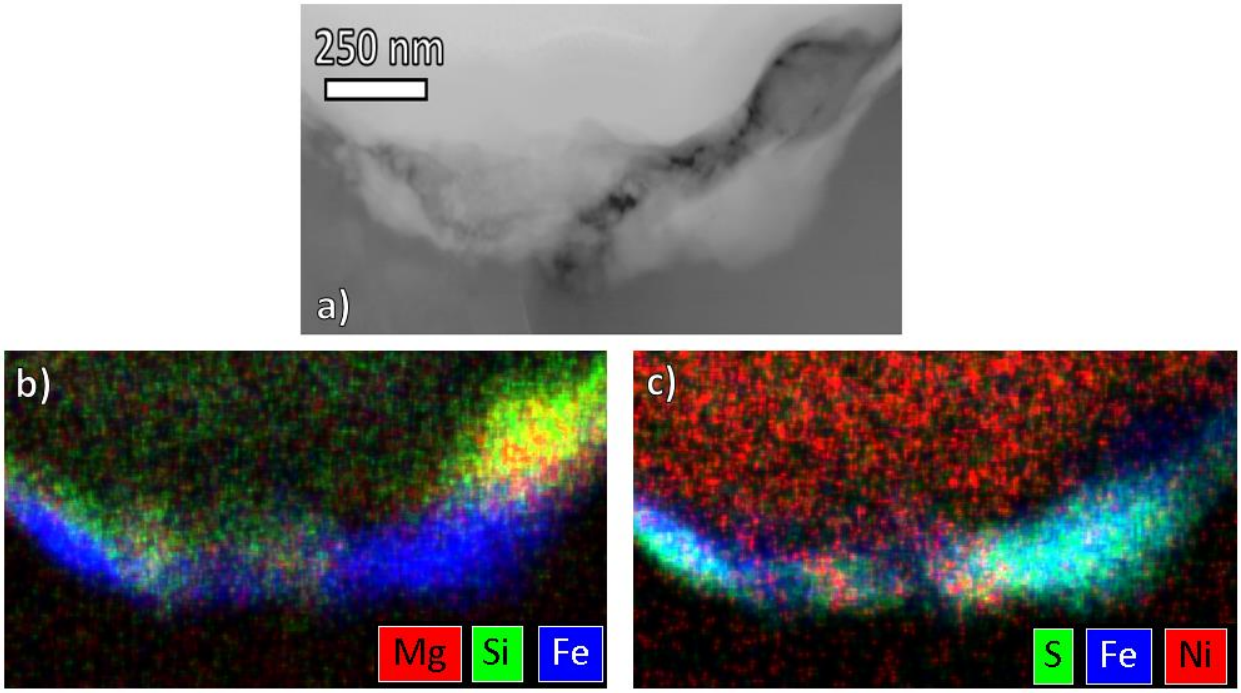

FIGURE 5.18: a) STEM HAADF image of residue in crater C2118N-B #2 and the corresponding b) Mg/Si/Fe STEM-EDXS and c) S/Fe/Ni STEM-EDXS maps of the residue.

5.4.3 Stardust Foils C2113N-B and C2118N-B Discussion

Our crater morphologies were largely consistent with previous investigations of analog and authentic Stardust impactors. Our depth/diameter ratios ranged from 0.50 to 0.68, and previous analog investigations of silicate mineral impactors found depth/diameter ratios between 0.48 and 0.70 were within the first standard deviation of the depth/diameter distribution (Kearsley *et al*., 2008). Additionally, our crater compositions were largely combinations of Si- and Mg-rich materials coupled with iron nickel sulfides. Previous SEM-EDXS analyses (Hörz *et al*., 2006) and FIB-TEM analyses (Leroux *et al*., 2008) have largely identified similar compositions in their studies of micron-scale Stardust craters.

O, Si, and Mg were the most abundant elements in the residue layers. Crater compositions were extremely heterogeneous, but the O, Si, and Mg compositions were generally consistent with combinations of olivine and pyroxene subgrains. Fe, S, and Ni were less abundant in our crater residues, but the Fe/S ratios were generally consistent with pyrrhotite and troilite with small Ni abundances, possibly contributed from materials such as taenite (particularly in crater C2113N-B #1). Taenite, though less frequently observed in Stardust materials than other iron sulfides, has been observed in Stardust aerogel samples (Ogliore *et al*., 2010). The small Fe/S ratios were consistent with previous Stardust studies (Leroux *et al*., 2008) and further indicate that the S loss that characterized our analog studies is not seen to such a degree in authentic Stardust foils. Though some S loss may have occurred due to the collection process, the effect appears to have been fairly minimal, contrary to our analog results.

Definitively identifying the impactors is challenging. Our cross section thicknesses ranged from 100-150 nm while individual subgrains, such as the Ni-rich regions in crater C2113N-B #1, were as small as 10 nm. Additionally, STEM instruments, while useful for their ability to generate EDXS maps, do not have SAD analysis functionality. Pyroxene and olivine, while capable of explaining the observed O, Mg, and Si elemental abundances, are not the only potential sources of these impactors. Pyroxene and olivine compositions, coupled with our observed iron sulfides, are also consistent with GEMS impactors (Keller & Messenger, 2011). As a result, our crater impactors may have been the result of amorphous silicates and iron sulfides rather than crystalline impactors such as olivine and pyroxene. Further analysis with TEM SAD techniques is necessary to characterize the structure of the impactors.

Few materials were present in the crater outside of silicates and iron nickel sulfides. Crater C2113N-B #1 had an unusually large Mg abundance that appears to be due to an impacting spinel

grain. While we cannot definitively identify spinel due to our inability to accurately measure Al abundances, as well as our lack of SAD patterns, spinel has previously been observed in Stardust samples (Joswiak *et al*., 2017). However, spinel has not been previously observed in micron-scale Stardust foil craters. The presence of spinel, a metamorphic mineral found as a component of some CAIs in chondritic meteorites (Chaumard *et al*., 2014), indicates that some fraction of the fine component of Wild 2 is composed of refractory materials that likely originated in the inner Solar System. Ca was observed, but in low abundances (< 1 at. %) in a single crater. Calcium-aluminum-rich inclusions (CAIs) (Chi *et al*., 2009) and kosmocholoric Ca-rich pyroxene and olivine (Kool) grains (Joswiak *et al*., 2009) have both been identified in Stardust materials. However, given the low Ca abundances amid abundant Mg- and Si-rich melt, low-Ca pyroxenes are a more likely source of this Ca, and they have been observed in previous investigations of Stardust craters (Leroux *et al*., 2008) and aerogels (Jacob *et al*., 2009). Thus, this Ca does not appear to be more evidence of refractory materials within the Wild 2 fine component.

5.4.4 Stardust Foils C2113N-B and C2118N-B Conclusions

We extracted four impact craters from Stardust foils C2113N-B and C2118N-B with diameters between 1.5 µm and 4.8 µm. All four crater residues were dominated by heterogeneous Si- and Mg-rich materials that are consistent with combinations of olivine and pyroxene. All four crater residues also contained iron sulfides with abundant S that were generally consistent with pyrrhotite and troilite.

The inability to collect SAD patterns prevented us from determining the crystallinity of the impacting material. The crater bulk compositions were consistent with GEMS material as well as olivines and pyroxenes and thus may be the result of amorphous impactors. The craters' consistency with GEMS, coupled with our earlier results from foil C2010W, suggest that GEMS

or other amorphous Si-rich materials may constitute a larger portion of the Wild 2 fine component than previously thought. However, further TEM studies are required to confirm that the residue layers are amorphous such as our previous results from Stardust foil C2010W.

STEM-EDXS results suggested that residues within crater C2113N-B #1 contained taenite as a result of Ni-rich subgrains within the residue layers. Additionally, STEM-EDXS results suggested that a portion of the residue within crater C2113N-B #2 was contributed by a spinel grain. Though spinel has been observed in Stardust residues before, it has not been observed in studies of micron-scale Stardust foil craters. The presence of spinel within these residues indicates that metamorphic minerals likely to have formed in the inner solar system are present within the Wild 2 fine component.

5.5 Stardust Foil C2113N-A

Following the completion of the studies of craters C2010W, C2113N-B, and C2118N-B we had still not identified any Stardust craters containing surviving crystalline material. This result was considered unusual considering that initial studies of the Stardust foils had identified surviving crystalline material in 10 out of 22 studied craters (Leroux *et al*., 2008; Leroux *et al*., 2010; Stroud *et al*., 2010). Our previous investigations of the refractory analog foils and Acfer 094 analog foils had indicated that smaller craters were likely to experience lower peak temperatures and pressures, and thus were less likely to have altered any impacting crystalline material. As a result, we decided to focus on smaller (submicron) impact craters in future studies.

5.5.1 Stardust Foil C2113N-A Experimental Methods

Stardust Foil C2113N-A did not have any craters larger in size than 1 micron after initial SEM imaging was completed. We focused on identifying submicron craters that were likely unidentified during initial investigation of the foil due to the high magnifications needed to be able

to see such craters. We captured SEM images across a 5.28 mm^2 subsection of the foil with a ~24 nm pixel size using Washington University's Tescan Mira3 Fe-SEM. We identified 20 crater candidates with diameters <0.5 µm. We performed SEM-EDXS analyses on the 20 located craters with a JEOL JSM-840A SEM in order to identify potential cometary materials within the residues. 10 of these craters returned measurable Si, Fe, S, or Ca signals. 6 craters were selected for further study with FIB-TEM techniques based on the strength of the observed SEM-EDXS signals (Table 5.3 and Figure 5.19). Further quantitative analyses with SEM-EDXS were not performed because the X-ray interaction volume was much larger than the crater residue, making quantification inaccurate.

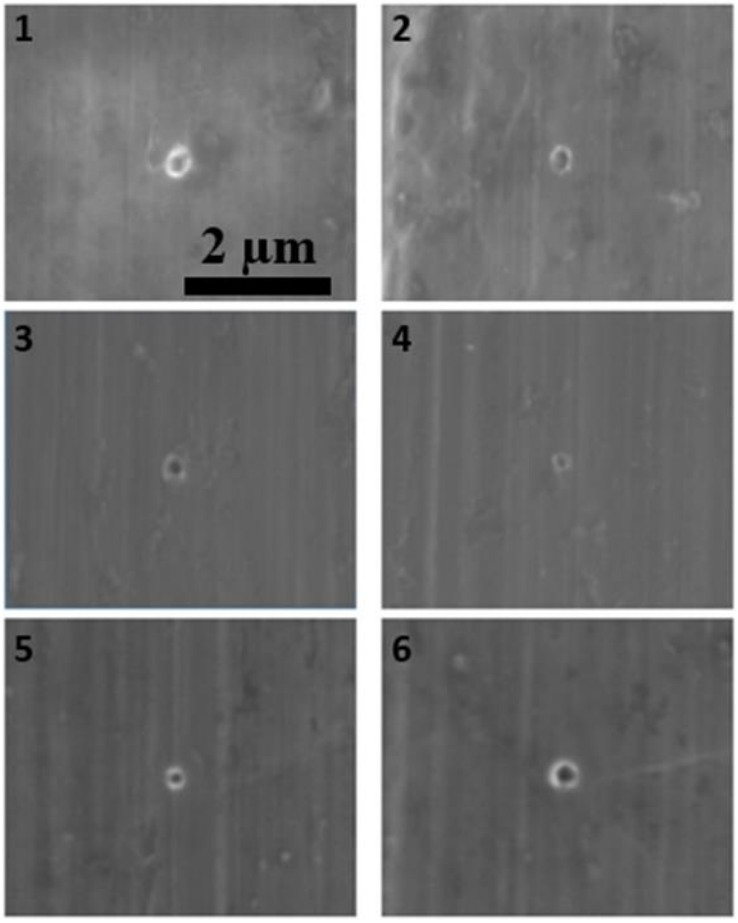

FIGURE 5.19: Secondary electron images of submicron craters 1 to 6.

TABLE 5.3: Characteristics of the craters selected for further FIB-TEM analysis. Crater diameters are measured from the inside edge of each crater lip. Crater depths are measured from the top of the crater to the deepest location of the protective Pt cap deposited during the FIB extraction process. Observed elements are listed in order of decreasing peak intensity.

Crater #	Crater Diameter (nm)	Crater Depth (nm)	Depth/Diameter Ratio	Elements Observed (SEM-EDXS)
1	320	155	0.48	Fe, S, Si, Ca
2	220	140	0.63	Si, Fe, S
3	310	155	0.50	Fe, S, Ca, Si
4	200	60	0.30	Si
5	205	105	0.51	Fe, S, Si
6	350	180	0.51	Fe, S

Cross sections of the craters were prepared for further TEM analysis by in situ FIB lift-out with Washington University's FEI Quanta 3D FIB. The crater cross sections were thinned to 100-150 nm in order to allow for sufficient electron transparency to perform further TEM analyses while also maximizing the preservation of cometary material for potential isotope analyses.

TEM bright-field and dark-field imaging, along with SAD analyses of the crater residues, were performed with Washington University's JEOL 2000FX TEM operated at 200 KeV. High-resolution TEM-EDXS characterization was performed on the same instrument operated at 160 KeV, rather than 200 KeV, in order to improve the electron interaction cross section and improve overall X-ray count rates while also maintaining sample transparency for imaging. Quantification of the TEM-EDXS spectra was performed with NIST DTSA-II software (Ritchie 2011; Ritchie 2012) using elemental standards to perform Cliff-Lorimer analysis coupled with ZAF corrections primarily added to light elements. Al, Pt, and Cu were excluded from the analysis due to the majority of the counts in those elements arising from the Al foil substrate, the protective Pt coat applied during the FIB process, and the Cu TEM grid holder. Further imaging and elemental mapping was performed on Washington University's JEM-2100F Field-Emission STEM with an attached Bruker SDD EDS system.

5.5.2 Stardust Foil C2113N-A Results

Craters 2 through 6 had rounded, bowl-shaped crater bottoms indicative of a compact impactor. Crater 1 contained a double-bowl shape, suggesting the impactor was bilobate with a central region of lower mass or lower density. Crater 4, though containing a bowl-shaped bottom, had no discernable residue layer. All the craters had fairly symmetric shapes that are generally consistent with acute angles of incidence relative to the surface normal for the impacting material (Kearsley *et al.*, 2007).

No crystalline material was observed in the crater residues. Materials in the residue layers were largely heterogeneous, indicative of rapid melting and resolidification (Wozniakiewicz *et al.*, 2012b). Crater elemental compositions are detailed in Table 5.4.

Crater #1's residue is separated into two bowl-shaped indentations located on each side of the crater that are connected by a thinner melt layer (Figure 5.20). Residue thickness was 40 nm along the tops of the crater walls, 95 nm in the smaller of the indentations, and 180 nm in the larger indentation.

Si and Mg were a minor part of the residue with the majority of the residue composed of less than 2.5 at. % for each element (Table 5.4). Oxygen was abundant throughout the residue. The large O to Si ratios were not stoichiometrically consistent with olivines or pyroxenes which have been observed frequently in Stardust collection media (Zolensky *et al.*, 2006). The right side of the crater was dominated by the presence of iron-nickel sulfides. Fe/S ratios in this region of the crater ranged from 1.4-2.0 while Fe/Ni ratios ranged from 12.2-26.9. The region separating the two crater depressions contained high Fe though this was not correlated with an increase of S or Ni, suggesting an alternate Fe source than iron nickel sulfides. Ca was present in small amounts throughout the crater residue (1-3 at. %), along with trace K (< 1 at. %). Zn was the most abundant element on the left side of the crater, composing up to 63.0 at. % of regions on the left crater walls.

Zn abundance was not correlated with S abundances, demonstrating that the Zn is unlikely to originate from sulfide impactors. The regions with the highest Zn concentrations also contained up to 5.0 at. % Mn.

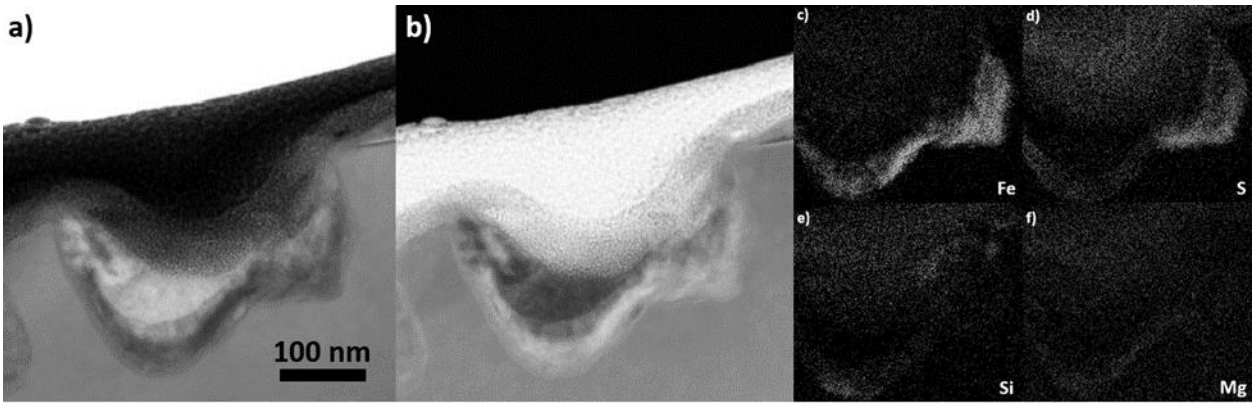

FIGURE 5.20: a) Bright-field and b) high-angle annular dark-field STEM images taken of crater #1 at 300k magnification. STEM-EDXS mapping of c) Fe, d) S, e) Si, and f) Mg.

Crater #2's residue in the crater bottom is skewed to one side with the thickest part of the residue lying off center (Figure 5.21). Residue thickness ranged from 20 nm on the crater walls to nearly 100 nm at the crater bottom.

Si and Mg were present throughout the crater residue. Si was nearly three times as abundant as Mg with residue in the crater bottom composed of 7.5 and 2.8 at. % of Si and Mg, respectively. O was abundant throughout the crater, resulting in nonstoichiometric O/Si ratio values greater than 6.0 throughout the crater residue. Fe, S, and Zn were also major components of the crater residue. The Fe/S ratio of material in the crater bottom was 1.36. The (Fe+Zn)/S ratio of this material was 2.52, suggesting that sulfur loss occurred if iron and zinc sulfides were the primary sources of these elements. Ni abundances were high relative to Fe abundances, with a Fe/Ni ratio of 5.54 for material in the crater bottom.

TABLE 5.4: Representative compositions (at. %) for crater residue regions measured by TEM-EDXS. Uncertainties are listed in parentheses, rounded up to the nearest 0.1%. Al, Pt, and Cu have been excluded from quantification due to possible contamination from the foil substrate, FIB preparation, and TEM sample holder, respectively. nd indicates the element was not detected, and na indicates the value is not available. Crater 4 is not listed as it did not contain residue.

Crater	Sub-region	O	Si	Mg	Fe	S	Ni	Ca	Zn	Other Elements	O/Si	Fe/S	Fe/Ni
1													
	1	21.5 (1.0)	2.2 (0.1)	nd	36.1 (0.4)	25.8 (0.3)	1.3 (0.1)	1.1 (0.1)	11.5 (0.1)	K	9.77	1.40	26.9
	2	39.4 (0.2)	1.7 (0.1)	nd	7.4 (0.1)	4.2 (0.1)	0.6 (0.1)	2.3 (0.1)	37.9 (0.6)	K, Mn	23.2	1.75	12.2
	3	26.7 (0.6)	0.9 (0.1)	1.3 (0.1)	3.2 (0.1)	1.3 (0.1)	0.2 (0.1)	2.9 (0.1)	63.0 (0.3)	K, Mn, Cl	29.7	2.48	16.6
	4	45.4 (0.5)	1.7 (0.1)	0.7 (0.1)	22.3 (0.2)	3.4 (0.1)	0.7 (0.1)	1.9 (0.1)	22.3 (0.1)	K	26.7	5.72	33.2
	5	43.0 (0.5)	6.6 (0.1)	1.0 (0.1)	15.9 (0.1)	4.5 (0.1)	0.9 (0.1)	2.1 (0.1)	25.7 (0.1)	K	6.51	3.50	17.6
2													
	1	46.6 (0.5)	7.5 (0.1)	2.8 (0.1)	15.3 (0.3)	11.2 (0.1)	2.8 (0.1)	0.2 (0.1)	13.0 (0.1)	K	6.21	1.36	5.54
3													
	1	35.3 (1.0)	8.1 (0.1)	3.7 (0.1)	25.4 (0.5)	19.8 (0.3)	1.6 (0.1)	2.6 (0.1)	3.5 (0.2)	nd	4.36	1.28	15.9
	2	22.8 (1.3)	4.9 (0.1)	3.2 (0.1)	31.4 (0.4)	35.1 (0.4)	1.5 (0.1)	0.9 (0.1)	nd	Ti	4.65	0.89	21.5
	3	42.6 (0.8)	8.8 (0.1)	4.3 (0.1)	21.1 (0.4)	16.5 (0.3)	0.9 (0.1)	3.4 (0.1)	2.5 (0.2)	nd	4.85	1.28	24.3
5													
	1	60.5 (0.4)	28.5 (0.9)	0.4 (0.2)	7.3 (0.1)	2.4 (0.2)	1.0 (0.2)	nd	nd	nd	2.12	3.05	7.25
	2	35.9 (1.3)	5.6 (0.1)	4.0 (0.1)	20.1 (0.5)	31.3 (0.9)	1.6 (0.1)	0.1 (0.1)	0.6 (0.4)	nd	6.42	0.67	12.9
	3	53.1 (0.4)	7.5 (0.1)	2.4 (0.1)	13.2 (0.4)	19.7 (0.6)	1.6 (0.2)	nd	2.6 (0.4)	nd	7.08	0.67	8.52
6													
	1	41.5 (1.0)	6.0 (0.1)	nd	20.6 (0.5)	26.9 (0.7)	1.4 (0.2)	1.3 (0.1)	3.4 (0.3)	nd	6.92	0.77	14.4
	2	58.2 (0.1)	7.9 (0.1)	1.9 (0.1)	11.1 (0.2)	8.8 (0.1)	0.9 (0.1)	0.2 (0.1)	10.7 (0.1)	Ti	7.37	1.26	13.1
	3	73.3 (1.8)	10.3 (0.5)	nd	7.4 (0.3)	1.2 (0.3)	nd	0.6 (0.1)	4.7 (0.4)	Ti, K, Cl	7.11	6.72	na

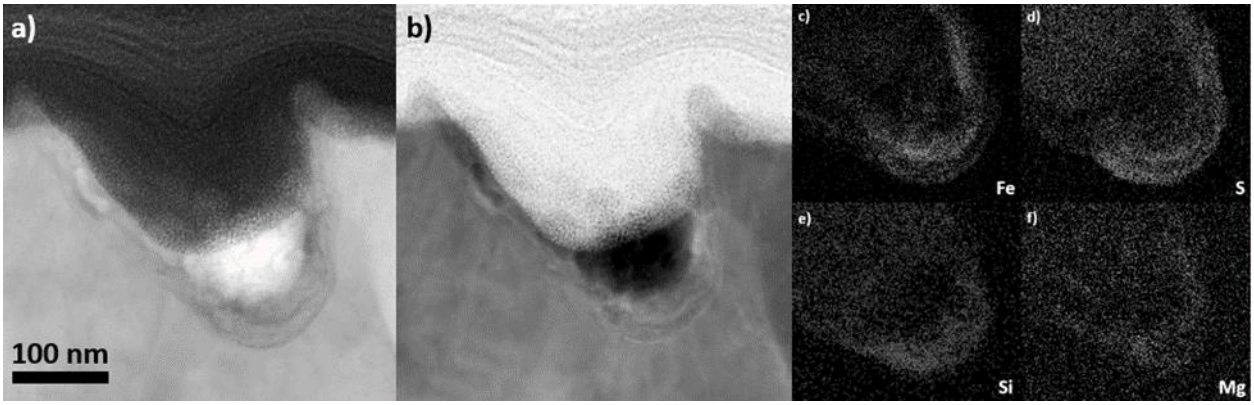

FIGURE 5.21: a) Bright-field and b) high-angle annular dark-field STEM images taken of crater #2 at 600k magnification. STEM-EDXS mapping of c) Fe, d) S, e) Si, and f) Mg.

Crater #3's residue was distributed symmetrically (Figure 5.22). Residue in the crater bottom was of a similar size to that seen in crater 2, with thicknesses ranging from 20 nm on the crater walls to 100 nm at the center of the crater's bowl.

The crater residue contained Si and Mg throughout with Si abundances ranging from 4.5 to 8.8 at. % and Mg abundances ranging from 3.2 to 4.5 at. %. Si/O ratios consistently ranged between 4.0 and 5.0, placing Si abundances slightly too low for olivinic stoichiometry. Iron nickel sulfides were the dominant phase in the crater residues with Fe/S ratios and Fe/Ni ratios ranging from .89-1.28 and 15.9-24.3, respectively. Zn was present throughout the crater in smaller abundances (2.5-3.5 at. %), suggesting zinc sulfides were a component of the impacting material. Ca was also present throughout the crater residue (0.9-3.4 at. %).

Crater #4 was extremely shallow, having a depth of only 60 nm and a depth to diameter ratio of 0.30 (Figure 5.23). This depth to diameter ratio is smaller than ratios seen in previously investigated Stardust craters and analogs fired at ~6.1 km/s (Kearsley *et al.*, 2007; Leroux *et al.*, 2008). No residue was observed in the crater bottom. The crater may have been an irregularity in the aluminum foil itself arising from the removal of precipitates during foil manufacturing (Stroud

et al., 2014) rather than the result of a cometary impactor, explaining the small depth to diameter ratio. However, this alone would not explain the weak Si signal seen during the SEM-EDXS analysis as no Si was observable during TEM-EDXS analysis. Another possibility is that we missed the center of the crater during the final cross section-thinning of the FIB preparation procedure. In this case we may have created a cross section lacking the deepest part of the crater as well as any impactor residue, which also allows for the lack of Si in TEM-EDXS spectra if the crater was not cometary in origin. A third option is that the crater was the result of a secondary impactor, potentially from the Stardust solar cell glass, which is rich in Si and has been observed many times in the interstellar Stardust foil (Stroud *et al*., 2014). Such an impactor could have produced the Si signal seen during SEM-EDXS analysis, as well as created an asymmetric, shallow crater whose residue was later missed during the FIB extraction due to the combination of the crater's asymmetry and our goal of isolating the crater's center.

Crater #5's impactor residue was thin and uniform around the crater, with the crater residue ranging from 15 nm to 30 nm deep (Figure 5.24).

The crater residue was highly heterogeneous. The right side of the crater contained abundant Si composing up to 28.5 at. % of the residue material. Mg abundance was not correlated with Si, and despite high Si concentrations Mg was never observed above 4.0 at. %. O/Si values ranged from approximately 2.0 to 7.5 throughout the crater, potentially allowing for olivine or pyroxene as sources of the observed Si though the crater's thoroughly heterogeneous composition and lack of crystalline material makes positive identification of these minerals difficult. The left side and center depression of the crater contained more Fe than Si, with compositions ranging from 13.2 to 20.1 at. %. Fe abundance was correlated with S and Ni, and Fe/S ratios ranged from 0.67

to 1.0 on the left side of the crater. Zn was also present in the Fe-rich regions of the crater, with measured abundances ranging from 0.6 to 2.6 at. %.

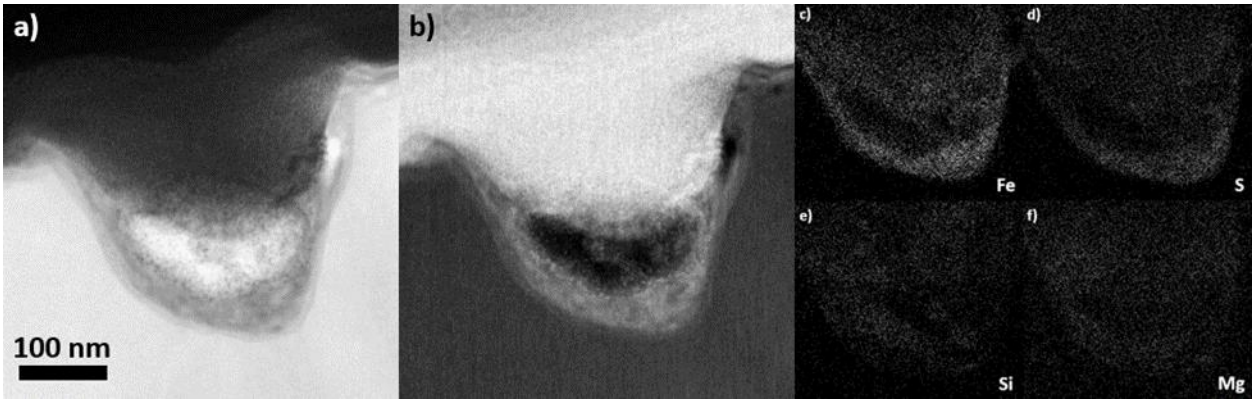

FIGURE 5.22: a) Bright-field and b) high-angle annular dark-field STEM images taken of crater #3 at 400k magnification. STEM-EDXS mapping of c) Fe, d) S, e) Si, and f) Mg.

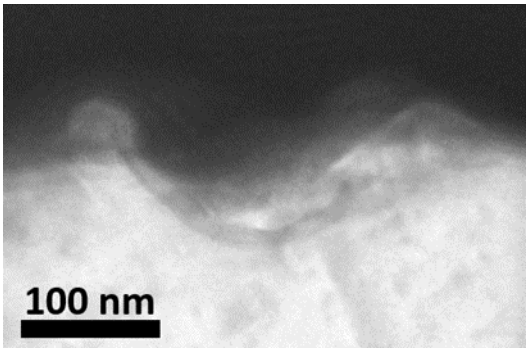

FIGURE 5.23: TEM bright-field image of crater #4 at 200k magnification.

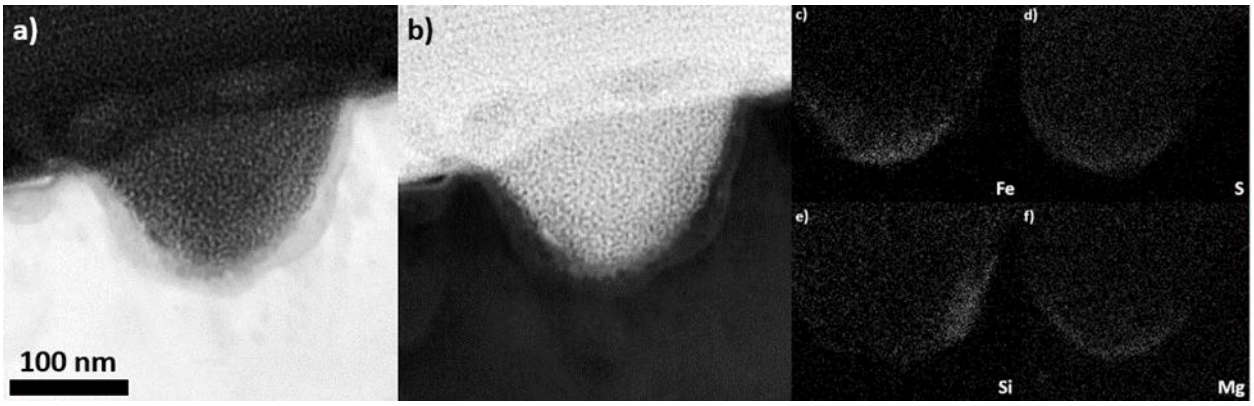

FIGURE 5.24: a) Bright-field and b) high-angle annular dark-field STEM images taken of crater #5 at 500k magnification. STEM-EDXS mapping of c) Fe, d) S, e) Si, and f) Mg.

Crater #6's residue was heavily concentrated into one bulb located slightly off-center from the crater's deepest point (Figure 5.25). The residue thickness ranged from 15 nm along the crater walls to 90 nm in the off-center bulb.

Si was present throughout the crater residue, with Si abundances ranging from 6.0-10.3 at. %. Mg was largely absent and generally not detected, though Mg abundances in some regions reached 2.0 at. %. Si and O abundances were correlated, though O/Si ratios were typically close to 7.0 and far above stoichiometries consistent with olivine or pyroxene. O and Si abundances were anti-correlated with Fe, S, and Ni abundances. Fe, S, and Ni composed up to half the residue material in the upper right portion of the residue, with Fe/S and Fe/Ni ratios ranging from 0.77-1.26 and 13.1-14.4 in this region, respectively. Zn was also common in the crater residue with abundances typically close to 4.0 at. % but ranging as high as 10.7 at. %. Small amounts (< 1.5 at. %) of Ca and Ti were also observed in the crater residues.

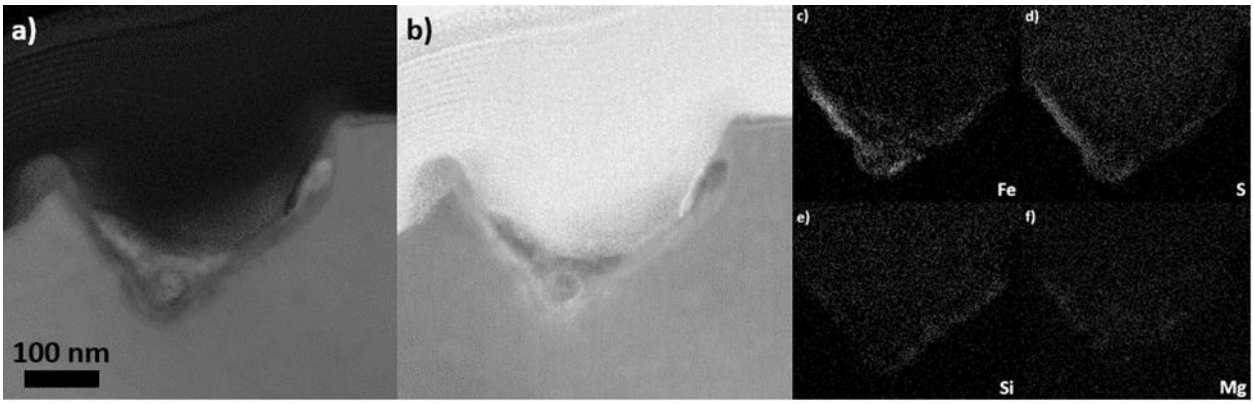

FIGURE 5.25: a) Bright-field and b) high-angle annular dark-field STEM images taken of crater #6 at 300k magnification. STEM-EDXS mapping of c) Fe, d) S, e) Si, and f) Mg.

5.5.3 Stardust Foil C2113N-A Discussion

The morphologies of the craters, aside from crater #4 which contained no observable residue, were largely consistent with previous investigations of analog and authentic Stardust impactors. The craters' rounded, bowl-shaped bottoms differ from the shallow, elongated crater shapes indicative of terrestrial contamination in the form of secondary impacts from material

native to the Stardust spacecraft (Stroud *et al*., 2014). Depth/diameter ratios of residue-containing craters ranged from 0.48 to 0.63, with an average value of 0.53. Investigations of silicate mineral impactors on flight-spare Stardust foils fired at 6.1 km/s found depth/diameter ratios largely centered between 0.52 and 0.65 with values between 0.48 and 0.70 still lying within the first standard deviation (Kearsley *et al*., 2008). Our depth/diameter ratios may have been slightly smaller than average due to our impactors having lower densities or higher porosities than the previously investigated silicate impactors, as both factors can result in smaller depth/diameter ratios (Kearsley *et al*., 2007). However, depth/diameter ratios can be affected by a number of other factors, such as angle of incidence, impactor velocity, and volatile contents, making the determination of impactor density or porosity difficult (Price *et al*., 2010).

None of our investigated craters contained any crystalline material. These results were unexpected given that previous reports on FIB-TEM investigated Stardust craters returned crystalline material in 10 out of 22 investigated craters (Leroux *et al*., 2008; Leroux *et al*., 2010; Stroud *et al*., 2010). Additionally our previous analog investigations suggested that smaller crystalline impactors are less likely to be amorphized during impact processing and our investigation focused on craters smaller than the majority of those previously reported to contain surviving crystalline material. Studies focused on coarser grains captured by the Stardust aerogels have also indicated that crystalline materials are abundant in Wild 2 (Zolensky *et al*., 2006). However, the lack of crystalline material in our previous studies of Stardust craters indicates that crystalline material in the crater residues may be rarer than previously thought.

Analog studies have shown that crystalline material is frequently destroyed during the impact processing on the foils, particularly when the impactor is an aggregate of crystalline subgrains (Wozniakiewicz *et al*., 2012b). Given that our craters are universally aggregates of

silicate and iron sulfide components, the possibility exists that all impacting crystalline material was destroyed during the collection process. An alternative explanation for our lack of crystalline material is that our impactors were amorphous prior to the impact. Astronomical observations have shown comets contain abundant amorphous silicates (Hanner 2003). Studies of fine grained Wild 2 components collected by the aerogel tiles have found amorphous silicates and iron sulfide vesicles constituting GEMS-like material to be abundant (Stodolna *et al*., 2012), though the GEMS-like material may have resulted from melting and intermixing of the Stardust aerogel with crystalline materials that contained silicates and sulfides (Ishii *et al*., 2008). There is a strong possibility that our impactor residues are a quenched combination of amorphous silicates and sulfides. However, it is difficult to prove any impactor material was amorphous prior to collection given the impact conditions.

Silicon was observed throughout the studied craters. Excluding crater #1, whose Zn composition indicate it suffered from terrestrial contamination, Si composed at least 4.9 at. % of all observed crater residues. Mg was also observed in all craters, though was missing from some residue subregions and was lower in abundance than Si, with Mg abundances ranging from 0.4-4.3 at. %. Definitively identifying the silicate impactors is difficult. Our cross section thicknesses ranged from 100-150 nm while individual subgrains in the impacting aggregates were likely smaller, making the isolation of any individual impactor challenging. Additionally, our crater residues were amorphous, meaning that any grains present in the original impactor have likely mixed with other subgrains composing the aggregate. Pyroxene and olivine are potential components of the impactors but cannot fully explain the observed elemental abundances. O/Si ratios in craters #2, #3, #5, and #6 largely fell within the range 4.0-7.5 and are too high for pyroxene or olivine to be the sole O sources. Previous analog foil experiments have not observed preferential

loss of Si, Mg, or Fe relative to O in olivine and diopside impactors, making the loss of cations in the impactors unlikely (Wozniakiewicz *et al*., 2012b). O/Si values in chondrites are largely influenced by the oxidation state of Fe, and O/Si values can reach 7.9 for CI chondrites containing hydrated silicates, carbonates and sulfates (Mason 1979). O overabundances can also be explained by oxygen-rich species such as iron oxides constituting a fraction of the impactor material. O/Si ratios observed in IDPs frequently range from 4.0-6.0, allowing IDP components such as GEMS to be a potential contributor to the O and Si observed in our residues (Schramm *et al*., 1989). However, while GEMS can have Mg/Si ratios as low as 0.05, they are typically more Mg-rich than our residues with average Mg/Si ratios close to 0.67 (Keller & Messenger, 2011).

Iron sulfides were ubiquitous within our crater residues. While Fe/S ratios in the craters ranged between 0.67-3.05, the majority of Fe/S ratios were greater than 1.0, indicating that S loss, which is common in analog foil experiments, may have occurred (Wozniakiewicz *et al*., 2011). However, given the ubiquitous presence of Si in our residues, some Fe may have been contributed by silicate impactors (e.g., Fe-rich olivine) that would lead to Fe/S ratios greater than 1.0. Ni abundances in craters #2, #5, and #6 were too high relative to the Fe abundances in the craters for pyrrhotite or troilite alone to be responsible for the observed Fe and S. The Fe/Ni ratios in these craters ranged from 5.54-14.4 while pyrrhotite reported in GEMS grains, although capable of having similarly low Fe/Ni ratios, largely have Fe/Ni ratios of 15.7 or higher (Keller & Messenger, 2011; Bradley & Zai, 2004). Our Ni abundances can be explained by a minor fraction of pentlandite among pyrrhotite and troilite impacting materials.

Though individually the O-Si-Mg and Fe-S-Ni components of these craters can be explained by GEMS impactors, the ratios of these two components cannot. Fe/Si ratios in GEMS have been observed to range from 0.09 up to 1.63 with an average of 0.56 (Keller & Messenger,

2011). Craters #1, #2, and #3 have no regions where Fe/Si ever falls below 2.04. Craters #5 and #6, though containing subregions with Fe/Si ratios ranging between 0.26 and 0.72, both have average Fe/Si ratios that fall above reported Fe/Si ratios for GEMS. While GEMS grains could potentially represent a component of our impactors, our crater residues are too heavily dominated by iron-nickel sulfides to have been sourced entirely from GEMS. Similarly, while our Si/Fe ratios fall within the range of values seen within IDPs, our craters are more Si-depleted compared to the majority of reported Si/Fe values seen in IDPs (Schramm *et al*., 1989).

Zn was abundant in our crater residues and appeared in all craters containing a residue layer. S was also present in each crater's residue, and craters #3, #5, and #6 all contained subregions with Fe/S ratios less than 1, allowing for zinc sulfides to be a potential source of both the Zn and abundant S in these subregions. S loss within the foils is also expected due to the high collection velocity, allowing for zinc sulfides as a possibility even within regions with (Zn+Fe)/S ratios greater than 1 (Wozniakiewicz *et al*., 2011). Zinc sulfides have been observed in previous FIB-TEM investigations of Stardust foil craters (Leroux *et al*., 2008). Zinc sulfides have also been observed in the form of Fe-rich sphalerite in both IDPs (Christoffersen & Buseck 1986; Reitmeijer *et al*., 1998) as well as Stardust aerogel tracks (Zolensky *et al*., 2006). Current estimates suggest over 85% of stratospheric IDPs originated from comets (Nesvorny *et al*., 2010), suggesting zinc sulfides are likely a component of Wild 2's fine grains. Cubanite ($CuFe_2S_3$) has been observed in the Stardust aerogels as well (Berger *et al*., 2011) demonstrating that Wild 2 contains sulfides with a variety of chalcophilic elements.

While Zn concentrations are sufficiently low in craters #2, #3, #5, and #6 to be explained as the remains of impacting zinc sulfides, crater #1 had extremely large Zn abundances with Zn reaching values as high as 63 at. % in subregions of the crater (Figure 5.26). Additionally, Zn

abundances in crater #1 were anti-correlated with S abundances within the crater residue. Zn observations in the Stardust interstellar foils have frequently been tied to secondary impacts from cover glass present on the Stardust spacecraft solar cells (Stroud *et al*., 2014). While traces of K were observed throughout the crater, which is also a component of the solar cell cover glass, Zn is only believed to compose a small fraction of the cover glass (3-4 wt. %) (Stroud *et al*., 2014), making the cover glass an unlikely source for the crater's Zn. The crater's morphology, indicative of an impactor that was moving roughly perpendicular to the sample collector, also does not support a secondary impact from the spacecraft itself. Another possibility is that the Zn is the result of terrestrial contamination. Zn is known to be a low-level contaminant of the Stardust foils (~75 ppm), but it is not known whether the Zn is evenly distributed throughout the foil or if it appears as discrete Zn-rich inclusions similar to Fe-rich inclusions more commonly seen in the foils (Kearsley *et al*., 2007). Impact with a discrete Zn-rich inclusion could potentially lead to the high Zn abundances that we observe.

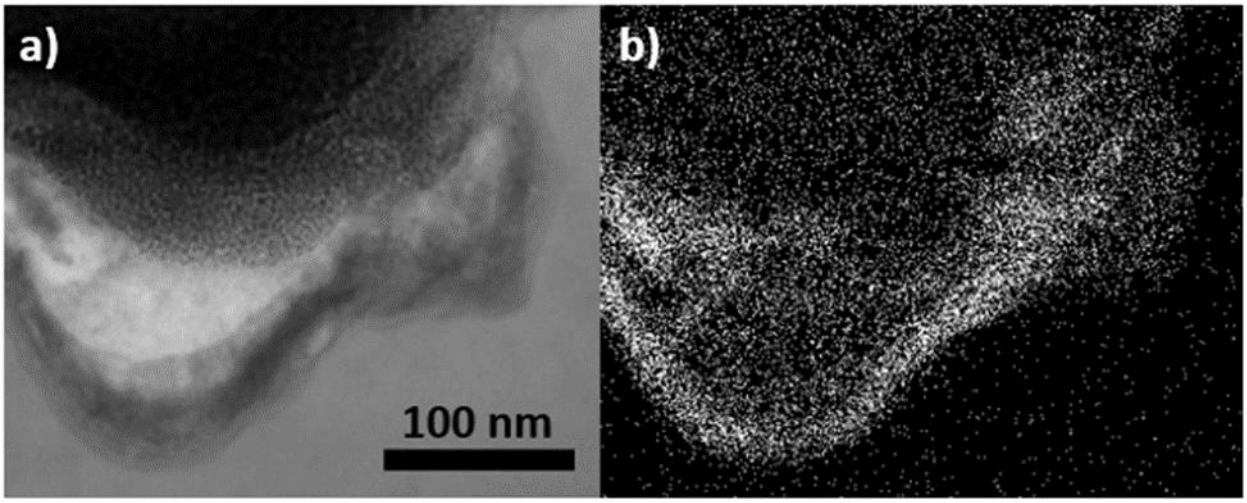

FIGURE 5.26: a) STEM bright-field image of crater #1 and b) STEM-EDXS Zn map of the same region.

Zn, though present in IDPs and collected Wild 2 materials, is not frequently a component of these materials. Non-random impact distributions within the Stardust cometary collector could

potentially explain the presence of Zn in each of our craters, which were only spread across a region of 5.28 mm^2. Clustering does appear in the Stardust collection media, with the most statistically significant results occuring on scales smaller than ~10 cm (Westphal *et al*., 2008). However, no hypothesis fully explains the observed clustering, making it difficult to assess why Zn was present throughout our crater residues. Zn's presence throughout our craters may also be the result of our study's small sample size, and further studies of the Stardust submicron impactors are necessary to accurately characterize the Zn component of the Wild 2 fine grains.

Ca was present in 4 out of 5 craters but was present only in small quantities (0.2-3.4 at. %). The source of this Ca is difficult to determine. Calcium–aluminum-rich inclusions (CAIs) have been found in the Stardust sample collector (Brownlee *et al*., 2006; Joswiak *et al*., 2017). Traces of Ti in craters 3 and 6 are both indicative of potential CAI impactors. Fassaite ($Ca(Mg,Ti,Al)(Si,Al)_2O_6$) and nanocrystalline osbornite (Ti(V)N) have both been observed in Stardust-collected CAIs (Chi *et al*., 2009). However, ubiquitous Al contamination makes positive identification of CAIs in the foil samples difficult.

Kosmocholoric Ca-rich pyroxene and olivine (Kool) grains have been commonly observed in Stardust aerogels as a source of cometary Ca (Joswiak *et al*., 2009). However, our low Mg abundances, coupled with our lack of Cr and Na, suggest an alternate source for the Ca observed in our craters.

Pyroxene grains are the most likely source for the observed Ca. Pyroxene grains have previously been observed and linked with Ca abundance in Stardust foil residues (Leroux *et al*., 2008), and low-Ca pyroxenes are common in the Stardust aerogel tracks (Jacob *et al*., 2009). Though the O/Si ratios are inconsistent with pyroxene as a whole, Si, O and Ca abundances allow for a portion of these elements to have been contributed by Ca-containing pyroxene impactors. Ca

concentrations in craters #2, #5, and #6 are low enough to have been fully contributed by low-Ca pyroxenes. Craters #1 and #5 have Ca/Si ratios greater than 0.2 and would require higher-Ca pyroxene impactors (e.g., pigeonite) that appear less commonly in the Stardust aerogel tracks (Jacob *et al*., 2009).

Our average crater residue compositions for craters #2, #3, #5, and #6 are shown in Figure 5.27 with our values normalized to Si and CI chondrite abundances (Lodders 2003). We also compare our results to meteorite Acfer 094's matrix as comet Wild 2 is believed to have experienced minimal thermal processing after accretion and Acfer 094 is known to have experienced minimal thermal processing (Grossman & Brearley, 2005). Overall our crater residues are Si- and Mg-poor relative to CI chondrites causing our craters to appear enriched in Fe, Ni, S, and Zn. Our craters also contained a higher proportion of iron-nickel sulfides and zinc sulfides relative to silicates when compared to Acfer 094 matrix material and CP IDPs. Zn was the most abundant element in our residues relative to CI chondrite abundances, with Zn/Si ratios normalized to CI abundances ranging from 52.7 to 594.3 in craters #2, #3, #5, and #6. S was the second most abundant element in these crater residues relative to CI chondrite abundances, with S/Si ratios normalized to CI abundances ranging from 2.9 to 7.5. Given the potential loss of volatiles during the capture process the impactors' Zn and S abundances may have been higher than measured (Wozniakiewicz *et al*., 2011).

Reports on S abundances in Wild 2 material have differed. Flynn's 2006 study focusing on full aerogel tracks (lengths of 250-10,000 μm) and large foil craters (diameters of 57-238 μm) observed that S was depleted relative to CI values whereas the chalcophilic elements Cu, Ga, and Zn were enriched. However, the study may have underestimated S in their fluorescence measurements due to the attenuation of S Kα X-rays in the sample. The size of the tracks and

craters also resulted in the majority of the studied Wild 2 mass originating from larger impactors. Westphal *et al*. (2009) studied fragments in Stardust aerogel tracks and observed an excess of Fe bound as iron sulfides compared to other major meteorite groups and no overall S depletions. However, the Westphal *et al*. (2009) measurements were bulk track measurements, mostly dominated by large terminal fragments.

Our measurements of high Zn and S abundances in small Wild 2 impactors support the hypothesis that Wild 2 fine material is not depleted in the moderately volatile elements relative to the bulk Solar System abundances. While the sample size is small, our crater compositions suggest that the fine component of Wild 2 is fundamentally different from its coarse component. Wild 2's coarse components typically have high-temperature origins and volatile element depletions, and appear to have formed far from where the parent body accreted (Brownlee *et al*., 2012). The small cometary impactors that produced the craters we studied appeared to be enriched in moderately volatile elements and likely did not have an igneous origin. However, our craters constitute only a fraction of the collected Wild 2 fines and a more comprehensive analysis of the fine impactors is necessary to fully characterize their volatile components.

5.5.4 Stardust Foil C2113N-A Conclusions

We extracted six submicron impact craters from Stardust foil C2113N-A. One crater was contaminated with a terrestrial source of Zn, another lacked any impactor residue, and the remaining four contained amorphous, glassy residue layers made up of a combination of silicate and sulfide impactors. Our crater residues, though potentially partially composed of GEMS materials, cannot be composed entirely of GEMS grains given our low amounts of Si and Mg relative to iron-nickel sulfide and zinc sulfide components (Keller & Messenger, 2011). Our

residues contain materials found in IDPs such as zinc sulfides, but are more sulfur rich than the majority of studied IDPs (Schramm *et al*., 1989).

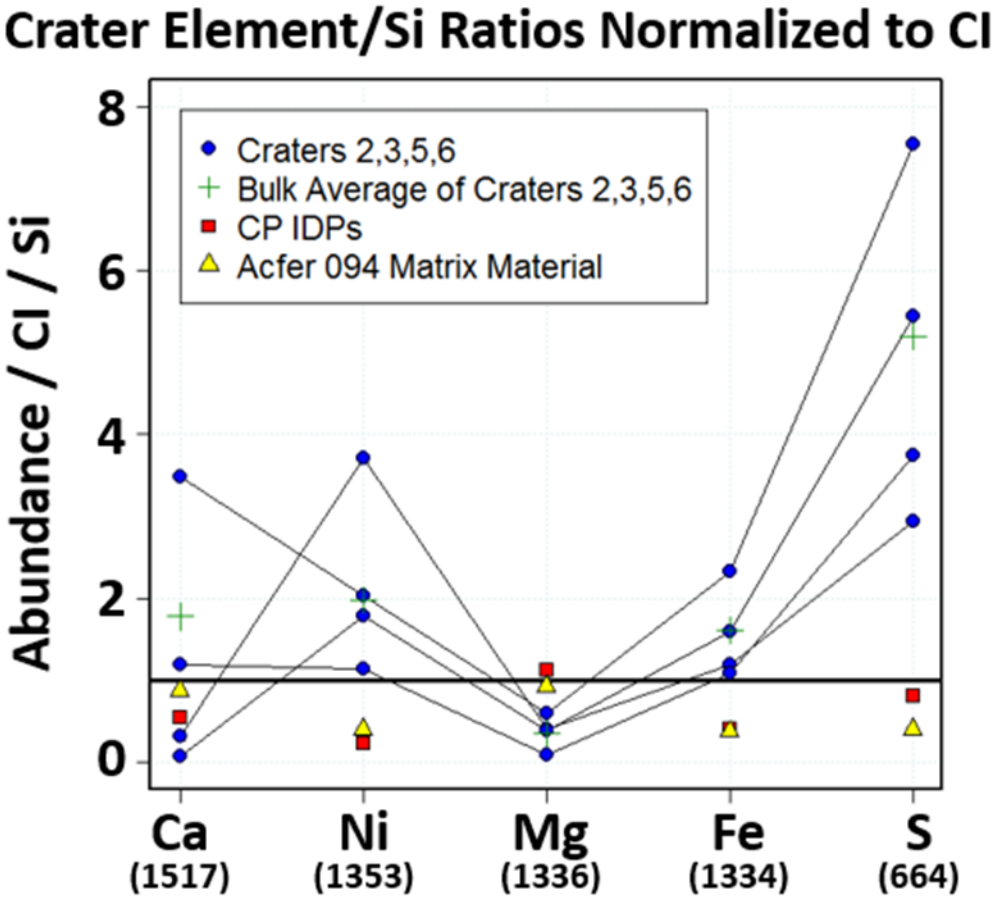

Figure 5.27: Element/Si ratios observed in craters #2, #3, #5, and #6 with results normalized to CI chondrite values (Lodders 2003). Values were calculated by summing each crater subregions' composition. Lines connect measurements from the same crater. Elements are listed in order of decreasing temperature values for 50% element condensation, listed in parentheses in Kelvin below each element (Lodders 2003). Also pictured are values from CP IDPs (Schramm *et al*., 1989) and Acfer 094 (ungrouped carbonaceous chondrite) matrix material (Grossman & Brearley, 2005). CI values are represented by the horizontal black line. Zn (not pictured) had values between 52.7 and 594.3.

The crater residues, excluding the contaminated crater, are enriched in S and Zn when normalized to Si and CI chondrite abundances. Though this study is a small sample size and may not be representative of the bulk comet, the material's enrichment in moderately volatile elements in the small-crater residue studied so far suggests that the Wild 2 fines did not form by igneous

processes, distinguishing the comet's fine component from the large terminal particles in aerogel tracks which mostly formed by high-temperature events.

5.6 Conclusions of the Stardust Foil Studies

Our analyses of the Stardust foils were split amongst three studies that encompassed four different foils. The first study focused on 11 craters on foil C2010W between 0.71-3.28 μm in diameter, the second study focused on 4 craters split across foils C2113N-B and C2118N-B between 1.5-4.8 μm in diameter, and the third study focused on 6 craters on foil C2113N-A between 0.20-0.35 μm in diameter. One crater was contaminated by Fe native to the foils, one of the craters was contaminated by terrestrial Zn, and one crater had no discernable residue layer.

The first study agreed with the limited previous investigations of Stardust foil craters of similar (micron-scale) sizes (Leroux *et al*., 2008; Leroux *et al*., 2010; Stroud *et al*., 2010) in many ways. Crater morphologies and residue distributions were similar to previously investigated Stardust craters. The craters' heterogeneous compositions indicated they were largely the result of aggregate impactors. The residues were dominated by Si- and Mg-rich materials consistent with either Si-rich minerals (e.g., olivine and pyroxene) or amorphous silicates (e.g., GEMS). Iron nickel sulfides were abundant in the craters and demonstrated limited volatile loss, and a lack of vesiculation in crater residues further indicated that our craters experienced similar amounts of alteration as previously investigated craters.

Our results differed from previous investigations primarily through our lack of surviving crystalline material. We observed no crystalline material in 10 uncontaminated craters whereas previous investigations found surviving crystalline material in 10 out of 22 craters of similar sizes (Leroux *et al*., 2008; Leroux *et al*., 2010; Stroud *et al*., 2010). We hypothesized that this was due to the craters resulting from similar impactors, as suggested by the high crater density on the foil

as well as impact clustering (Westphal *et al*., 2008) known to exist on the Stardust foils. The impactors were likely amorphous prior to impact given the lack of alteration in the craters, suggesting that amorphous materials such as GEMS constitute a larger portion of the Wild 2 fine component than previously thought. However, proving this is difficult given the impact conditions.

The second study, performed on foils C2113N-B and C2118N-B in order to eliminate any clustering effects, observed crater residues that were similar to the first study in many ways. The crater sizes were similar to first, as were the crater morphologies and residue distributions. Crater residues were dominated by Mg- and Si-rich materials consistent with olivine and pyroxene coupled with iron nickel sulfides showing limited S loss. The elemental abundances were also consistent with amorphous materials such as GEMS.

Two materials not observed in the first study may be present in the second, as subregions of two craters had regions elementally consistent with taenite and spinel. While both of these materials have previously been observed in Stardust aerogel studies, neither had previously been observed in micron-scale Stardust foil craters. These materials are more closely associated with refractory materials that formed in warmer environments than the outer Solar System, and indicate that some portion of the fine component of comet Wild 2 is composed of more refractory materials than olivinic silicates or iron sulfides. However, further studies capable of obtaining information about the crater residue's crystal structures are necessary to confirm these results.

The third study, performed on foil C2113N-A, investigated craters smaller (200-350 nm) than the previous studies in order to focus on impactors that likely experienced less alteration than their larger counterparts. One crater had no discernable residue layer, and one crater was contaminated by terrestrial Zn. The other four craters, similar to our previous results, contained

amorphous melt layers composed of a combination of Mg- and Si-rich materials and iron nickel sulfides. Additionally, no crystalline material was found. The lack of crystalline material again suggests that amorphous materials are a larger component of the Wild 2 fines than previously believed. However, the Fe/Si ratio in these craters was too large for the impactors to be composed of GEMS alone, though the melt layers were consistent with combinations of olivine, pyroxene, amorphous silicates (GEMS), iron nickel sulfides, and other O-rich components (e.g., iron oxides).

The crater residues were enriched in volatiles (S and Zn) when normalized to Si and CI chondrite abundances, suggesting that the Wild 2 fines didn't form by igneous processes, further distinguishing the comet's fine component from the coarse grains that have been heavily studied from the Stardust aerogels.

Overall, our studies probed 21 Stardust craters, nearly doubling the number that had been reported in previous investigations. 18 of these craters appeared to contain cometary residues. Our studies suggest that, unlike the coarse (>1 μm) component, much of the cometary fine (<1 μm) component is amorphous. The fraction of amorphous material in the fines is difficult to determine. Our earlier analog craters were far more altered than the Stardust foils and thus cannot help with estimating the crystalline component of the Wild 2 fines. However, previous investigations of the Stardust foils (Leroux *et al*., 2008; Leroux *et al*., 2010; Stroud *et al*., 2010), which identified surviving crystalline material in 10 out of 22 investigated craters, likely overrepresented the fraction of Stardust craters containing crystalline fine grains.

The abundance of volatiles in our submicron craters further separate our results from the coarse grains of previous Stardust studies. The enrichment of these craters in moderately volatile elements indicates that the material was not formed by igneous processes. However, we also

identified what appear to be taenite and spinel grains within the residues of two of the investigated craters, indicating that the fine component contains heated, refractory phases as well.

Our studies, though nearly doubling the number of investigated micron-scale Stardust foil craters, still represent a small fraction of the collected Wild 2 fine material and an even smaller fraction of the Wild 2 fines. Additionally, the high temperatures and pressures reached by the collected materials make it difficult to definitively identify many features of the Wild 2 fines (e.g., crystallinity). Further investigation of the Stardust foils would aid in determining the bulk composition of the Wild 2 fines with better statistical precision, and as a result would help with determining the provenance of primordial dust in the Solar System.

Chapter 6: Stardust Interstellar Foils

6.1 Preface

Adapted from the conference abstract:

Haas B. A., Stroud R. M., & Floss C. (**2017**), "FIB/STEM Study of 2 Stardust ISPE Craters from foil 1031N,1", in "80th Annual Meeting of the Meteoritical Society", Abstract #6316, URL https://www.hou.usra.edu/meetings/metsoc2017/pdf/6316.pdf.

6.2 Introduction

The Stardust interstellar foils, though identical in construction to the cometary foils, aimed to collect very different particles. The Stardust Interstellar Dust Collector was exposed to the interstellar dust (ISD) stream for 195 days in 2000 and 2002 with the goal of collecting ISPs while en route to comet Wild 2 (Westphal *et al*., 2014a). However, the low flux of ISD (only ~120 ISPs were expected to impact the Stardust Interstellar Dust Collector), the small size of the ISD particles (two thirds of the particles were expected to be less than 2 microns in diameter), and the extremely high collection speeds (> 20 km/s) made analysis of the interstellar foils difficult (Stroud *et al*., 2014).

The Stardust Interstellar Preliminary Examination (ISPE) successfully identified 25 craters on the aluminum foils with secondary electron imaging in SEMs, four of which were found to have likely resulted from ISD impactors based upon their elemental composition and crater morphologies (Westphal *et al*., 2014c). Two asymmetric sub-micron craters from foil 1031N,1 (216@45 and 239@11) and one circular sub-micron crater from foil 1061N,1 (022@44) appeared to be promising candidates for containing ISD (Floss *et al*., 2011). The three craters were analyzed with Auger spectroscopy. All three craters had Mg and Si signals in addition to the Al, C, and O signals seen in all studied craters (Figure 6.1) (Stroud *et al*., 2014). Carbon present in the spectra was likely due to the presence of a thin layer of organic contamination known to build up on the

foils, particularly after exposure to the electron beam in oil-pumped SEMs (Kearsley *et al*., 2008). The collected Auger spectra could not verify that the impactors were interstellar in origin with Mg and Si signatures alone (Stroud *et al*., 2014). Through collaboration with Rhonda Stroud at NRL, I performed FIB/STEM analysis of the craters in order to obtain higher resolution elemental characterization of the crater residues. STEM analysis of the crater residues has improved sensitivity relative to Auger spectroscopy studies, allowing for the detection of minor elements that can clarify the origins of the foil impactors.

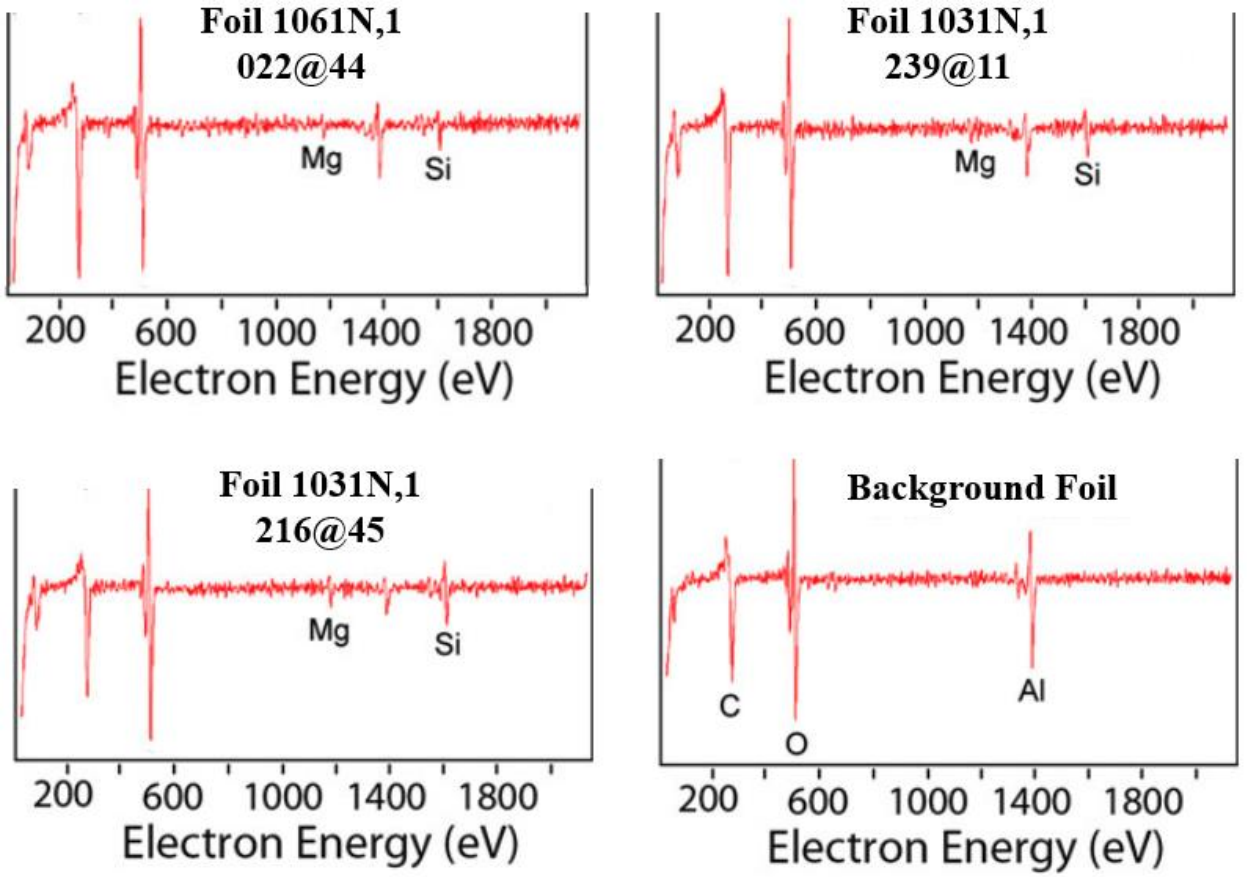

FIGURE 6.1: Numerical derivatives of Auger spectra of craters 022@44 on foil 1061N,1, 239@11 on foil 1031N,1, and 216@45 on foil 1031N,1, taken from Figure 9 in Stroud *et al*. (2014). A spectrum collected from the background foil is shown as a reference. Auger spectra were acquired using a 10 kV, 10 nA beam over an energy range of 30-2130 eV. While Mg and Si were identified in all three craters (in addition to Al, C, and O), the lack of additional elemental spectra prevented definitive charcterization of the crater impactors as interstellar or terrestrial (e.g., material from the spacecraft itself).

6.3 Experimental Methods

The initial identification of the craters with SE imaging was performed with a JEOL 840a SEM equipped with Noran System Seven software (Floss *et al*., 2011). Verification of the crater candidates, as well as elemental characterization of the residues within the craters (Figure 6.1), was performed with the PHI 700 Auger Nanoprobe at Washington University.

Cross sections of the craters were prepared and extracted with a FEI Nova 600 FIB-SEM at NRL. The craters were covered in a protective carbon coating and thinned to 100-150 nm to preserve sufficient material for potential future isotope analyses. High-resolution bright-field and HAADF images of the crater cross sections and EDXS maps of the crater residues were collected using a Nion UltraSTEM 200 aberration-corrected STEM operated at 200 KeV at NRL. Elemental quantification of the STEM-collected EDXS spectra was performed with Cliff-Lorimer routines.

6.4 Results

When searching foil 1061N,1 it immediately became apparent that crater 022@44 had already been lifted out and removed from the foil with FIB techniques (Figure 6.2). The result was a surprise as all literature regarding the crater and the foil (Floss *et al*., 2011; Stroud *et al*., 2014) noted that the crater had not been extracted following its identification and elemental characterization. The most likely scenario is that FIB extraction was attempted during the ISPE and the FIB process failed following the extraction of the crater cross section from the foil. The study of the crater's cross section was thus never conducted, and the status of the crater may not have been appropriately updated as a result.

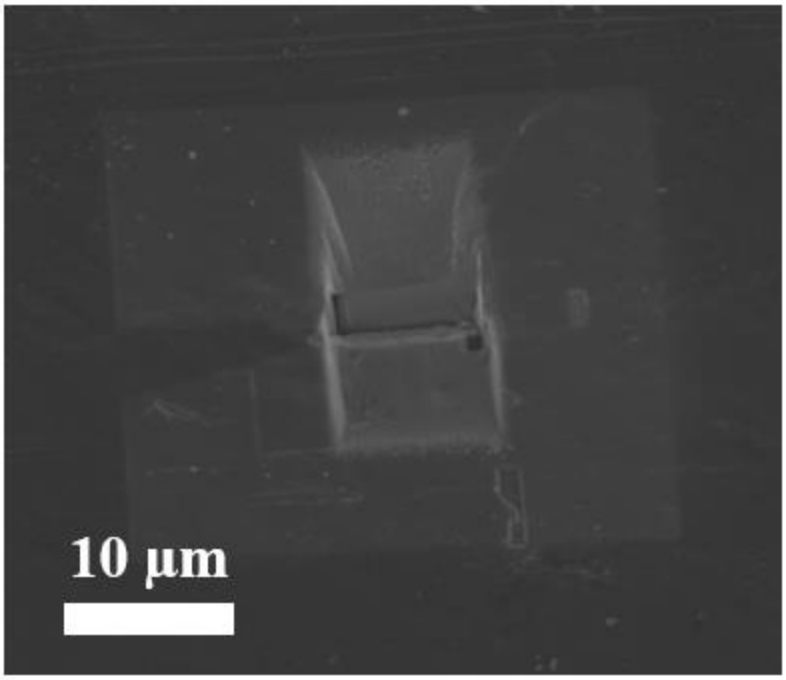

FIGURE 6.2: FIB-SEM image of crater 022@44 on foil 1061N,1 at the time I inspected the foil. The crater had previously been removed with FIB techniques, though the ISPE noted that the crater should still be present on the foil (Stroud *et al*., 2014).

Craters 216@45 and 239@11 were both still present on foil 1031N,1. Crater 216@45 was shallow, with a bowl-shaped bottom that suggested that the impactor was a compact object (Figure 6.3). The crater's diameter, measured from the inside of the crater lips, was 650 nm, while the crater's depth, measured from the top of the crater to the deepest location of the protective C cap, was 270 nm, resulting in a depth/diameter ratio of 0.42. Crater 239@11 was similarly shallow and bowl-shaped, with a diameter of 675 nm and a depth of 260 nm, resulting in a depth/diameter ratio of 0.39 (Figure 6.3). The depth to diameter ratios were smaller than expected. Previously investigated Stardust craters and analogs fired at ~6.1 km/s both saw depth/diameter ratios consistently larger than 0.5 even for low density impactors in the analog foils (Kearsley *et al*., 2007; Leroux *et al*., 2008). However, depth/diameter ratios can be affected by a variety of factors, such as the angle of incidence of the impactor, the density of the impactor, the impact velocity, and the impactor's volatile contents, and thus the depth/diameter ratios alone are not enough to

characterize the impactors as the result of secondary impactors originating from the spacecraft itself (Kearsley *et al*., 2008; Price *et al*., 2012).

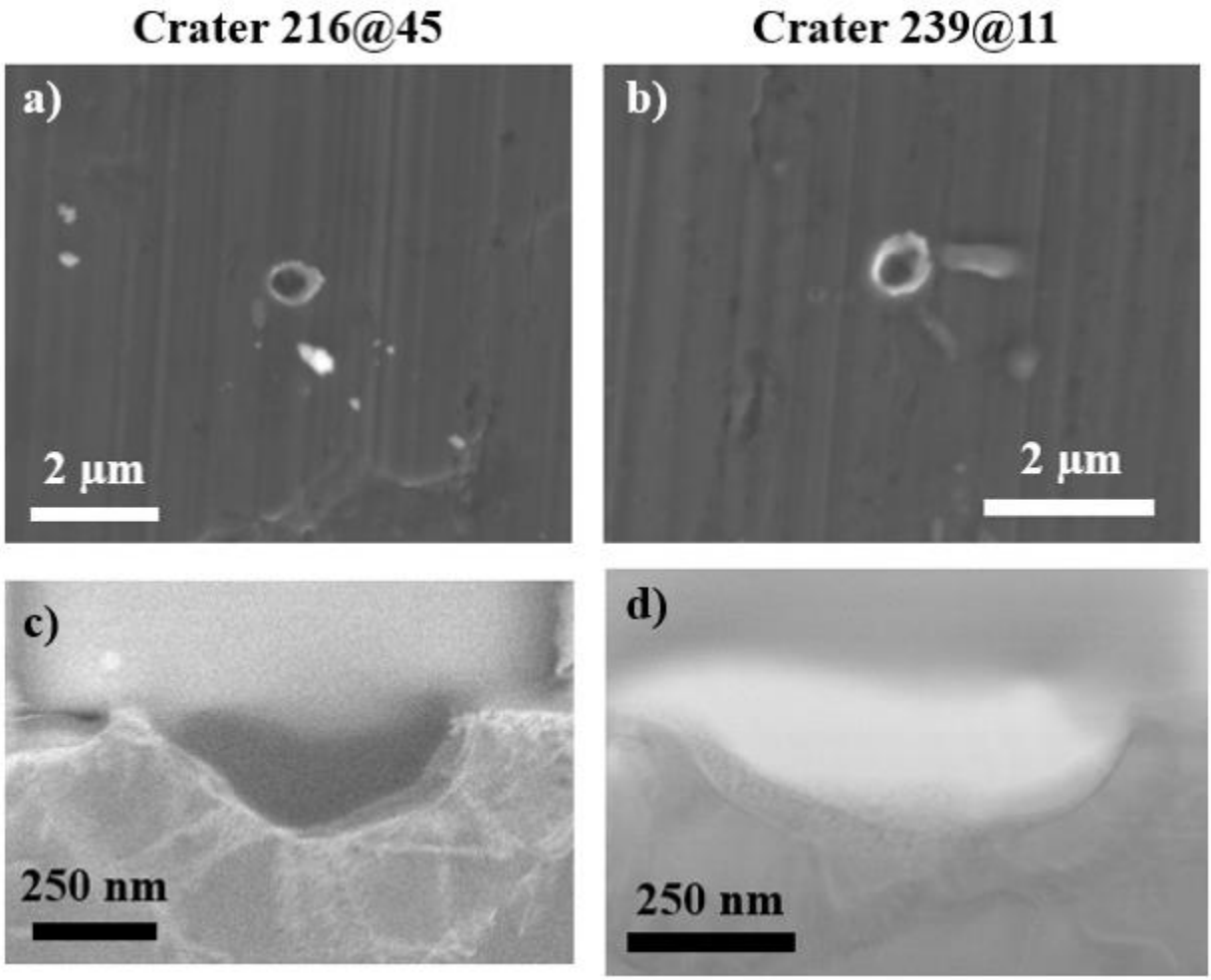

FIGURE 6.3: Secondary electron images of craters a) 216@45 and b) 239@11 prior to extraction above STEM medium angle annular dark-field images (MAADF) of craters c) 216@45 and d) 239@11 collected after FIB preparation.

Thin impactor melt layers were present in the crater bottoms, with the residue thickness varying from 10 to 50 nm, depending on the location within the craters. Asymmetry in the crater shapes was reflected in the melt layer distributions, with melt being more prevalent on one side of each crater. Asymmetry in the crater shapes can result from oblique impacts or a highly nonspherical impactor (Stroud *et al*., 2014).

STEM-EDXS mapping characterized the elemental makeup of the crater residues with Cliff-Lorimer analysis (Table 6.1). Al and C were excluded from the quantification of the elemental makeup of the residue due to the elements' presence in the foil substrate and the protective cap deposited during FIB preparation, respectively. O, Si, and Mg were abundant in the crater residues, conforming with the earlier characterization of the crater residues with Auger spectroscopy. The Si/Mg ratios in both craters were large, with values for crater 216@45 and 239@11 being 5.4 and 4.1, respectively. Fe and Pt were observed in crater 239@11, along with trace (< 0.2 at. %) Ti. Crater 216@45 also contained significant F (6.3 at. %), and crater 239@11 contained significant Ce (0.5 at. %).

TABLE 6.1: Elemental composition of craters 216@45 and 239@11 in atomic %, excluding C and Al, with uncertainty (3 sigma). Not detected is denoted by 'n.d.' and not available is denoted by 'n.a'. Al and C were excluded due to their presence in the foil substrate and the protective cap deposited during FIB preparation, respectively.

Element	**Crater 216@45**		**Crater 239@11**	
	Atomic %	**3 Sigma %**	**Atomic %**	**3 Sigma %**
Oxygen	58.8	2.6	60.3	1.1
Silicon	29.4	2.3	30.1	1.0
Magnesium	5.4	1.1	7.3	0.9
Iron	n.d.	n.a.	0.9	0.4
Platinum	n.d.	n.a.	0.9	2.6
Fluorine	6.3	1.2	n.d.	n.a.
Cerium	n.d.	n.a.	0.5	1.1

6.5 Discussion

The presence of Ce and F within the crater residues, along with the asymmetric crater shapes and small depth/diameter ratios, indicates that the impactors that produced these craters are the result of secondary ejecta produced by micrometeoroid impact to the spacecraft's solar cells rather than the result of ISD.

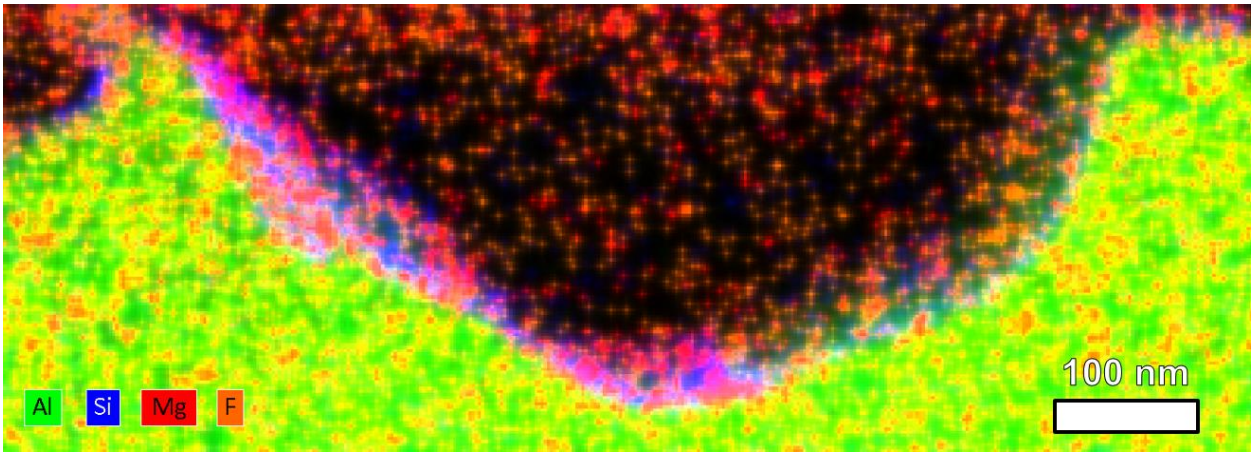

FIGURE 6.4: STEM-EDXS map of Al, Si, Mg, and F in crater 216@45. The map is created by additively combining pixel color values for each element. Pixel locations are determined through peak heights at each location rather than background-normalized counts. The asymmetric residue layer is only present on the left side of the crater. F is present within the crater residues, indicating that the crater is likely the result of terrestrial contamination rather than ISD.

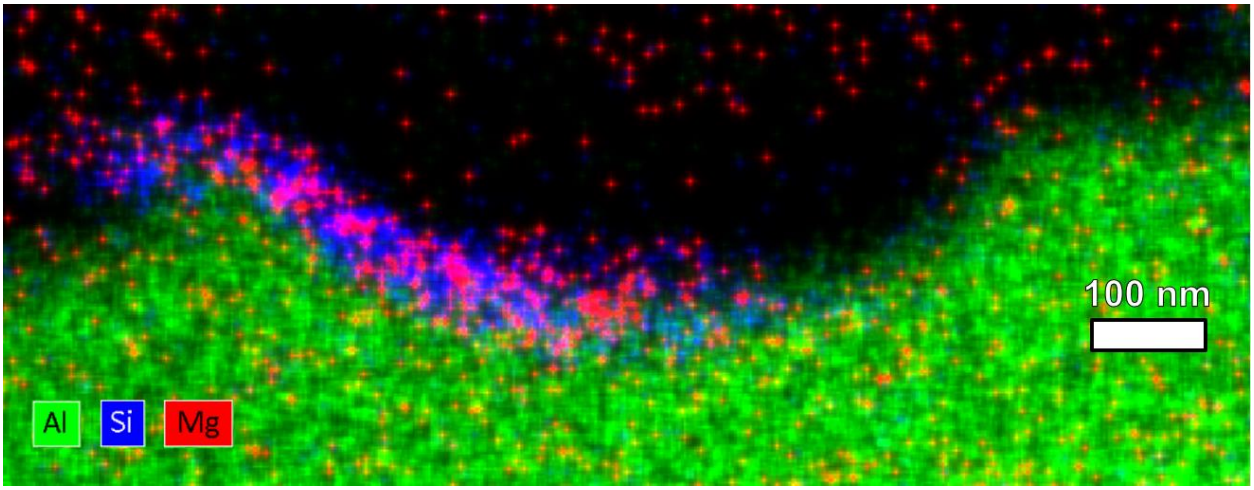

FIGURE 6.5: STEM-EDXS map of Al, Si, and Mg in crater 239@11. The asymmetric residue layer is only present on the left side of the crater. Ce was identified in the crater residues, though the Ce concentration was too weak to view in the EDXS maps of the crater. The presence of Ce in the crater indicates the crater is the result of terrestrial contamination rather than ISD.

Crater asymmetry alone is not proof that the craters were created by a secondary impactor. Studies of analog foils have demonstrated that asymmetric craters can form from an oblique impact or a normal incidence impact of a particle with a highly non-spherical shape (e.g., a whisker or aggregate grain) (Kearsley *et al*., 2008). Similarly, small crater depth/dimeter ratios are not proof of a secondary impactor. The interstellar foils were expected to collect higher velocity impactors

than the cometary foils (~20 km s^{-1} versus 6.1 km s^{-1}) and higher velocity impactors have been shown to produce deeper craters (Stroud *et al*., 2014). Studied cometary craters showed larger depth/diameter ratios exceeding 0.5 (Leroux *et al*., 2008) compared to our values of 0.42 and 0.39 for craters 216@45 and 239@11, respectively. However, crater depth is a function of impact velocity, particle composition, density, and simple or aggregate particle structures, so depth/diameter ratios alone cannot prove that the crater was the result of a secondary impactor (Stroud *et al*., 2014).

The crater compositions, coupled with the crater shapes, suggest that the craters are the result of secondary impacts from micrometeoroid impacts on the Stardust spacecraft. The Stardust solar cell cover glass most widely used for space-exposure is rich in O and Si, with a few weight % of Na, K, Ti, Zn, and Ce (Burchell *et al*., 2012). Additionally, the glass had a thin magnesium fluoride coating several tens of nanometers thick (Burchell *et al*., 2012). Residues resulting from secondary solar cell array fragments can vary greatly in composition depending on the ratio of antireflection (Mg-containing) coating to solar cell cover glass. However, Ce and F are known components of Stardust solar cell glass and are not expected to be detected in the amounts observed in our craters assuming they came from ISD (Stroud *et al*., 2014). Additionally, Ti, though only detected as a trace element in crater 239@11 and a possible component of ISD, is also a known component of the Stardust solar cell cover glass. These results, coupled with the crater shapes, indicate the craters are likely the result of a secondary impact with the Stardust solar cells. ISD or other material likely impacted the Stardust solar cells, ejecting a small piece of the solar cell cover glass as well as the antireflection coating. This material then impacted the interstellar foils, resulting in the asymmetric, shallow craters that contain Fe, Ce, and Ti in addition the O, Si, and Mg.

The discovery that the craters are the result of secondary impactors is not unexpected. Preliminary imaging of the interstellar foils showed that the abundance of observed craters is roughly 50 to 100 times the expected value for interstellar particle impacts on the foils (Stroud *et al*., 2011; Landgraf *et al*., 1999). These results raise the number of ISPE craters caused by solar cell secondary impacts to 13 out of 25, demonstrating the difficulty in studying the Stardust Interstellar Dust Collector foils (Stroud *et al*., 2014).

Chapter 7: Analog and Stardust Aerogels

7.1 Preface

Adapted from two conference abstracts:

Haas B. A., Ogliore R. C., & Floss C. (**2017**), "Application of Plasma Ashing to the Study of Stardust Mission Aerogel Samples", in "48th Lunar and Planetary Science Conference", Abstract #2058, Lunar and Planetary Institute, Houston, URL https://www.hou.usra.edu/meetings/lpsc2017/pdf/2058.pdf.

Haas B. A., Ogliore R. C., Westphal A. J., Croat T. K., & Floss C. (**2018**), "Study of Fine-Grained Material Recovered from a Stardust Aerogel Track Using Plasma Asher Preparation", in "49th Lunar and Planetary Science Conference", Abstract #2245, Lunar and Planetary Institute, Houston, URL https://www.hou.usra.edu/meetings/lpsc2018/pdf/2245.pdf.

7.2 Introduction

The Stardust spacecraft's aerogel tiles were successful at decelerating and capturing cometary material, but fine grains (< 1 μm) captured by the aerogel have proven difficult to study. Coarse (> 1 μm) grains in the aerogels frequently appear as terminal grains at the ends of aerogel tracks, and can be extracted using an automated keystone system (Westphal *et al*., 2004). The fine grains captured by the aerogels were frequently spread across bulbous impact features, and the insulating nature of the aerogels complicate in situ analysis of cometary materials with electron microscopy techniques (Burchell *et al*., 2008a). As a result, the fine component of comet Wild 2 has not been well-characterized in the Stardust aerogels.

Selectively removing the aerogel, while minimizing damage to the collected cometary material, would greatly simplify the study of the fine cometary grains spread throughout the aerogel tracks. Etching with HF liquid has frequently been used to remove Si-rich material, thus isolating organic material, from chondritic material (Amari *et al*., 1994). Previous attempts to destroy the aerogels utilized HF vapor etching as a means of bonding F atoms with Si atoms in

aerogel to form SiF_4, a relatively inert gas at room temperature, in order to destroy the aerogel and free the collected cometary material (Westphal *et al*., 2004b). HF etching was successful in destroying the Stardust aerogels and freeing collected cometary materials. However, this technique resulted in a liquid drop forming around the etched material that was likely the result of 4 HF molecules combining with a SiO_2 molecule to from SiF_4 alongside 2 water molecules (Westphal *et al*., 2004b). The formation of a water droplet with this technique discouraged further use, as aqueous alteration, dispersal of cometary materials in the water droplet, and the formation of silicic acid (SiF_4 decomposes into silicic acid and HF in water) near the cometary materials all threatened to alter the freed cometary materials.

Plasma ashing aims to replicate the success of the HF vapor etching technique while minimizing alteration to the collected cometary materials. The plasma asher draws a carrier gas (CF_4) over the sample and RF power, provided by a crystal-controlled oscillator at 13.56 MHz, ionizes the gas under vacuum, creating a plasma of CF_3^+ and F^- ions. Similar to previous techniques, F ions combine with Si atoms forming SiF_4. However, the procedure is performed under vacuum and does not suffer from the buildup of a vapor drop that discouraged the use of HF vapor etching. Thus, the plasma ashing technique that we have developed aims to improve upon previous methods for freeing collected cometary material from the Stardust aerogels.

The plasma ashing described in this chapter was performed using Washington University's SPI Plasma Prep II Etcher/Asher.

7.3 Studies of Plasma Ashing Effects on Sample Materials

Prior to ashing authentic Stardust aerogels, we aimed to test the ashing technique on materials similar to the aerogel as well as potential cometary materials captured by the aerogels. Additionally, we aimed to create a sample holder that would house the delicate aerogels while still

allowing for ashing to occur and minimizing contamination from F plasma interactions with other materials present in the sample holder. The sample holder setup is shown in chapter 3.5 of this thesis. The idea behind the sample holder was to mount the aerogel sample directly onto a TEM grid to allow direct deposition of the collected cometary material onto the sample analysis medium. We used a Si_3N_4 window to contain the aerogel during transportation while providing a barrier breachable by F^- plasma. This setup simplifies sample transportation and analysis by minimizing the number of times the sample needs to be transferred from one sample holder to another.

7.3.1 Tests of Sample Holder Materials

Initial tests of the asher focused on the sample chamber itself. Many ashers utilize a sample chamber made of borosilicate glass because this material is cheap and easy to manufacture. Borosilicate glass is an effective sample chamber with some carrier gases (e.g., O_2), however we quickly noted that borosilicate glass is slowly degraded by ashing when using CF_4 as a carrier gas. The borosilicate glass became cloudy over time and left a white, ashy substance in the sample chamber. Si within the borosilicate glass reacts with F^- ions created by the plasma, creating SiF_4 and slowly degrading the sample chamber. In order to prevent potential contamination resulting from degradation to the sample chamber, we purchased a quartz (SiO_2) sample chamber to be used in the asher. Despite also containing Si, quartz's combination of hardness, high wear resistance, dielectric strength, high corrosion resistance, and chemical stability has made quartz a valued material in the plasma etching and semiconductor industries (Wang *et al*., 2018). The quartz sample chamber has shown no visible degradation after use with CF_4 and O_2 carrier gases and minimizes potential contamination to Stardust samples.

The sample holders also needed to be F^- plasma resistant in order to minimize contamination to the collected cometary materials. Many stubs we used for mounting materials

for SEM study are composed of stainless steel with gold-plated tops that the samples rest on. However, initial tests discovered that neither of these materials were appropriate for plasma ashing studies. Stainless steel appeared to suffer minor damage to its surface, possibly due to the presence of small (a few % by weight) amounts of Si in the material. Gold also reacted with the F plasma, forming gold fluoride, thus damaging and contaminating the surface of the SEM stub. I also observed that formvar, a thermoplastic resin frequently used to strengthen carbon meshes in between copper TEM grids, reacted with the F^- plasma, resulting in the destruction of the TEM grid mesh. As a result, TEM grids with formvar-strengthened meshes could not be used in the plasma asher.

Several materials were unaffected by the F^- plasma. I tested copper metal from Auger spectrometer sample holders as well as from TEM grids. Copper did not react with the F plasma. As a result, we constructed our sample holders, detailed in Chapter 3.5 of this thesis, out of copper. Additionally, I observed that the pure carbon meshes between TEM grids were unaffected by F^- plasma, allowing them to be used to capture deposited cometary materials for TEM analysis.

7.3.2 Tests of Analog Materials

In order to ensure that cometary materials could survive the ashing process, as well as guarantee destruction of the Stardust aerogels, we conducted tests on several analog materials. While meteoritic materials such as iron sulfides are known to be unaffected by fluorine ions, silicates (e.g., olivine and pyroxene) suffer damage from Si atoms combining with F ions to create SiF_4 (Amari *et al.*, 1994). We first aimed to ensure that silicates such as olivine would be capable of surviving the ashing process. We ashed San Carlos olivine (~$Fo_{90.1}$) at 17.2 kPa for an hour in order to observe full destruction of ~10 μm^3 grains (Figure 7.1). Significantly shorter ashing times, on the timescale of several minutes, should allow for the survival of micron-scale silicates.

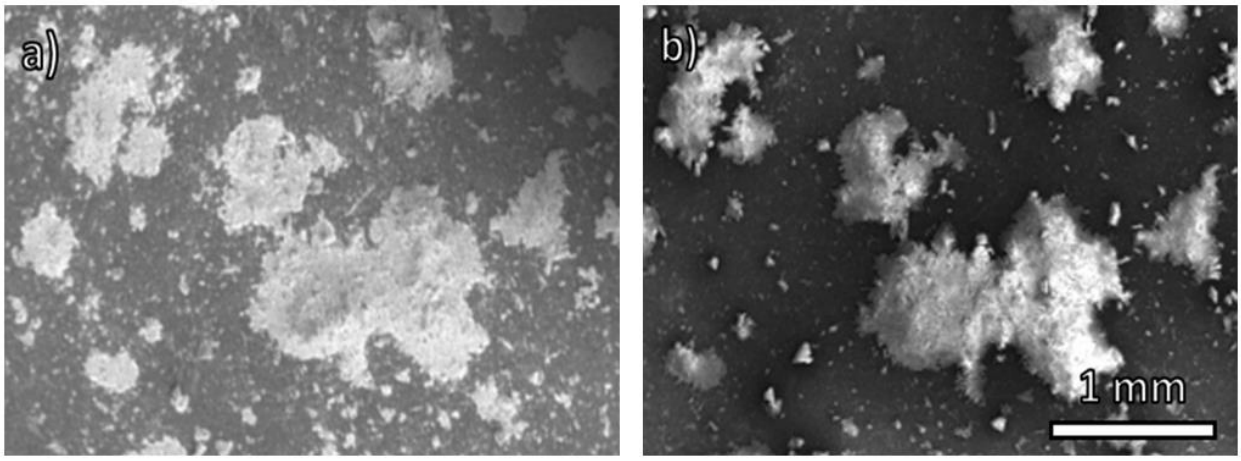

FIGURE 7.1: Secondary electron images of San Carlos olivine grains a) before and b) after exposure to F plasma at 17.2 kPa for one hour. Grains ~10 μm^3 in size were fully ashed within this time while larger grains survived.

In order to ensure that cometary material from the fine component of the comet could survive the ashing process, we performed additional tests on a variety of minerals, including calcite ($CaCO_3$), plagioclase ($NaAlSi_3O_8$ – $CaAl_2Si_2O_8$), dolomite ($CaMg[CO_3]_2$), hematite (Fe_2O_3), magnetite (Fe_3O_4), and San Carlos olivine (40.8% SiO_2, 9.5% FeO, and 49.4% MgO atomically). Each of these minerals were powdered with a mortar and pestle and placed on a TEM grid before being ashed for 5 minutes at 17.2 kPa. The materials were viewed and elementally characterized in Washington University's JEOL 2000FX TEM both before and after the ashing process. Hematite and magnetite showed no alteration, as expected. Calcite, plagioclase, dolomite, and San Carlos olivine all showed minor alteration on the scale of tens of nanometers, indicating that they should survive the ashing process so long as ashing times are sufficiently low. Additionally, minor F contamination (several atom. %) was present within these materials. Thus, it appeared that cometary material freed from the aerogels would likely be able to survive the ashing process.

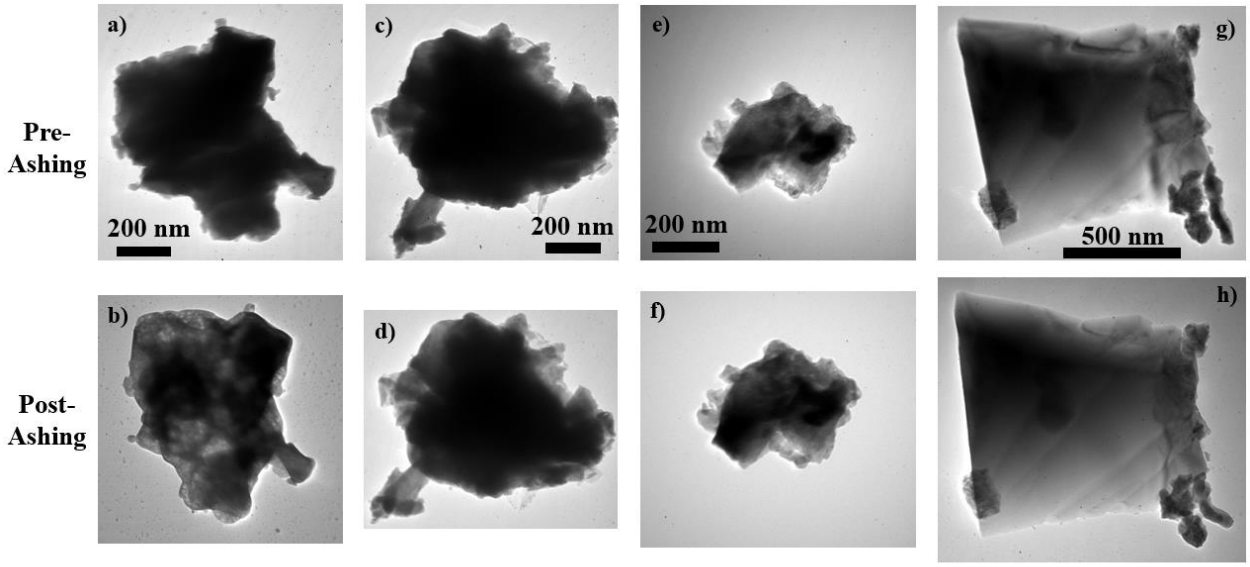

FIGURE 7.2: TEM bright-field images of mineral grains before and after 5 minutes of exposure to F^- plasma at 17.2 kPa. Most grains, even olivine, showed minimal alteration, indicating that captured cometary material in the Stardust aerogels should survive the ashing process.

We also tested the effect of O plasma (O^+ and O^-) on carbonaceous materials. O plasma, resulting from using O_2 as a carrier gas instead of CF_4, has no effect on silicate materials, but proved extremely efficient at destroying carbonates. C contamination is known to exist within the Stardust aerogels, with C composing 0.1-0.5% of the aerogels by weight (Burchell *et al*., 2006). We conducted tests on 98.0% pure graphite grains (Figure 7.3). We observed full destruction of grains less than ~5.0 μm in diameter after 30 minutes of exposure to O plasma at 17.2 kPa. Thus, O plasma was effective at destroying carbonaceous terrestrial contamination. However, O plasma also destroys the carbon mesh on TEM grids, preventing direct deposition of cometary materials onto TEM grids for study if this step were taken. Additionally, any carbonaceous materials collected from the comet would also be destroyed. Thus, while O plasma could be effective for removing carbonaceous contamination in future studies focusing on other materials present in the comet (e.g., silicates), it was not used throughout this study.

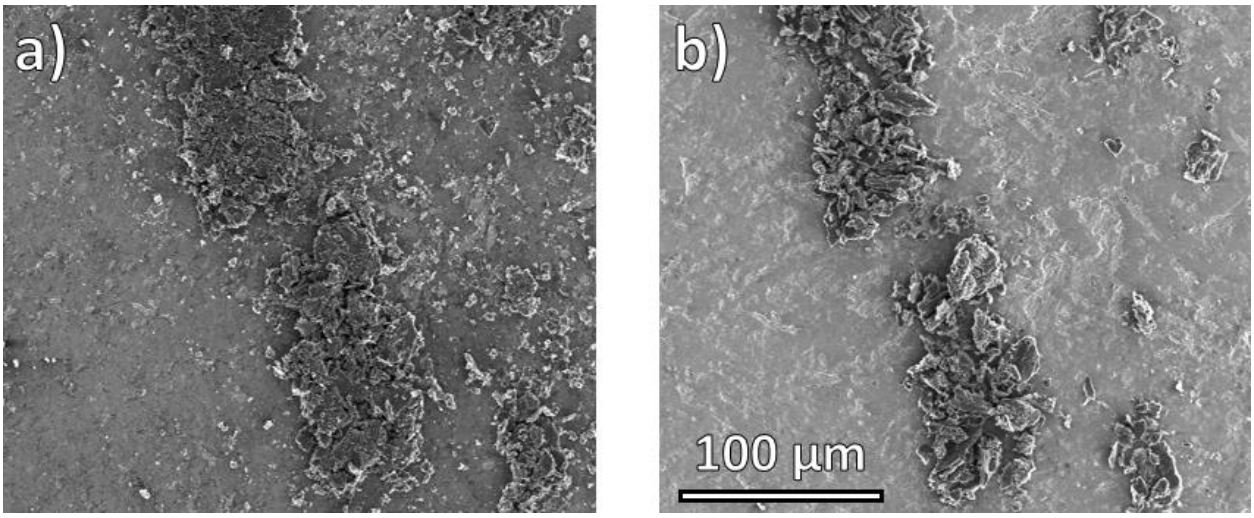

FIGURE 7.3: SEM images of graphite grains a) before and b) after exposure to O plasma at 17.2 kPa for 30 minutes.

We also tested the effect of F plasma on silica aerogel similar in composition to the aerogels used on the Stardust sample collector. Determining the ashing rate of the aerogels was difficult. The aerogel is extremely porous, with over 98% of the volume composed of ambient gases (Burchell *et al*., 2006). As a result, the aerogel has an extremely large effective surface area, allowing it to ash far quicker than denser materials such as the previously tested San Carlos olivine. As aerogel is ashed it undergoes homologous collapse, greatly decreasing in size while losing porosity (Figure 7.4). This behavior has also been noted in previous HF vapor etching experiments (Westphal *et al*., 2004b). The aerogel's initially large surface area decreases extremely quickly and ashing rates greatly decrease with time. Thus, aerogel particles of nearly all sizes are ashed in similar time frames, with a small, concentrated portion of aerogel remaining afterwards (Figure 7.4). Additional ashing once the aerogel has undergone homologous collapse will slowly destroy the remaining aerogel, but will also damage any freed materials that have since escaped from the ashed material. Our tests found ashing times of roughly 7 minutes (at 17.2 kPa) resulted in destruction of most of the aerogel before additional ashing had minimal effect on the condensed, remaining aerogel. Thus, in our later studies of Stardust aerogels we aimed for roughly 7 minutes

of F plasma exposure in order to destroy the aerogels while minimizing damage to freed silicate particles.

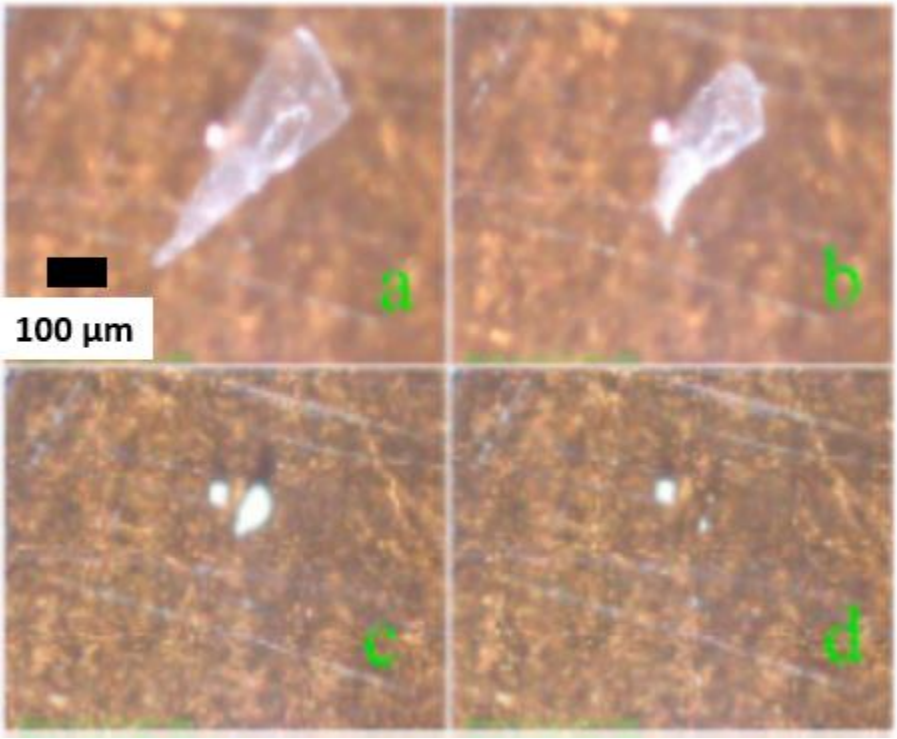

FIGURE 7.4: Figure 1 from Westphal *et al*., (2004b). The images show the homologous collapse of an aerogel keystone over time when destroyed with HF vapor etching: a) The keystone before etching, b) the beginning of homologous collapse, c) the end of the first phase of homologous collapse, and d) the final aerogel residue.

The final analog test we performed was on an analog aerogel that contained spinel grains in order to test the procedure on material similar to the Stardust aerogels. We ashed the aerogel for 10 minutes at 17.2 kPa on top of a TEM grid beneath a protective Si_3N_4 window. The Si_3N_4 window ashed after ~3 minutes, resulting in the aerogel experiencing 7 minutes of exposure time to the F plasma. We identified intact spinel grains on the TEM grid following completion of the ashing process (Figure 7.5), indicating that materials contained within the aerogels are capable of being freed and deposited onto the TEM grids.

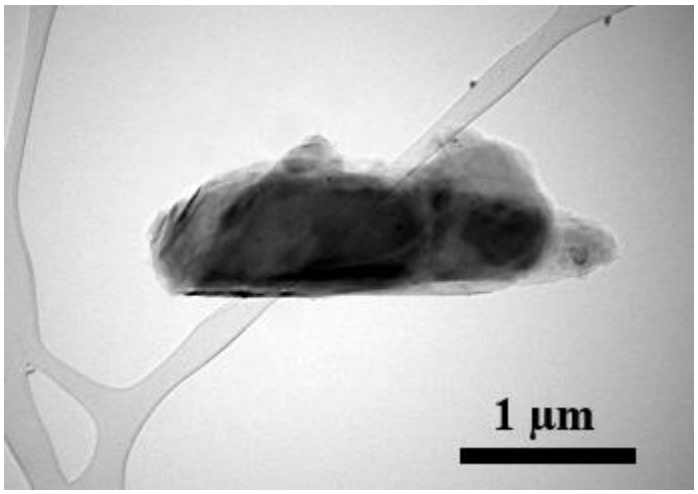

FIGURE 7.5: TEM bright-field image of a surviving spinel grain deposited onto a TEM grid following the plasma ashing of a spinel-containing analog Stardust aerogel.

7.4 Stardust Aerogel Track 35 Bulb Section

Following the success of the analog experiments performed with the plasma asher, we began the study of Stardust aerogels. The first aerogel that we studied was a section of the bulb of track 35 (allocation number C2054,44,35,0,0). Track 35 is one of the largest tracks in the Stardust aerogels, with a length of 11.7 mm and a bulbous shape. The bulbous shape of the track suggested that the original impacting particle was made up of fine grained, volatile-rich material, making the track a good candidate for study with plasma ashing (Caro *et al*., 2008).

7.4.1 Stardust Aerogel Track 35 Sample Preparation and Methods

The aerogel was prepared in the sample holder described in Chapter 3.5 of this thesis by Andrew Westphal at the University of California, Berkeley before it was transported to Washington University for ashing. The aerogel track was ashed for 10 minutes at 17.2 kPa (Figure 7.6). The initial ~3 minutes of the ashing duration was necessary for the penetration of the protective Si_3N_4 window, resulting in ~7 minutes of F plasma exposure to the aerogel sample. The sample underwent homologous collapse as expected from the results of previous HF etching studies (Figure 7.4). Material from the aerogel was deposited directly onto a TEM grid during the

ashing process. TEM investigations were performed on Washington University's JEOL 2000FX TEM.

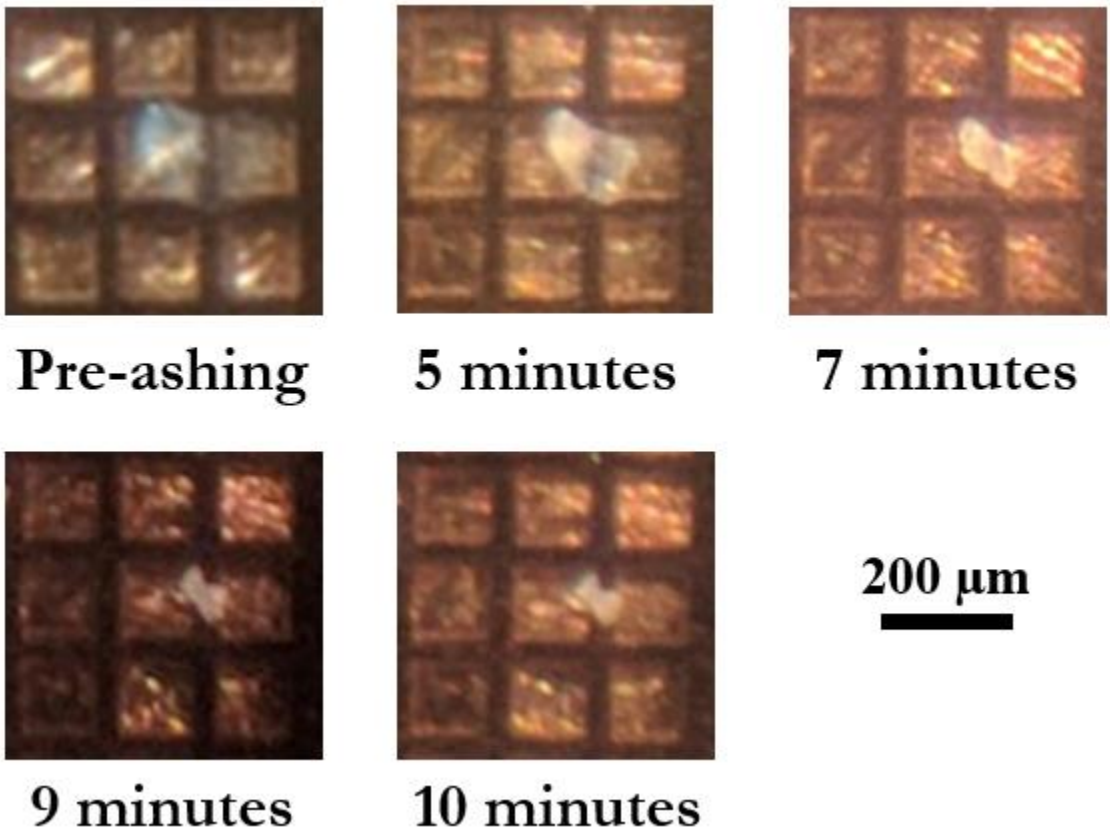

FIGURE 7.6: Ashing progression on the bulb section of aerogel track 35 (allocation number C2054,44,35,0,0). The initial ~3 minutes were required to penetrate the protective Si_3N_4 window containing the aerogel sample. The sample underwent homologous collapse, similar to the results seen in previous HF etching experiments (Westphal *et al*., 2004b).

7.4.2 Stardust Aerogel Track 35 Results

We identified four particles of potential cometary origin on our TEM grid following the completion of the ashing procedure. The four particles ranged in size from 100 nm to 250 nm in diameter (Figure 7.7), and all four particles were located in one subgrid that was located directly beneath the aerogel during the ashing process.

The four grains were predominantly composed of C and O, with C being the most abundant element in each grain. Precise quantification of the grain compositions was difficult due to the weak C and O peaks present in the JEOL 2000 TEM and the lack of precalculated K factors for

Cliff-Lorimer quantification in the JEOL 2100 TEM. However, standardless quantification of the JEOL 2100 TEM EDXS spectra indicated that C atomic compositions ranged from ~60% to 90% in the grains while O atomic compositions ranged from ~5% to 30%. Elements heavier than O and C were quantified accurately with EDXS spectra from the JEOL 2000 TEM with precalculated K factors. Significant Si and Fe were also present in all of the grains. Ca was present in 3 grains, Mg was present in 2 grains, and S and Al were also present in one grain (Table 7.1). Trace Cr (< 1.0 at. %) was also present in 2 grains. The lack of S alongside strong Fe signatures suggests that the Fe is a component of silicates rather than iron sulfides. F was present in each EDXS spectra, indicating some F contamination resulted from the ashing process. Cl contamination was also present in three of the EDXS spectra.

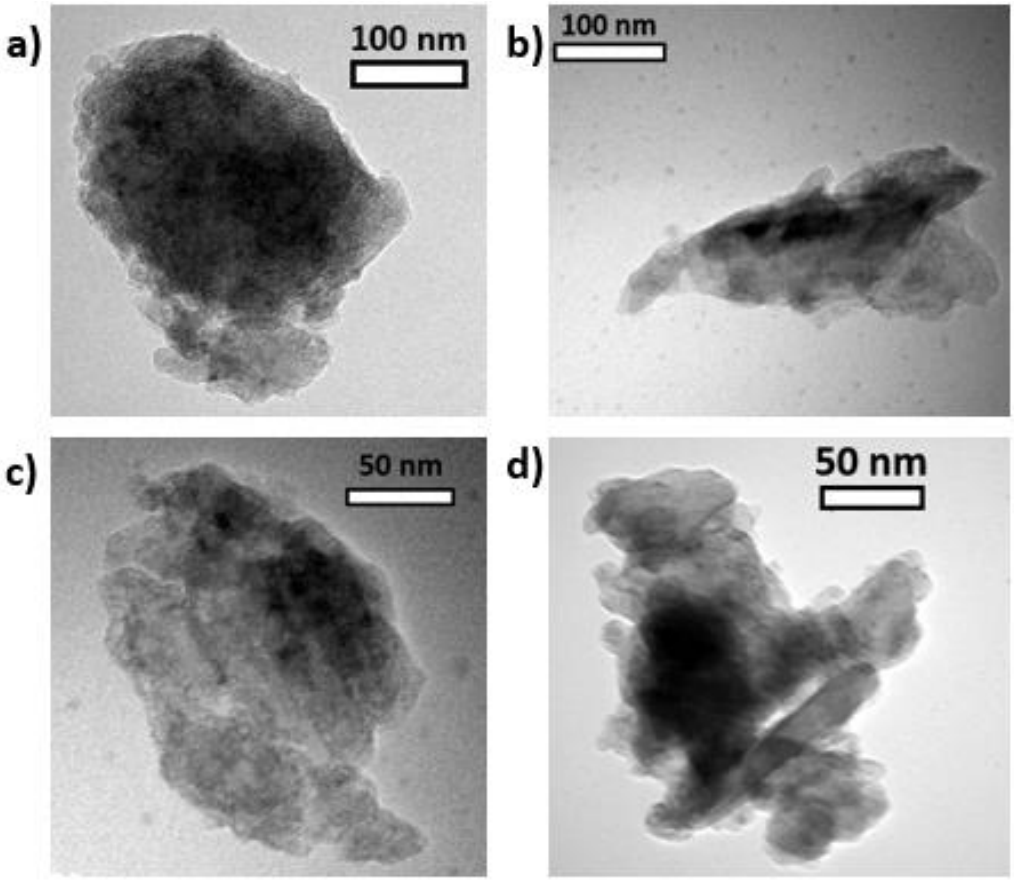

FIGURE 7.7: TEM bright-field images of the four particles located on the TEM grid after ashing. Particle diameters ranged from 100 nm to 250 nm.

TABLE 7.1: Composition in atomic % of the four collected grains, excluding O and C, normalized to 100% as determined through Cliff-Lorimer analysis of TEM-EDXS analyses. Standard deviation values are shown in parentheses. O and C, though composing ~90 at. % of each grain, are excluded as their X-rays were largely absorbed prior to collection in the JEOL 2000 TEM and as a result could not be accurately quantified. nd indicates that the element was not detected.

Element	Grain 1	Grain 2	Grain 3	Grain 4
Si	33.6 (0.5)	70.0 (7.3)	63.0 (2.9)	65.0 (1.1)
Mg	3.8 (0.2)	nd	nd	6.2 (0.4)
Fe	49.0 (0.6)	30.0 (4.7)	28.5 (1.9)	13.6 (0.5)
S	2.4 (0.2)	nd	nd	nd
Ca	1.5 (0.2)	nd	8.5 (1.0)	15.1 (0.5)
Al	9.7 (0.3)	nd	nd	nd

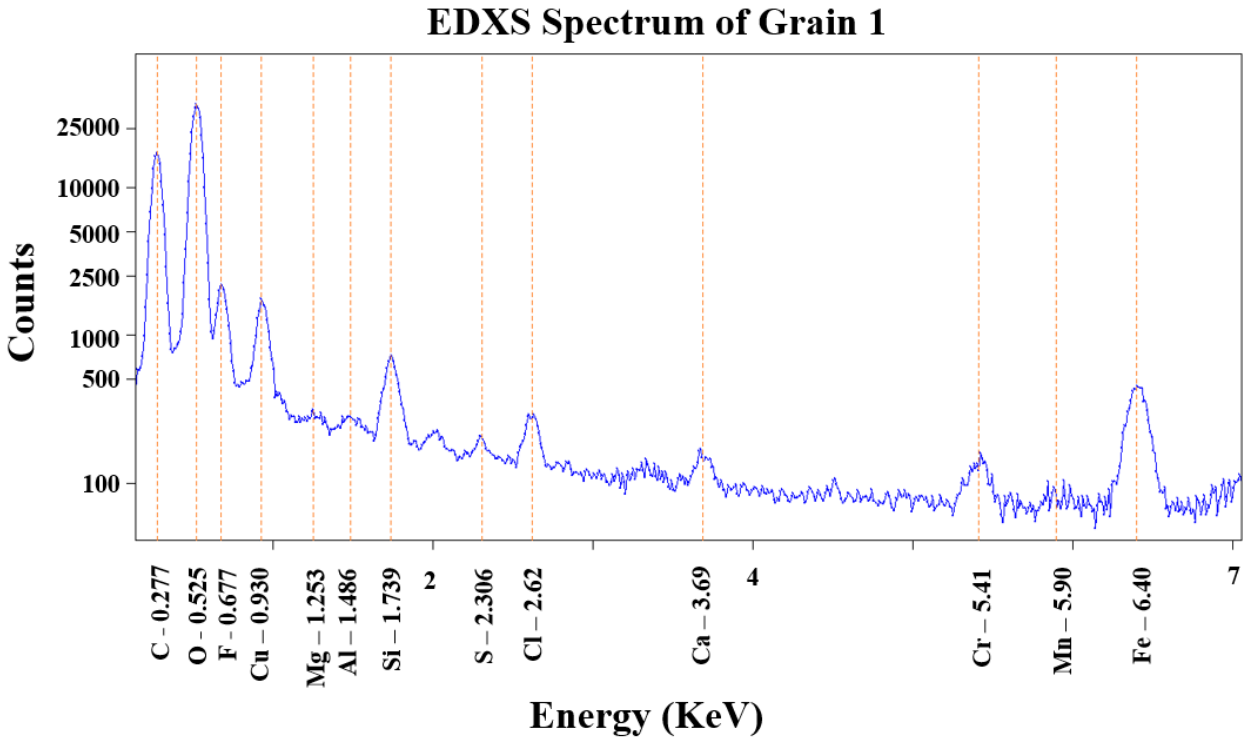

FIGURE 7.8: Logarithmic plot of the EDXS spectrum of grain 1 collected in the JEOL 2100 TEM. The spectrum is dominated by C and O signals. Cu present in the spectrum is the result of Cu present in the TEM grid.

All four of the observed particles were aggregates of crystalline and amorphous materials. The four grains appeared to be aggregates composed of many smaller crystalline grains. Dark-field images of the aggregates suggest the component grains range in size from 1 to 25 nm (Figure 7.9). Orientations of the component grains' crystal lattices appeared to be random. The subgrains'

small sizes, coupled with their seemingly random orientations, resulted in diffraction patterns that did not contain discrete points, but instead took on a ringed appearance more typical of powdered samples (Figure 7.9). The lack of discrete points makes the determination of the crystal structure and lattice spacings more difficult, particularly given the resulting SAD pattern may be the result of multiple crystal structures from numerous subgrains. Comparing the SAD pattern to patterns from known crystal structures was difficult. Our grains were extremely C-rich, but the patterns did not appear to match any single C-rich material (e.g., graphite or diamond). Classifying the SAD patterns may require a more complex analysis of multiple overlapping SAD patterns from different minerals consistent with the EDXS results.

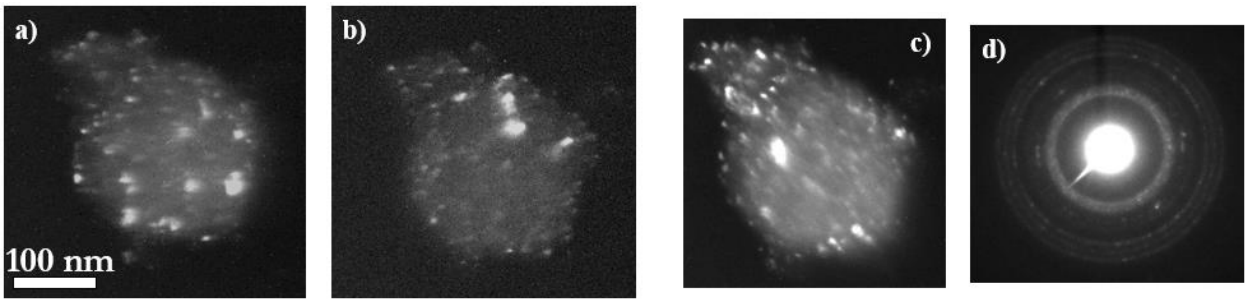

FIGURE 7.9: a), b), and c) show TEM dark-field images of grain #1 taken at different sample orientations. Different subgrains appear illuminated at different orientations, indicating that their crystal structures have different orientations. d) shows the resulting SAD pattern.

7.4.3 Stardust Aerogel Track 35 Discussion

The plasma ashing technique appeared to be successful when applied to authentic Stardust aerogel keystones. The aerogel was largely destroyed and particles were deposited onto a TEM grid for further analysis, simplifying the study of small grains captured within the bulbous aerogel impact features. The technique appeared to improve upon previous attempts using HF etching as we did not risk altering the sample through the formation of condensation on the sample. However, gauging the effectiveness of the technique is difficult. We cannot determine how many fine grains were part of the Stardust aerogel prior to ashing, and thus we cannot determine to what degree

material is being freed and successfully deposited onto the TEM grid. The aerogel is not completely ashed as it collapses under homologous collapse, and additional particles may remain trapped within the remaining aerogel that cannot be recovered. However, other techniques result in destruction of much of the sample prior to performing necessary analyses (e.g., FIB preparation). Additionally, many of these samples were unlikely to be studied given the difficulty of finding and analyzing fine grains within the aerogels. Overall, plasma ashing appears to be a promising technique for investigating the fine component of Wild 2 that was captured by the aerogels.

The particles we observed were C and O-rich, with ~90 at. % composed of combinations of C and O, with C being the most abundant element in each grain. Track 35's bulbous shape indicated that the original impacting particle was likely composed of fine-grained, volatile-rich material (Caro *et al*., 2008). Previous analyses of Stardust track 35 have identified carbonaceous materials (Sandford *et al*., 2006; Caro *et al*., 2008). Infrared spectroscopy studies indicated that cometary carbonaceous material is present in the aerogel surrounding bulb, but the presence of C contamination in the aerogels made separating and quantifying the cometary portion difficult (Caro *et al*., 2008). Raman spectroscopy studies discovered much of the cometary carbonaceous material in track 35 had features characteristic of disordered carbonaceous material such as graphite-like sp^2-bonded carbon in the form of condensed carbon rings (Sandford *et al*., 2006). However, our SAD patterns did not agree with graphitic carbon. Additionally, our grains did not contain any N whereas previous investigations noted significant N within the majority of the carbonaceous residues (Sandford *et al*., 2006). Thus, while carbonaceous material was expected within our aerogel sample, the carbonaceous material we observed in our grains appears to differ from the majority of the previously observed material.

Some of the observed C in our grains may be the result of contamination from the aerogels. The aerogels are known to have C concentrations ranging from ~0.2 wt. % to ~ 3.5 wt. % (Burchell *et al*., 2006). Much of this C is in the form of simple Si-CH_3 groups (Sandford *et al*., 2006). However, our EDXS measurements are not H-sensitive and cannot identify CH_3 groups. Si was present throughout our grains, but the presence of Fe and Mg indicates that, while portions of our grains may remnants of the aerogel contaminants or the aerogel itself, some component of our grains is likely cometary. Further TEM studies focused on isolating spot diffraction patterns, coupled with SIMS analyses to observe H abundances, could be effective in determining whether the C in our grains is refractory or organic carbon. Refractory carbon is more likely to be the result of cometary impactor, allowing these studies to better determine the source of our collected grains.

Determining the minerals responsible for the Si, Fe, and Mg present in the grains is difficult. O within the grains may have originated from the aerogel itself, complicating stoichiometric calculations. Si, similar to O, also may have originated from the aerogel. The lack of S within the residues suggests the Fe is not the result of sulfides, and instead came from silicates, carbides, oxides, or metallic phases. The large Fe abundance in grain 1 may indicate the presence of iron oxides. Diffraction patterns help in determining mineralogy, but our observed patterns are likely the result of C-bearing phases rather than silicates. Ca within the residues suggests that pyroxene or CAIs may have been a component of the impactors. Al within the first grain alongside Ca could be the results of a CAI impactor. However, grains 3 and 4 had no Al signature while containing significant Ca. Pyroxene grains have previously been observed and linked with Ca abundance in Stardust foil residues (Leroux *et al*., 2008), and other Ca-bearing phases such as CAIs and Kool grains would require the presence of elements not seen in our spectra such as Al, Cr, and Na (Joswiak *et al*., 2009).

7.4.4 Stardust Aerogel Track 35 Conclusions

The ashing process was successful in freeing material from the Stardust aerogels and depositing it onto TEM grids for further analysis. The aerogel largely collapsed as expected from previous HF etching experiments. However, it was difficult to fully assess the technique's success. The homologous collapse of the aerogel prevents full destruction of the aerogel, and without additional knowledge of the aerogel's contents it is unknown how much material is not freed from the aerogel.

The four observed grains were largely composed of O and C, but Si, Mg, Fe, Ca, S, and Al were also present in the EDXS spectra. The material was largely composed of nm-scale crystallites, but further analysis is required to determine the crystal structure of the observed material. H-sensitive analysis techniques coupled with investigations of the material's crystal structure may allow for better determination of the grains' mineralogies as well as to what extent the observed grains may be remnants of the aerogel or aerogel contaminants.

7.5 Stardust Aerogel Track 200

Following the successful identification of grains after the ashing of aerogel material from Stardust track 35 we continued to utilize the ashing technique to isolate potential cometary materials. Aerogel material from track 200 (Figure 7.10) was available for further analysis and had the correct dimensions for ashing preparation with our Cu-based sample holder.

7.5.1 Stardust Aerogel Track 200 Sample Preparation and Methods

The aerogel was prepared in the sample holder described in Chapter 3.5 of this thesis by Andrew Westphal at the University of California, Berkeley before I transported it by hand to Washington University for ashing. The aerogel track was ashed for 10 minutes at 17.2 kPa. The initial ~3 minutes of the ashing duration was necessary for the penetration of the protective Si_3N_4

window, resulting in ~7 minutes of F plasma exposure to the aerogel sample. The sample underwent homologous collapse as expected. Material from the aerogel was deposited directly onto a TEM grid during the ashing process. TEM investigations were performed on Washington University's JEOL 2000FX TEM.

7.5.2 Stardust Aerogel Track 200 Results

We identified a cluster of particles of potential cometary origin on our TEM grid following the completion of the ashing procedure. The individual grains within the cluster were largely rectangular in shape, with grain lengths ranging from ~100 nm up to several microns (Figure 7.10). All particles belonging to this cluster were located in the same TEM grid, which was located directly beneath the aerogel sample at the time of ashing.

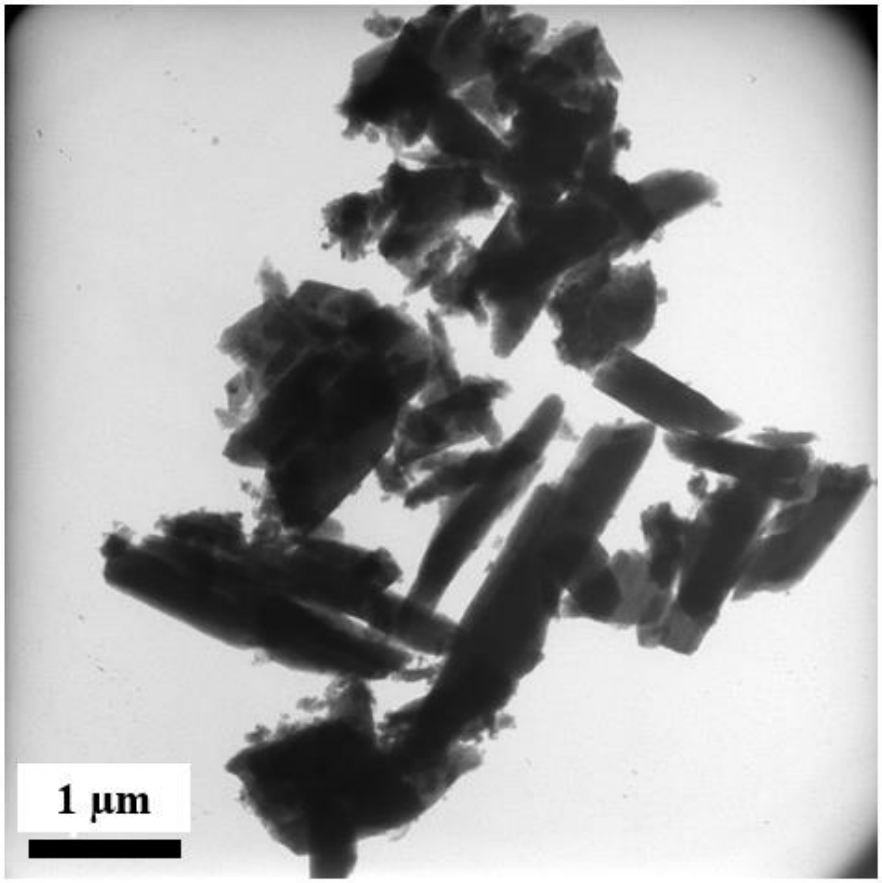

FIGURE 7.10: TEM bright-field image of the grain cluster observed after ashing aerogel material from Stardust track 200.

TABLE 7.2: Elemental compositions of deposited grains from aerogel track 200. EDXS spectra were collected on the JEOL 2000 TEM. Quantification was performed by measuring TEM-EDXS spectra with DTSA II software. F was also present throughout the spectra, but is not listed as it is contamination from the ashing process. nd indicates that the element was not measured. Standard deviations are shown in parentheses. The average composition of the grains was calculated without taking uncertainties in compositions into account.

Grain #	O at. %	Si at. %	S at. %	Ca at. %
1	14.2 (0.3)	3.1 (0.1)	45.1 (0.6)	37.6 (0.6)
2	25.5 (2.2)	2.7 (0.1)	40.1 (0.5)	31.6 (0.5)
3	nd	2.8 (0.1)	17.5 (0.1)	79.6 (2.3)
4	33.6 (2.7)	3.0 (0.1)	35.6 (0.6)	27.8 (0.6)
5	nd	4.1 (0.1)	54.0 (1.8)	41.9 (1.6)
6	26.2 (2.0)	2.9 (0.1)	38.4 (0.4)	32.5 (0.5)
7	44.0 (1.4)	1.6 (0.1)	34.3 (0.4)	20.1 (0.3)
8	33.0 (1.9)	2.4 (0.1)	38.7 (0.5)	25.9 (0.4)
9	45.3 (1.2)	0.8 (0.1)	35.9 (0.4)	17.9 (0.2)
10	23.3 (2.6)	3.2 (0.1)	40.7 (0.6)	32.8 (0.6)
11	49.4 (1.2)	0.9 (0.1)	32.9 (0.4)	16.8 (0.2)
12	37.4 (2.6)	2.9 (0.1)	32.7 (0.6)	27.0 (0.6)
13	35.3 (2.2)	3.0 (0.1)	32.7 (0.5)	29.0 (0.6)
14	32.9 (2.3)	2.5 (0.1)	37.6 (0.6)	27.1 (0.5)
15	36.2 (1.8)	2.1 (0.1)	38.0 (0.5)	23.7 (0.4)
16	39.1 (1.9)	2.2 (0.1)	36.4 (0.5)	22.4 (0.4)
17	34.9 (2.0)	2.3 (0.1)	38.9 (0.5)	24.0 (0.4)
Average	30.0	2.5	37.0	30.5

The cluster of grains all appeared to be predominantly composed of Ca, S, and O, with traces of Si and F also present in collected EDXS spectra (Figure 7.11). The thickness of the samples indicated that ZAF corrections were necessary for accurately quantifying the collected EDXS spectra. DTSA II software elementally characterized the grains through use of precollected standard spectra in combination with ZAF corrections (Table 7.2). Si was present in small amounts (0.8 to 4.1 at. %) throughout the spectra. O compositions varied greatly throughout the quantified grains (0 to 49.4 at. %). However, determining the extent to which these elements were cometary or remains from the aerogels was difficult. S and Ca were the most abundant elements throughout the residues, with S abundances ranging from 17.5 at. % to 45.1 at. % and Ca abundances ranging from 16.8 at. % to 79.6 at. %. The overall Ca/S ratio was 0.82. The overall O abundances were

too low relative to S and Ca to indicate the presence of calcium sulfate ($CaSO_4$). If the majority of the observed O and Si is the result of contamination from the aerogel the Ca and S abundances may reflect the presence of oldhamite (CaS).

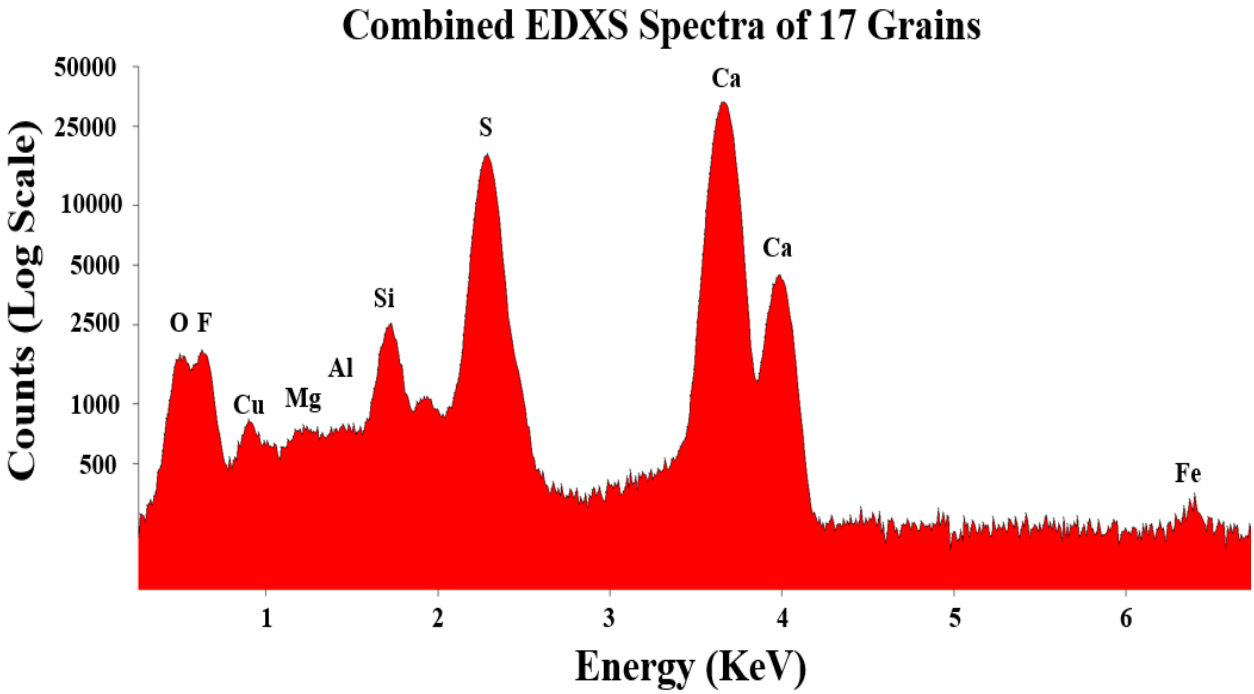

FIGURE 7.11: Logarithmic plot of the combined EDXS spectra of the 17 EDXS spectra listed in Table 7.2. Each individual spectrum was collected for 2 minutes of livetime, giving a cumulative 34 minutes of livetime for this plot.

The majority of the material appeared to be crystalline in nature. Dark-field images of the grains revealed many of the grains were composed of seemingly randomly-oriented crystalline subgrains on the scale of several nanometers (Figure 7.12). The polycrystalline nature of the grains made it difficult to collect clear diffraction patterns from the material. Diffraction patterns from the material appeared to indicate that the material's crystal structure was cubic (Figure 7.13). D spacings for the crystal planes were calculated through comparison to diffraction patterns from known Al crystal structures. The majority of the diffraction patterns that I was able to collect were the result of many crystalline subgrains, resulting in a ring pattern (Figure 7.14). The brightest rings had d spacings corresponding to the [111], [200], and [220] planes (using the Miller indices

convention [hkl]). Different crystal structures have different allowed Miller indices (Table 7.3). The spot diffraction patterns we observed correspond to a cubic crystal structure, and the brightest rings we observed had d spacings corresponding to the Miller indices resulting from a face centered cubic structure. Other weaker rings were visible in our ring diffraction patterns (Figure 7.14), but these may be the result of other less prevalent phases within our collected grains as these patterns are the result of many contributing subgrains. Our current diffraction pattern analysis indicates that the grains are likely the result of a face centered cubic crystal structure with D spacings within ~7% of oldhamite. Oldhamite (CaS) has an elemental composition consistent with our EDXS results and also has a face centered cubic crystal structure (Skinner & Luce, 1971).

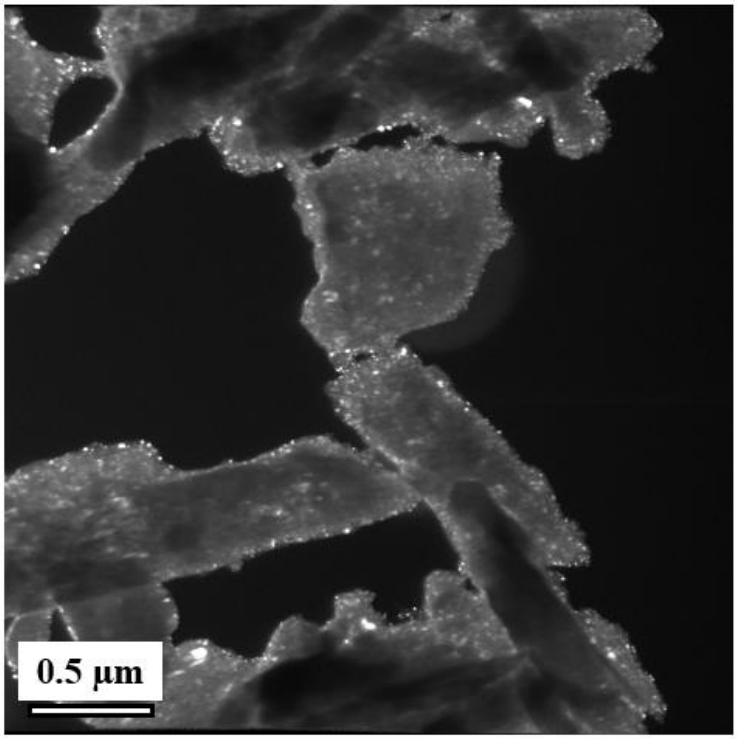

FIGURE 7.12: TEM dark-field image of grains from ashed aerogel from track 200. The individual bright points are subgrains with crystalline structures aligned with the camera location.

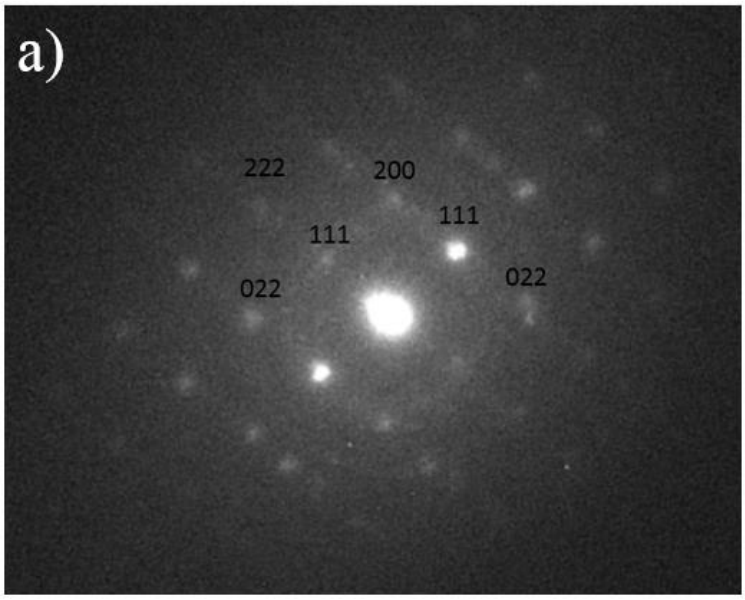

b)

h,k,l	d spacings(Å)	a (Å)
111	3.10	5.37
200	2.44	4.9
022	1.97	5.57
222	1.57	5.43

FIGURE 7.13: a) Diffraction pattern from a grain deposited during the ashing of aerogel track 200. The crystal planes are labeled. The pattern appears consistent with a cubic crystal structure. b) D spacings for the observed crystal planes corresponding to the shown miller indices. D spacings were calculated through comparison to a known Al crystal structure. The resulting a values were on average ~7% smaller than those observed in oldhamite (a = 5.69 Å).

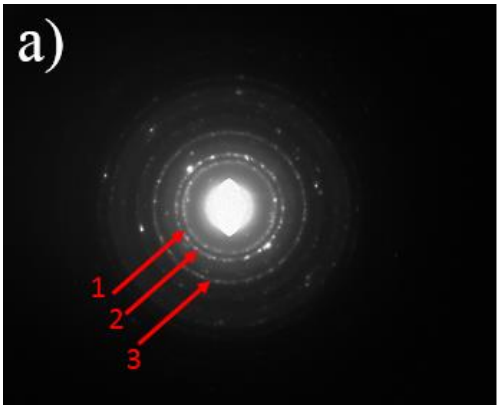

b)

Circle	d spacing (Å)	Proposed h k l	Resulting a
1	2.769	1 1 1	4.79
2	2.395	2 0 0	4.79
3	1.695	2 2 0	4.79

FIGURE 7.14: a) Diffraction pattern collected from a grain deposited during the ashing of aerogel track 200. The ring-like pattern is the result of observing diffraction patterns from many individual crystalline subgrains. The three brightest rings are indicated by red arrows. b) D spacings and the proposed crystal lattices responsible for the formation of these ring patterns and the a values resulting from the proposed h,k,l values. The proposed h,k,l values suggest that the pattern is the result of a face-centered cubic structure (Table 7.3).

TABLE 7.3: Allowed Miller indices for different cubic crystal structures.

Crystal Structure	Allowed $h^2 + k^2 + l^2$ Values
Simple Cubic	1,2,3,4,5,6,8,9,10…
Face Centered Cubic	3,4,8,11,12,16…
Body Centered Cubic	2,4,6,8,10,…..

7.5.3 Stardust Aerogel Track 200 Discussion

The materials deposited on our TEM grid were dominated by Ca and S abundances while lacking other elemental signatures outside of F, Si, and O. Si and F are likely remnants of the Stardust aerogel and the F plasma. Determining the source of the O is more difficult. Calcium sulfate ($CaSO_4$) is a common mineral present in materials such as plaster of Paris. However, the O abundances appear too low for our minerals to be dominated by calcium sulfate. Additionally, calcium sulfate has an orthorhombic crystal structure that does not appear to match the diffraction patterns we observed that suggested a cubic crystal structure. The minerals may also be oldhamite (CaS) with the O resulting from the Stardust aerogel rather than the mineral itself. Our initial results indicate that the observed diffraction patterns, though resulting from a face centered cubic structure (similar to oldhamite), have d spacings slightly smaller than oldhamite's. However, our collected diffraction patterns suffered from poor spot resolution as a result of contribution from multiple subgrains.

Identifying oldhamite in the Wild 2 impactors would be scientifically significant when considering the origin of comet Wild 2. Oldhamite is only found in highly reduced enstatite chondrites and enstatite achondrites (aubrites) (Lodders 1996). Many bulk isotope system (e.g., O_{16}, O_{17}, O_{18}) analyses have revealed an isotopic dichotomy among meteorites that suggest the two isotopic populations coexisted separately in the protoplanetary disk, most likely as a result of a gap in the disk created by proto-Jupiter (Scott *et al.*, 2018). Oldhamite has only been observed in the NC group of meteorites, and this hypothesis (the Warren Gap hypothesis) would prohibit material from the NC group of meteorites from being in the outer Solar System at the time that Wild 2 formed (>3 Myr after the formation of CV CAIs) (Scott *et al.*, 2018). As a result, positively identifying oldhamite in these samples would disrupt current understandings of early Solar System chronology, and further investigation of the possible comet Wild 2 oldhamite is warranted.

Further investigation is required to better constrain the mineralogy of our deposited minerals. The collection of additional diffraction patterns with better spot resolutions or with different ring patterns could help to establish the true crystal structure of the material and determine the mineralogy of the collected material. Rare earth elements are concentrated in oldhamite found in aubrites and enstatite chondrites (Lodders 1996). Further analyses performed on Washington University's Cameca 7F Ion Probe would be able to measure the abundances of the rare earth elements within our grains. A measurement of the rare earth element pattern will tell us if these grains are indeed oldhamite, and if the formation conditions of Wild 2 oldhamite (e.g., by condensation) are consistent with this source.

7.5.4 Stardust Aerogel Track 200 Conclusions

Similar to our study of aerogel track 35, the ashing process appears to have been successful in freeing material from the Stardust aerogels and depositing it onto TEM grids for further analysis. The grains that we observed were largely composed of Ca and S, but Si, O, and F were also present in the EDXS spectra. The material was largely composed of nm-scale crystallites, and initial analyses appear to indicate the material has an elemental composition and crystal structure (face centered cubic) consistent with oldhamite (CaS). Further analysis of the material is required to better constrain the mineralogy of the material. Identifying oldhamite in the Stardust aerogels would be scientifically significant because it would imply that enstatite material was present during Wild 2's formation and thus provide evidence against the current Warren gap hypothesis.

7.6 Conclusions

Plasma ashing sample preparation appears to be a promising technique for studying the fine component of comet Wild 2 that was collected in the Stardust aerogels. We observed material on our TEM grids after ashing material from Stardust aerogel tracks 35 and 200. The ability to

isolate fine material from Stardust aerogels would greatly improve our ability to characterize Wild 2's fine component, and further investigation of aerogel materials with this technique appears scientifically valuable.

The grains deposited from material from aerogel track 35 were largely composed of O and C, whereas grains deposited from material from aerogel track 200 were dominated by Ca and S. In both cases the material appeared extremely polycrystalline, with individual grains on the scale of nanometers. Further analyses of these grains are required to fully characterize the material's crystal structure and thus its mineralogy.

The Ca- and S-rich materials from aerogel track 200 may be oldhamite. The presence of oldhamite in Wild 2 would call into question the Warren gap hypothesis, demonstrating the importance of continued analysis of these samples and the Stardust aerogels in general.

Chapter 8: Convolutional Neural Networks for Finding Foil Features

8.1 Preface

Neural networks are a form of machine learning that have gained popularity in recent decades with the overall improvement of computer processing power and memory storage. Convolutional neural networks (CNNs) are a specific form of neural networks that aim to compress complex, 3-dimensional data structures (e.g., digital images) by performing a series of convolutions on the input data. Due to CNNs' ability to quickly parse image data they have the potential to save countless man-hours of labor by independently identifying features of interest in images collected with an SEM (e.g., craters in Stardust foils).

8.2 CNN Theory

CNNs are a specific form of traditional neural networks (NNs). NNs seek to emulate the biological process of neurons firing within the brain to imitate brain function. CNNs add convolution and pooling steps to NNs in order to speed up the process of analyzing complex image data.

8.2.1 Traditional Neural Networks (NNs)

NNs were originally created to simulate the behavior of neurons in the brain and are composed of a network of artificial neurons called nodes. The network is composed of an input layer, at least one hidden layer, and an output layer (Figure 8.1).

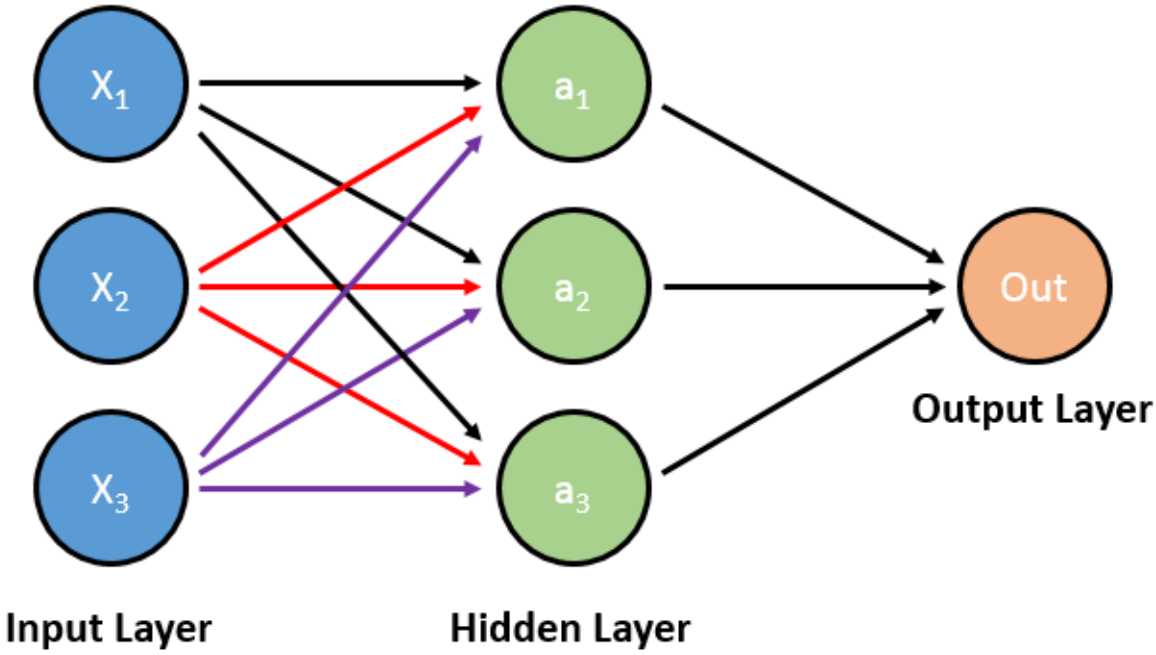

FIGURE 8.1: The layout of a simple NN. In this figure we have three inputs (X_1, X_2, and X_3) that each feed independently into each node in the hidden layer (a_1, a_2, a_3). These hidden layers then contribute to the output layer.

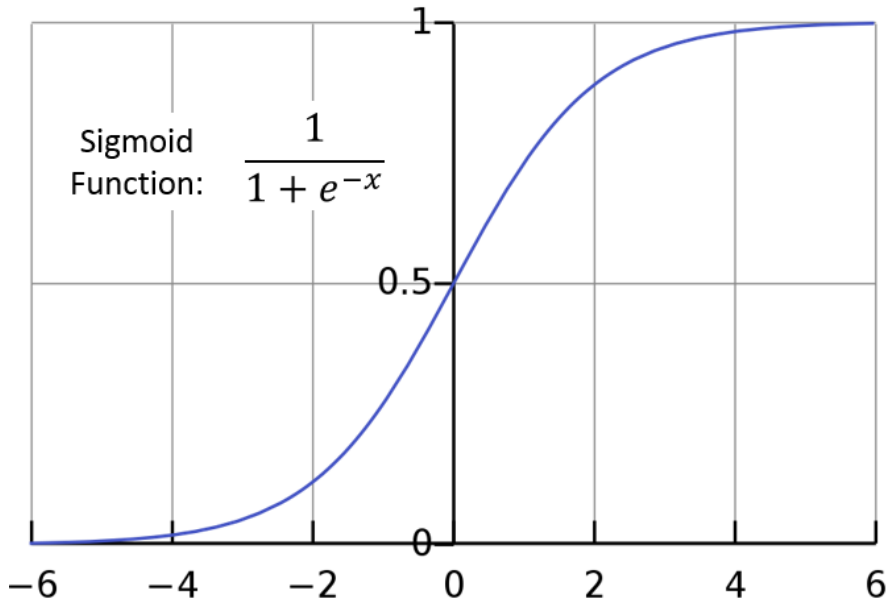

FIGURE 8.2: The sigmoid function frequently used as an activation function in neural network nodes. For values much greater than zero, the function's value approaches 1, while for values much lower than zero, the function's value approaches 0.

Each node in a given layer is connected to each of the nodes in the previous and following layers. These connections are modeled as weights. When moving along a connection from one node to another in the following layer, the value in the earlier layer is multiplied by a weight factor before being applied to the following layer. An activation function is then present in the node to control the amplitude of the node's output before the process is repeated again when moving onwards to the next layer. A sigmoid function is an example of a commonly used activation function (Figure 8.2). When the value passed to a sigmoid function is much greater than zero, the sigmoid function will return a value close to 1, whereas when the value passed to a sigmoid function is much lower than zero, the sigmoid function will return a value close to 0. In this way a sigmoid function can return values between 0 and 1, which will then be utilized for the next layer in the neural network.

Through careful calculation of the weights connecting each node of a NN the NN can be crafted to return a desired output with a given input. Figure 8.3 shows an example of an XNOR gate, or a NN that will output the value 1 if and only if the two inputs (X_1 and X_2) both share the same binary value (0 or 1). By increasing the complexity of a NN through the addition of more inputs, nodes, and layers, one can create a NN capable of performing more complex calculations given that the appropriate weights are established between each node.

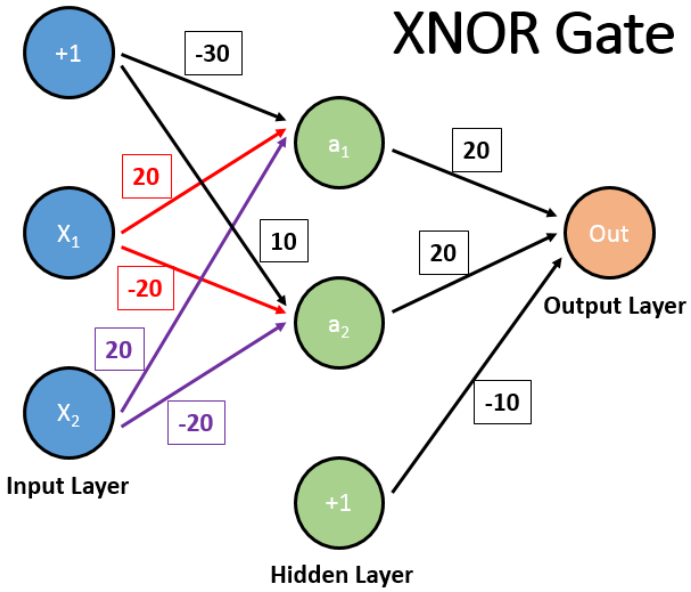

Input and Results

X_1	X_2	a_1	a_2	Out
0	0	0	1	1
0	1	0	0	0
1	0	0	0	0
1	1	1	0	1

FIGURE 8.3: The layout and appropriate weights (shown in boxes of appropriate color) of an XNOR gate. In this gate each activation function (similar to the sigmoid function from Figure 8.2) is established such that a value of the input to a node greater than 0 will return a 1, and a value of the input to a node less than 0 will return a 0.

8.2.2 Convolutional Neural Networks (CNNs)

CNNs use the basic structure of a NN (nodes connected through weights) but use convolutions to simplify the input. An example of the convolution function is shown in Figure 8.4. Using convolutions allows for the reduction of free parameters in the neural network. A 100 by 100 pixel image would typically have 10000 weights for each neuron in the second layer, which would lead to an extremely large number of calculations to be performed to analyze even a relatively small image. Using convolutions, the weights between layers are removed and the values of our filter become the parameters we are solving for. Thus, passing an image through a 3 by 3 filter will result in only having 9 parameters to solve for, regardless of the size of the input image, greatly reducing the processing power needed to analyze the image. This architecture is effective due to the property of parameter sharing. A feature detector (such as a vertical edge detector) is likely to be as useful in one part of an image as any other. Thus, by creating a filter

that can detect features we are interested in (such as vertical lines), we can reuse that filter repeatedly and reduce the number of calculations that need to be performed.

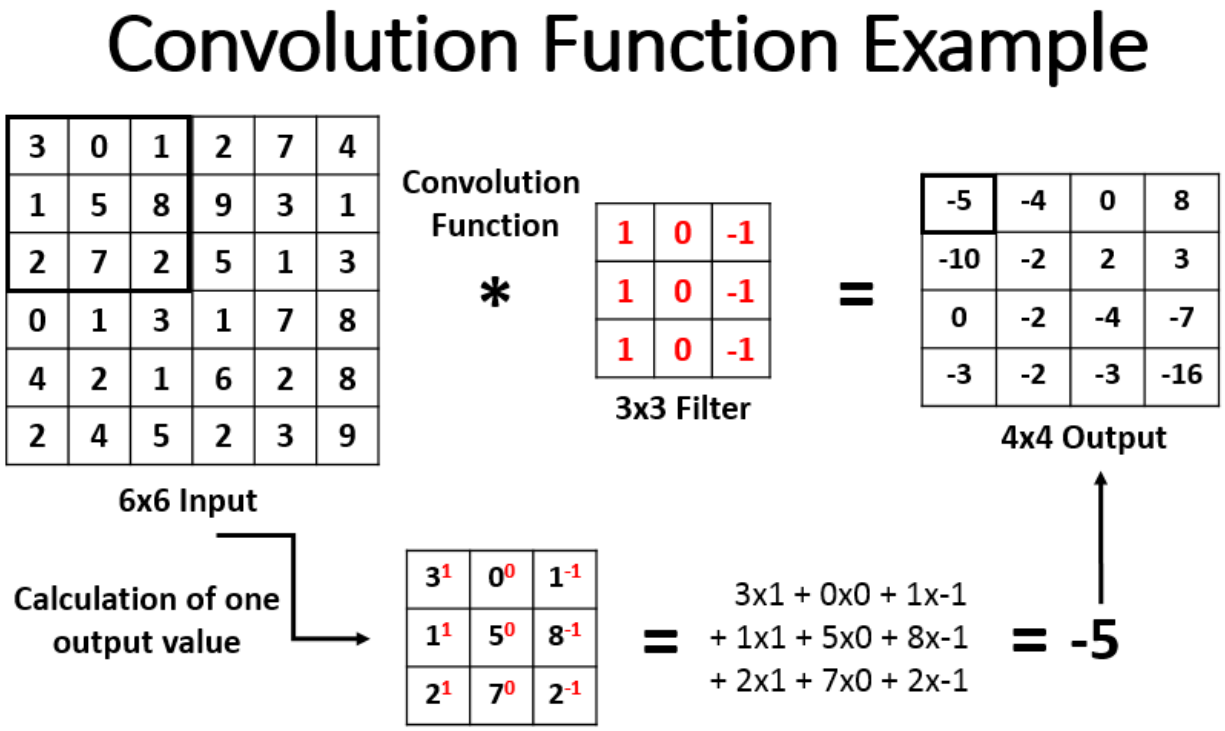

FIGURE 8.4: The calculations necessary to perform a convolution function with a 3x3 filter on a 6x6 input matrix. The 6x6 input matrix can be thought of as a small 6x6 pixel image, with each number representing a pixel intensity. The filter shown here is a vertical line detector since it will return the highest values (both positive and negative) when the filter is positioned over a part of the image with large value differences between the right and left sides.

CNNs will also typically make use of a pooling step. An example of a pooling step is shown in Figure 8.5. The pooling step condenses the results of filtering steps to futher reduce the parameters to reduce computing time.

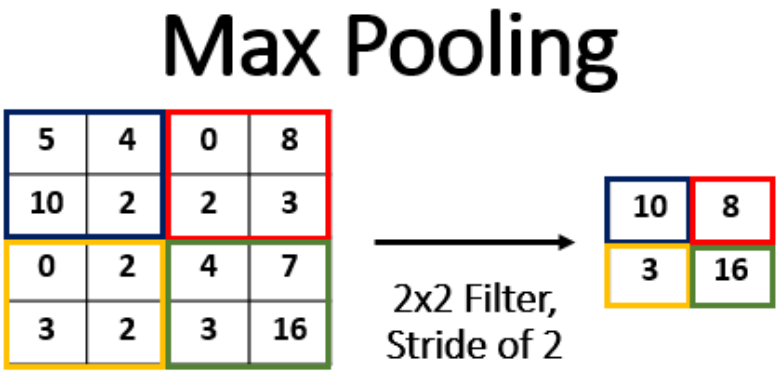

FIGURE 8.5: An example of maximum pooling, where the largest value in each pool is taken and passed on to the next layer of the CNN. In this example, we took the absolute value of our result from Figure 8.3 and applied a 2x2 filter (4 values are analyzed in each pooling step) along with a stride of 2 (filters are only placed over every other pixel value).

A complete CNN (Figure 8.6) will typically combine multiple convolution and pooling steps along with fully connected layers at the end, which behave the same as layers present in a traditional neural network. The final output can vary. In a CNN designed to identify handwritten numbers, there may be 10 outputs (one for each numeral from 0 to 9), each representing a probability (values between 0 and 1) that an individual numeral was written. In the case of identifying a singular feature (such as whether an image contains an impact crater or not) the output will typically be the probability of that feature being present in the input image.

8.2.3 Training NNs

After creating a CNN with the appropriate architecture, the appropriate parameters present in the convolutional and fully connected layers need to be determined in order for the CNN to perform the desired task. In our case, we wish to input a secondary electron image obtained with an SEM and have the CNN determine whether that image contains a crater or not. In other words, if we choose the weights between nodes correctly, when we input an image of a crater into our neural network the final output will be 1, and otherwise that final output will be 0.

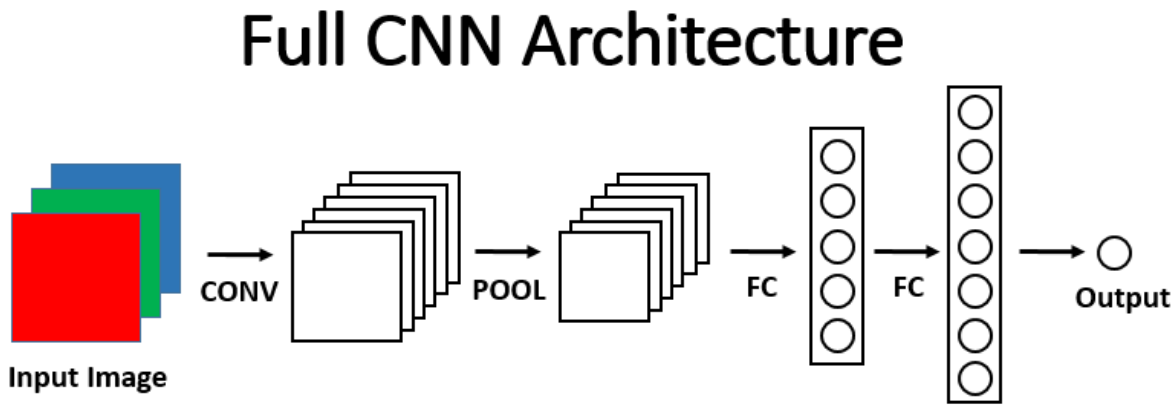

FIGURE 8.6: An example of a basic CNN. The input image (represented as three matricies for the red, green, and blue inputs in a colored pixel value) goes through the convolution (CONV), pooling (POOL), and fully connected (FC) layers before outputting a single probability. Most CNNs will use multiple convolution and pooling layers. Note that the six matricies present after the initial convolution step indicates that six filters were applied to the input image.

Training a NN is the process of feeding the neural network images with known results and altering the values of the weights when the returned output is incorrect. Training a NN utilizes a 'cost function' that takes an average difference of all the results of the hypothesis (the NN output) and the known results. If the NN incorrectly labels an image, the cost function's value increases. Squared error functions, frequently seen in statistics or logistical regression, are the most common form of cost functions.

Once a cost function has been obtained, we need a way to minimize it in order to obtain the best possible weights between our NN nodes, or in the case of CNNs, the best possible values for numbers in our filters. Backpropagation algorithms are used to minimize the cost function. Backpropagation algorithms will contain partial derivatives of the cost function with respect to a matrix representing our node weights (or our filter values), and will thus derive the change in the cost function with respect to these numbers and will adjust the weights (or our filter values) in the appropriate direction. Implementation of the cost function and backpropagation algorithms are

frequently complex, particularly in large CNNs. Fortunately, modern programming packages automate the implementation of these algorithms.

8.3 CNN Packages

The details behind the implementation of modern CNNs are beyond the scope of this thesis. Creating NNs has been greatly simplified in recent years with the creation of software packages that automatically perform and calculate, amongst other functions, the complicated cost function and backpropagation algorithms. Amongst the most frequently used are the packages Tensorflow, which was originally designed by engineers at Google, and Keras, an offshoot of the Tensorflow package. Both packages are used with the Python programming language. I utilized these packages in the creation of the CNN that I used to search for craters on the Stardust foils. Full documentation on these packages can be found at https://www.tensorflow.org/api_docs/python/tf and https://keras.io.

8.4 CNN Implementation

The code and the outputs presented in this chapter can be found at https://github.com/BrendanAHaas/CNN_IdentifyingStardustCraters. The code is written for Python 3.4. The following package versions are used, though other versions may work but have not been tested:

- `NumPy 1.14.2`
- `Pandas 0.23.4`
- `Matplotlib 2.2.2`
- `pillow 5.0.0`
- `sci-kit-learn 0.19.2`
- `tensorflow 1.11.0`
- `keras 2.2.4`

This section of the chapter summarizes important aspects of the code as well as the outputs relevant to demonstrating the effectiveness of the CNN's crater identification algorithm.

8.4.1 CNN Training and Test Sets

In order to train our CNN to be able to identify craters, we first need to provide the CNN with as many examples of crater images as possible. While many modern neural networks train on millions of data points, preliminary results can be obtained with hundreds. Relatively few images of hypervelocity micron-scale impact craters on aluminum foils exist, and as a result the training set for this application will be relatively small. Additionally, crater images need to be complemented by images without craters to allow the CNN to differentiate between the two. Examples of images from the two test sets are shown in Figure 8.7.

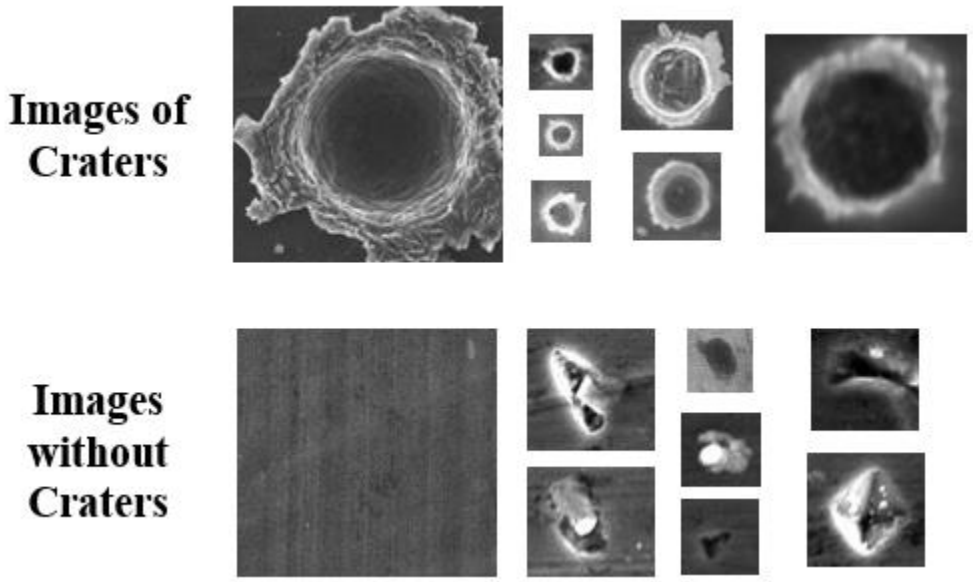

FIGURE 8.7: Examples of images with and without craters that were used for training and for testing the performance of the CNN. Many of the images without craters were selected to contain dust or foil defects in order to help the CNN differentiate between these features and authentic craters.

For the implementation of this CNN I used images of craters and regions without craters obtained from the Acfer 094 analog foils and Tagish Lake analog foils discussed in chapter 4 of this thesis. 1098 total images were used, 301 of which contained images of craters. 80% of the images (878 total) were used as a training set to teach the CNN to identify images of craters and non-craters and 20% of the images (220 total) were used to test the accuracy of the trained CNN.

The images ranged in size from 175086 pixels (411 x 426 pixels) to 361 pixels (19 x 19 pixels) as they represented craters varying in size from a few hundred nanometers to tens of microns in diameter.

8.4.2 Image Compression

NNs require each input to contain the same number of dimensions, meaning that inputting images of varying sizes is not possible. Additionally, reducing the dimensions of the input can greatly speed NN processing time. For images the number of dimensions is equal to their area in pixels multiplied by the number of color channels present in these images. Most images contain three color channels for the red, green, and blue color inputs. As a result these images consist of integer values (0 to 255) for each channel for each pixel. In order to speed processing of images through the CNN, I resized each image to be 20 pixels by 20 pixels. This does cause some of the data from the original images to be lost, but the general characteristics of the craters (rounded shape, bright crater rims, dark interior) are preserved. The images used in this study had previously been converted from greyscale (single-channel) to RGB (three channel) images. As a result, I had to convert back to single-channel images in order to decrease computation time by a factor of three. After these adjustments each image only contains 400 dimensions and can be processed by the CNN relatively quickly. Higher accuracy could be obtained by retaining more pixels from the original images, but would come at the cost of higher computation times. Examples of this compression is shown in Figure 8.8.

8.4.3 CNN Architecture

The CNN architecture, constructed through use of the Keras package, is shown in Figure 8.9. The CNN begins with our input image that is 20x20 pixels in size and constitutes a single channel. In the first convolution step the image has 40 5x5 filters applied to it resulting in 40

channels. In the second convolution step the image has 50 5x5 filters applied to it, resulting in 50 channels. A max pooling step is applied with a 2x2 filter and a stride of 2. A third convolution step has 70 3x3 filters applied to it, resulting in 70 channels. A second max pooling step with a 2x2 filter and a stride of 2. A fourth and final convolution step has 100 3x3 filters applied, resulting in 100 channels. A third and final max pooling step with a 2x2 filter and a stride of 2 is applied to the 100 channels. The channels are fed into a full connection layer with 100 nodes. This full connection layer outputs to a single value between 0 and 1 that identifies how likely the input image is a crater, with 0 being extremely unlikely and 1 being certainty that a crater is present.

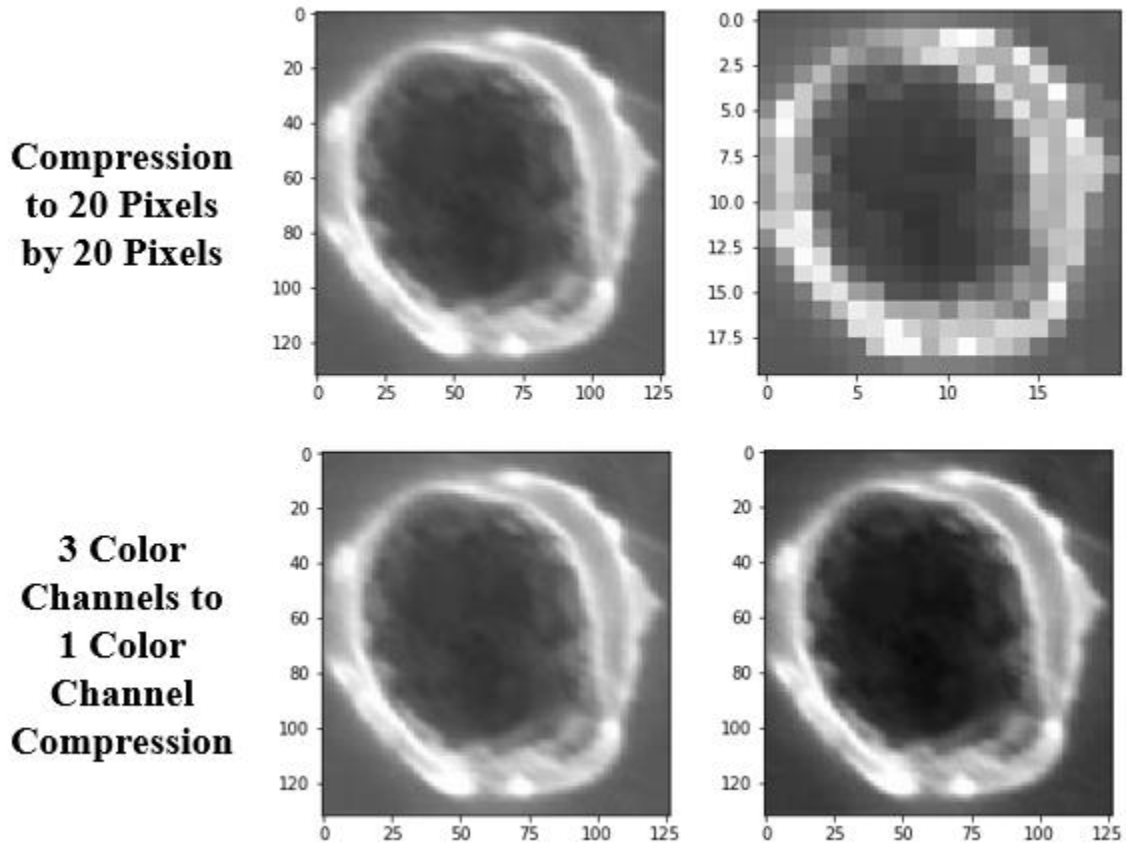

FIGURE 8.8: Examples of a crater image being compressed to 20 pixels by 20 pixels, as well as an example of the crater image being converted from 3 channels to 1 channel. The crater's primary features of a bright, circular outer rim and dark interior are both preserved through each compression.

The architecture of our CNN adheres to common CNN architectures through the gradual increase in channels and the decrease in the size of these layers through the use of max pooling steps. Not listed are dropout steps present after each pooling step, which randomly select channels (in our case 40% of the channels) to be excluded from the training of the CNN. This prevents the CNN from relying too heavily on filter values attached to specific channels and thus prevents overfitting of the training data. A more optimal architecture likely exists, but optimizing NN architectures is extremely difficult.

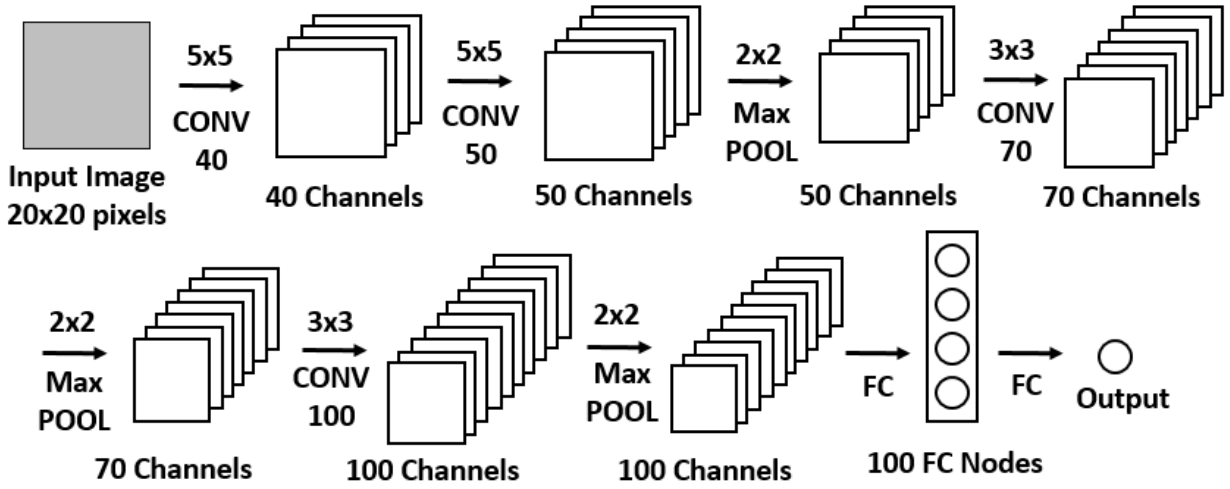

FIGURE 8.9: CNN architecture diagram. As the image progresses through the CNN the input data is expanded into additional channels through convolution steps. The channels are further compressed through max pooling steps. The channels are finally fed through a fully connected layer that leads to the output, a single number between 0 and 1 that identifies how likely the input image is a crater, with 0 being extremely unlikely and 1 being certainty that a crater is present.

8.4.4 CNN Effectiveness on Training and Test Datasets

The CNN trains by taking in training images (e.g., images in Figure 8.7), feeds the image through its architecture, and outputs a prediction that the image is a crater or not. In instances where the CNN is incorrect (which is determined by previous human analysis of the training images), the CNN alters the weights present in its filters in its convolution steps to improve its ability to correctly label the images. Images that are used in this way to train the CNN constitute the training set. We can examine the accuracy of the CNN's predictions by having the CNN input

images that are not used to alter its weights and see the rate at which these images are correctly labeled. These images constitute the test set. In our CNN we began with 1098 images, 301 of which contained craters. These images were randomly split into a training and test set in an 80/20 ratio. Each run of the entire training set through the CNN constitutes an epoch. The effectiveness of the CNN on labeling the images after each epoch is shown in Figure 8.10. After roughly 50 epochs the CNN's performance did not vary considerably. The weights after the CNN performed best on the test set were saved and used in further analysis of the foil images.

We only used 1098 total images in our combined training and test sets. This is a very small size for the training and test sets compared to many modern applications of NNs and CNNs that frequently use hundreds of thousands, millions, or even billions of training examples (Halevy *et al*., 2009). Increasing the size of the training set for any NN almost always increases the NN's accuracy. However, obtaining additional secondary electron images of hypervelocity impact craters is time consuming and the amount of time necessary to appreciably increase the size of the training and test sets for this application may not be worth the possibly minimal increase in accuracy, particularly when simpler solutions (such as increasing the size of the input image and compensating with increased computational power) are available.

Figure 8.10 shows that, despite the addition of dropout steps to our CNN, overfitting of the training data occurred. Overfitting occurs when the NN attempts to minimize its loss function by overfocusing on features present on craters in the training set, thus reducing the NN's accuracy when it is applied to craters not in the training set. Due to overfitting, our CNN's accuracy peaked at epoch 70, when its accuracy on the test set was maximized and prior to the onset of overfitting.

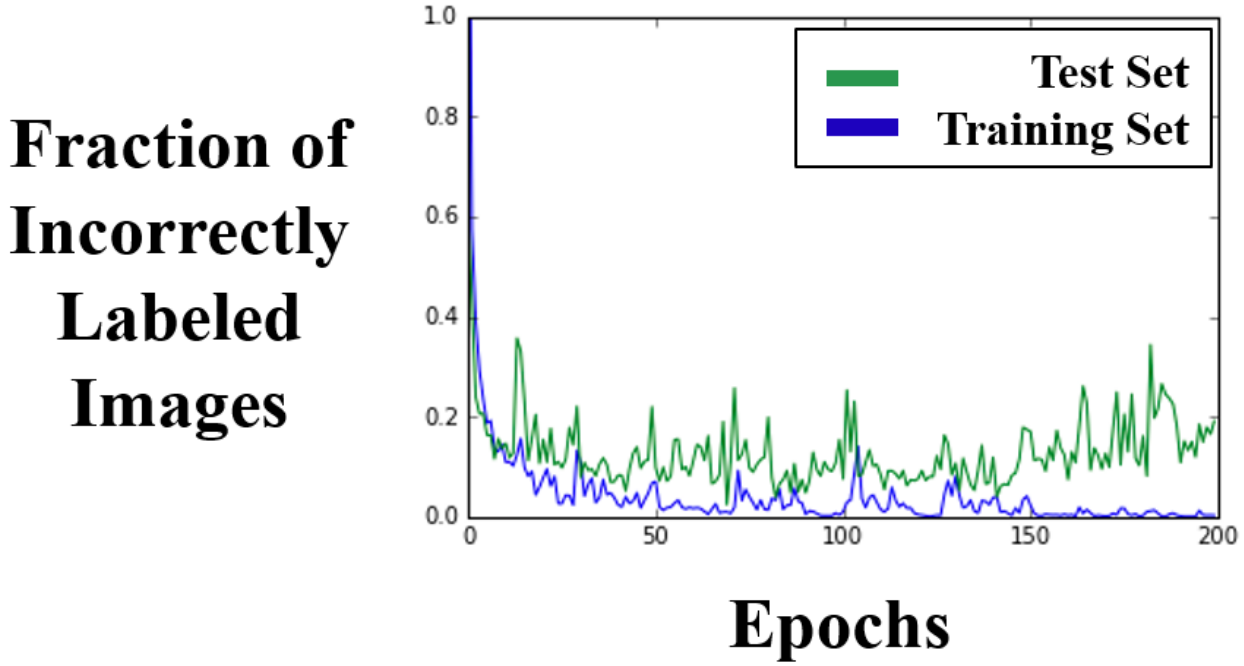

FIGURE 8.10: Fraction of images incorrectly labeled by the CNN after each epoch. The CNN's accuracy does not noticeably improve after roughly 50 epochs. The weights obtained on the epoch after which the CNN performed best on the test set (here, epoch 70) are saved for further use.

8.4.5 Applying the CNN with a Sliding Window

The CNN is trained to identify images of craters where the crater constitutes almost the entire image. Secondary electron images of Stardust foils, if they contain a crater, will only have the crater be present in a small part of the image. As a result, if we wish for our CNN to be effective, we have to isolate small portions of each secondary electron image step by step in order to verify that the portion contains or does not contain a crater. Beginning in the top left of the image, the program grabs the first 20x20 pixel subsection of the image, feeds it through the CNN, and has the CNN determine if the image subsection contains an image of a crater. The program can then shift the subsection of the image over any number of pixels, feed it through the CNN again, and repeat until the entire image has been sampled. This is called a sliding window procedure.

My implementation of the sliding window utilized a subsection shift of only 1 pixel in order to maximize the possibility that craters were found if present on the images. Larger shifts

could be used to decrease computation time, but would come at the cost of a decreased accuracy in positively identifying craters on the images.

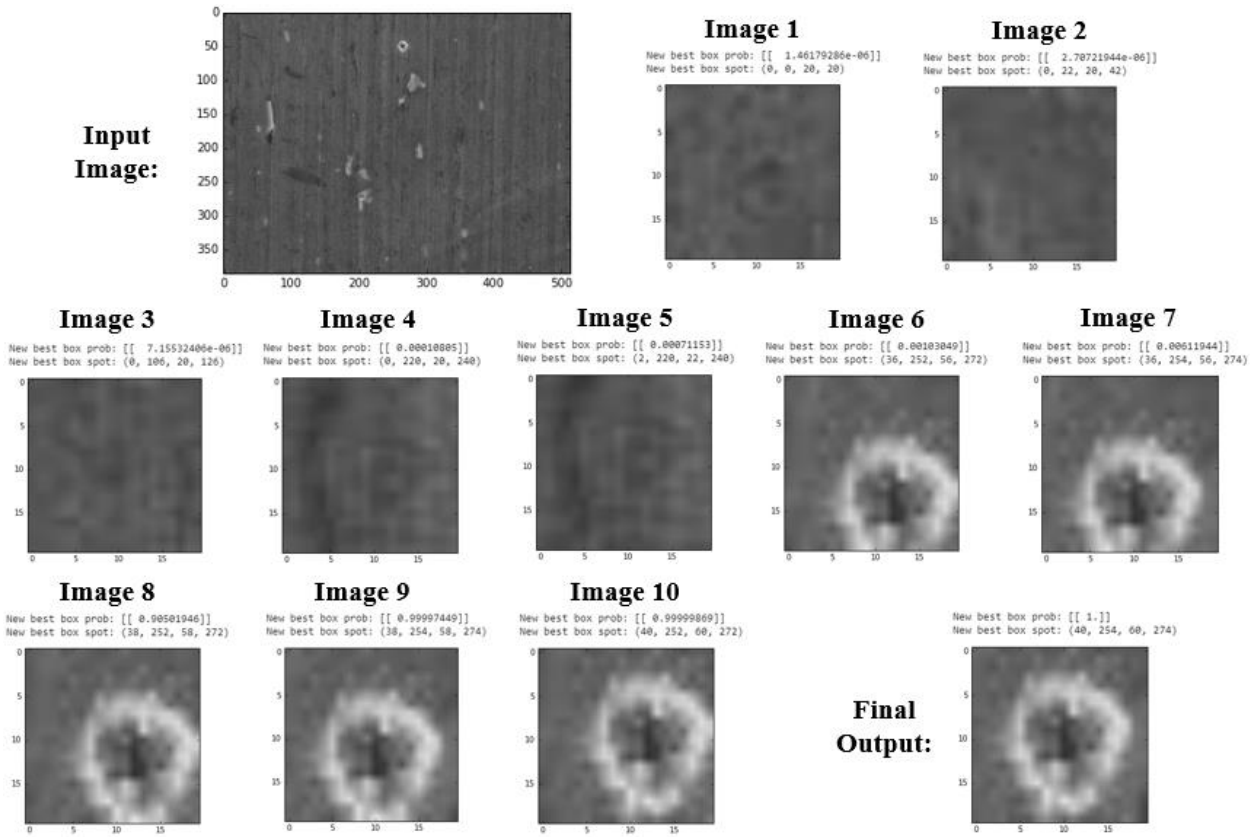

FIGURE 8.11: Illustration of the CNN's identification of a crater. The input image contains a crater near the top middle of the image. The CNN slides an input window across the image and updates after each step in which the probability of there being a crater reaches a new largest value. The final output is the image with the highest probability of containing a crater coupled with the crater's location in the image and the CNN's crater probability calculation. If the final highest crater probability is too low the program determines that no crater was found.

8.4.6 Examples of the CNN Output

The program operates by analyzing subsections of the images with the sliding window method. Each section is fed through the CNN and the CNN calculates the probability that the subsection contains a crater. Whenever a subsection's probability is higher than the current largest probability, the program notes the subsection's location and the probability that the subsection contains a crater. An example of the program's output is shown in Figure 8.11. The final output

after an image is fully analyzed is the highest obtained probability of a crater being present in any subsection present in the original image as well as the location in the image of the identified crater.

8.4.7 The CNN's Effectiveness

The effectiveness of a CNN can be interpreted in many ways depending upon the goals of the implementer. In the case of crater searching on the Stardust foils I valued the minimization of false negatives (the CNN incorrectly deciding that no crater was present) over the minimization of false positives (the CNN incorrectly deciding that a crater was present). Craters on the Stardust foils are rare, particularly on the Interstellar foils, and finding these craters is the primary goal of implementing the CNN. The presence of false positives does increase the amount of labor required from researchers, since they will need to spend more time inspecting images that do not in actuality contain craters, but so long as a significant fraction of the original images are still correctly identified as not containing craters the number of man hours required to search the images will be greatly decreased. Additionally, the program notes the location of features that it identifies as craters and thus will allow researchers to quickly identify images that are false positives.

A further measure of effectiveness of the CNN is the rate at which it is able to process the images and return a probability that the image contains a crater. Faster analyses of the crater images is desired, but if it comes at a large cost in accuracy a slower analysis may be preferable.

I tested the performance of the CNN by running it on images taken on the Stardust Interstellar foils that are available for viewing through the Stardust@Home program (http://stardustathome.ssl.berkeley.edu/). The Stardust@Home program utilized the work of volunteers from around the world to search millions of secondary electron images of the Stardust Interstellar foils, as well as many optical images of the interstellar aerogel tiles, for craters and tracks (Westphal *et al*., 2014b; Frank *et al*., 2014). I tested the effectiveness of the CNN by running

the CNN on 62 crater containing images and 193 images without any craters taken from Stardust@Home. The initial test used only 20x20 pixel sliding windows and a step size of 2. The CNN took on average 66 seconds to analyze each image when run on my laptop with an Intel Core i5 7300HQ processor with a core speed of 3090 MHz. Using a threshold of >.90 probability as positive crater identification, the CNN correctly located half of the craters, and correctly excluded roughly half of the images without craters (Figure 8.12).

Initial performance of the CNN was suboptimal. Half of the craters were not positively identified. A large number of craters were not being identified because they were extremely small. Many of the craters from the Stardust Interstellar Foil images were 10 pixels or less in diameter, and thus did not fill the sliding window box of 20x20 pixels. In order to identify these craters I added a second sliding window to the sliding window algorithm that imaged subsections that were 10x10 pixels. In addition to the small sizes of the craters, several craters were incorrectly missed due to the step size of 2 used for the sliding window algorithm. By skipping pixels, some craters were not exactly centered in the subsections obtained by the sliding window algorithm and thus were given lower probabilities of being craters. I also lowered the sliding window step size to 1 in order to ensure that any crater that may be present would have at least one image subsection that would contain an image of the crater precisely centered for CNN analysis. Making these changes also increases the false positive rate, as additional subsections of these foils will be analyzed and could appear significantly crater-like to generate a positive output. However, I deemed that positive identification of the existing craters was more important than the potential increase in false positive results. The result of adding an additional window and reducing the step size is shown in Figure 8.13.

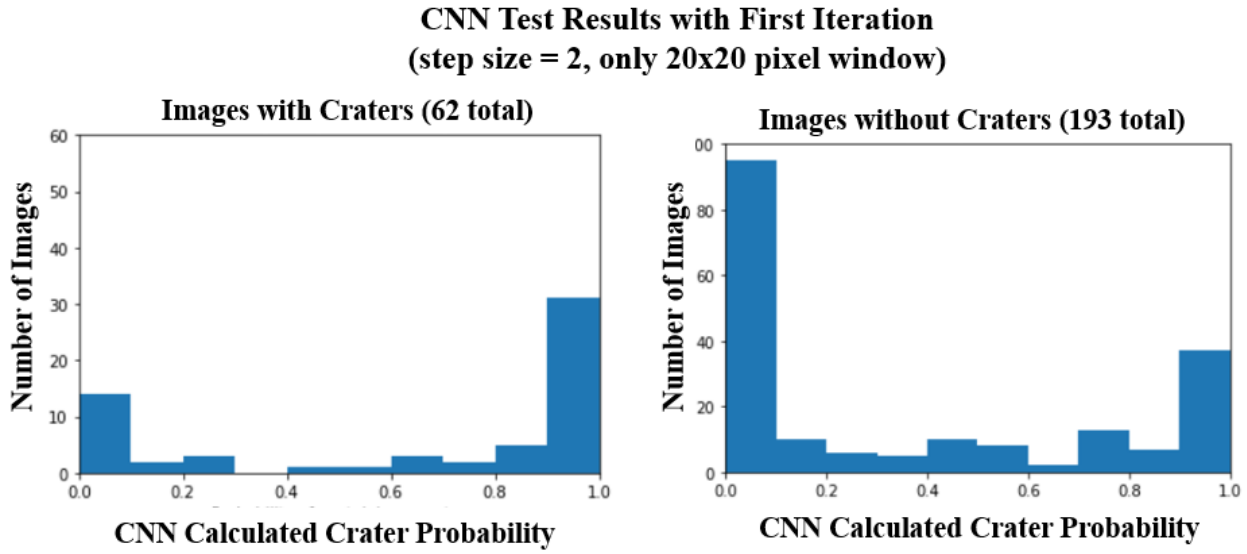

FIGURE 8.12: Performance of the CNN on images from Stardust@Home images with and without craters. Roughly half of each type of image was correctly placed at having a low (0-.10) or a high (.9-1.0) chance of containing a crater.

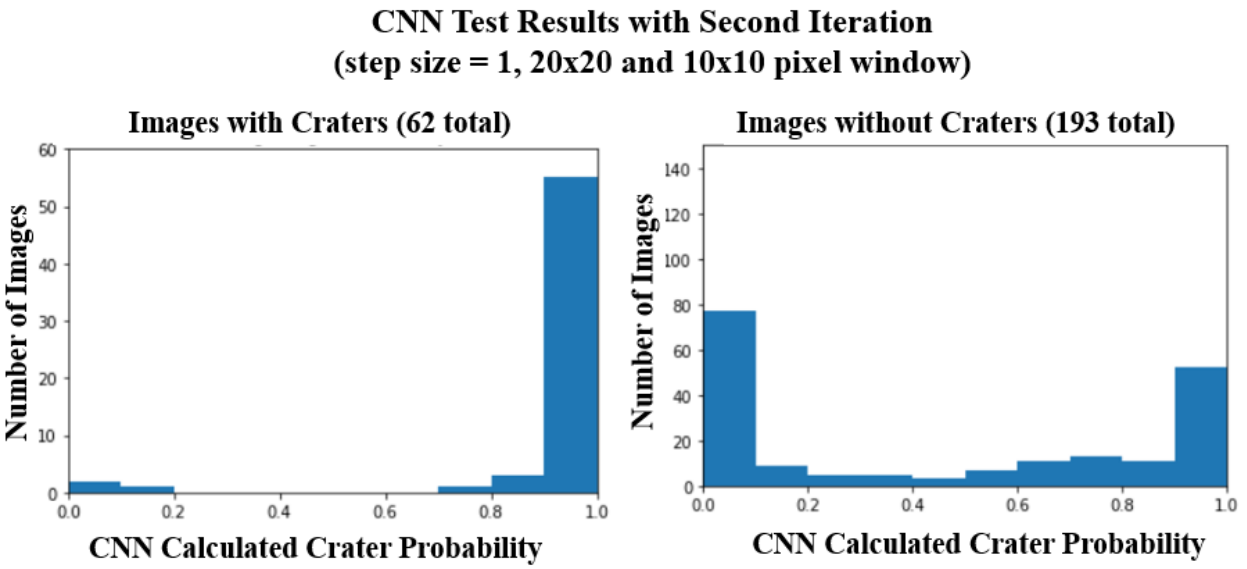

FIGURE 8.13: Performance of the CNN on images from Stardust@Home images with and without craters after reducing sliding window step size and adding a second window. Detection of authentic craters improved dramatically to a nearly 90% detection rate with a threshold of 0.9. False positive rates increased as well, though only ~25% of images without craters were falsely labeled.

Crater detection improved considerably following the window and step size modifications.

55 out of 62 crater containing images were correctly labeled as having a high probability (>0.9) of

containing a crater, nearly doubling the correct detection rates of the first iteration. As expected, an increase in false positives was also observed. 50 out of 193 images without craters were now labeled as having a high probability (>0.9) of containing a crater, an increase from 38 out of 193 in the previous iteration. However, the increase in false positives appears minor when compared to the dramatic increase in authentic crater detection rates. Results would likely improve if looking for larger craters constituting a larger number of pixels as these features would be easier to identify and crater-like foil features (that are not true craters) are less likely to occur on larger size scales. The Stardust@Home images are a challenging dataset. Many observed craters from the Stardust@Home secondary electron images constitute a region of 7x7 pixels or smaller, making their identification difficult even with a more sophisticated CNN. Higher magnification images with fewer nanometers per pixel would improve the CNN's ability to accurately identify craters.

While CNN performance improved with these changes, computation time greatly increased. Analysis of an image took on average 525 seconds, a large increase from the 66 seconds per image on the first iteration. Adding a second window increased the computation time per image by roughly a factor of 2, and decreasing the step size from 2 to 1 increased the computation time by roughly a factor of 4, overall increasing the computation time per image by roughly a factor of 8. Computation times could be dramatically reduced by running the CNN on more powerful hardware. Keras is capable of running across multiple GPUs (graphics processing units) which would greatly decrease the computation times.

The current iteration of the CNN is not more effective than other attempts to automate crater searches. A study using a normalized cross correlation algorithm was able to analyze 3 megapixel images within 6 minutes, achieving a sensitivity of 96% and a false positive rate of 8.7% (Ogliore *et al*., 2012b). Our current iteration of the CNN analyzes a ~.2 megapixel image

within 9 minutes, achieving a detection rate of ~90% and a false positive rate of 25%. However, the CNN has potential to become quicker and more accurate. Adding more craters to the CNN training set will increase its accuracy and will increase the amount of time necessary to train the CNN, but will not increase the time needed to scan the SEM images. As a result the CNN can become the more accurate tool as our library of example craters increases.

8.4.8 Potential Improvements to the CNN's Performance

The primary way to improve the performance of the CNN is through the elimination of the sliding window algorithm. The sliding window algorithm is fairly primitive and requires re-running thousands of subsections of the image through the CNN. Replacing the sliding window algorithm with an initial convolution of the full input image itself would greatly speed up the algorithm. Modern CNN models can search images of similar sizes to ours for a variety of features in fractions of a second (Redmon *et al*., 2016). Making this change would allow the CNN to operate extremely quickly, but would require a redesign of the program and a higher level understanding of CNN structures.

Improving the performance of the current iteration of the CNN will require a redefinition of the CNN's goals: Further accuracy improvements will come at the cost of additional computation time or additional effort on the part of the researcher.

The false positive and false negative rates could be improved by increasing the size of the CNN's input image, increasing the size of the CNN (e.g., increasing the number of hidden layers or increasing the number of nodes per layer), or by obtaining additional training and test images of crater and no crater images. Increasing the size of the CNN's input image from 20x20 pixels would allow for additional detail from the input images to be saved, allowing for the CNN to train on more detailed images and obtain more accurate weight values. Similarly, increasing the size of

the CNN by expanding the number of layers, channels, or nodes in its architecture would allow the CNN to perform more complex decision making. However, both of these changes would increase the time necessary to feed an image through the CNN and thus would come at the cost of additional computation time. Obtaining additional training images would also allow the CNN to be able to more accurately identify crater features, but obtaining these additional images could be time consuming for the researcher. The minor increase in accuracy afforded by additional training images may not be worth the time required to gather them.

Chapter 9: Conclusions

NASA's Stardust mission remains our only source of unambiguously cometary material, and as such it retains unique scientific significance. However, the collection media and conditions have made analysis of this material difficult. As a result, much of the returned cometary material remains uncharacterized despite its ability to provide insight into an unexplored region of the Solar System.

The Stardust samples have the unique ability to provide insight into the composition of a known outer Solar System body. As a result, they can provide insight into the evolution and formation processes of the early Solar System. In performing the research presented in this thesis, I aimed to provide answers or insight into the following questions:

• How are aggregate impactors processed compared to single-grain impactors?

The study of the Acfer 094 analog foils, coupled with the study of the refractory Ti- and Si-based impactors, appears to indicate that aggregate impactors experience more alteration than single-grain impactors. Individual grains in the refractory analogs showed less alteration than larger clusters of impactors, and the Acfer 094 aggregate impactors showed signs of excessive alteration such as amorphous melt layers, volatile loss, and vesicle formation. However, the analog foils contained more alteration overall than their authentic Stardust equivalents, indicating that the analog foils, which in the past have focused on investigating large (> 10 μm) craters, are not perfect replicas of the Stardust impactors. As a result, drawing quantitative, detailed conclusions about Stardust impact processing from LGG produced analog foils is difficult.

The cause of the excessive alteration in the analog foils has not yet been determined. The low compressive strength of cometary material may have resulted in a different partitioning of the

impactors' energy, minimizing alteration to the Stardust impactors. The most likely cause of the excessive alteration in the analog foils is the addition of an acceleration event (through use of a LGG to replicate Stardust impact speeds) to the deceleration event of impacting the foils.

• Are organic materials capable of surviving the impact processing?

The study of the Tagish Lake analog foils indicated that carbonaceous material, though likely to be destroyed, is capable of composing a component in the crater residues in the Stardust collector foils. The majority of the observed craters did not contain carbon, and some craters had features indicating that volatile or carbonaceous materials were lost during impact processing. Additionally, organic carbon materials are likely to be heavily altered by the temperatures and pressures experienced during collection. However, carbon was observed in one analog crater, and the analog craters experience more alteration than their authentic Stardust counterparts, indicating that carbon components can leave some residue in the Stardust craters. Previous observation of an N-rich presolar grain in isotopic measurements of the Stardust craters (Stadermann *et al*., 2008) suggest that some organic materials may be capable of surviving the collection process. However, our results indicate that observing carbon signals in the Stardust foils is unlikely.

• How is the fine component of Wild 2 fundamentally different from the coarse component?

The fine component of Wild 2 appears, in part, to be composed of refractory phases. Stardust foil C2113N-B appeared to have taenite and spinel within its crater residues, and Stardust aerogel track 200 may contain oldhamite. Thus, the fine component of Wild 2 does contain a fraction of material that formed in high temperature environments. Additionally, most of the Wild 2 fine material appears to be dominated by silicates roughly consistent with olivine or pyroxene

stoichiometrically, as well as iron-nickel sulfides, both of which are not unique to the comet's fine component.

The lack of crystalline material in our investigated Stardust craters differentiates our studies from previous investigations. Studies of the aerogel tracks by Westphal *et al.* (2009) noted that the crystalline silicate fraction ranged from 0.46-1.0, and previous FIB-TEM studies by Leroux *et al.* (2008; 2010) and Stroud *et al.* (2010) identified surviving crystalline material in 10 out of 22 micron-scale and submicron craters. Our results suggest that the fine component of Wild 2 may be more heavily composed of amorphous materials than previously thought, distinguishing it from the coarse component. Carbon-rich materials from aerogel track 35 indicate that carbon may also constitute a fraction of the Wild 2 fines that has not been observed in the Wild 2 foils, likely due to the destruction of these materials during the collection process. The submicron craters from Stardust Foil C2113N-A suggested that the fine component of Wild 2 may be distinguishable from the coarse component by an overabundance of volatile elements. However, a larger sample size of fines from Wild 2, from both the foils and aerogels, are necessary to improve our confidence in these assertions.

• What is the source of the Wild 2 fines?

Analysis of the submicron craters on Stardust foil C2113N-A indicated that the submicron component of Wild 2 may be enriched in volatiles relative to CI chondrites. Materials formed in the inner Solar System would be depleted in volatiles relative to CI chondrites whereas materials inherited from the Solar System's parent molecular cloud (that subsequently avoided thermal and aqueous processing) would not, indicating that the fine component may originate from the outer Solar System. This would distinguish the fine component from the coarse component, which has

largely been composed of refractory materials that likely formed in the inner Solar System. However, the presence of some refractory materials in the fine component, such as the observed taenite, spinel, and possible oldhamite, indicate that some fraction of the fine component likely formed in the inner Solar System.

• Extract and characterize two craters from the Stardust interstellar foils

I was successful in extracting and characterizing two Stardust interstellar craters remaining from the Stardust Interstellar Preliminary Investigation. However, in characterizing these craters it was revealed that the craters were the result of secondary impactors from the Stardust Solar cells. The result further emphasizes the difficulty in probing these samples.

• Create an automated image searching algorithm to improve crater detection on the Stardust foils

I was successful in using recent advances in convolutional neural network programming to create, train, and utilize a CNN to identify impact craters on the Stardust foils. The current performance of my algorithm is not yet competitive with current foil searching techniques. However, CNNs have the potential to outperform current foil searching techniques with additional convolutional steps or training data. CNNs thus appear to be a promising technique to pursue for future sample searches.

The results of this thesis suggest many avenues to pursue in future studies of Stardust material. Fine-grained material, collected in micron-scale and submicron Stardust foil craters, require further characterization in order to definitively determine the source of the Wild 2 fines. Thus, continued study of the Stardust foils, particularly the submicron craters, appears to be a

promising approach for characterizing Wild 2's fine component. The new plasma ashing technique for separating fine cometary components from the Stardust aerogels appears to be a useful complementary technique for isolating and analyzing fine grains from Wild 2. Additionally, refining CNN design would improve automated feature identification in a variety of sample collection media for a variety of features.

There remain many open questions regarding the composition and history of cometary material, several of which were explored in the work presented in this thesis. Sample collection missions, coupled with constant exploration and improvement of analysis techniques, will continue providing insight into the Solar System's distant materials and distant past.

Bibliography

Amari S., Lewis R. S., & Anders E. (**1994**), "Interstellar grains in meteorites: I. Isolation of SiC, graphite, and diamond; size distributions of SiC and graphite", *Geochimica et Cosmochimica Acta* **58**, 459-470, URL https://doi.org/10.1016/0016-7037(94)90477-4.

Berger E. L., Zega T. J., Keller L. P., & Lauretta D. S. (**2011**), "Evidence for aqueous activity on comet 81P/Wild 2 from sulfide mineral assemblages in Stardust samples and Ci chondrites", *Geochimica et Cosmochimica Acta* **75**, 3501-3513, URL https://doi.org/10.1016/j.gca. 2011.03.026.

Bottke W. F., Durda D. D., Nesvorný D., Jedicke R., Morbidelli A., Vokrouhlický, & Levison H. F. (**2005**), "Linking the collisional history of the main asteroid belt to its dynamical excitation and depletion", *Icarus* **175**, 111-140, URL https://doi.org/10.1016/j.icarus.2005.05.017.

Bradley J. P. & Dai Z. R. (**2004**), "Mechanism of formation of glass with embedded metal and sulfides", *The Astrophysical Journal* **617**, 650-655, URL https://doi.org/10.1086/425292.

Brown P. G., Hildebrand A. R., Zolensky M. E., Grady M., Clayton R. N., Mayeda T. K., Tagliaferri E., Spalding R., MacRae N. D., Hoffman E. L., Mittlefehldt D. W., Wacker J. F., Bird J. A., Campbell M. D., Carpenter R., Gingerich H., Glatiotis M., Greiner E., Mazur M. J., McCausland P. J. A., Plotkin H., & Mazur T. R. (**2000**), "The Fall, Recovery, Orbit, and Composition of the Tagish Lake Meteorite: A New Type of Carbonaceous Chondrite", *Science* **290**, 320-325, URL https://doi.org/10.1126/science.290.5490.320.

Brownlee D. E., Tsou P., Anderson J. D., Hanner M. S., Newburn R. L., Sekanina Z., Clark B. C., Hörz F., Zolensky M. E., Kissel J., McDonnel J. A. M., Sandford S. A., & Tuzzolino A. J. (**2003**), "Stardust: Comet and interstellar dust sample return mission", *Journal of Geophysical Research* **108**, URL https://doi.org/10.1029/2003JE002087.

Brownlee D. E., Hörz F., Newburn R. L., Zolensky M. E., Duxbury T. C., Sandford S., Sekanina Z., Tsou P., Hanner M. S., Clark B. C., Green S. F., & Kissel J. (**2004**), "Surface of young Jupiter family comet 81P/Wild 2: View from the Stardust spacecraft", *Science* **304**, 1764-1769, URL https://doi.org/10.1126/science.1097899.

Brownlee D., Tsou P., Aléon J., Alexander C. M. O'D., Araki T., Bajt S., Baratta G. A., Bastien R., Bland P., Bleuet P., Borg J., Bradley J. P., Brearley A., Brenker F., Brennan S., Bridges J. C., Browning N. D., Brucato J. R., Bullock E., Burchell M. J., Busemann H., Butterworth A., Chaussidon M., Cheuvront A., Chi M., Cintala M. J., Clark B. C., Clemett S. J., Cody G., Colangeli L., Cooper G., Cordier P., Daghlian C., Dai Z., D'Hendecourt L., Djouadi Z., Dominguez G., Duxbury T., Dworkin J. P., Ebel D. S., Economou T. E., Fakra S., Fairey S. A. J., Fallon S., Ferrini G., Ferroir T., Fleckenstein H., Floss C., Flynn G., Franchi I. A., Fries M., Gainsforth Z., Gallien J.-P., Genge M., Gilles M. K., Gillet Ph., Gilmour J., Glavin D. P., Gounelle M., Grady M. M., Graham G. A., Grant P. G., Green S. F., Grossemy F., Grossman L., Grossman J. N., Guan Y., Hagiya K., Harvey R., Heck P., Herzog G. F., Hoppe P., Hörz F., Huth J., Hutcheon I. D., Ignatyev K., Ishii H., Ito M., Jacob D., Jacobsen C., Jacobsen

S., Jones S., Joswiak D., Jurewicz A., Kearsley A. T., Keller L. P., Khodja H., Kilcoyne A. L. D., Kissel J., Krot A., Langenhorst F., Lanzirotti A., Le L., Leshin L. A., Leitner J., Lemelle L., Leroux H., Liu M.-C., Luening K., Lyon I., MacPherson G., Marcus M. A., Marhas K., Marty B., Matrajt G., McKeegan K., Meibom A., Mennella V., Messenger K., Messenger S., Mikouchi T., Mostefaoui S., Nakamura T., Nakano T., Newville M., Nittler L. R., Ohnishi I., Ohsumi K., Okudaira K., Papanastassiou D. A., Palma R., Palumbo M. E., Pepin R. O., Perkins D., Perronnet M., Pianetta P., Rao W., Rietmeijer F. J. M., Robert F., Rost D., Rotundi A., Ryan R., Sandford S. A., Schwandt C. S., See T. H., Schlutter D., Sheffield-Parker J., Simionovici A., Simon S., Sitnitsky I., Snead C. J., Spencer M. K., Stadermann F. J., Steele A., Stephan T., Stroud R., Susini J., Sutton S. R., Suzuki Y., Taheri M., Taylor S., Teslich N., Tomeoka K., Tomioka N., Toppani A., Trigo-Rodríguez J. M., Troadec D., Tsuchiyama A., Tuzzolino A. J., Tyliszczak T., Uesugi K., Velbel M., Vellenga J., Vicenzi E., Vincze L., Warren J., Weber I., Weisberg M., Westphal A. J., Wirick S., Wooden D., Wopenka B., Wozniakiewicz P., Wright I., Yabuta H., Yano H., Young E. D., Zare R. N., Zega T., Ziegler K., Zimmermann L., Zinner E., & Zolensky M. (**2006**), "Comet 81P/Wild 2 under a microscope", *Science* **314**, 1711-1716, URL https://doi.org/10.1126/science.1135840.

Brownlee D., Joswiak D., & Matrajt G. (**2012**), "Overview of the rocky component of Wild 2 comet samples: Insight into the early solar system, relationship with meteoritic materials, and the differences between comets and asteroids", *Meteoritics & Planetary Science* **47**, 453-470, URL https://doi.org/10.1111/j.1945-5100.2012.01339.x.

Burchell M J., Cole M. J., McDonnell J. A. M., & Zarnecki J. C. (**1999**), "Hypervelocity impact studies using the 2 MV Van de Graaff accelerator and two-stage light gas gun of the University of Kent at Canterbury", *Measurement Science and Technology* **10**, 41-50, URL https://doi.org/10.1088/0957-0233/10/1/011.

Burchell M. J., Graham G., & Kearsley A. (**2006**), "Cosmic Dust Collection in Aerogel", *Annual Review of Earth and Planetary Science* **34**, 385-418, URL https://doi.org/10.1146/annurev.earth.34.031405.124939.

Burchell M. J., Fairey S. A. J., Wozniakiewicz P., Brownlee D. E., Hörz F., Kearsley A. T., See T. H., Tsou P., Westphal A., Green S. F., Trigo-Rodríguez J. M., & Domingúez G. (**2008a**), "Characteristics of cometary dust tracks in Stardust aerogel and laboratory calibrations", *Meteoritics & Planetary Science* **43**, 23-40, URL https://doi.org/10.1111/j.1945-5100.2008.tb00608.x

Burchell M. J., Foster N. J., Kearsley A. T., & Creighton J. A. (**2008b**), "Identification of mineral impactors in hypervelocity impact craters in aluminum by Raman spectroscopy of residues", *Meteoritics & Planetary Science* **43**, 135-142, URL https://doi.org/10.1111/j.1945-5100.2008.tb00614.x.

Burchell M. J., Cole M. J., Price M. C., and Kearsley A. T. (**2012**), "Experimental investigation of impacts by solar cell secondary ejecta on silica aerogel and aluminum foil: Implications for the Stardust Interstellar Dust Collector", *Meteoritics & Planetary Science* **47**, 671-683, URL https://doi.org/10.1111/j.1945-5100.2011.01294.x.

Caro G. M. M., Dartois E., & Nakamura-Messenger K. (**2008**), "Characterization of the carbon component in cometary Stardust samples by means of infrared and Raman spectroscopy", *Astronomy & Astrophysics* **485**, 743-751, URL https://doi.org/10.1051/0004-6361:20078879.

Chaumard N., Devouard B., Bouvier A., & Wadhwa M. (**2014**), "Metamorphosed calcium-aluminum-rich inclusions in CK carbonaceous chondrites", *Meteoritics & Planetary Science* **49**, 419-452, URL https://doi.org/10.1111/maps.12260.

Chi M., Ishii H. A., Simon S. B., Bradley J. P., Dai S., Joswiak D., & Browning N. (**2009**), "The origin of refractory minerals in comet 81P/Wild 2", *Geochimica et Cosmochimica Acta* **73**, 7150-7161, URL https://doi.org/10.1016/j.gca.2009.08.033.

Christoffersen R. & Buseck P. R. (**1986**), "Mineralogy of Interplanetary dust particles from the 'olivine' infrared class", *Earth & Planetary Science Letters* **78**, 53-66, URL https://doi.org/10.1016/0012-821X(86)90172-X.

Cliff G. & Lorimer G. W. (**1975**), "The quantitative analysis of thin specimens", *Journal of Microscopy* **103**, 203-207, URL https://doi.org/10.1111/j.1365-2818.1975.tb03895.x.

Croat T. K., Haas B., & Floss C. (**2016**), "The Composition of Surviving Fine-Grained Cometary Material in Stardust Al Foil Craters", in "47th Lunar and Planetary Science Conference", Abstract #2204, Lunar and Planetary Institute, Houston, URL https://www.hou.usra.edu/meetings/lpsc2016/pdf/2204.pdf.

Farinella P. & Davis D. (**1996**), "Short-period comets: Primordial bodies or collisional fragments?", *Science* **273**, 938-941, URL https://doi.org/10.1126/science.273.5277.938.

Floss C., Allen C., Bajt S., Bechtel H. A., Borg J., Brenker F., Bridges J., Brownlee D. E., Burchell M., Burghammer M., Butterworth A. L., Cloetens P., Davis A. M., Doll R., Flynn G. J., Frank D., Gainsforth Z., Grün E., Heck P. R., Hillier J. K., Hoppe P., Nittler L., Ogliore R. C., Ong W. J., Postberg F., Price M. C., Sandford S. A., Sans Tresseras J. A., Schmitz S., Schoonjans T., Schreiber K., Silversmit G., Simionovici A., Srama R., Stadermann F. J., Stephan T., Stodolna J., Stroud R. M., Sutton S. R., Toucoulou R., Trieloff M., Tsou P., Tsuchiyama A., Tyliczszak T., Vekemans B., Vincze L., Westphal A. J., Zolensky M. E., & >29,000 Stardust@home dusters. (**2011**), "Stardust Interstellar Foils I1061N,1 and I1031N,1: First results from automated crater searches and future analytical possibilities" in "42nd Lunar and Planetary Science Conference", Abstract #1576, Lunar and Planetary Institute, Houston, URL https://www.lpi.usra.edu/meetings/lpsc2011/pdf/1576.pdf.

Floss C., Stadermann F. J., Kearsley A. T., Burchell M. J., & Ong W. J. (**2013**), "The abundance of presolar grains in comet 81P/Wild 2", *The Astrophysical Journal* **763**, 140, URL https://doi.org/10.1088/0004-637X/763/2/140.

Flynn G., Bleuet P., Borg J., Bradley J. P., Brenker F., Brennan S., Bridges J. C. Brownlee D. E., Bullock E., Burghammer M., Clark B. C., Dai Z. R., Daghlian C. P., Djouadi Z., Fakra S., Ferroir

T., Floss C., Franchi I. A., Gainsforth Z., Gallien J.-P., Gillet P., Grant P. G., Graham G. A., Grossemy F., Heck P., Herzog G. F., Hoppe P., Hörz F., Huth J., Igantyev K., Ishii H., Janssens K., Joswiak D., Kearsley A. T., Khodja H., Lanzirotti A., Leitner J., Lemelle L., Leroux H., Luening K., MacPherson G., Marhas K., Matrajt G., Nakamura T., Nakamura-Messenger K., Nakano T., Newville M., Papanastassiou D. A., Pianetta P., Rao W., Riekel C., Rietmeijer F., Rost D., Schwandt C. S., See T. H., Sheffield-Parker J. A., Simionovici S., Sitnitsky S. I., Snead C. J., Stadermann F. J., Stephan T., Stroud R. M., Susini J., Suzuki Y., Sutton S. R., Taylor S., Teslich N., Troadec D., Tsou P., Tsuchiyama A., Uesugi K., Vekemans B., Vicenzi E., Vincze L., Westphal A. J., Wozniakiewicz P. A., Zinner E., & Zolensky M. (**2006**), "Elemental compositions of comet 81P/Wild 2 samples collected by Stardust", *Science* **314**, 1731-1735, URL https://doi.org/10.1126/science.1136141.

Flynn G. J., Leroux H., Tomeoka K., Tomioka N., Ohnishi I., Mikouchi T., Wirick S., Keller L. P., Jacobsen C., & Sandford S. A. (**2008**), "Carbonate in comets: A comparison of comets 1P/Halley, 9P/Temple 1, and 81P/Wild 2", in "39th Lunar and Planetary Science Conference", Abstract #1979, Lunar and Planetary Institute, Houston, URL https://www.lpi.usra.edu/meetings/lpsc2008/pdf/1979.pdf.

Foster N. F., Wozniakiewicz P. J., Price M. C., Kearsley A. T., & Burchell M. J. (**2013**), "Identification by Raman spectroscopy of Mg-Fe content of olivine samples after impact at 6 km s-1 onto aluminum foil and aerogel: In the laboratory and in Wild-2 cometary samples", *Geochimica et Cosmochimica Acta* **121**, 1-14, URL https://doi.org/10.1016/j.gca.2013.07.022.

Frank D. R., Westphal A. J., Zolensky M. E., Gainsforth Z., Butterworth A. L., Bastien R. K., Allen C., Anderson D., Ansari A., Bajt S., Bassim N., Bechtel H. A., Borg J., Brenker F. E., Bridges J., Brownlee D. E., Burchell M., Burghammer M., Changela H., Cloetens P., Davis A. M., Doll R., Floss C., Flynn G., Grün E., Heck P. R., Hillier J. K., Hoppe P., Hudson B., Huth J., Hvide B., Kearsley A., King A. J., Lai B., Leitner J., Lemelle L., Leroux H., Leonard A., Lettieri R., Marchant W., Nittler L. R., Ogliore R., Ong W. J., Postberg F., Price M. C., Sandford S. A., Tresseras J.-A. S., Schmitz S., Schoonjans T., Silversmit G., Simionovici A. S., Solé V. A., Srama R., Stephan T., Sterken V. J., Stodolna J., Stroud R. M., Sutton S., Trieloff M., Tsou P., Tsuchiyama A., Tyliszczak T., Vekemans B., Vincze L., Korff J. V., Wordsworth N., and Zevin D., & >30,000 Stardust@home dusters. (**2014**), "Stardust Interstellar Preliminary Examination II: Curating the interstellar dust collector, picokeystones, and sources of impact tracks", *Meteoritics & Planetary Science* **49**, 1522-1547, URL https://doi.org/10.1111/maps.12147.

Frisch P. C. (**1994**), "Characteristics of Nearby Interstellar Matter", *Space Science Reviews* **72**, 499-592, URL http://adsabs.harvard.edu/full/1995SSRv...72..499F.

Gerasimov M. V., Yakovlev O. I., Dikov Y. P., & Wlotzka F. (**2000**), "Evaporative differentiation of impact-produced melts: Laser-simulation experiments and comparison with impact glasses from the Logoiski crater", in "Large meorite impacts III", edited by Kenkmann T., Hörz F., & Deutsch A., *Geological Society of America, Special Paper* **384**, 351-366, URL https://doi.org/10.1130/0-8137-2384-1.351.

Grady M. M., Verechovsky A. B., Franchi I. A., Wright I. P., & Pillinger C. T. (**2002**), "Light element geochemistry of the Tagish Lake CI2 chondrite: Comparison with CI1 and CM2 meteorites", *Meteoritics & Planetary Science* **37**, 713-735, URL https://doi.org/10.1111/j.1945-5100.2002.tb00851.x.

Greshake A. (**1997**), "The primitive matrix components of the unique carbonaceous chondrite Acfer 094: a TEM study", *Geochimica et Cosmochimica Acta* **61**, 437-452, URL https://doi.org/10.1016/S0016-7037(96)00332-8.

Grossman J. N. & Brearley A. J. (**2005**), "The onset of metamorphism in ordinary and carbonaceous chondrites", *Meteoritics & Planetary Science* **40**, 87-122, URL https://doi.org/ 10.1111/j.1945-5100.2005.tb00366.x.

Halevy A., Norvig P., & Pereira F. (**2009**), "The Unreasonable Effectiveness of Data", *Intelligent Systems IEEE* **24**, 8-12, URL https://doi.org/10.1109/MIS.2009.36.

Hanner M. S. (**2003**), "The Mineralogy of Cometary Dust", in "Astromineralogy", edited by Henning T., 171-188, URL https://link.springer.com/chapter/10.1007%2F3-540-45840-9_4.

Hashimoto A. (**1983**), "Evaporative metamorphism in the early solar nebula – Evaporation experiments on the melt FeO-MgO-SiO_2-CaO-Al_2O_3 and chemical fractionations of primitive materials", *Geochemical Journal* **17**, 111-145, URL https://doi.org/10.2343/geochemj.17.111.

Heinisch P., Auster H.-U., Gundlach B., Blum J., Güttler C., Tubiana C., Sierks H., Hilchenbach M., Biele J., Richter I., & Glassmeier K. H. (**2018**), "Compressive strength of comet 67P/Churyumov-Gerasimenko derived from Philae surface contacts", *Astronomy & Astrophysics*, forthcoming article, URL https://doi.org/10.1051/0004-6361/201833889.

Hörz F., Bastien R., Borg J., Bradley J. P., Bridges J. C., Brownlee D. E., Burchell M. J., Chi M., Cintala M. J., Dai Z. R., Djouadi Z., Dominguez G., Economou T. E., Fairey S. A. J., Floss C., Franchi I. A., Graham G. A., Green S. F., Heck P., Hoppe P., Huth J., Ishii H., Kearsley A. T., Kissel J., Leitner J., Leroux H., Marhas K., Messenger K., Schwandt C. S., See T. H., Snead C., Stadermann F. J., Stephan T., Stroud R., Teslich N., Trigo-Rodríguez J. M., Tuzzolino A. J., Troadec D., Tsou P., Warren J., Westphal A., Wozniakiewicz P., Wright I., & Zinner E. (**2006**), "Impact Features on Stardust: Implications for Comet 81P/Wild 2 Dust", *Science* **314**, 1716-1719, URL https://doi.org/10.1126/science.1135705.

Ishii H. A., Bradley J. P., Dai Z. R., Chi M., Kearsley A. T., Burchell M. J., & Browning N. (**2008**), "Comparison of comet 81P/Wild 2 dust with interplanetary dust from comets", *Science* **319**, 447-450, URL https://doi.org/10.1126/science.1150683.

Jacob D., Stodolna J., Leroux H., Langenhorst F., & Houdellier F. (**2009**), "Pyroxenes microstructure in comet 81P/Wild 2 terminal Stardust particles", *Meteoritics & Planetary Science* **44**, 1475-1488, URL https://doi.org/10.1111/j.1945-5100.2009.tb01187.x.

Joswiak D. J., Brownlee D. E., Matrajt G., Westphal A. J., & Snead C. J. (**2009**), "Kosmochloric Ca-rich pyroxenes and FeO-rich olivines (Kool grains) and associated phases in Stardust tracks and chondritic porous interplanetary dust particles: Possible precursors to FeO-rich type II chondrules in ordinary chondrites", *Meteoritics & Planetary Science* **44**, 1561-1588, URL https://doi.org/10.1111/j.1945-5100.2009.tb01192.x.

Joswiak D. J., Brownlee D. E., Matrajt G., Westphal A. J., Snead C. J., & Gainsforth Z. (**2012**), "Comprehensive examination of large mineral and rock fragments in Stardust tracks: Mineralogy, analog extraterrestrial materials and source regions", *Meteoritics & Planetary Science* **47**, 1-52, URL https://doi.org/10.1111/j.1945-5100.2012.01337.x.

Joswiak D. J., Brownlee D. E., Nguyen A. N., & Messenger S. (**2017**), "Refractory materials in comet samples", *Meteoritics & Planetary Science* **52**, 1612-1648, URL https://doi.org/10.1111/maps.12877.

Kearsley A. T., Burchell M. J., Hörz F., Cole M. J., & Schwandt C. S. (**2006**), "Laboratory simulation of impacts on aluminum foils of the Stardust spacecraft: Calibration of dust particle size from comet Wild-2", *Meteoritics & Planetary Science* **41**, 167-180, URL https://doi.org/10.1111/j.1945-5100.2006.tb00201.x.

Kearsley A. T., Graham G. A., Burchell M. J., Cole M. J., Dai Z. R., Teslich N., Bradley J. P., Chater R., Wozniakiewicz P. A., Spratt J., & Jones G. (**2007**), "Analytical scanning and transmission electron microscopy of laboratory impacts on Stardust aluminum foils: Interpreting impact crater morphology and the composition of impact residues", *Meteoritics & Planetary Science* **42**, 191-210, URL https://doi.org/10.1111/j.1945-5100.2007.tb00227.x.

Kearsley A. T., Borg J., Graham G. A., Burchell M. J., Cole M. J., Leroux H., Bridges J. C., Hörz F., Wozniakiewicz P. J., Bland P. A., Bradley J. P., Dai Z. R., Teslich N., See T., Hoppe P., Heck P. R., Huth J., Stadermann F. J., Floss C., Marhas K., Stephan T., & Leitner J. (**2008**), "Dust from comet Wild 2: Interpreting particle size, shape, structure, and composition from impact features on the Stardust aluminum foils", *Meteoritics & Planetary Science* **43**, 41-73, URL https://doi.org/10.1111/j.1945-5100.2008.tb00609.x.

Kearsley A. T., Burchell M. J., Price M. C., Graham G. A., Wozniakiewicz P. J., Cole M. J., Foster N. J., & Teslich N. (**2009**), "Interpretation of Wild 2 dust fine structure: Comparison of Stardust aluminum foil craters to the three-dimensional shape of experimental impacts by artificial aggregate particles and meteorite powders", *Meteoritics & Planetary Science* **44**, 1489-1509, URL https://doi.org/10.1111/j.1945-5100.2009.tb01188.x.

Kearsley A. T., Westphal A. J., Stadermann F. J., Armes S. P., Ball A. D., Borg J., Bridges J. C., Brownlee D. E., Burchell M. J., Chater R. J., Davis A. M., Floss C., Flynn G., Gainsforth Z., Grün E., Heck P., Hoppe P., Hörz F., Howard L. E., Howe G., Huss G. R., Huth J., Landgraf M., Leitner J., Leroux H., Nittler L., Ogliore R., Postberg F., Price M. C., Srama R., Stroud R., Trieloff M., Trigo-Rodriguez J., Sandford S. A., Stephan T., Sternovsky Z., Tsou P., & Zolensky M. E. (**2010**), "Finding Interstellar Particle Impacts on Stardust Aluminum Foils: The Safe Handling, Imaging, and Analysis of Samples Containing Femtogram Residues", in "41st Lunar

and Planetary Science Conference", Abstract #1593, Lunar and Planetary Institute, Houston, URL https://www.lpi.usra.edu/meetings/lpsc2010/pdf/1593.pdf.

Keller L. P. & McKay D. S. (**1997**), "The nature and origin of rims on lunar soil grains", *Geochimica et Cosmochimica Acta* **61**, 2331-2341, URL https://doi.org/10.1016/S0016-7037(97)00085-9.

Keller L. P. & Messenger S. (**2011**), "On the origins of GEMS grains", *Geochimica et Cosmochimica Acta* **75**, 5336-5365, URL https://doi.org/10.1016/j.gca.2011.06.040.

Landgraf M., Müller M., & Grün E. (**1999**), "Prediction of the In-Situ Dust Measurements of the Stardust Mission to Comet 81P/Wild 2", *Planetary and Space Science* **47**, 1029-1050, URL https://doi.org/10.1016/S0032-0633(99)00031-8.

Leitner J., Hoppe P., & Heck P. R. (**2010**), "First discovery of presolar material of possible supernova origin in impact residues from comet 81P/Wild 2", in "41st Lunar and Planetary Science Conference", Abstract #1607, Lunar and Planetary Institute, Houston, URL https://www.lpi.usra.edu/meetings/lpsc2010/pdf/1607.pdf.

Leitner J., Heck P. R., Hoppe P., & Huth J. (**2012**), "The C-, N-, and O-isotopic composition of cometary dust from comet 81P/Wild 2", in "43rd Lunar and Planetary Science Conference", Abstract #1839, Lunar and Planetary Institute, Houston, URL https://www.lpi.usra.edu /meetings/lpsc2012/pdf/1839.pdf.

Leroux H., Stroud R. M., Dai Z. R., Graham G. A., Troadec D., Bradley J. P., Teslich N., Borg J., Kearsley A. T., & Hörz F. (**2008**), "Transmission electron microscopy of cometary residues from micron-sized craters in the Stardust Al foils", *Meteoritics & Planetary Science* **43**, 143-160, URL https://doi.org/10.1111/j.1945-5100.2008.tb00615.x.

Leroux H., Kearsley A. T., & Troadec D. (**2010**), "Mineralogy of Wild 2 Residues in Micron-Sized Craters from the Stardust Al-Foils", in "41st Lunar and Planetary Science Conference", Abstract #1621, Lunar and Planetary Institute, Houston, URL https://www.lpi.usra.edu/ meetings/lpsc2010/pdf/1621.pdf.

Lodders K. (**1996**), "Oldhamite in Enstatite Achondrites (Aubrites)", in "Twentieth Symposium on Antarctic Meteorites. Proceedings of the NIPR Symposium No. 9", National Institute of Polar Research, 127-142, URL http://adsabs.harvard.edu/full/1996AMR.....9..127L.

Lodders K. (**2003**), "Solar System Abundances and Condensation Temperatures of the Elements", *The Astrophysical Journal* **591**, 1220-1247, URL https://doi.org/10.1086/375492.

Mason B. (**1979**), "Data of Geochemistry", in "Geological Survey Professional Paper", 440-B-1, 132.

McKeegan K. D., Aleon J., Bradley J., Brownlee D., Busemann H., Butterworth A., Chaussidon M., Fallon S., Floss C., Gilmour J., Gounelle M., Graham G., Guan Y., Heck P. R., Hoppe P.,

Hutcheon I. D., Huth J., Ishii H., Ito M., Jacobsen S. B., Kearsley A., Leshin L. A., Liu M.-C., Lyon I., Marhas K., Marty B., Matrajt G., Meibom A., Messenger S., Mostefaoui S., Mukhopadhyay S., Nakamura-Messenger K., Nittler L., Palma R., Pepin R. O., Papanastassiou D. A., Robert F., Schlutter D., Snead C. J., Stadermann F. J., Stroud R., Tsou P., Westphal A., Young E. D., Ziegler K., Zimmermann L., & Zinner E. (**2006**), "Isotopic compositions of cometary matter returned by Stardust", *Science* **314**, 1724-1728, URL https://doi.org/10.1126/science.1135992.

Nakamura T., Noguchi T., Tsuchiyama A., Ushikubo T., Kita N. T., Valley J. W., Zolensky M. E., Kakazu Y., Sakamoto K., Mashio E., Uesugi K., & Nakano T. (**2008**), "Chondrule-like objects in short-period comet 81P/Wild 2", *Science* **321**, 1664-1667, URL https://doi.org/10.1126/sceince.1160995.

Nesvorny D., Jenniskens P., Levison H. F., Bottke W. F., Vokrouhlický D., & Gounelle M. (**2010**), "Cometary origin of the zodiacal cloud and carbonaceous micrometeorites. Implicates for hot debris disks", *The Astrophysical Journal* **713**, 816-836, URL https://doi.org/10.1088/0004-637X/713/2/816.

Newbury D. E. & Ritchie N. W. M. (**2015**), "Performing elemental microanalysis with high accuracy and high precision by scanning electron microscopy/silicon drift detector energy-dispersive X-ray spectrometry (SEM/SDD-EDS)", *Journal of Materials Science* **50**, 493-518, URL https://doi.org/10.1007/s10853-014-8685-2.

Newton J., Bischoff A., Arden J. W., Franchi I. A., Geiger T., Greshake A., & Pillinger C. T. (**1995**), "Acfer 094, a uniquely primitive carbonaceous chondrite from the Sahara", *Meteoritics* **30**, 47-56, URL https://doi.org/10.1111/j.1945-5100.1995.tb01211.x.

Noble S. K., Keller L. P., Christoffersen R., & Rahman Z. (**2015**), "The Microstructure of a Micrometeorite Impact into Lunar Olivine", in "2015 Workshop on Space Weathering of Airless Bodies", Abstract #2034, Solar System Exploration Research Virtual Institute, Houston, URL https://www.hou.usra.edu/meetings/airlessbodies2015/pdf/2034.pdf.

Ogliore R. C., Butterworth A. L., Fakra S. C., Gainsforth Z., Marcus M. A., & Westphal A. J. (**2010**), "Comparison of the oxidation state of Fe in comet 81P/Wild 2 and chondritic-porous interplanetary dust particles", *Earth and Planetary Science Letters* **296**, 278-286, URL https://doi.org/10.1016/j.epsl.2010.05.011.

Ogliore R. C., Huss G. R., Nagashima K., Butterworth A. L., Gainsforth Z., Stodolna Z. J., Westphal A. J., Joswiak D., & Tyliszczak T. (**2012a**), "Incorporation of a late-forming chondrule into Comet Wild 2", *Astrophysical Journal Letters* **745**, L19, URL https://doi.org/10.1088/2041-8205/745/2/L19.

Ogliore R. C., Floss C., Stadermann F. J., Kearsley A. T., Leitner J., Stroud R. M., & Westphal A. J. (**2012b**), "Automated searching of Stardust interstellar foils", *Meteoritics & Planetary Science* **47**, 729-736, URL https://doi.org/10.1111/j.1945-5100.2011.01325.x.

Ogliore R. C., Nagashima K., Huss G. R., Westphal A. J., Gainsforth Z., & Butterworth A. L. (**2015**), "Oxygen isotopic composition of coarse- and fine-grained material from comet 81P/Wild 2", *Geochimica et Cosmochimica Acta* **166**, 74-91, URL https://doi.org/10.1016/j.gca. 2015.04.028.

Price M. C., Kearsley A. T., Burchell M. J., Hörz F., Borg J., Bridges J. C., Cole M. J., Floss C., Graham G., Green S. F., Hoppe P., Leroux H., Marhas K. K., Park N., Stroud R., Stadermann F. J., Telisch N., & Wozniakiewicz P. J. (**2010**), "Comet 81P/Wild 2: The size distribution of finer (sub-10 μm) dust collected by the Stardust spacecraft", *Meteoritics & Planetary Science* **45**, 1409-1428, URL https://doi.org/10.1111/j.1945-5100.2010.01104.x.

Price M. C., Kearsley A. T., Burchell M. J., Howard L. E., Hillier J. K., Starkey N. A., Wozniakiewicz P. J., & Cole M. J. (**2012**), "Stardust interstellar dust calibration: Hydrocode modeling of impacts on Al-1100 foil at velocities up to 300 km s^{-1} and validation with experimental data", *Meteoritics & Planetary Science* **47**, 684-695, URL https://doi.org/ 10.1111/j.1945-5100.2011.01300.x.

Redmon J., Divvala S. K., Girshick R. B., & Farhadi A. (**2016**), "You Only Look Once: Unified, Real-Time Object Detection", in "IEEE Conference on Computer Vision and Pattern Recognition", URL https://doi.org/10.1109/CVPR.2016.91.

Rietmeijer F. J. M. (**1998**), "Interplanetary dust particles", in "Planetary Materials", edited by Papike J. J. *Reviews in Mineralogy* **36**, 2-1–2-95.

Ritchie N. W. M. (**2011**), "Standards-Based Quantification in DTSA-II – Part I", *Microscopy Today* **19**, 30-36, URL https://doi.org/10.1017/S155192951100085X.

Ritchie N. W. M. (**2012**), "Standards-Based Quantification in DTSA-II – Part II", *Microscopy Today* **20**, 24-28, URL https://doi.org/10.1017/S15519295110001398.

Sandford S. A., Aléon J., Alexander C. M. O'D., Araki T., Bajt S., Baratta G. A., Borg J., Bradley J. P., Brownlee D. E., Brucato J. R., Burchell M. J., Busemann H., Butterworth A., Clemett S. J., Cody G., Colangeli L., Cooper G., D'Hendecourt L., Djouadi Z., Dworkin J. P., Ferrini G., Fleckenstein H., Flynn G. J., Franchi I. A., Fries M., Gilles M. K., Glavin D. P., Gounelle M., Grossemy F., Jacobsen C., Keller L. P., Kilcoyne A. L. D., Leitner J., Matrajt G., Meibom A., Mennella V., Mostefaoui S., Nittler L. R., Palumbo M. E., Papanastassiou D. A., Robert F., Rotundi A., Snead C. J., Spencer M. K., Stadermann F. J., Steele A., Stephan T., Tsou P., Tyliszczak T., Westphal A. J., Wirick S., Wopenka B., Yabuta H., Zare R. N., & Zolensky M. E. (**2006**), "Organics Captured from Comet 81P/Wild 2 by the Stardust Spacecraft", *Science* **314**, 1720-1724, URL https://doi.org/10.1126/science.1135841.

Schlichting H., Ofek E., Sari R., Nelan E., Gal-Yam A., Wenz M., Muirhead P., & Javanfar N. (**2012**), "Measuring the abundance of sub-kilometer-sized Kuiper Belt objects using stellar occultations", *The Astrophysical Journal* **761**, 150, URL https://doi.org/10.1088/0004-637X/761/2/150.

Schramm L. S., Brownlee D. E., & Wheelock M. M. (**1989**), "Major element composition of stratospheric micrometeorites", *Meteoritics* **24**, 99-112, URL https://doi.org/10.111/j.1945-5100.1989.tb00950.x.

Scott E. R. D., Krot A. N., & Sanders I. S. (**2018**), "Isotopic Dichotomy among Meteorites and Its Bearing on the Protoplanetary Disk", *The Astrophysical Journal* **854**, 164, URL https://doi.org/10.3847/1538-4357/aaa5a5.

Seiler H. (**1983**), "Secondary electron emission in the scanning electron microscope", *Journal of Applied Physics* **54**, R1-R18, URL https://aip.scitation.org/doi/pdf/10.1063/1.332840.

Sekanina Z. & Yeomans D. K. (**1985**), "Orbital motion, nucleus precession, and splitting of periodic Comet Brooks 2", *Astronomical Journal* **90**, 2335-2352, URL https://doi.org/10.1086/113939.

Sekanina Z. (**2003)**, "A model for comet 81P/Wild 2", *Journal of Geophysical Research* **108**, URL https://doi.org/10.1029/2003JE002093.

Simon S. B., Joswiak D. J., Ishii H. A., Bradley J. P., Chi M., Grossman L., Aléon J., Brownlee D. E., Fallon S., Hutcheon I. D., Matrajt G., & McKeegan K. D. (**2008**), "A refractory inclusion returned by Stardust from comet 81P/Wild 2", *Meteoritics & Planetary Science* **43**, 861-877, URL https://doi.org/10.1111/j.1945-5100.2008.tb00648.x.

Skinner B. J. & Luce F. D. (**1971**), "Solid Solutions of the Type (Ca,Mg,Mn,Fe)S and Their Use as Geothermometers for the Enstatite Chondrites", *The American Mineralogist* **56**, 1271-1296, URL https://pubs.geoscienceworld.org/msa/ammin/article-pdf/56/7-8/1269/4250637/am-1971-1269.pdf.

Stadermann F. J., Hoppe P., Floss C., Heck P. R., Hörz F., Huth J., Kearsley A. T., Leitner J., Marhas K. K., McKeegan K. D., & Stephan T. (**2008**), "Stardust in Stardust – The C, N, and O isotopic compositions of Wild 2 cometary matter in Al foil impacts", *Meteoritics & Planetary Science* **43**, 299-313, URL https://doi.org/10.1111/j.1945-5100.2008.tb00624.x.

Stodolna J., Jacob D., & Leroux H. (**2012**), "Mineralogy and petrology of Stardust particles encased in the bulb of track 80: TEM investigation of the Wild 2 fine-grained material", *Geochimica et Cosmochimica Acta* **87**, 35-50, URL https://doi.org/10.1016/j.gca.2012.03.026.

Stroud R. M., Koch I. M., Bassim N. D., Piccard Y. N., & Nittler L. R. (**2010**), "Structure and Composition of Comet Wild 2 Residues in Sub-Micron to Micron-Sized Craters", in "41st Lunar and Planetary Science Conference", Abstract #1792, Lunar and Planetary Institute, Houston, URL https://www.lpi.usra.edu/meetings/lpsc2010/pdf/1792.pdf.

Stroud R. M., Allen C., Bajt S., Bechtel H. A., Borg J., Brenker F., Bridges J., Brownlee D. E., Burchell M., Burghammer M., Butterworth A. L., Cloetens P., Davis A. M., Floss C., Flynn G. J., Frank D., Gainsforth Z., Grün E., Heck P. R., Hillier J. K., Hoppe P., Howard L., Huss G. R., Huth J., Kearsley A., King A. J., Lai B., Leitner J., Lemelle L., Leroux H., Nittler L. R., Ogliore

R. C., Postberg F., Price M. C., Sandford S. A., Sans Tresseras J. A., Schmitz S., Schoonjans T., Silversmit G., Simionovici A., Srama R., Stadermann F. J., Stephan T., Stodolna J., Sutton S. R., Toucoulou R., Trieloff M., Tsou P., Tsuchiyama A., Tyliczszak T., Vekemans B., Vincze L., Westphal A. J., Zolensky M. E., & >29,000 Stardust@home dusters. (**2011)**, "Identification of impact craters in foils from the Stardust interstellar dust collector", in "42nd Lunar and Planetary Science Conference", Abstract #1753, Lunar and Planetary Institute, Houston, URL https://www.lpi.usra.edu/meetings/lpsc2011/pdf/1753.pdf.

Stroud R. M., Allen C., Ansari A., Anderson D., Bajt S., Bassim N., Bastien R. S., Bechtel H. A., Borg J., Brenker F. E., Bridges J., Brownlee D. E., Burchell M., Burghammer M., Butterworth A. L., Changela H., Cloetens P., Davis A. M., Doll R., Floss C., Flynn C. G., Frank D. R., Gainsforth Z., Grün E., Heck P. R., Hillier J. K., Hoppe P., Huth J., Hvide B., Kearsley A., King A. J., Kotula P., Lai B., Leitner J., Lemelle L., Leroux H., Leonard A., Lettieri R., Marchant W., Nittler L. R., Ogliore R., Ong W. J., Postberg F., Price M. C., Sandford S. A., Tresseras J.-A. S., Schmitz S., Schoonjans T., Schreiber K., Silversmit G., Simionovici A. S., Solé V. A., Srama R., Stephan T., Sterken V. J., Stodolna J., Sutton S., Trieloff M., Tsou P., Tsuchiyama A., Tyliszczak T., Vekemans B., Vincze L., Westphal A. J., Von Korff J., Zevin D., & Zolensky M. E. (**2014**), "Stardust interstellar preliminary examination XI: Identification and elemental analysis of impact craters on Al foils from the Stardust Interstellar Dust Collector", *Meteoritics & Planetary Science* **49**, 1698-1719, URL https://doi.org/10.1111/maps.12136.

Trigo-Rodríguez J. M., Domínguez G., Burchell M. J., Hörz F., & Llorca J. (**2008**), "Bulbous tracks arising from hypervelocity capture in aerogel", *Meteoritics & Planetary Science* **43**, 75-86, URL https://doi.org/10.1111/j.1945-5100.2008.tb00610.x.

Tsou P. (**1995**), "Silica aerogel captures cosmic dust intact", *Journal of Non-Crystalline Solids* **186**, 415-427, URL: https://doi.org/10.1016/0022-3093(95)00065-8.

Tsou P., Brownlee D. E., Sandford S. A., Hörz F., & Zolensky M. E. (**2003**), "Wild 2 and interstellar sample collection and Earth return", *Journal of Geophysical Research* **108**, URL: https://doi.org/10.1029/2003JE002109.

Tsou P., Brownlee D. E., Anderson J. D., Bhaskaran S., Cheuvront A. R., Clark B C., Duxbury T., Economou T., Green S. F., Hanner M. S., Hörz F., Kissel J., McDonnell J. A. M., Newburn R. L., Ryan R. E., Sandford S. A., Sekanina Z., Tuzzolino A. J., Vellinga J. M., & Zolensky M. E. (**2004**), "Stardust encounters comet 81P/Wild 2", *Journal of Geophysical Research* **109**, URL https://doi.org/10.1029/2004JE002317.

Wang W.-K., Lin Y.-X., & Xu Y.-J. (**2018**), "Structural and Fluorine Plasma Etching Behavior of Sputter-Deposition Yttrium Fluoride Film", *Nanomaterials (Basel)* **8**, 936, URL https://doi.org/10.3390/nano8110936.

Wasson J. T. & Rubin A. E. (**2010**), "Matrix and whole-rock fractionations in the Acfer 094 type 3.0 ungrouped carbonaceous chondrite", *Meteoritics & Planetary Science* **45**, 73-90, URL https://doi.org/10.1111/j.1945-5100.2009.01006.x.

Westphal A. J., Snead C., Butterworth A., Graham G. A., Bradley J. P., Bajt S., Grant P. G., Bench G., Brennan S., & Pianetta P. (**2004a**), "Aerogel keystones: Extraction of complete hypervelocity impact events from aerogel collectors", *Meteoritics & Planetary Science* **39**, 1375-1386, URL: https://doi.org/10.1111/j.1945-5100.2004.tb00952.x.

Westphal A. J., Butterworth A. L., Snead C. J., Dominguez G., Weber P. K., Hutcheon I. D., Huss G. R., Nguyen C. V., Graham G. A., Ryerson F., & Bradley J. P. (**2004b**), "Technique for concentration of carbonaceous material from aerogel collectors using HF-vapor etching", in "35th Lunar and Planetary Science Conference", Abstract #1860, Lunar and Planetary Institute, Houston, URL https://www.lpi.usra.edu/meetings/lpsc2004/pdf/1860.pdf.

Westphal A. J., Bastien R. K., Borg J., Bridges J., Brownlee D. E., Burchell M. J., Cheng A. F., Clark B. C., Djouadi Z., Floss C., Franchi I., Gainsforth Z., Graham G., Green S. F., Heck P. R., Horányi M., Hoppe P., Hörz F. P., Huth J., Kearsley A., Leroux H., Marhas K., Nakamura‐Messenger K., Sandford S. A., See T. H., Stadermann F. J., Teslich N. E., Tsitrin S., Warren J. L., Wozniakiewicz P. J., & Zolensky M. E. (**2008**), "Discovery of non-random spatial distribution of impacts in the Stardust cometary collector", *Meteoritics & Planetary Science* **43**, 415-429, URL https://doi.org/10.1111/j.1945-5100.2008.tb00630.x.

Westphal A. J., Fakra S. C., Gainsforth Z., Marcus M. A., Ogliore R. C., & Butterworth A. L. (**2009**), "Mixing fraction of inner solar system material in comet 81P/Wild 2", *The Astrophysical Journal* **694**, 18-28, URL https://doi.org/10.1088/0004-637X/694/1/18.

Westphal A. J., Bechtel H. A., Brenker F. E., Butterworth A. L., Flynn G., Frank D. R., Gainsforth Z., Hillier J. K., Postberg F., Simionovici A. S., Sterken V. J., Stroud R. M., Allen C., Anderson D., Ansari A., Bajt S., Bastien R. K., Bassim N., Borg J., Bridges J., Brownlee D. E., Burchell M., Burghammer M., Changela H., Cloetens P., Davis A. M., Doll R., Floss C., Grün E., Heck P. R., Hoppe P., Hudson B., Huth J., Hvide B., Kearsley A., King A. J., Lai B., Leitner J., Lemelle L., Leroux H., Leonard A., Lettieri R., Marchant W., Nittler L. R., Ogliore R., Ong W. J., Price M. C., Sandford S. A., Sans Tresseras J.-A., Schmitz S., Schoonjans T., Silversmit G., Solé V. A., Srama R., Stadermann F., Stephan T., Stodolna J., Sutton S., Trieloff M., Tsou P., Tsuchiyama A., Tyliszczak T., Vekemans B., Vincze L., Korff J. von, Wordsworth N., Zevin D., Zolensky M. E., & >30,000 Stardust@home dusters. (**2014a**), "Final reports of the Stardust Interstellar Preliminary Examination", *Meteoritics & Planetary Science* **49**, 1720-1733, URL https://doi.org/10.1111/maps.12221.

Westphal A. J., Anderson D., Butterworth A. L., Frank D. R., Lettieri R., Marchant W., Von Korff J., Zevin D., Ardizzone A., Campanile A., Capraro M., Courtney K., Criswell III M. N., Crumpler D., Cwik R., Gray F. J., Hudson B., Imada G., Karr J., Lau Wan Wah L., Mazzucato M., Motta P. G., Rigamonti C., Spencer R. C., Woodrough S. B., Cimmino Santoni I. C., Sperry G., Terry J.-N., Wordsworth N., Yahnke T. Sr., Allen C., Ansari A., Bajt S., Bastien R. K., Bassim N., Bechtel H. A., Borg J., Brenker F. E., Bridges J., Brownlee D. E., Burchell M., Burghammer M., Changela H., Cloetens P., Davis A. M., Doll R., Floss C., Flynn G., Gainsforth Z., Grün E., Heck P. R., Hillier J. K., Hoppe P., Huth J., Hvide B., Kearsley A., King A. J., Lai B., Leitner J., Lemelle L., Leroux H., Leonard A., Nittler L. R., Ogliore R., Ong W. J., Postberg F., Price M. C., Sandford S. A., Sans Tresseras J.-A., Schmitz S., Schoonjans T., Silversmit G., Simionovici

A. S., Solé V. A., Srama R., Stephan T., Sterken V. J., Stodolna J., Stroud R. M., Sutton S., Trieloff M., Tsou P., Tsuchiyama A., Tyliszczak T., Vekemans B., Vincze L., & Zolensky M. E. (**2014b**), "Stardust interstellar preliminary examination I: Identification of tracks in aerogel", *Meteoritics & Planetary Science* **49**, 1509-1521, URL https://doi.org/10.1111/maps.12168.

Westphal A. J., Stroud R. M., Bechtel H. A., Brenker F. E., Butterworth A. L., Flynn G. J., Frank D. R., Gainsforth Z., Hillier J. K., Postberg F., Simionovici A. S., Sterken V. J., Nittler L. R., Allen C., Anderson D., Ansari A., Bajt S., Bastien R. K., Bassim N., Bridges J., Brownlee D. E., Burchell M., Burghammer M., Changela H., Cloetens P., Davis A. M., Doll R., Floss C., Grün E., Heck P. R., Hoppe P., Hudson B., Huth J., Kearsley A., King A. J., Lai B., Leitner J., Lemelle L., Leonard A., Leroux H., Lettieri R., Marchant W., Ogliore R., Jia Ong W., Price M. C., Sandford S. A., Sans Tresseras J.-A., Schmitz S., Schoonjans T., Schreiber K., Silversmit G., Solé V. A., Srama R., Stadermann F., Stephan T., Stodolna J., Sutton S., Trieloff M., Tsou P., Tyliszczak T., Vekemans B., Vincze L., Von Korff N., Wordsworth M., Zevin D., Zolensky M. E., & 30714 Stardust@home dusters. (**2014c**), "Evidence for interstellar origin of seven dust particles collected by the Stardust spacecraft", *Science* **345**, 786-791, URL https://doi.org/10.1126/science.1252496.

Westphal A. J., Bridges J. C., Brownlee D. E., Butterworth A. L., De Gregorio B. T., Dominguez G., Flynn G. J., Gainsforth Z., Ishii H. A., Joswiak D., Nittler L. R., Ogliore R. C., Palma R., Pepin R. O., Stephan T., & Zolensky M. E. (**2017**), "The future of Stardust science", *Meteoritics & Planetary Science* **52**, 1859-1898, URL https://doi.org/10.1111/maps.12893.

Williams D. B. & Carter C. B. (**1996**), "Transmission Electron Microscopy – A Textbook for Materials Science", Plenum Press.

Williams K. R., Gupta K., & Wasilik M. (**2003**), "Etch Rates for Micromachining Processing – Part II", *Journal of Microelectromechanical Systems* **12**, 761-778, URL http://www.montana.edu/tjkaiser/ee505/homework/Williams_etch_rates.pdf.

Wirick S., Leroux H., Tomeoka K., Zolensky M., Tyliszczak T., Butterworth A., Tomioka N., Ohnishi I., Nakamura Messnger K., Sandford S., Keller L., & Jacobsen C. (**2007**), "Carbonates found in Stardust aerogel tracks", in "38th Lunar and Planetary Science Conference", Abstract #1534, Lunar and Planetary Institute, Houston, URL https://www.lpi.usra.edu/meetings/lpsc2007/pdf/1534.pdf.

Wozniakiewicz P. J., Kearsley A. T., Burchell M. J., Foster N. J., Cole M. J., Bland P. A., & Russell S. S. (**2009**), "In situ analysis of residues resulting from laboratory impacts into aluminum 1100 foil: Implications for Stardust crater analyses", *Meteoritics & Planetary Science* **44**, 1541-1559, URL https://doi.org/10.1111/j.1945-5100.2009.tb01191.x.

Wozniakiewicz P. J., Ishii H. A., Kearsley A. T., Burchell M. J., Bland P. A., Bradley J. P., Dai Z., Teslich N., Collins G. S., Cole M. J., & Russell S. S. (**2011**), "Investigation of iron sulfide impact crater residues: A combined analysis by scanning and transmission electron microscopy", *Meteoritics & Planetary Science* **46**, 1007-1027, URL https://doi.org/10.1111/j.1945-5100.2011.01206.x.

Wozniakiewicz P. J., Kearsley A. T., Ishii H. A., Burchell M. J., Bradley J. P., Teslich N., Cole M. J., & Price M. C. (**2012a**), "The origin of crystalline residues in Stardust Al foils: Surviving cometary dust or crystallized impact melts?", *Meteoritics & Planetary Science* **47**, 660-670, URL https://doi.org/10.1111/j.1945-5100.2011.01328.x.

Wozniakiewicz P. J., Ishii H. A., Kearsley A. T., Burchell M. J., Bradley J. P., Price M. C., Teslich N., Lee M. R., & Cole M. J. (**2012b**), "Stardust impact analogs: Resolving pre- and postimpact mineralogy in Stardust Al foils", *Meteoritics & Planetary Science* **47**, 708-728, URL https://doi.org/10.1111/j.1945-5100.2012.01338.x.

Wozniakiewicz P. J., Ishii H. A., Kearsley A. T., Bradley J. P., Price M. C., Burchell M. J., Teslich N., & Cole M. J. (**2015**), "The survivability of phyllosilicates and carbonates impacting Stardust Al foils: Facilitating the search for cometary water", *Meteoritics & Planetary Science* **50**, 2003-2023, URL https://doi.org/10.1111/maps.12568.

Zhukovska S., Gail H.-P., & Trieloff M. (**2008**), "Evolution of interstellar dust and stardust in the solar neighbourhood", *Astronomy & Astrophysics*, **479**, 453-480, URL https://doi.org/10.1051/0004-6361:20077789.

Zinner E. (**2014**), "Presolar Grains", in K. K. Turekian & H. D. Holland (Eds.), "Treatise on Geochemistry", chapter 1.04, 181-213, Elsevier, 2nd edition, URL https://doi.org/10.1016/B978-0-08-095975-7.00101-7.

Zolensky M. E., Zega T. J., Yano H., Wirick S., Westphal A. J., Weisberg M. K., Weber I., Warren J. L., Velbel M. A., Tsuchiyama A., Tsou P., Toppani A., Tomioka N., Tomeoka K., Teslich N., Taheri M., Susini J., Stroud R., Stephan T., Stadermann F. J., Snead C. J., Simon S. B., Simionovici A., See T. H., Robert F., Rietmeijer F. J. M., Rao W., Perronnet M. C., Papanastassiou D. A., Okudaira K., Ohsumi K., Ohnishi I., Nakamura‐Messenger K., Nakamura T., Mostefaoui S., Mikouchi T., Meibom A., Matrajt G., Marcus M. A., Leroux H., Lemelle L., Le L., Lanzirotti A., Langenhorst F., Krot A. N., Keller L. P., Kearsley A. T., Joswiak D., Jacob D., Ishii H., Harvey R., Hagiya K., Grossman L., Grossman J. N., Graham G. A., Gounelle M., Gillet P., Genge M. J., Flynn G., Ferroir T., Fallon S., Ebel D. S., Dai Z. R., Cordier P., Clark B., Chi M., Butterworth A. L., Brownlee D. E., Bridges J. C., Brennan S., Brearley A., Bradley J. P., Bleuet P., Bland P. A., & Bastien R. (**2006**), "Mineralogy and petrology of comet 81P/Wild 2 nucleus samples", *Science* **314**, 1735-1739, URL https://doi.org/10.1126/science.1135842.

Zolensky M., Nakamura-Messenger K., Fletcher L., & See T. (**2008a**), "Curation, spacecraft recovery, and preliminary examination for the Stardust mission: A perspective from the curatorial facility", *Meteoritics & Planetary Science* **43**, 5-21, URL https://doi.org/10.1111/j.1945-5100.2008.tb00607.x.

Zolensky M., Nakamura-Messenger K., Rietmeijer F., Leroux H., Mikouchi T., Ohsumi K., Simon S., Grossman L., Stephan T., Weisberg M., Velbel M., Zega T., Stroud R., Tomeoka K., Ohnishi I., Tomioka N., Nakamura T., Matrajt G., Joswiak D., Brownlee D., Langenhorst F., Krot A.,

Kearsley A., Ishii H., Graham G., Dai Z. R., Chi M., Bradley J., Hagiya K., Gounelle M., Keller L., & Bridges J. (**2008b**), "Comparing Wild 2 particles to chondrites and IDPs", *Meteoritics & Planetary Science* **43**, 261-272, URL https://doi.org/10.1111/j.1945-5100.2008.tb00621.x.

Appendix

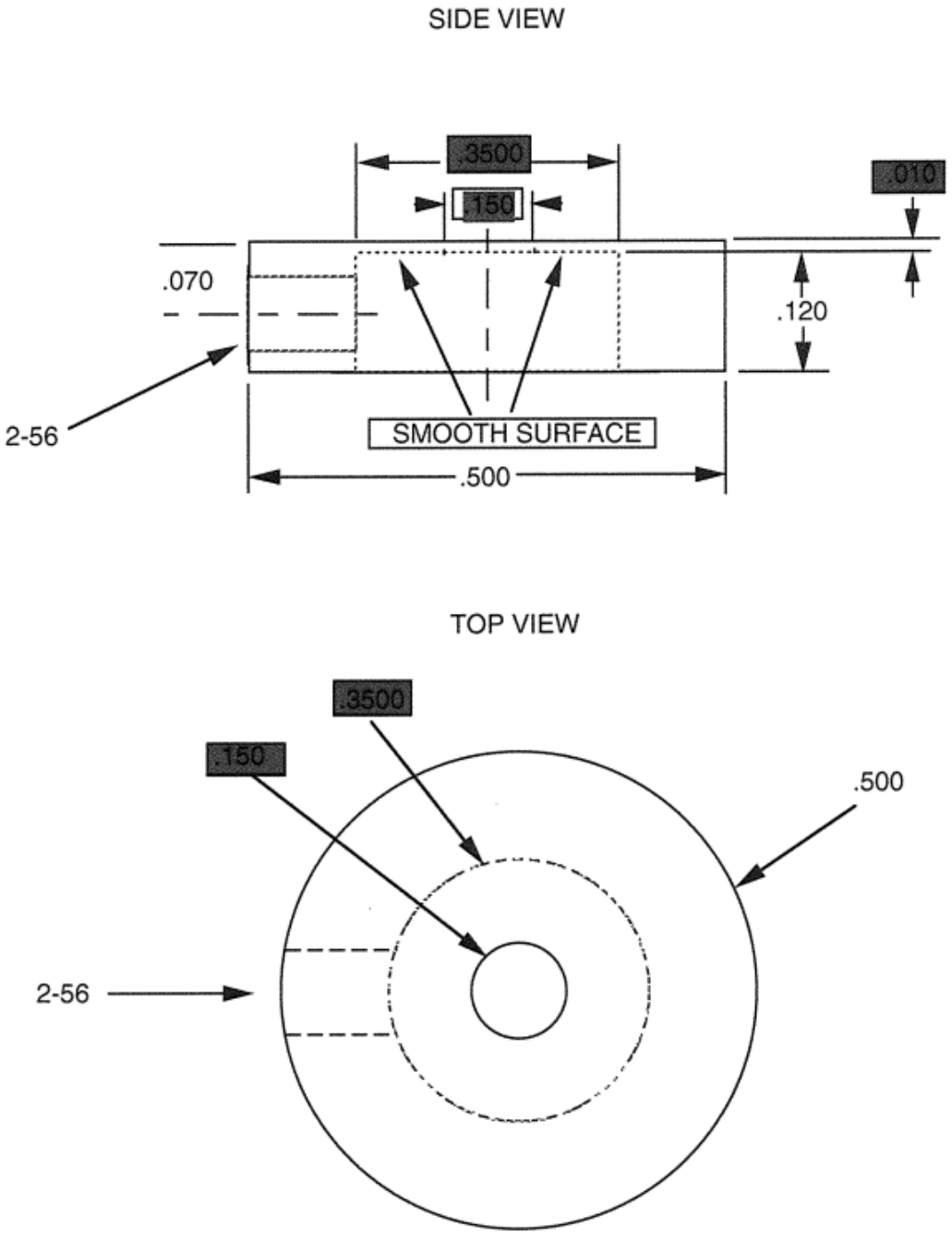

FIGURE A.1: First part of the schematics for the Cu base and cap designed for housing the aerogel, TEM grid, and SiN window for ashing experiments. All dimensions are in inches.

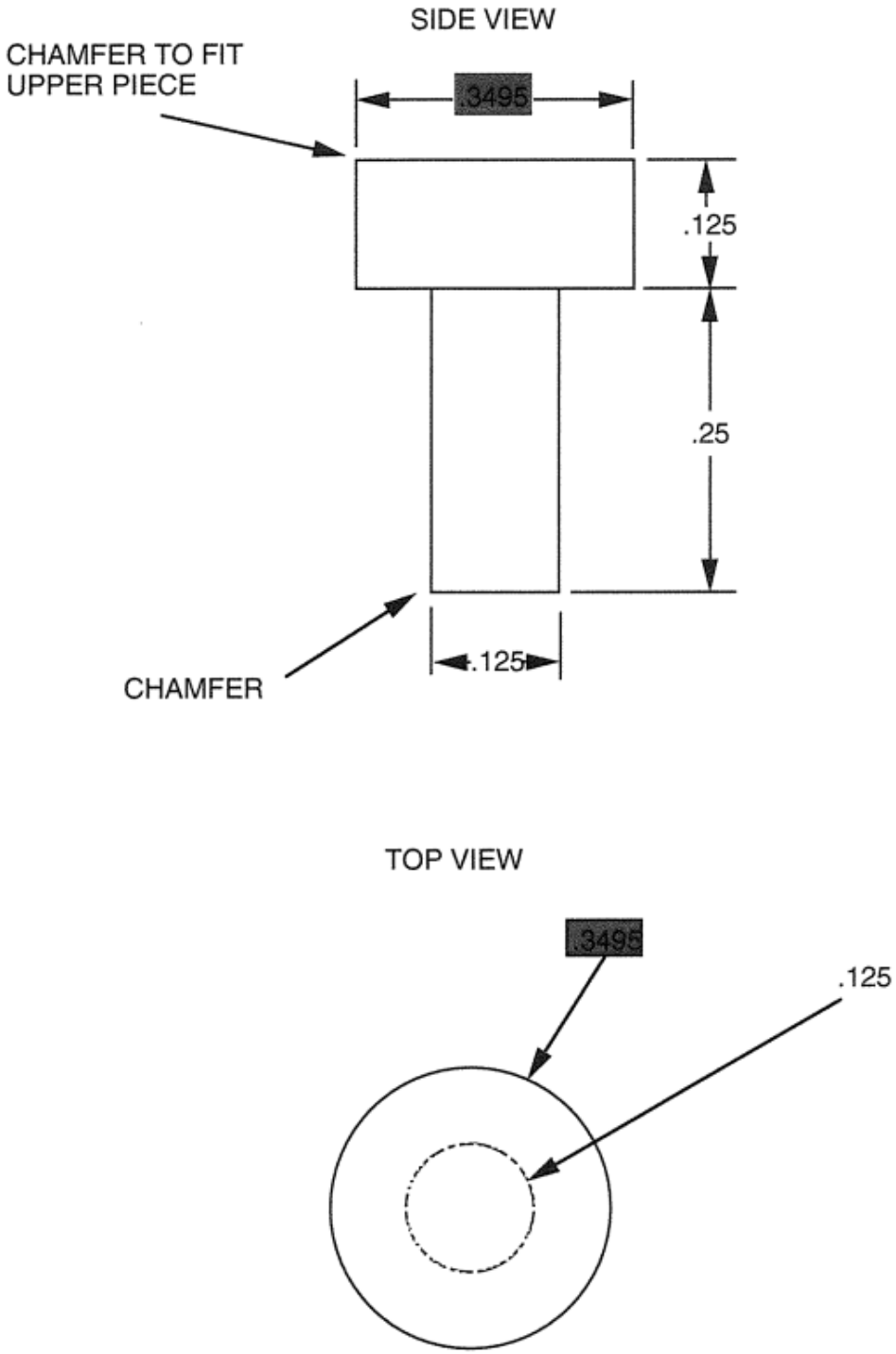

FIGURE A.2: Second part of the schematics for the Cu base and cap designed for housing the aerogel, TEM grid, and SiN window for ashing experiments. All dimensions are in inches.